Universiteit
Leiden
The Netherlands

Resolving the building blocks of galaxies in space and time

Clauwens, B.J.F.; Clauwens B.J.F.

Citation

Clauwens, B. J. F. (2017, December 6). *Resolving the building blocks of galaxies in space and time*. *Casimir PhD Series*. Retrieved from https://hdl.handle.net/1887/56022

Version:	Not Applicable (or Unknown)
License:	Licence agreement concerning inclusion of doctoral thesis in the Institutional Repository of the University of Leiden
Downloaded from:	https://hdl.handle.net/1887/56022

Note: To cite this publication please use the final published version (if applicable).

Cover Page

Universiteit Leiden

The handle http://hdl.handle.net/1887/56022 holds various files of this Leiden University dissertation.

Author: Clauwens, B.J.F.
Title: Resolving the building blocks of galaxies in space and time
Issue Date: 2017-12-06

Resolving the building blocks of galaxies in space and time

De opbouw van sterrenstelsels in ruimte en tijd

Proefschrift

ter verkrijging van
de graad van Doctor aan de Universiteit Leiden,
op gezag van Rector Magnificus prof. mr. C.J.J.M. Stolker,
volgens besluit van het College voor Promoties
te verdedigen op woensdag 6 december 2017
klokke 13:45 uur

door

Bartolomeüs Johannes Firmin Clauwens
geboren te Veghel
in 1981

Promotores:	Prof. dr. J. Schaye	
	Prof. dr. M. Franx	
Promotiecommissie:	Prof. dr. P. van Dokkum	(Yale University, New Haven, U.S.A.)
	dr. P. A. Torrey	(MIT, Cambridge, U.S.A.)
	Prof. dr. S. C. Trager	(Rijksuniversiteit Groningen)
	dr. C. A. Correa	
	Prof. dr. E. R. Eliel	
	Prof. dr. H. J. A. Röttgering	

Casimir PhD series, Delft-Leiden 2017-43
ISBN: 978-90-8593-327-4
An electronic version of this thesis can be found at https://openaccess.leidenuniv.nl.

The work described in this thesis is part of the Leiden de Sitter Cosmology program that is funded by the Netherlands Organisation for Scientific Research (NWO).

Omslagontwerp: Bart Clauwens. The cover image is based on a picture of Messier 101, which is comprised of 51 individual exposures with the Hubble Space Telescope in addition to ground-based observations from the Canada France Hawaii Telescope and the National Optical Astronomy Observatory. Credit for Hubble Image: NASA, ESA, K. Kuntz (JHU), F. Bresolin (University of Hawaii), J. Trauger (Jet Propulsion Lab), J. Mould (NOAO), Y.-H. Chu (University of Illinois, Urbana), and STScI. Credit for CFHT Image: Canada-France-Hawaii Telescope/ J.-C. Cuillandre/Coelum. Credit for NOAO Image: G. Jacoby, B. Bohannan, M. Hanna/ NOAO/AURA/NSF. For artistic purposes I have inverted the colours in the image, thus making the black background appear white and the light-blue star-forming regions appear dark-brown.

Contents

1 Introduction **1**
1.1 The study of galaxy formation 1
1.1.1 Galaxies 1
1.1.2 The building blocks of galaxies 2
1.2 This thesis 11
1.2.1 Chapter 2: An assessment of the evidence from ATLAS^{3D} for a variable initial mass function 11
1.2.2 Chapter 3: Implications of a variable IMF for the interpretation of observations of galaxy populations 12
1.2.3 Chapter 4: A large difference in the progenitor masses of active and passive galaxies in the EAGLE simulation . . . 12
1.2.4 Chapter 5: The average structural evolution of massive galaxies can be reliably estimated using cumulative galaxy number densities 13
1.2.5 Chapter 6: The three phases of galaxy formation 14

2 An assessment of the evidence from ATLAS^{3D} for a variable initial mass function **17**
2.1 Introduction 18
2.2 The ATLAS^{3D} Survey 20
2.3 The ATLAS^{3D} evidence for a non universal IMF 21
2.4 Correlations with the IMF mismatch parameter 29
2.5 Galaxy Stellar Mass Function and mass completeness 31
2.6 Mass completeness effects on the IMF dispersion trend 33
2.7 Distance effects and SBF calibration 36
2.8 Conclusions 46

3 Implications of a variable IMF for the interpretation of observations of galaxy populations 51
3.1 Introduction . . . 52
3.2 Method . . . 56
3.2.1 The Vazdekis IMF . . . 56
3.2.2 The matched low-end IMF . . . 60
3.2.3 Star formation rates . . . 63
3.2.4 Stellar masses . . . 65
3.3 Star Formation Main Sequence . . . 67
3.4 Galaxy Stellar Mass Function . . . 73
3.5 Metals . . . 77
3.6 Rapid Galaxy Quenching . . . 81
3.7 Conclusions . . . 83
3.8 Appendix . . . 86

4 A large difference in the progenitor masses of active and passive galaxies in the EAGLE simulation 91
4.1 Introduction . . . 91
4.2 Simulation . . . 93
4.3 Results . . . 95
4.4 Conclusions . . . 102

5 The average structural evolution of massive galaxies can be reliably estimated using cumulative galaxy number densities 105
5.1 Introduction . . . 105
5.2 Method . . . 107
5.3 Results . . . 110
5.4 Comparison with observations . . . 113
5.5 Conclusions . . . 115

6 The three phases of galaxy formation 119
6.1 Introduction . . . 119
6.2 The EAGLE simulation . . . 123
6.3 Kinematic morphology . . . 124
6.4 Morphology evolution . . . 128
6.5 The origin of bulge stars . . . 133
6.6 The effects of star formation and mergers on morphology . . . 135
6.7 The merger contribution to spheroid and disk formation rates . . . 138
6.8 Conclusions . . . 143
6.9 Appendix A . . . 146

6.10 Appendix B 146

7 Samenvatting in het Nederlands **150**
7.1 De vorming van sterrenstelsels 150
7.1.1 Sterrenstelsels 150
7.1.2 De bouwstenen van sterrenstelsels 151
7.2 Dit proefschrift 157
7.2.1 Hoofdstuk 2: Een analyse van het bewijs van ATLAS^{3D} voor een variabele initiële massa functie 157
7.2.2 Hoofdstuk 3: Implicaties van een variabel IMF voor de interpretatie van waarnemingen van populaties van sterrenstelsels 158
7.2.3 Hoofdstuk 4: Een groot verschil in de progenitor massa's van actieve en passieve sterrenstelsels in de EAGLE simulatie 158
7.2.4 Hoofdstuk 5: De gemiddelde structurele evolutie van massieve sterrenstelsels kan op een betrouwbare manier bepaald worden op basis van cumulatieve getals-dichtheden van sterrenstelsels. 159
7.2.5 Hoofdstuk 6: De drie fases in de vorming van sterrenstelsels 160

Bibliography **162**

Curriculum Vitae **182**

List of publications **184**

Acknowledgements **186**

In the beginning the Universe was created. This has made a lot of people very angry and been widely regarded as a bad move.

-- Douglas Adams[1]

[1](Adams 1986)

1 Introduction

1.1 The study of galaxy formation

1.1.1 Galaxies

Galaxies are enormous conglomerations of worlds, housing trillions of stars and planets, and possibly even more sentient beings that call their planet, their solar system or their galaxy `home'. But to us, astrophysicists, galaxies are mere test particles that outline the large scale structure of the Universe. They are vague blobs of light in the night sky of which we try to take a beautiful picture. After staring at many of these pictures, over time, these galaxies come to life. We envisage them as living creatures, breathing gas and forming new tissue in the form of stars and planets.

These creatures grow up in a harsh world of eat or be eaten. If their environment does not devour them whole, it will still shape them in a multitude of non-lethal ways. Yet, even more important for their development are internal processes. These processes take place inside the stellar birth clouds, the individual stars or even inside the individual atoms that make up a galaxy. We try to learn about these processes by creating virtual galaxies that live as a sort of lab rats inside our largest supercomputers.

Despite the fact that our conception of galaxies becomes ever more sophisticated, in many of our scientific graphs they are reduced to single data points in a vast point cloud, which you could say is somewhat of a simplification. Surely, our own Milky Way will appear in many similar graphs across the Universe, without anyone giving two thoughts about us living here on planet earth. For the purpose of this thesis galaxies will be these sophisticated, yet highly simplified mental pictures we make of them, devoid of emotional attachment and a real sense of place, time and belonging. This is partly due to a lack of our imagination, but more importantly

due to a lack of information.

1.1.2 The building blocks of galaxies

The precision with which we observe all but the closest galaxies does not allow us to count the individual stars that produce the light of a galaxy, nor does our short lifespan allow us to see these galaxies evolve and interact. We rely on a myriad of techniques and models to distill this information from what is given to us by the night sky. Here I will give a short overview of the accomplishments of the scientific community in resolving the basic building blocks of galaxies both in space and in time. This is not meant to be a balanced account of all the factors that contribute to galaxy evolution, but rather focuses on the main concepts needed to understand the subsequent chapters.

Stars

We believe that galaxies consist of many components, a hot gaseous halo, cool clumps of molecular gas, a dark matter halo and massive (central) black holes, but there is really only one component that is crucial for a stand-alone bound structure of matter to be classified as a galaxy: it must contain many stars. Observations indicate that many can mean anything from roughly 10^3 to 10^{12} stars. There are many more galaxies with small or modest masses than there are massive ones, but still most stars reside in galaxies at the massive end. Our sun is no exception in that regard, since the Milky Way is estimated to house $\approx 2.5 \times 10^{11}$ stars.

Not all stars are born equal. They have a variety of intrinsic properties such as mass, angular momentum, metallicity[1] and age and secondary properties that depend on those such as size, luminosity and temperature. The most important property by far is the mass of a star. Stars are born with a large range of masses ($0.08\mathrm{M}_\odot \lesssim M \lesssim 120\mathrm{M}_\odot$)[2] which determine their appearance and fate.

Stars with small masses lead a quiet and long life, whereas massive stars shine brightly, burn up their fuel quickly and die in massive explosions that inject large amounts of hot metal-enriched gas into the interstellar matter. The difference in energy output between low- and high-mass galaxies is quite dramatic. The luminosity of a star scales roughly with the 3.5^{th} power of its mass, meaning that the luminosity per unit of mass scales roughly with the 2.5^{th} power of the mass. There is only a finite amount of energy that can be released from any unit of stellar mass,

[1] The metallicity of a star, gas cloud or other astronomical object is the fraction of elements heavier than helium. Oxygen is thus considered to be a metal for astronomy's sake. The exact definition of metallicity can differ widely, depending on the way in which it is observed.

[2] The commonly used unit of mass in astronomy is the solar mass, $\mathrm{M}_\odot = 1.99 \times 10^{30}\mathrm{kg}$.

after which a star enters its final stages. The faster a star burns its energy, the faster this end will come. The lifetime of a star is thus roughly proportional to the -2.5th power of the mass. This means that a star that is 10 times more massive will appear $\approx$ 3000 times brighter (with a hotter blue colour), but will have a lifetime reduced by a factor $\approx$ 300. In practice this means that the light of a galaxy is dominated by young massive stars, as long as they are around, after which the galaxy will turn red and less luminous. Even for galaxies that are no longer actively forming stars, most of the light will come from the most massive, still present stars. These stars may constitute only a small fraction of the mass, since a significant fraction of the stellar mass could be locked up in dwarf stars and in the remnants of the deceased massive stars such as neutron stars and black holes.

The rate at which stars return energy and metals to the gas clouds from which they are born thus depends strongly on the mass of those stars. We call this process `stellar feedback'. Stars are born from very cold ($\approx$ 30 K) and dense clouds of molecular gas. This feedback, which can come in the form of radiation, stellar winds, cosmic rays or supernovae explosions, is thought to either heat up or blow away those stellar birth clouds, thereby regulating the rate at which stars form. Without stellar feedback, hydrodynamical simulations are unable to prevent runaway star formation, but this feedback can also locally enhance star formation by compressing the interstellar matter in shock waves and it can enhance star formation at later times by injecting the interstellar matter with lots of metals, which are effective coolants.

Observations of the stellar content in the local region of the Universe for which we can count stars (e.g. the Milky Way, its globular clusters, young clusters in Andromeda) indicate that the distribution of stellar masses at birth is the same in different environments. We call this distribution of the masses with which stars are born the initial mass function (IMF). See section 3.2 for a precise definition and Fig. 3.1 for the shape of the IMF in our local region, as derived by Chabrier (2003). For most of the time since the introduction of the IMF by Salpeter (1955), the observationally driven consensus has been that the IMF is universal, meaning that it is the same across the Universe and thus does not depend on the specifics of the stellar birth clouds.

A universal IMF is convenient for the modelling of stellar populations and galaxies as a whole. Generally the assumption is that the stellar content of a galaxy is a superposition of multiple simple stellar populations (SSPs): populations with a single metallicity and age, evolved from a universal IMF. Observational models for matching galaxy spectra generally assume a single metallicity and a simple functional form for the superposition of different stellar ages. In hydrodynamic simulations typically each virtual stellar particle represents a simple stellar pop-

ulation. The galactic stellar content is then given by a superposition over many particles, which can each have a different age and metallicity.

However, in the last decade, the universality of the IMF has been questioned as a result of a variety of observations. Many teams have made an effort to constrain the IMF either on galactic scales or in extreme environments by using creative methods that do not involve the counting of stars. There are now many claims of observed IMF variations, which are both exciting but also hard to reconcile with each other. The most influential works are by van Dokkum and Conroy (2012) & Conroy and van Dokkum (2012) and by Cappellari et al. (2012).

Van Dokkum and Conroy (2012), Conroy and van Dokkum (2012) estimate the IMF of early-type[3] galaxies by fitting very precise models of absorption lines, including lines that appear differently in dwarf stars than in giant stars, to the integrated spectra of these galaxies.

Cappellari et al. (2012) use a completely different method to estimate the IMF. They try to weigh the central regions of nearby early-type galaxies by modelling the stellar motions. They then ascribe any gravitational mass, above what is expected from the stars, central black hole and dark matter, to a surplus of `invisible' stars.

Both groups conclude, loosely speaking, that galaxies with high velocity dispersions (indicative of high masses) tend to have an IMF with a surplus of `invisible' stellar mass with respect to the Chabrier IMF. For van Dokkum and Conroy (2012); Conroy and van Dokkum (2012) this surplus is due to dwarf stars, whereas for Cappellari et al. (2012) it could be due to either dwarf stars or stellar remnants. Both works seem to be in rough agreement. However, they do not agree on the specifics. Sections 2.1 and 3.1 provide a more in-depth discussion of the current state of affairs regarding observations that can be interpreted as evidence for IMF variations.

Mergers

It takes a long time to grow a galaxy. In fact, for most galaxies it takes the age of the Universe to grow them to their current size and mass. In part, this growth occurs in isolation from other galaxies. Gas cools and falls onto a galaxy. It then generally forms a rotating cold gas disk from which stars are born. This star formation can either take place gradually or in episodes of enhanced star formation alternated with episodes during which feedback temporarily reduces the star formation. Observations of the star-formation rate as a function of galaxy mass indicate that star formation is well regulated. Galaxies form new stars at a rate roughly proportional

[3]The term `early-type' is used roughly interchangeably with `elliptical' or `spherical'. `Late-type' is used interchangeably with `disk' or `spiral'. See the `morphological components' subsection for a short introduction on galaxy classification based on morphology and/or colour.

to their mass. That is, unless they stop forming new stars altogether. This tight relation between the mass of a galaxy and its star formation rate is called the star forming main sequence (Brinchmann et al. 2004; Salim et al. 2007). It is not only in place at the present time, but also in the early Universe (albeit with a different normalisation). There is a completely different way in which galaxies can grow, however. They can grow by colliding into each other. This process, whereby typically a less massive galaxy is trapped in the gravitational field of a more massive one, after which both galaxies melt together, is called a merger.

Mergers can have an effect on the shape of a galaxy. It is thought that mergers of a mass ratio close to unity can deform an ordered, rotating stellar disk into a more random spheroidal shape. Figure 1.1 shows an image of two galaxies that are in the process of merging. Mergers also have a direct effect on the gas in between the stars, the interstellar matter, because this gas actually collides (in contrast to the stars that just fly past each other). This can lead to a compression of the gas, followed by cooling and a phase of enhanced star formation. During a merger a galaxy can thus grow in mass both by accreting old stars and by forming new stars. This last mode, which would appear as irregular star formation triggered by mergers, is subject to the same observational constraint set by the star forming main sequence that also applies to star formation in isolation, which sets an upper limit to the fluctuations in the star-formation rate allowed by observations.

A typical galaxy will undergo many minor and major mergers over its lifetime. Tracing a galaxy backward in time is only possible in a literal sense for galaxies in a cosmological simulation, for which we have access to the whole history. A typical galaxy, when followed backward in time, will branch out into many smaller progenitor galaxies, the building blocks out of which the galaxy has assembled. The `family tree' of a galaxy, thus obtained, is called a merger tree. In this merger tree we define the most massive branch as the `main branch' consisting of the main progenitor galaxies (at any one time only one progenitor galaxy is deemed the main progenitor). In most cases this main progenitor is clearly the core galaxy that acted as the seed for the present-day galaxy. However, in the rare cases where two equally massive galaxies merge, the choice of which progenitor is the main progenitor is somewhat arbitrary. Galaxy evolution is generally understood to mean the evolution of the properties of the main progenitor. All other progenitors `die' at some point in time.

Within the ΛCDM[4] cosmology the rate at which galaxies merge is relatively

[4]This is the current cosmological model, which is assumed for all `observables' such as intrinsic luminosities of galaxies, sizes, ages, masses and star formation rates, with the exception of raw data such as apparent luminosities and spectral line ratios. Λ stands for the `dark energy' component or the cosmological constant introduced by Einstein. It represents an accelerated expansion of the current Universe. CDM stands for cold dark matter, the dominant component of gravitational matter in the

Figure 1.1: The interacting galaxy pair NGC 6621 (bottom) and NGC 6622 (top). Released by the Hubble Space Telescope in April 2008. Credits: NASA, ESA, Hubble Heritage Team (STScI/AURA).

well understood. Galaxies are believed to be dominated in mass by a cold dark matter component. This component is less concentrated than the ordinary matter, since it can not radiate away its energy, cool and contract, because, as far as we know, it only interacts through gravity. Each galaxy is believed to reside in a dark matter halo. Precisely because dark matter only reacts to gravity, it is much easier to simulate. Simulations (e.g. Genel et al. 2009) indicate that dark matter halos assemble partly through smooth accretion and partly through mergers in a bottom-up fashion, with smaller halos merging earlier on average than larger halos. The important point here is that the assembly of dark matter halos does not care much about the ordinary matter that resides within these halos. Within the ΛCDM cosmology the merger rates are thus derivable from first principles and do not share many of the uncertainties that plague our understanding of the much more complex `ordinary' matter. The main uncertainty in deriving galaxy merger rates within the ΛCDM cosmology lies in the translation from dark matter halo masses to the stellar masses of the galaxies that reside within them. Not all dark matter halos contain the same fraction of stellar mass, thus a dark matter merger mass ratio cannot be directly translated into a galaxy merger mass ratio. One way to circumvent this problem is to assume that, at any time, the stellar masses of the observed galaxy population can be mapped monotonically onto the theorised dark-matter halo population, with the most massive galaxy in a given volume residing in the most massive dark-matter halo, etc. At the massive end this would mean that a relatively wide range of halo masses is populated with a relatively narrow range of galaxy masses. Mergers between those galaxies will thus have a merger ratio closer to unity when defined as a stellar mass ratio rather than a dark matter mass ratio. Merger rates and ratios can also be determined observationally by counting interacting galaxy pairs and galaxies that show signs of morphological disturbances which could have been caused by a recent merger, but this is not a very exact science as it depends on assumptions about the involved merger time scales and the extent to which mergers of varying mass ratios cause morphological disturbances.

Morphological components

Galaxies come in various shapes and sizes. Some show a very organised structure, a flat rotating stellar disk, while others appear irregular, may be in the process of merging or have a spheroidal morphology with stars moving on highly radial orbits. Most of the stellar mass in the Universe can, however, be attributed to two morphological components: disks and spheroids. Most present-day galaxies classify either as a pure disk, see Fig. 1.2, as a disk with a central spheroid (a bulge), see Fig. 1.3, or as a pure spheroid (an elliptical galaxy), see Fig. 1.4.

Universe.

Figure 1.2: The disk galaxies NGC 4302 (left, seen edge-on) and NGC 4298 (right, seen at an angle). The image is taken by the Wide Field Camera 3 (WFC3) on the Hubble Space Telescope in between January 2 and January 22, 2017. The image is comprised of observations in three visible light bands. Credits: NASA, ESA, STScI.

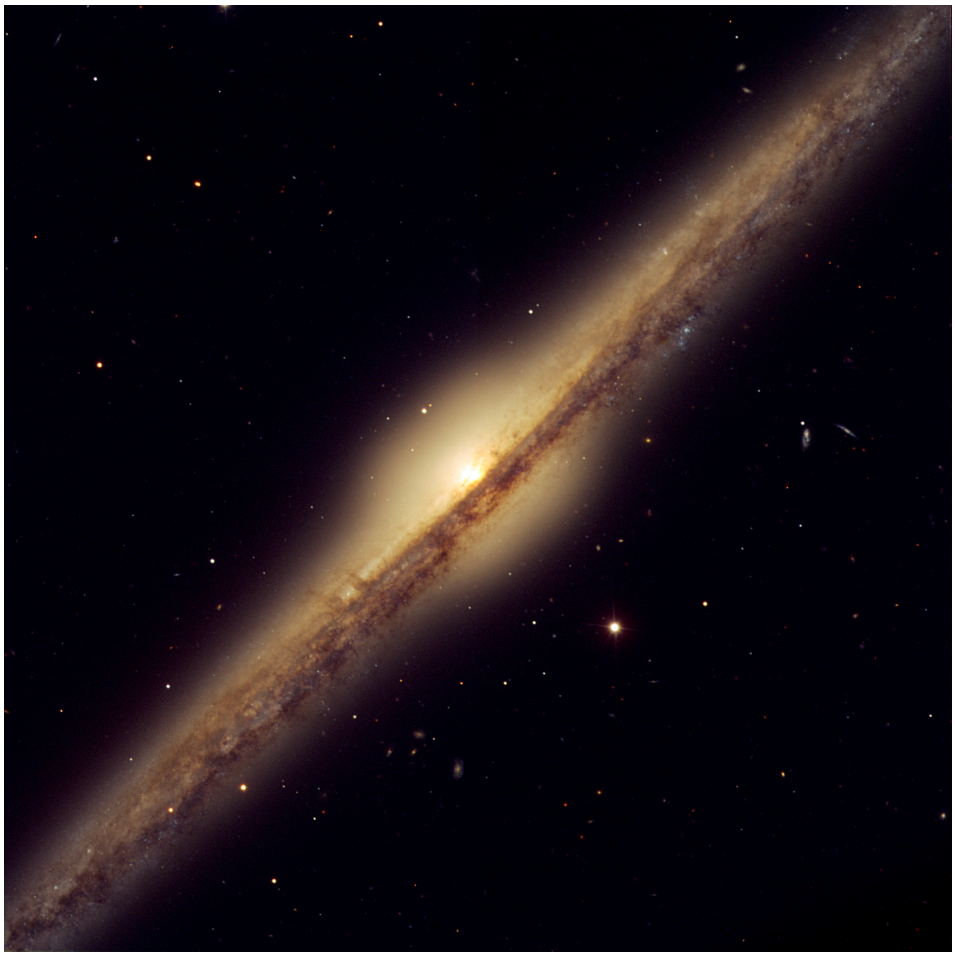

Figure 1.3: Disk galaxy NGC 4565 which has a prominent central stellar bulge. This image was taken by the FORS1 and FORS2 instruments on the very large telescope (VLT) in Chile and has been released in April 2005. The image is comprised of observations in visible and near-infrared bands. Credit: ESO.

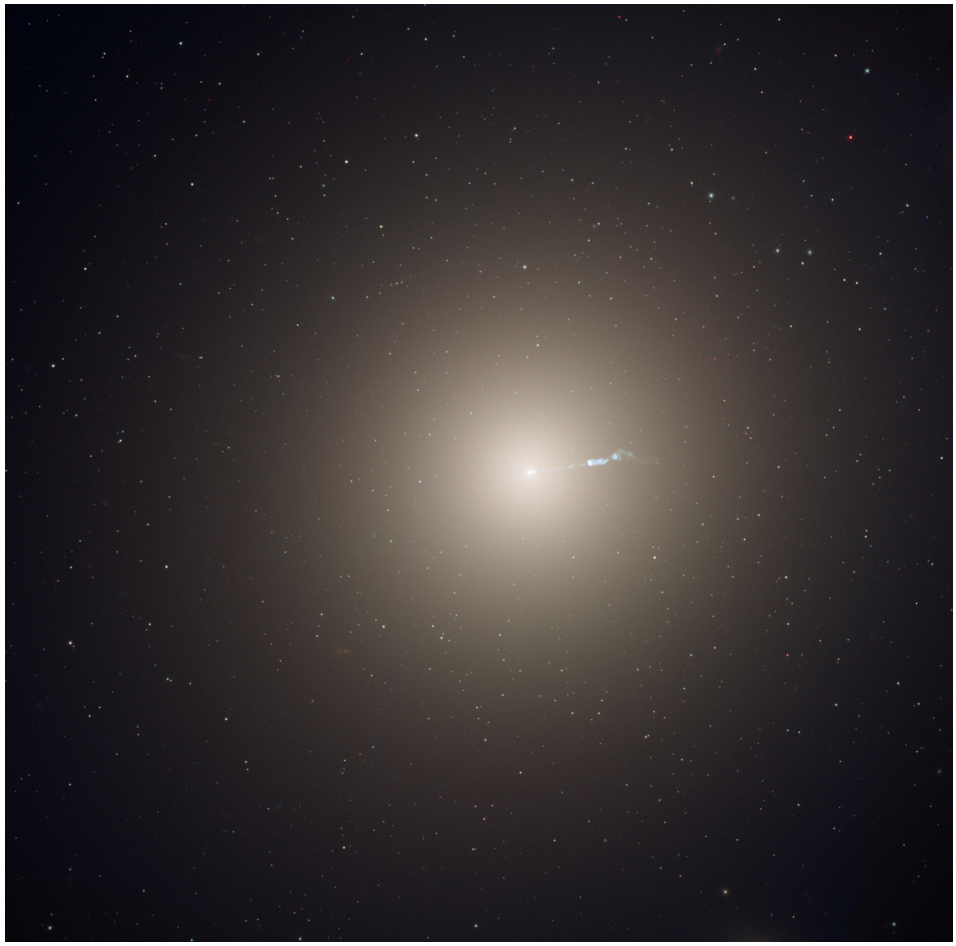

Figure 1.4: The elliptical galaxy M87, the most massive galaxy in the nearby Virgo Cluster. This image was taken with the Advanced Camera for Surveys on the Hubble Space Telescope in 2003 and 2006. The image is comprised of observations in visible and infrared bands. Credits: NASA, ESA, Hubble Heritage Team (STScI/AURA).

Galaxy morphology is linked to colour. The colour distribution of galaxies is roughly bimodal. Galaxies can be classified, based on their colour, into `blue cloud' galaxies and `red sequence' galaxies (Strateva et al. 2001; Bell et al. 2004). Blue cloud galaxies are actively forming stars and have predominantly a disk-like morphology. Their light is dominated by massive young stars. Red-sequence galaxies have stopped forming stars and have predominantly a spheroidal morphology. Their light is dominated by older intermediate-mass stars. The central spheroids of disk galaxies (bulges) also tend to be red. They consist mainly of old stars and show no or very little ongoing star formation.

There are only few galaxies that fall in between the `blue cloud' and `red sequence' categories in the so-called `green valley'. This means that the transition from the blue cloud to the red sequence must happen relatively fast. One of the main challenges of galaxy formation is to recreate a representative population of galaxies that shares this bimodality, in the controlled environment of a cosmological simulation.

Section 6.1 gives a more detailed overview of the observed morphological components of galaxies, the way in which they are determined and their potential formation mechanisms.

1.2 This thesis

1.2.1 Chapter 2: An assessment of the evidence from ATLAS^{3D} for a variable initial mass function

Cappellari et al. (2012) determine IMF variations by weighing the centres of 260 nearby early-type galaxies. These galaxies have been observed with the SAURON integral field spectrograph on the William Herschel Telescope. This provides us, after some data reduction, with a two-dimensional image in which each pixel contains a distribution of the stellar velocities in the line-of-sight direction. Cappellari et al. (2012) then model these stellar motions under the assumption that they are in dynamical equilibrium and trace the underlying mass distribution. They subtract the expected dark matter mass to obtain an estimate of the gravitational mass of the stars in these galaxy centres. An independent `photometric' estimate of the stellar mass is given by fitting models of galaxy spectra to the integrated light from these galaxy centres. These models build up the spectrum of a galaxy as a sum over the spectra of individual stars, for which they assume a universal IMF. Differences between the gravitational stellar mass and the photometric stellar mass are then attributed to variations in the IMF.

This is a risky procedure, because differences in the two mass estimates can

also be due to a variety of measurement and modelling errors. An underestimate of those errors would lead to an overestimate of the intrinsic IMF variations.

This chapter investigates these errors. We show that the results of Cappellari et al. (2012) can be replicated to a large degree by assuming a universal IMF in combination with larger modelling errors. Furthermore, we investigate completeness effects and selection effects. We report an unexpected trend of the inferred IMF variations with the distance to earth and we estimate how the proposed IMF variations, if real, would alter the mass distribution of the observed galaxy population in the Universe[5].

1.2.2 Chapter 3: Implications of a variable IMF for the interpretation of observations of galaxy populations

Martín-Navarro et al. (2015d) determine the IMF in galaxy regions based on the analysis of IMF-sensitive spectral features in the CALIFA survey. Their sample covers a large range of metallicities and they report a strong dependence of the inferred IMF on metallicity.

In this chapter we investigate what the proposed metallicity-dependent IMF would mean for the interpretation of observed galaxy properties. We apply their IMF on a galaxy-by-galaxy basis to a sample of 186,886 galaxies from the Sloan Digital Sky Survey. We show that the implications for the star formation main sequence, the galaxy stellar mass function, and the mass-metallicity relation, depend strongly on assumptions about the functional form of the IMF and range from mild, but significant, to absolutely dramatic.

Furthermore, we investigate a scenario wherein star formation in the late, metal-rich, phase of galaxy evolution is dominated by dwarf stars. This could help to explain the bimodality in the observed galaxy population by, on the one hand, increasing the inferred star formation rates of these `dead' galaxies (thereby softening the intrinsic bimodality in star formation rates) and, on the other hand, decreasing the gas consumption time scale, resulting in a faster transition from the `blue cloud' to the `red sequence'.

1.2.3 Chapter 4: A large difference in the progenitor masses of active and passive galaxies in the EAGLE simulation

An important question in the field of galaxy formation is how to distill, from the observed evolving galaxy population, the typical evolution of individual galaxies.

[5]The number density of galaxies as a function of stellar mass, corrected for completeness effects, is called the galaxy stellar mass function (GSMF). It is characterised by a steep drop-off above $\approx 10^{10.75} M_{\odot}$. Most stellar mass in the Universe resides just below this drop-off.

If we had a precise method to do this, it would help us tremendously to trace and understand the buildup of galaxies and the associated evolution of their properties such as size, metallicity, morphology and star formation activity. Regrettably, such a precise method is not at hand. We have to rely on simplifying assumptions. Generally we use a method called `cumulative number density matching' which assumes that main progenitor galaxies can be identified based on their cumulative[6] number density.

The performance of this method can only be checked within a cosmological simulation, for which we have access to the full galaxy merger tree from the beginning of time. I was fortunate that during my years as a PhD student, the EAGLE cosmological simulation came to life (Schaye et al. 2015), which, in my view, is the first cosmological simulation that has a sufficient resemblance to the observed Universe that it can be confidently applied to this problem.

We find that, in the EAGLE simulation, the median stellar mass of main progenitors at early times depends strongly on the present-day star formation activity of the descendant galaxies (selected in a fixed mass bin). This is the case for present-day descendant galaxies with a stellar mass up to $10^{10.75}\mathrm{M}_{\odot}$.

If the same is true for the real Universe then this severely constrains the applicability of the `cumulative number density matching' method, at least in its current form. Moreover, it is hard to envision an extension to the method that solves this problem without relying on input from a cosmological hydrodynamic simulation/model (which would take away the main appeal of the method: that it only depends on observations and on robust dark-matter-only simulations).

1.2.4 Chapter 5: The average structural evolution of massive galaxies can be reliably estimated using cumulative galaxy number densities

In the previous chapter we have seen that the `cumulative number density matching' method is expected to be unreliable below $10^{10.75}\mathrm{M}_{\odot}$ due to a large difference in the progenitor masses of active and passive galaxies. For more massive galaxies this problem does not occur and we can expect the method to perform well.

However, for these massive galaxies there still is a large scatter in main progenitor masses. This makes it necessary to check the method applied to each galaxy property separately. The median/average property of the true main progenitor sample (with a broad mass distribution) might not be the same as the median/average

[6] Cumulative here refers to stellar mass, although other variables such as velocity dispersion are also used. The cumulative number density of any galaxy at any time is then defined as the number density of galaxies at the same time within a comoving volume (Mpc^{-3}) that have a stellar mass larger than the given galaxy.

property of a sample of galaxies selected at the median cumulative number density (with a narrow mass distribution).

We show that, despite this complication, cumulative number density matching works reasonably well when applied to the evolution of the density profile of massive galaxies in EAGLE. An improvement can be made by modelling also the expected scatter in main progenitor masses, based on dark-matter simulations only.

Furthermore, we apply the method to observations from UltraVISTA and CANDELS up to[7] $z = 5$. We infer that massive galaxies have grown in an inside-out manner since $z = 5$. Since $z = 2$ this inside-out trend is modest. Here the evolution of the observed galaxy profiles is more self-similar than it is in the EAGLE simulation.

1.2.5 Chapter 6: The three phases of galaxy formation

Although the morphology of galaxies has been studied extensively and we can categorise observed galaxies into very specific morphological types, the processes that determine galaxy morphology are not well understood. Stellar disks form from cold gas disks, but cosmological simulations show that their extent depends critically on the implementation of various feedback processes and can not, for the moment, be derived from first principles. For spheroids there is no shortage of hypothetical formation mechanisms, but at the moment it is not clear which mechanisms dominate where and when.

In this chapter we study the morphology transformations of galaxies in the EAGLE simulation, with an emphasis on the formation of spheroids. Feedback processes in EAGLE have been calibrated to reproduce the observed low-redshift mass-size relation, thus roughly reproducing the observed disk sizes (Schaye et al. 2015). Moreover the simulation contains a representative population of massive, red, elliptical galaxies (Correa, Schaye, Clauwens et al. 2017). It is thus a useful test bed to study the emergence of galaxy morphology.

By tracing the morphological buildup of the main progenitors of $10^{10.5}\mathrm{M}_\odot < M_* < 10^{12}\mathrm{M}_\odot$ galaxies, we find that galaxy formation in EAGLE is a three phase process. At low masses ($M_* \lesssim 10^{9.5}\mathrm{M}_\odot$) galaxies grow in a messy, disorganised way, mainly in merger-induced star formation episodes that result in spheroidal morphologies. In the mass range $10^{9.5}\mathrm{M}_\odot \lesssim M_* \lesssim 10^{10.5}\mathrm{M}_\odot$ galaxies enter quieter waters and build up a prominent stellar disk through in-situ star formation. During this phase bulges continue to grow. They consist mostly of stars formed in-situ, but their formation is largely triggered by merger activity. For $M_* \gtrsim 10^{10.5}\mathrm{M}_\odot$ galaxies enter their last phase. The in-situ star formation slows

[7] z stands for the redshift of the observed light. Redshift $z = 5$ refers to observations of galaxies seen at a time when the Universe was a factor $z + 1 = 6$ smaller (or a factor $6^3 = 216$ in volume).

down considerably while disk-dominated galaxies are transformed into spheroid-dominated galaxies under the influence of mergers.

All creation presupposes at its origin a sort of appetite that is brought on by the foretaste of discovery. This foretaste of the creative act accompanies the intuitive grasp of an unknown entity already possessed but not yet intelligible, an entity that will not take definite shape except by the action of a constantly vigilant technique.

-- Igor Stravinsky[8]

[8](Stravinsky 1942)

2 An assessment of the evidence from ATLAS^{3D} for a variable initial mass function

Based on:
Bart Clauwens, Joop Schaye, Marijn Franx
An assessment of the evidence from ATLAS^{3D} for a variable initial mass function
Published in MNRAS

The ATLAS^{3D} Survey has reported evidence for a non-universal stellar initial mass function (IMF) for early type galaxies (ETGs) (Cappellari et al. 2012, 2013b,a). The IMF was constrained by comparing stellar mass measurements from kinematic data with those from spectral energy distribution (SED) fitting. Here we investigate possible effects of scatter in the reported stellar mass measurements and their potential impact on the IMF determination. We find that a trend of the IMF mismatch parameter with the kinematic mass to light ratio, comparable to the trend observed by Cappellari et al. (2012), could arise if the Gaussian errors of the kinematic mass determination are typically 30%. Without additional data, it is hard to separate between the option that the IMF has a true large intrinsic variation or the option that the errors in the determination are larger than anticipated. A correlation of the IMF with other properties would help to make this distinction, but no strong correlation has been found yet. The strongest correlation is with velocity dispersion. However, it has a large scatter and the correlation depends on sample selection and distance measurements. The correlation with velocity dispersion could be partly caused by the colour-dependent calibration of the surface brightness fluctuation distances of Tonry et al. (2001). We find that the K-band luminosity limited ATLAS^{3D} Survey is incomplete for the highest M/L galaxies below $10^{10.3}\mathrm{M}_{\odot}$. There is a significant IMF - velocity dispersion trend for galaxies with SED masses above this limit, but no trend for galaxies with kinematic masses above this limit. We also find an IMF trend with distance, but no correlation between nearest neighbour ETGs, which excludes a large environmental dependence. Our findings do not rule out the reported IMF variations, but they suggest that further study is needed.

2.1 Introduction

The stellar initial mass function (IMF) has historically been assumed to be universal, in the sense that it does not depend on environment. The IMF was assumed to be independent of galaxy age, galaxy type, metallicity or any other astrophysical variable, with the possible exception of population III stars and stars forming near the galactic center e.g. (Kroupa et al. 2013). Since the exact mechanisms that cause the formation of stars of varying masses from an initial cloud of gas and dust are not well understood, the assumption of the universality of the IMF is partially motivated by a desire for simplicity, but it is also supported by direct measurements of stellar mass distributions in our immediate vicinity e.g. (Chabrier 2003; Kroupa et al. 2013; Bastian et al. 2011; Kirk and Myers 2011). It is reasonable to assume that the IMF does differ in more extreme environments, but this is hard to measure directly.

On a galactic scale, evidence has recently been found in favour of a non-universal IMF for early type galaxies (ETGs), typically depending on the velocity dispersion of the galaxy. The evidence comes partly from differing spectral features of low- and high-mass stars (La Barbera et al. 2013; van Dokkum and Conroy 2012; Conroy and van Dokkum 2012; Pastorello et al. 2014) and partly from mass measurements of stellar systems via strong gravitational lensing (Treu et al. 2010; Brewer et al. 2012; Oguri et al. 2014; Barnabè et al. 2013) or the modeling of stellar kinematics (Conroy et al. 2013; Tortora et al. 2013; Dutton et al. 2013; Cappellari et al. 2012, 2013b,a). However, the nearest known strong lens provides conflicting evidence (Smith and Lucey 2013) and a recent study of the low mass X-ray binary population in eight ETGs also points towards a universal IMF (Peacock et al. 2014). Conroy et al. (2013) find good agreement between IMF variations from spectral features and from kinematics for stacks of galaxies. On the other hand, a recent comparison between dynamical and spectroscopic results by Smith (2014) shows that the IMF measurements of Conroy and van Dokkum (2012) and those of Cappellari et al. (2013a) agree only superficially and not on a galaxy by galaxy basis. Also, a recent detailed spectral analysis of three nearby ETGs by Martín-Navarro et al. (2015a) found at least one massive galaxy (NGC4552) for which the IMF varies strongly with radius from the centre.

Estimating the IMF via a mass measurement independent of the spectral features has the obvious disadvantage that it is only sensitive to the overall missing mass, which could be a superposition of low-mass stars, stellar remnants and dark matter. The advantage is, however, that the measurement is independent of broad-band SED fitting or the fitting of specific gravity sensitive spectral lines and therefore it can either confirm or refute IMF trends that might be deduced from the

intricacies of integrated spectra of galaxies. Gravitational lensing has the disadvantage that it is a mass measurement along a cylinder and therefore is relatively sensitive to dark matter or any other matter along the line of sight. A potentially cleaner way to obtain a mass estimate of only the baryonic matter, is to analyze the kinematics of the central parts of ETGs, whose mass is believed to be dominated by baryons.

An attempt to observe and explain the stellar kinematics in the central regions of ETGs has been undertaken by the ATLAS^{3D} Survey (Cappellari et al. 2011a). The aim of this survey has been to obtain integral field spectroscopy with SAURON (Bacon et al. 2001) of all 260 ETGs with mass approximately greater than $6 \times 10^9 M_\odot$ that are within 42 Mpc distance from us in the northern hemisphere. This volume-limited sample yields a large collection of kinematic data, which has been used, among other things, to estimate the stellar masses of these galaxies. Comparing these kinematic measurements with the stellar masses measured by fitting the SEDs with stellar population synthesis models, provides a direct probe of the IMF normalization in these galaxies. A clear trend of IMF normalization with velocity dispersion or with mass-to-light ratio has been reported by Cappellari et al. (2012, 2013b,a), resulting in: (I) A Chabrier-like normalization at low mass-to-light ratios, which agrees with the one inferred for spiral galaxies, (II) A Salpeter normalization at larger (M/L) consistent, on average, with some results from strong lensing and (III) a normalization more massive than Salpeter for some of the galaxies with high (M/L) broadly consistent with measurements of spectral features in massive galaxies that indicate a substantial population of dwarf stars (Cappellari et al. 2012).

This article consists of a critical review of some of the methods and results from the ATLAS^{3D} Survey. Section 2.2 introduces the ATLAS^{3D} Survey and the JAM method used to fit the kinematical data. In section 2.3 the evidence from Cappellari et al. (2012) for a non-universal IMF is investigated. Specifically it is shown that the large reported trend between the kinematic mass to light ratio and the IMF mismatch parameter, interpreted as an effect of IMF variations, could also be caused by measurement errors in the kinematic mass of the order 30%. Section 2.4 presents correlations of the IMF normalization with astrophysical variables. Section 2.5 shows that the effect of the non-universal IMF implied by the original ATLAS^{3D} analysis on observations of the Galaxy Stellar Mass Function (GSMF) at higher redshift is small. Also the stellar mass completeness limit of the ATLAS^{3D} Survey is shown to be $10^{10.3} M_\odot$. In section 2.6 we demonstrate that the inferred systematic IMF trend with velocity dispersion is dependent on the precise selection cut that is made at the low mass end. In particular we show that this trend is virtually absent for the mass complete sample of galaxies with kinematic stellar masses larger than $10^{10.3} M_\odot$. In section 2.7 we show that the

systematic variation of the IMF with velocity dispersion is accompanied by a systematic variation with distance. This could be interpreted as a genuine effect of the cosmic environment on the IMF, but more probably it points towards biases in the used distance catalog which, as a side-effect, show up as a dependence of the IMF on the velocity dispersion of an ETG. Part of the IMF trend can be attributed to colour-dependent calibration issues of the surface brightness fluctuation (SBF) distance measurements and we show that the IMF trend is absent for galaxies at a distance larger than 25 Mpc. Finally, we summarize our conclusions in section 2.8.

2.2 The ATLAS^{3D} Survey

The ATLAS^{3D} project improves on previous studies in two ways. On the one hand the number of observed objects, 260, is much larger than before. On the other hand, progress has been made in modeling the observed stellar dynamics. The ATLAS^{3D} team's Jeans Anisotropic Multi-Gaussian Expansion (JAM) modeling method is introduced in Cappellari (2008, 2012). The JAM method uses the minimum number of free parameters that are needed to fit the integral field observations. It assumes axisymmetry for all galaxies, with the inclination i as a free parameter. The mass-to-light ratio Υ is assumed to be the same throughout the whole observed region, but it can vary from galaxy to galaxy. The conversion of the observed luminosity density to a matter density depends on i and Υ and is done with the multi Gaussian Expansion (MGE) parameterization of Emsellem et al. (1994).

The JAM method consists of solving the Jeans equations, with the extension (with respect to the isotropic case) of an orbital anisotropy parameter β_z. The velocity ellipsoid is assumed to be aligned at every position in the galaxy with the cylindrical coordinates (R, z) and the ratio between the two axes of this ellipsoid is assumed to be the same within the central part of the galaxy, leaving one extra free parameter, $\beta_z = 1 - \overline{v_z{}^2}/\overline{v_R{}^2}$. Although the velocity ellipsoid will in reality be more complicated, this simple β_z parameter suffices to connect the model to the observations. Apart from the three parameters i, Υ and β_z, six different parameterizations of the dark matter halo are used, but the main conclusions are found to be insensitive to dark matter, because for all six halo parameterizations the kinematics of the central part of the ETGs are dominated by baryonic matter.

As shown in Cappellari et al. (2012), this model not only suffices to fit the integral field spectroscopic observations, it also puts very tight constraints on the Υ parameter. It is this feature that makes it possible to measure the IMF normalization, but let us first take a quick look at the other two free parameters.

The main argument in favour of the model is the fact that it is able to reproduce the integral field spectroscopy of a complete and very diverse set of galaxies using only a small number of free parameters. However this same argument also works against it, because Cappellari (2008) note that for galaxies observed at low inclination, the lowest χ-squared fit is often obtained for an unrealistic set of parameter values, because of a degeneracy between i and β_z. The model prefers too high values for i and too low values for β_z. Restricting the anisotropy to a flat ellipsoid, $\beta_z > 0.05$ as observed for edge-on galaxies, does remove the degeneracy, but this example shows that a good fit does not necessarily prove that the model corresponds to physical reality.

Because of the large size of the survey we can look at the distribution of inclinations. Figure 2.1 compares the observed distribution of inclinations with that expected for randomly oriented galaxies. The Kolmogorov-Smirnov statistic for this comparison is 0.22 with a corresponding probability $p < 10^{-11}$. With respect to the isotropic case there is a shortage of $\sim$ 20% of galaxies with inclinations smaller than 45° and an excess of $\sim$ 20% of galaxies with inclinations larger than 85°. This either indicates that the model still has a tendency to overestimate the inclination or that the ETGs in our local neighborhood are preferably aligned with our line of sight. In principle a measurement error in the inclination could result in an error in the determined IMF mismatch parameter. A priori there is no clear reason to assume that this would not bias the determination of the IMF. However there is no significant correlation (Pearson $R^2 = 0.01$) between inclination and the IMF mismatch parameter, lending an a posteriori credibility to the retrieved IMF normalization[1]. In the following section we will take a detailed look at the predictions for the mass-to-light ratio Υ and the implications for the IMF normalization.

2.3 The ATLAS^{3D} evidence for a non universal IMF

The precision with which deviations from universality in the IMF can be measured, depends on the errors in the two independent measurements of (M/L)[2] from respectively SED fitting and the stellar kinematics via the JAM method. $(M/L)_{\rm SED}$[3] is obtained by using the spectral fitting models of Vazdekis et al. (2012), with stan-

[1]However the fact that the five galaxies with the lowest IMF mismatch parameter all have an inclination larger than 85° suggests that at least for these galaxies the true inclination might be smaller, or the IMF mismatch parameter dependent on the assumed inclination.

[2]The (M/L) and luminosity measurements in this paper refer to the r-band, as is the case for the ATLAS^{3D} papers.

[3]The ATLAS^{3D} papers denote this variable as $(M/L)_{\rm Salp}$. We will refer to it as $(M/L)_{\rm SED}$ in this paper.

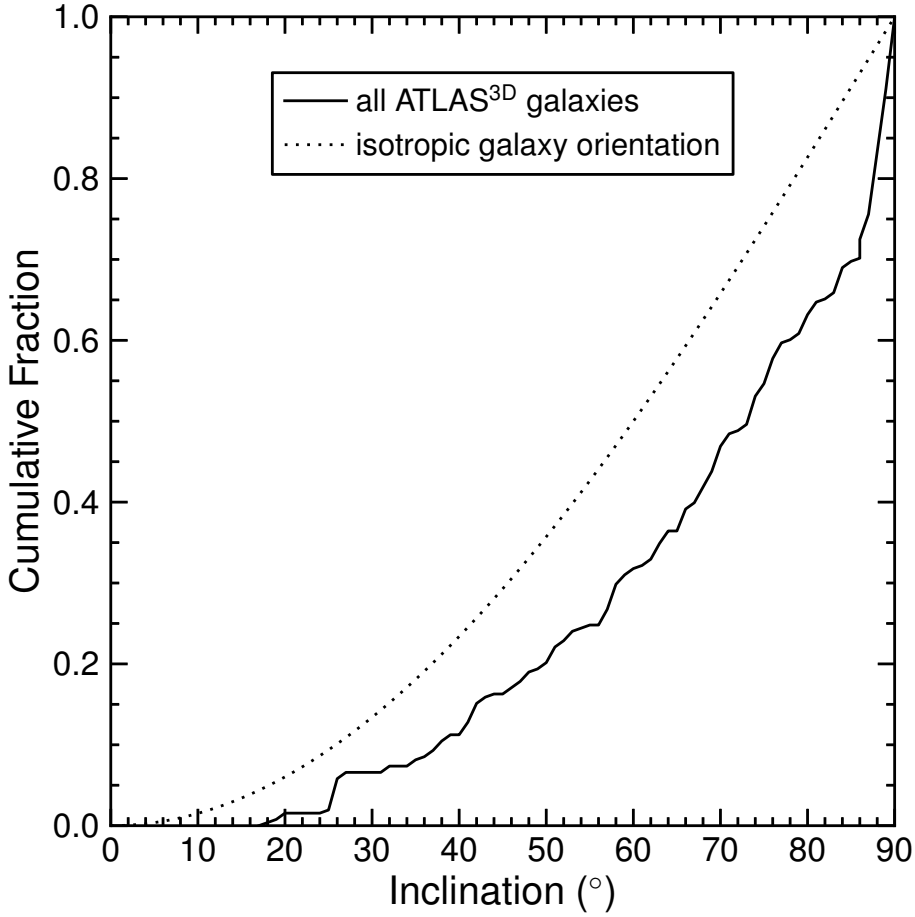

Figure 2.1: Distribution of the JAM model inclinations of all the ATLAS^{3D} ETGs compared to an isotropic distribution of inclinations. The Kolmogorov-Smirnov statistic for this comparison is 0.22 with a corresponding probability $p < 10^{-11}$.

dard lower and upper mass cut-offs for the Salpeter IMF of $0.1\,M_\odot$ and $100\,M_\odot$. A comparison has been made with the (M/L) values from Conroy and van Dokkum (2012), who use an independent set of spectra spanning a longer wavelength range and a different stellar population synthesis model. For the set of 35 galaxies that are present in both studies, the differences between the two (M/L) measurements are consistent with an error per galaxy per measurement of 6%, which suggests that $(M/L)_{\rm SED}$ is quite robust (Cappellari et al. 2013a).

By comparing predictions from models with different dark matter halos, Cappellari et al. (2013b) estimate the JAM modeling errors in $(M/L)_{\rm kin}$ to be 6%. We will use $(M/L)_{\rm kin}$[4] to denote the stellar mass-to-light ratio of the best fit JAM model with a NFW dark matter halo with a fitted virial mass M_{200}, also referred to as model B by Cappellari et al. (2012), where M_{200} denotes the mass of a 200 times overdensity dark matter halo. Galaxies with a clear bar structure give lower quality fits than galaxies with no bars. Apart from this there may be errors from distance measurements and from photometry.

[4]The ATLAS^{3D} papers denote this variable as $(M/L)_{\rm stars}$. We will refer to it as $(M/L)_{\rm kin}$ in this paper.

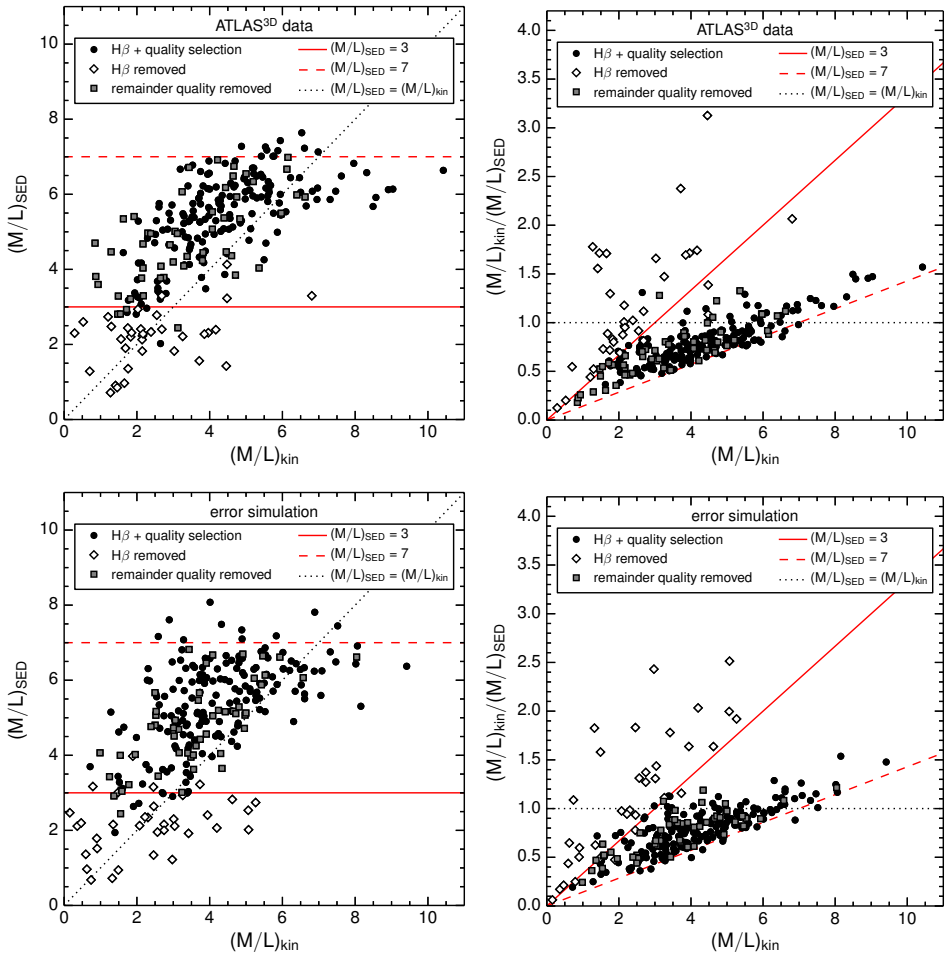
ATLAS3D data
Hβ + quality selection
Hβ removed
remainder quality removed
(M/L)SED = 3
(M/L)SED = 7
(M/L)SED = (M/L)kin
(M/L)SED
(M/L)kin
(M/L)kin/(M/L)SED
error simulation

Figure 2.2: Top left panel: comparison of the JAM model stellar mass-to-light ratio, $(M/L)_{\rm kin}$, with the ratio inferred from Stellar Population Synthesis SED fits assuming a Salpeter IMF, $(M/L)_{\rm SED}$, for the ATLAS^{3D} dataset. Open diamonds indicate galaxies with a young stellar population, selected by having Hβ absorption with an equivalent width larger than 2.3 Å. These galaxies tend to have strong radial gradients in their population which makes both (M/L) determinations uncertain (Cappellari et al. 2012). This selection is almost identical to selecting all galaxies with $(M/L)_{\rm SED} < 3$ (horizontal solid line). Grey squares indicate the remaining galaxies with a (quality = 0) label, meaning: "either inferior data quality (low S/N) or a problematic model (e.g. due to the presence of a strong bar or dust, or genuine kinematic twists)." Black circles are the remaining high-quality galaxies. The horizontal dashed line at $(M/L)_{\rm SED} \approx 7$ denotes the theoretical maximum for a simple stellar population of the age of the universe with a Salpeter IMF; Top right panel: the "IMF mismatch parameter", i.e. the ratio $(M/L)_{\rm kin}/(M/L)_{\rm SED}$, as a function of $(M/L)_{\rm kin}$. This plot is similar to the upper middle panel of Figure 2 from Cappellari et al. (2012) apart from the selection of galaxies and a logarithmic axis; The bottom panels show the same plots for simulated data for which it is assumed that there are no intrinsic IMF variations (within the black and grey data points), but for which the perceived variations are caused by a random Gaussian errors of 6% in $(M/L)_{\rm SED}$ and 29.9% in $(M/L)_{\rm kin}$. The black and grey data points are also renormalised by a factor of 0.785, see Table 2.1. The error of 29.9% is chosen such that the standard deviation in the mismatch parameter in the error simulation is exactly the same as in the ATLAS^{3D} data. Both the qualitative as the quantitative behaviour are reproduced pretty well. The Pearson R^2 for the black and grey points of the right panels is 0.674 for the data and 0.605 ± 0.040 for 10.000 runs of the Gaussian error simulation (for the specific run that is shown here it is 0.630). The white diamonds require a larger normalisation of 1.192 and error of 51.2%.

Figure 2.2 (top panels) compares the two types of (M/L) determinations from the ATLAS^{3D} Survey. Clearly, $(M/L)_{\rm SED}$ and $(M/L)_{\rm kin}$ do not agree within the 6% error associated with the $(M/L)_{\rm SED}$ determination and the 6% JAM model error. The difference could be due to a systematic IMF trend, random variations in the IMF, distance measurement errors and photometry errors. Our aim is to better understand these effects.

Cappellari et al. (2012) present the ATLAS^{3D} results in a way analogous to Figure 2.2 (top right panel), without the open diamond symbols. One should be cautious drawing conclusions about the IMF from the correlation in this graph between $(M/L)_{\rm kin}$ and the ``IMF mismatch parameter'' $\alpha \equiv [(M/L)_{\rm kin}]/[(M/L)_{\rm SED}]$ for three reasons. Firstly, galaxies with still ongoing star formation (selected by having Hβ absorption with an equivalent width larger than 2.3 Å) generally have a strong radial gradient in their stellar population. This makes both (M/L) determinations uncertain, which is the reason why they are excluded from the analysis by Cappellari et al. (2012). This does, however, induce an unavoidable bias. Figure 2.2 (top left panel) shows that this Hβ selection is almost equivalent to removing

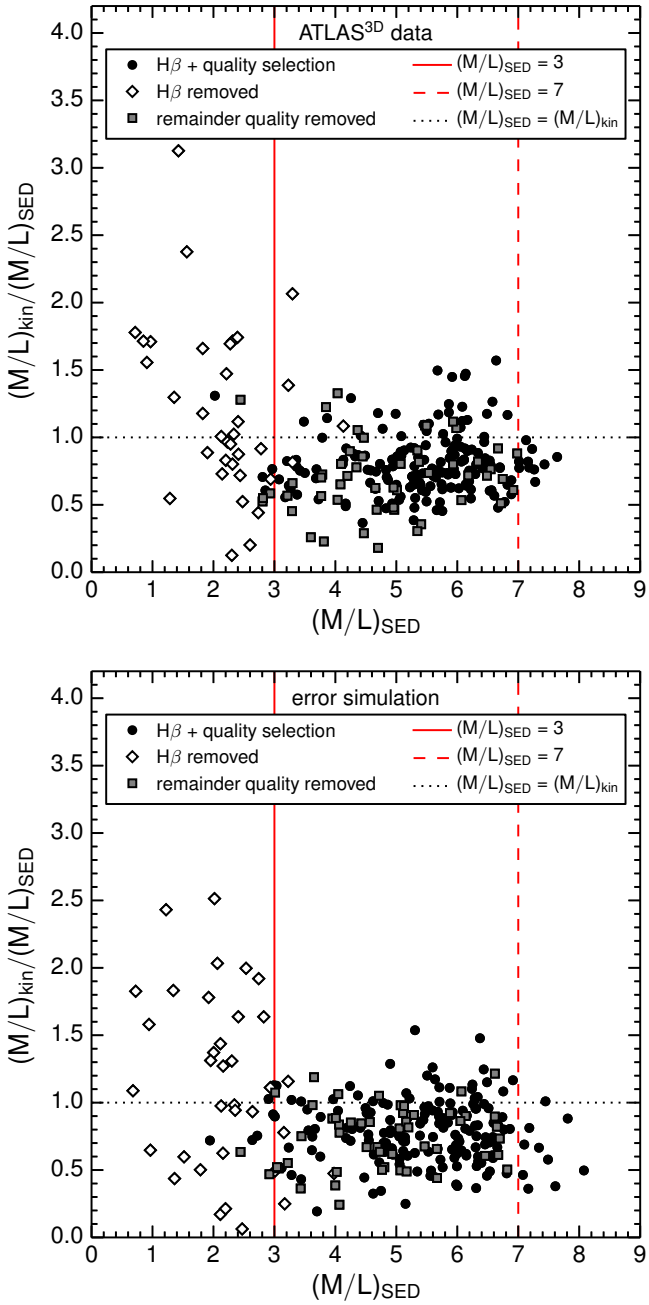

Figure 2.3: For the same data as Figure 2.2 this shows the dependency of the IMF mismatch parameter on $(M/L)_{\rm SED}$. Both the ATLAS$^{\rm 3D}$ data and the error simulation show a negligible correlation for the black and grey data points, with a Pearson R^2 of 0.02 for the data and 0.00 for the simulation.

galaxy selection	$\overline{\alpha}$	$\sigma(\alpha)$	$\sigma(\alpha)/\overline{\alpha}$	number of galaxies
Hβ + quality selection (black circles)	0.808	0.226	28.0%	171
Hβ removed (white diamonds)	1.192	0.615	51.6%	35
remainder quality removed (grey squares)	0.710	0.265	37.3%	52
(black circles + grey squares)	0.785	0.239	30.5%	223

Table 2.1: Average IMF mismatch parameter $\overline{\alpha}$, the standard deviation $\sigma(\alpha)$, the relative standard deviation $\sigma(\alpha)/\overline{\alpha}$ and the number of galaxies in the selection for the galaxy samples corresponding to different selection methods as used in Figure 2.2 and other Figures throughout this article.

all galaxies with $(M/L)_{\rm SED} < 3$. Figure 2.2 (top right panel) shows that this creates an ``upper zone of avoidance'' which strengthens the correlation between α and $(M/L)_{\rm kin}$.

Secondly, $(M/L)_{\rm SED}$ is not a pure measurement. It is a fit of measurements to a Salpeter stellar synthesis model and hence it does not have Gaussian random error behaviour. More specifically, there is a clear theoretical maximum value of $(M/L)_{\rm SED} \approx 7$ which corresponds to a simple stellar population of the age of the universe with a Salpeter IMF. Regardless of any errors in SED-fitting, JAM-modeling, distance measurements and photometry, this maximum will always be respected. As can be seen in Figure 2.2 (top right panel), this constitutes a ``lower zone of avoidance'' which is actually responsible for most of the correlation.

Thirdly, and not completely independent of the previous two points: any error in the kinematic (M/L) determination will show up as a radial scatter which emanates from the origin in Figure 2.2 (top right panel) and may thus induce a spurious correlation.

In order to assess to what extent the upper right panel of Figure 2.2 alone, or equivalently the upper middle panel of Figure 2 from Cappellari et al. (2012), constitutes convincing evidence for IMF variations, we simulate the effect of Gaussian random errors in both the determination of $(M/L)_{\rm SED}$ and $(M/L)_{\rm kin}$ on this figure. Assuming no intrinsic IMF variations, these errors will lead to an expected scatter in the perceived IMF mismatch parameter. We fix the Gaussian errors in $(M/L)_{\rm SED}$ to the reported value of 6%, but use a Gaussian error of 29.9% in $(M/L)_{\rm kin}$, which represents the total error in the kinematic mass-to-light determination, including a JAM modelling error (reported at 6%), errors from photometry and errors from the distance determination, which will be discussed at length in section 2.7. The value of 29.9% is chosen such that the kinematic and SED errors together combine to give the 30.5% scatter found in the data for all galaxies

that have not been rejected because of Hβ absorption, see Table 2.1. The question now is whether these random errors can produce at the same time a relation between $(M/L)_{\rm kin}$ and α similar to that in Figure 2.2 upper right panel.

Figure 2.2 (lower panels) shows the results of the error simulation for data with no intrinsic IMF variations. For all the galaxies that have not been rejected on basis of Hβ absorption we simulate a random value for $(M/L)_{\rm kin}$ based on the observed value of $(M/L)_{\rm SED}$ from ATLAS$^{\rm 3D}$ multipled by the average normalisation of 0.785 (see Table 2.1) and we add a random Gaussian error of 29.9%. Hereafter we add a 6% random Gaussian error to $(M/L)_{\rm SED}$. For the Hβ removed galaxies we use a normalisation of 1.192 and respective errors of 51.2% and 6%. As can be seen in the lower panels of Figure 2.2 the data from simulated errors looks very similar to that from the real ATLAS$^{\rm 3D}$ measurements. Especially we retrieve the strong trend of the IMF mismatch parameter with $(M/L)_{\rm kin}$. However the correlation of this trend in the real data (Pearson $R^2 = 0.674$ for the combined black circles and grey squares) is higher than that in most of the error simulations (Pearson $R^2 = 0.605 \pm 0.040$). This 1.7σ deviation could indicate that Gaussian errors alone are not enough to explain the observed trend between $(M/L)_{\rm kin}$ and α, although the significance of this is limited and non-Gaussianities in the errors are likely to increase this correlation. Figure 2.3 shows that also the relation between $(M/L)_{\rm SED}$ and α is well reproduced by the error simulation. The data has a Pearson R^2 of 0.02 versus 0.00 in the simulation. A negative correlation could have been the result of hypothetical large measurement errors in $(M/L)_{\rm SED}$.

These issues do not definitely imply that the observed trend is caused by errors. For the sake of the argument, true Gaussian IMF variations would look exactly the same as Gaussian measurement errors in $(M/L)_{\rm kin}$. It does show however that it is hard to draw conclusions based solely on the correlation between α and $(M/L)_{\rm kin}$. It is important to look for accompanying correlations of the IMF mismatch parameter α with different variables, not only to find the physical processes that might explain the trend, but also to rule out that the trend is a result of the complicated interplay between the selection effects and the different measurement and model errors.

Even in the extreme case when the variations of the IMF mismatch parameter α within the the ATLAS$^{\rm 3D}$ Survey would be completely due to errors, the average value of α from Table 2.1 can still be compared with determinations of the IMF by different studies, as alluded to in the introduction. This average normalization for the ATLAS$^{\rm 3D}$ ETGs is different from the Chabrier IMF which holds for our galaxy. However when comparing to other studies one has to take into account the unknown systematics of comparing different IMF determination methods. This is beyond the scope of this work. We will focus solely on the evidence for IMF

variations present within the ATLAS^{3D} Survey.

2.4 Correlations with the IMF mismatch parameter

In the previous section we confirmed that at face value the ATLAS^{3D} data suggests a non-universal IMF. The robustness of this outcome however critically depends on the size of the assumed modelling and measurement errors in the kinematic mass determination. For this reason, it would be good to find some independent correlation of the IMF mismatch parameter with some other observable in order to convince ourselves of the robustness of this result. Moreover, correlations are to be expected within any theoretical model for IMF variations. The IMF could for example correlate with the age of the galaxy through a dependence on redshift, it could be related to the mass of the galaxy via gas recycling, the pressure of the interstellar matter or the intensity of star formation, it could depend on the galaxy metallicity or it could be influenced by the cosmic environment etc. Any correlation could also point the way to an understanding of the underlying physical mechanisms.

The data show a clear correlation of the mismatch parameter with the effective velocity dispersion σ_e (Cappellari et al. 2013b). Surprisingly, it does not show a correlation with $(M/L)_{\rm SED}$, SDSS colour, luminosity, or even $M_{\rm SED}$ (even though σ_e and $M_{\rm SED}$, and σ_e and $(M/L)_{\rm SED}$ are tightly correlated). Figure 2.4 (top panel) shows the clear trend between the IMF mismatch parameter and the effective velocity dispersion for the high-quality data points (with a Pearson R^2 of 0.11). The variables σ_e and $M_{\rm SED}$ are tightly correlated (Pearson R^2 of 0.63) so naively one would expect to find a correlation between the IMF mismatch parameter and $M_{\rm SED}$ as well, but Figure 2.4 (bottom panel) shows that this is not the case (Pearson R^2 of 0.001). We also see from Figure 2.4 (top panel) that the trend with σ_e is affected by the exclusion of galaxies with strong Hβ absorption. The excluded galaxies on average have a small σ_e and a large α. Including all galaxies in the fit of α versus σ_e would reduce the best-fit slope from 1.6×10^{-3} to 0.4×10^{-3} and the Pearson R^2 from 0.112 to 0.003.

Although the trend of α with σ_e is very clear, it is much smaller than the scatter. Accounting for the trend for all galaxies that have not been rejected on basis of Hβ absorption only reduces the scatter in α from 30.6% to 28.7%. We note that since velocity dispersion is the main input of the JAM model, we expect it to be more prone to systematics. A very recent analysis of the ATLAS^{3D} results by McDermid et al. (2014) has found no significant dependence of the IMF on single stellar population equivalent ages or abundance ratios. In the following we will investigate further the IMF mismatch parameter dependence on velocity dispersion, especially

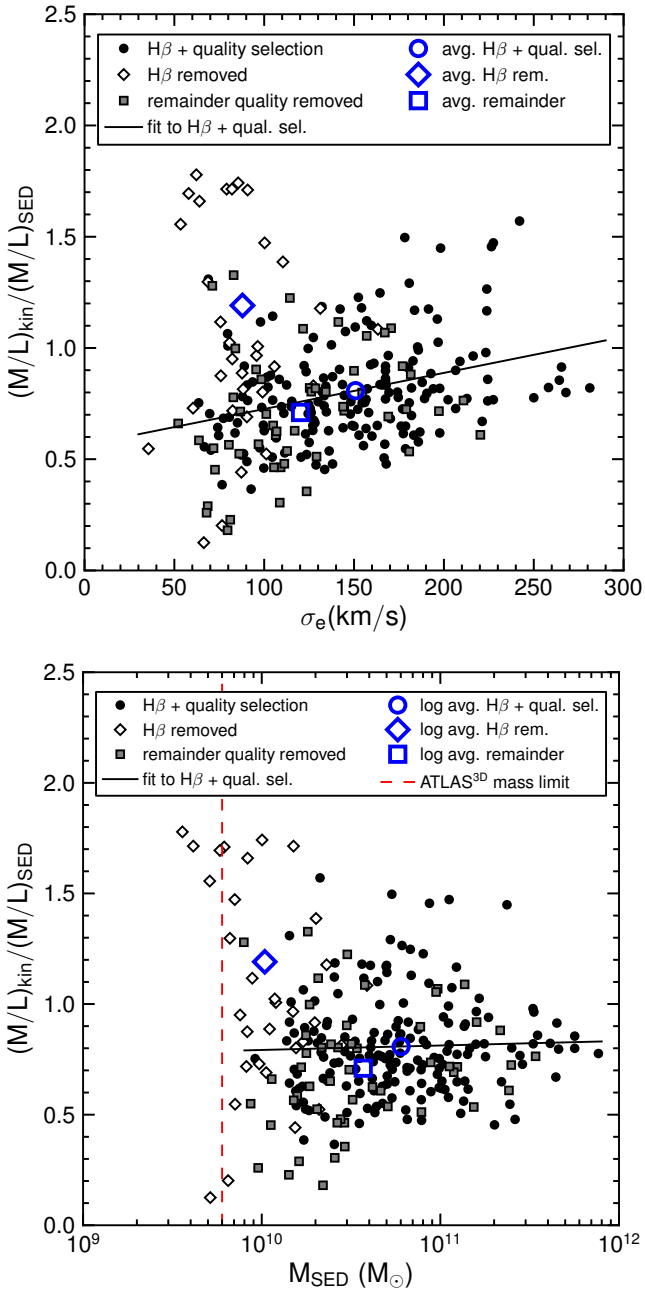

Figure 2.4: ATLAS^{3D} data for the IMF mismatch parameter $\alpha = (M/L)_{\rm kin}/(M/L)_{\rm SED}$ as a function of the effective velocity dispersion (top panel) and the mass measured from SED fitting assuming a Salpeter IMF (bottom panel). The three different data selections are the same as in Figure 2.2. Three open diamond data points with a mismatch parameter greater than 2 are not visible. For each selection the average is indicated in blue. The Pearson R^2 coefficients for the fits to the black filled circles are 0.11 for the left panel and 0.001 for the right panel (on a logarithmic mass scale).

in relation to the survey mass completeness and distance measurement effects, but first we take a short look at the implications of the IMF trend on the measurement of galaxy stellar mass functions.

2.5 Galaxy Stellar Mass Function and mass completeness

A non-universal IMF could affect the shape of the galaxy stellar mass function (GSMF) inferred from fitting stellar population synthesis models to the SEDs measured in galaxy surveys.

A recent attempt to quantify this effect is reported by McGee et al. (2014), who take different model assumptions for the dependence of the slope of the IMF on galaxy velocity dispersion and show that the implications for the high-mass end of the GSMF can be quite significant. For such an analysis it makes a difference what observations are taken as the starting point. Also, Figure 2.4 suggests that translating an IMF trend with σ_e into a trend with $M_{\rm SED}$ can be quite tricky. Here we want to address what would be the effect based solely on the ATLAS$^{\rm 3D}$ Survey. The advantage of this approach is that we know that the galaxy sample is representative, because it is aimed to be complete down to approximately 6×10^9 $\rm M_\odot$ within the given volume (Cappellari et al. 2011a).

As can be verified from Figure 2.4 (right panel) correcting the observed $M_{\rm SED}$ from any GSMF study to a $M_{\rm kin}$ value, results in the same correction by a factor 0.8 independent of the mass. This just shifts the GSMF of quiescent galaxies to lower masses without changing its shape. Accounting for the scatter in the mismatch parameter (assuming that the scatter is intrinsic and not caused by the observational analysis) would correspond to smoothing the GSMF with a kernel of about 0.2 dex. At the steep high mass end this smoothing kernel effectively shifts the GSMF to lower masses by an additional 0.05 dex. Hence, apart from a possible slight shift of the quiescent GSMF with respect to the star forming GSMF, the ATLAS$^{\rm 3D}$ results do not imply any changes in the shape of the GSMF.

We can also look directly at the GSMF for the 260 ETGs in the ATLAS$^{\rm 3D}$ Survey. For this number of galaxies the statistical and cosmic variation will be quite large, but it is the most direct approach. Figure 2.5 shows the GSMF separately for $M_{\rm SED}$ and $M_{\rm kin}$ and compares these with the GSMF for quiescent galaxies from Moustakas et al. (2013). Apart from the overall shift in mass by a factor 0.81, the two ATLAS$^{\rm 3D}$ mass determinations give very similar GSMFs. The high-mass fall off from ATLAS$^{\rm 3D}$ is the same as that from Moustakas et al. (2013). The overall normalization is approximately 30% lower, which could be due to cosmic variance or a difference in selection criteria for quiescence. At the low-mass end

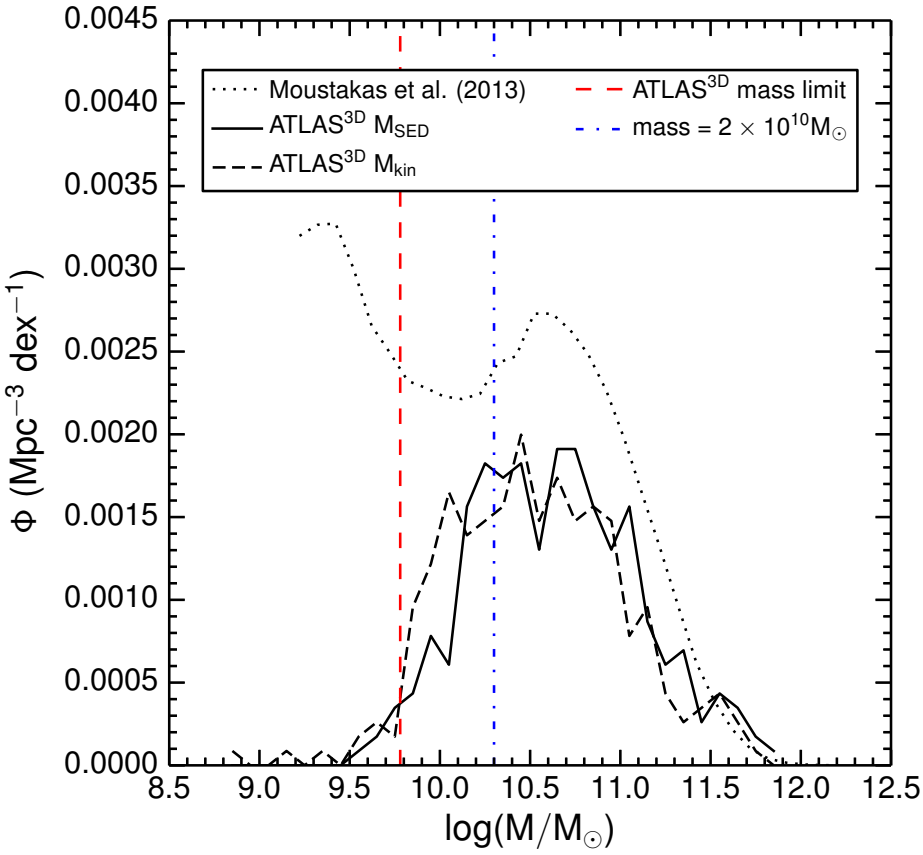

Figure 2.5: The galaxy stellar mass function (GSMF) for all ATLAS^{3D} ETGs as a function of respectively $M_{\rm SED}$ from SED fitting (solid curve) or $M_{\rm kin}$ from JAM model fitting (dashed curve). The JAM model GSMF is shifted to lower masses by a factor of about 0.8, but apart from that there are no major differences. The ATLAS^{3D} sample can be compared with the quiescent GSMF from Moustakas et al. (2013) (which has been shifted by 0.22 dex in order to correct to a Salpeter IMF). One difference is the overall normalization. On top of that the ATLAS^{3D} sample seems to become incomplete already for $M < 2\times10^{10}{\rm M}_\odot \approx 10^{10.3}{\rm M}_\odot$ (see Figure 2.6 blue dash-dotted line). The high-mass fall off is similar. The red dashed vertical line represents the approximate mass completeness limit of $6\times10^9{\rm M}_\odot$ reported by Cappellari et al. (2011a).

the ATLAS^{3D} GSMF falls off rapidly, which most likely indicates that the galaxy sample is incomplete[5].

In order to assess the mass completeness of the survey, Figure 2.6 (top row) shows the mass to light ratio in the K-band as a function of $M_{\rm SED}$ (left) and $M_{\rm kin}$ (right). The galaxy selection is based on K-band luminosity ($M_K < -21.5\ mag$). The selection is made in the K-band because (M/L) variations in the K-band are smaller than in the r-band. For masses smaller than $2 \times 10^{10}{\rm M}_\odot$ the survey is not mass complete. Galaxies with masses below this limit are bound by a progressively smaller upper limit on the K-band (M/L). Figure 2.6 (bottom row) shows that the r-band (M/L) follows the same mass completeness trend. The mass-completeness limit of $2 \times 10^{10}{\rm M}_\odot$ that we estimate is higher than the survey limit of $M \approx 6 \times 10^9{\rm M}_\odot$ reported by Cappellari et al. (2011a).

One should be cautious about the biases that these completeness effects might introduce. For instance, the Mass Plane projection of σ versus M of Cappellari et al. (2013a) has selected against red, high M/L galaxies with masses below $2 \times 10^{10}{\rm M}_\odot$. Inclusion of such galaxies might change the M/L dependence on M and σ significantly at the low mass end.

2.6 Mass completeness effects on the IMF dispersion trend

In the previous section we showed that the ATLAS^{3D} Survey is probably incomplete for galaxy masses below $10^{10.3}{\rm M}_\odot$. This introduces a complex bias. Most of the problematic galaxies, especially those with non-homogenous (M/L) ratios caused by recent star formation, also have masses below this limit. It therefore makes sense to look at the mass-complete sample of galaxies with masses higher than $10^{10.3}{\rm M}_\odot$. There are two possible ways to implement this. We can either impose a cut in $M_{\rm SED}$ or in $M_{\rm kin}$. Figure 2.7 shows the IMF trends obtained by imposing either of these constraints. Using a $M_{\rm SED}$ cut gives a very clear IMF trend with σ_e, whereas using a $M_{\rm kin}$ cut gives no trend at all. It is straightforward to understand what is the cause of this difference. Around galaxy masses of $10^{10.3}{\rm M}_\odot$ the first selection will favour high $(M/L)_{\rm SED}$ galaxies and hence low α, while the second selection will favour high $(M/L)_{\rm kin}$ galaxies and hence high α. The region where this selection effect shows up in a (σ_e, α) plot is at low σ_e, because of the tight correlation between velocity dispersion and mass.

[5]Alternatively this could be caused by a divergence of the selection criteria on quiescence from Moustakas et al. (2013) with respect to the ETG sample of ATLAS^{3D}, which occurs abruptly at masses $M \lesssim 10^{10.3}{\rm M}_\odot$.

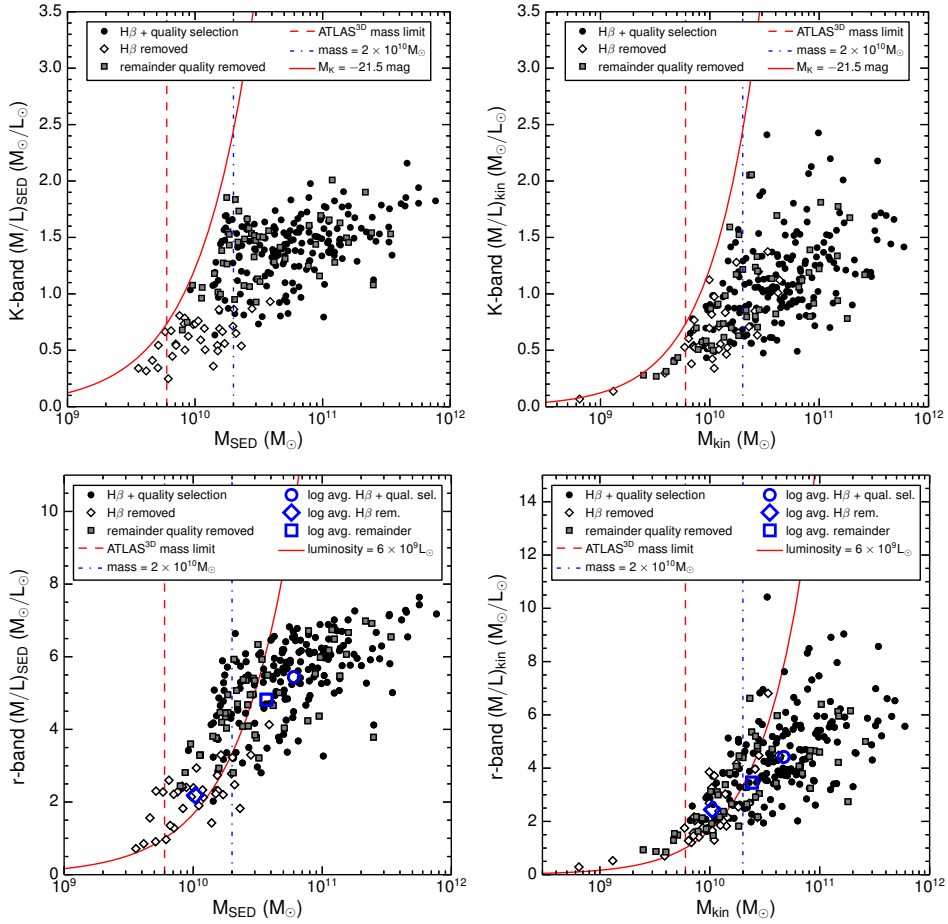

Figure 2.6: (M/L) versus M for both mass determinations. The data sets are the same as in previous figures. The left panels indicate the mass from SED fitting, the right panels indicate the kinetic mass determination by ATLAS^{3D}. The top row corresponds to K-band luminosities, with the solid red line indicating the selection limit of $M_K = -21.5\ mag$. The bottom row corresponds to the r-band luminosities used throughout the rest of this article and in the definition of the IMF mismatch parameter α. The upper row clearly demonstrates that the selection is not complete for masses (either $M_{\rm SED}$ or $M_{\rm kin}$) below $2 \times 10^{10} {\rm M}_\odot$. Under this limit galaxies with high K-band (M/L) are not selected. The blue dash-dotted line represents this conservative mass limit. The red dashed vertical lines denotes the approximate ATLAS^{3D} survey limit of $6 \times 10^9 {\rm M}_\odot$ reported by Cappellari et al. (2011a). The lower row shows the same completeness behavior in the r-band. For reference the red solid curve in the bottom panels indicates a constant luminosity of $6 \times 10^9 L_\odot$. Also in the r-band the selection edge runs roughly parallel to this constant luminosity curve.

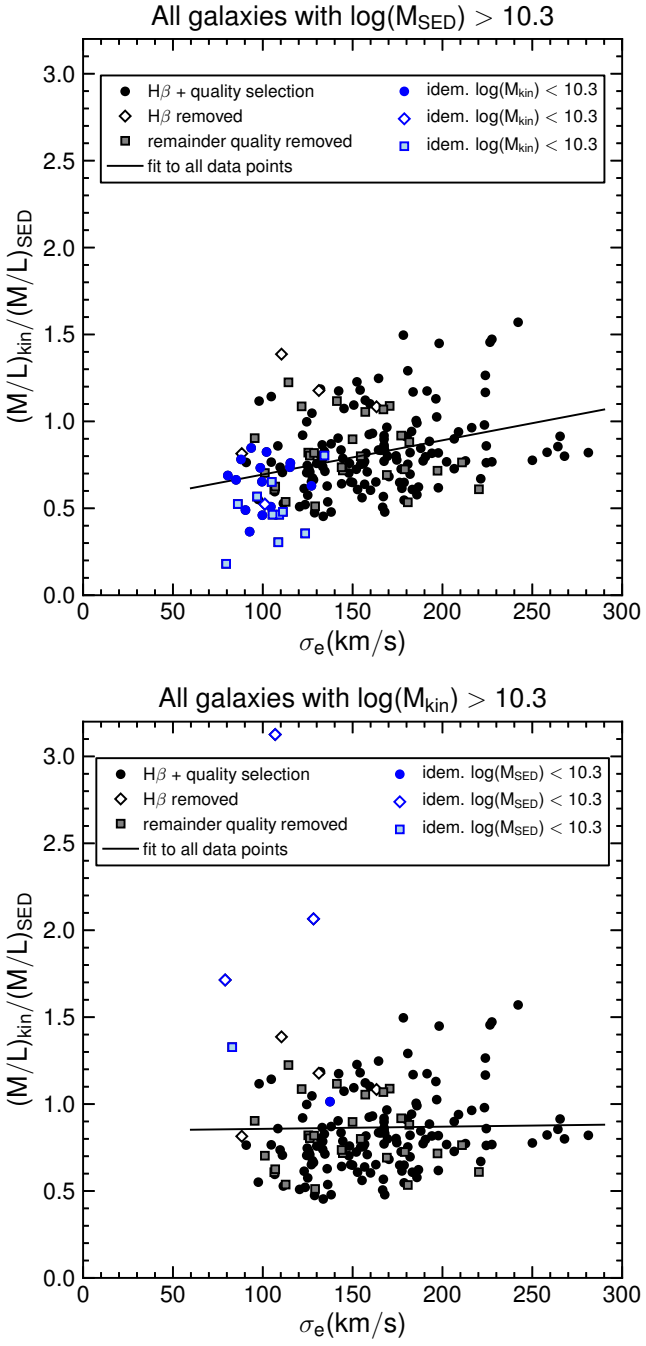

Figure 2.7: Trend of the IMF mismatch parameter $\alpha = (M/L)_{\rm kin}/(M/L)_{\rm SED}$ with velocity dispersion for all ETGs with $M_{\rm SED} > 10^{10.3}{\rm M}_{\odot}$ (top panel), or $M_{\rm kin} > 10^{10.3}{\rm M}_{\odot}$ (bottom panel). the top sample gives a slope of 0.0020, Pearson $R^2 = 0.12$, Spearman $R^2 = 0.13$. The bottom sample gives a slope of 0.0001, Pearson $R^2 = 0.0003$, Spearman $R^2 = 0.02$. Data points in blue indicate galaxies that are only present in one of the two panels.

It seems that the IMF trend with velocity dispersion depends on the mass selection criterion. For a mass complete sample of galaxies with $M_{\rm kin} > 2\times10^{10}{\rm M}_{\odot}$ one would conclude that there is no IMF trend with velocity dispersion over a large range of velocities. At the moment, the conclusions that we draw about the IMF dependency on velocity dispersion are dominated by the precise selection criterion at the low mass or low luminosity end of the galaxy sample. Therefore in the future it would be very useful to push this limit towards lower masses and lower luminosities.

2.7 Distance effects and SBF calibration

A source of error or bias in the determination of the IMF mismatch parameter lies in the distance determination. ATLAS^{3D} looks at nearby galaxies. For these galaxies the relative error in redshift-distances can be large. The distances used in the JAM method come from various sources: SBF distances from Tonry et al. (2001) and Mei et al. (2007), distances from the NED-D Catalogue and distances from the redshift, via the local flow field model of Mould et al. (2000) (using only the Virgo attractor).

The inferred value of $(M/L)_{\rm SED}$ is independent of the distance determination, but $(M/L)_{\rm kin}$ does depend on the distance. Suppose that the distance is overestimated by a factor η. This would mean that the luminosity of the galaxy is overestimated by a factor η^2 and that the size of the galaxy is overestimated by a factor η. Since the JAM fitting method is in effect a sophisticated way of determining a dynamical mass, the mass will follow $M \propto \sigma^2 r$ and will be overestimated by a factor η. This means that $(M/L)_{\rm kin}$ and hence the IMF mismatch parameter, will be a factor η too small. Thus, if a galaxy in reality is closer than determined, it will have a higher $(M/L)_{\rm kin}$ than determined and vice versa. Any errors and biases in the distance determination will therefore show up as errors and biases in the IMF determination[6].

Figure 2.8 (top panel) shows the dependence of the IMF mismatch parameter on distance. For the high-quality galaxies there is a trend of increasing IMF mismatch parameter with distance. One possibility is that this reflects a genuine systematic variation in the IMF on Mpc scales. If this were due to a dependence of the IMF on environment, then one would expect a stronger correlation between the IMF mismatch parameter of neighbouring galaxies. For example, Cappellari

[6]For galaxies around the completeness limit of sections 2.5, 2.6 the selection on K-band intrinsic luminosity will contain some galaxies that should fail the selection criterium, but are included due to an overestimate of the distance. This distance error propagates quadratically into the intrinsic luminosity. For these galaxies the perceived IMF mismatch parameter will be too small. Vice versa some galaxies with underestimated distances will be missed.

et al. (2011b) have used the ATLAS^{3D} data to show that the morphology of the galaxies depends on their immediate environment (the galaxy density defined by the closest three galaxies). However, we find no appreciable correlation between the IMF mismatch parameter of nearest neighbours (Pearson $R^2 = 0.02$, Spearman $R^2 = 0.03$).

Another possibility would be that the distance trend of the IMF mismatch parameter is related to the mass completeness issues from the previous section. This could be the case if the survey would have missed galaxies with low masses at larger distances. This is however not the case. There is no trend with distance for either velocity dispersion, kinematic mass or SED fitting mass (respective Pearson R^2 of 0.0008, 0.0005 and 0.0005).

This leaves the possibility that the IMF trend with distance is possibly caused by a bias in the distance determination. Figure 2.8 (bottom panel) shows the different sources for the distances that are used as input in the JAM fitting method. A relative distance error eventually translates into a relative error in the IMF mismatch parameter. Table 2.2 gives the mean and standard deviation of the IMF mismatch parameter for each set of distances. The ratio $\sigma(\alpha)/\overline{\alpha}$ is smallest for the samples using the SBF distances from Mei et al. (2007) and the distances from the redshift via the local flow field model of Mould et al. (2000), suggesting that these methods give the highest relative accuracy. The other three sets are considerably worse.

There is no clear cut way to unambiguously prove which distance method is causing the bias. Part of the overall correlation between α and distance is caused by the offset of the SBF distance determinations at small distances with the redshift distance determination at larger distances and part of it is caused by correlations within each data set. These correlations within each data set are biased by the selection effect of which galaxy belongs to which data set. Especially in the region around 25 Mpc, the choice between ``Tonry'' and ``V_{hel}'' can itself cause a correlation between the IMF mismatch parameter and distance of the corresponding subsets of galaxies. It is therefore better to look at a selection criterion based on distance ($D < 25$ Mpc versus $D > 25$ Mpc), which overlaps with the regions where both distance methods are used. Table 2.3 shows that the trend of the IMF mismatch parameter with distance originates from the galaxies closer than 25 Mpc that are not a member of the Virgo Cluster. This might point towards a bias in the SBF distance determination from Tonry et al. (2001).

The question arises whether this possible bias with distance is in any way related to a possible bias with velocity dispersion, since these appear to be the only two variables that show a systematic trend with the IMF mismatch parameter. Table 2.3 and Figure 2.9 show that this indeed seems to be the case. Exactly the

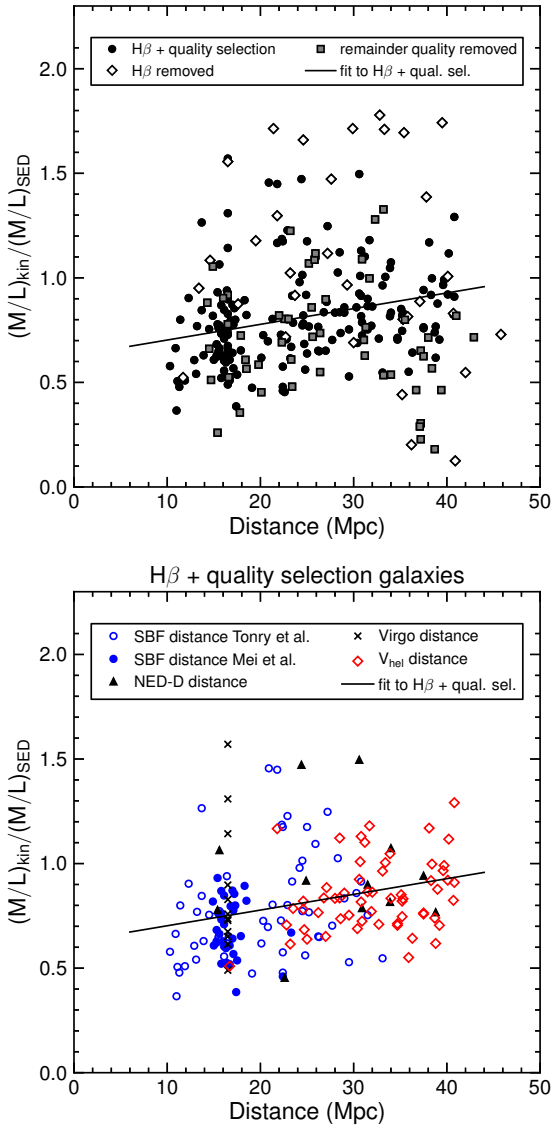

Figure 2.8: The IMF mismatch parameter $\alpha = (M/L)_{\rm kin}/(M/L)_{\rm SED}$ versus distance. Top panel: for the high-quality galaxies there is a clear trend with distance (Pearson $R^2 = 0.08$, Spearman $R^2 = 0.12$). Three open diamonds with a mismatch parameter larger than 2 are situated beyond the plotted range in the upper right. Bottom panel: only the galaxies selected on quality and Hβ absorption. The different symbols indicate the source of the distance measure that is used as input in the JAM fitting procedure. Blue open circles correspond to distances from Tonry et al. (2001), blue filled circles correspond to distances from Mei et al. (2007), black triangles are from the NED-D catalogue, black crosses indicate galaxies for which the distance is set at the distance of the Virgo cluster, red open diamonds correspond to distances via the heliocentric redshift velocity. The solid line in both panels is the same fit to the high quality galaxies.

distance method	$\overline{\alpha}$	$\sigma(\alpha)$	$\sigma(\alpha)/\overline{\alpha}$
SBF Mei	0.69	0.14	0.20
SBF Tonry	0.79	0.26	0.33
NED-D	0.96	0.30	0.31
Virgo	0.89	0.32	0.36
V_{hel}	0.85	0.17	0.20

Table 2.2: Average IMF mismatch parameter $\overline{\alpha}$ and the standard deviation $\sigma(\alpha)$ for the galaxy samples corresponding to different methods to measure their distances: "SBF Mei" refers to galaxies with a distance determination by Mei et al. (2007), "SBF Tonry" refers to distances by Tonry et al. (2001), "NED-D" are galaxies for which the distance is taken as the average of NED-D catalogue values, "Virgo" are galaxies whose distance is set equal to the distance of the Virgo cluster, "V_{hel}" are galaxies for which the distance is determined from their heliocentric redshift velocity.

same data set is responsible for most of the correlation of the IMF mismatch parameter α with velocity dispersion as was responsible for most of the correlation between α and distance. For galaxies at distances larger than 25 Mpc there is no clear indication of a systematic IMF variation, nor is there for Virgo galaxies. The systematic trend with velocity dispersion is almost entirely due to the non-Virgo galaxies closer than 25 Mpc. The same trends appear if we select on the three corresponding main distance methods.

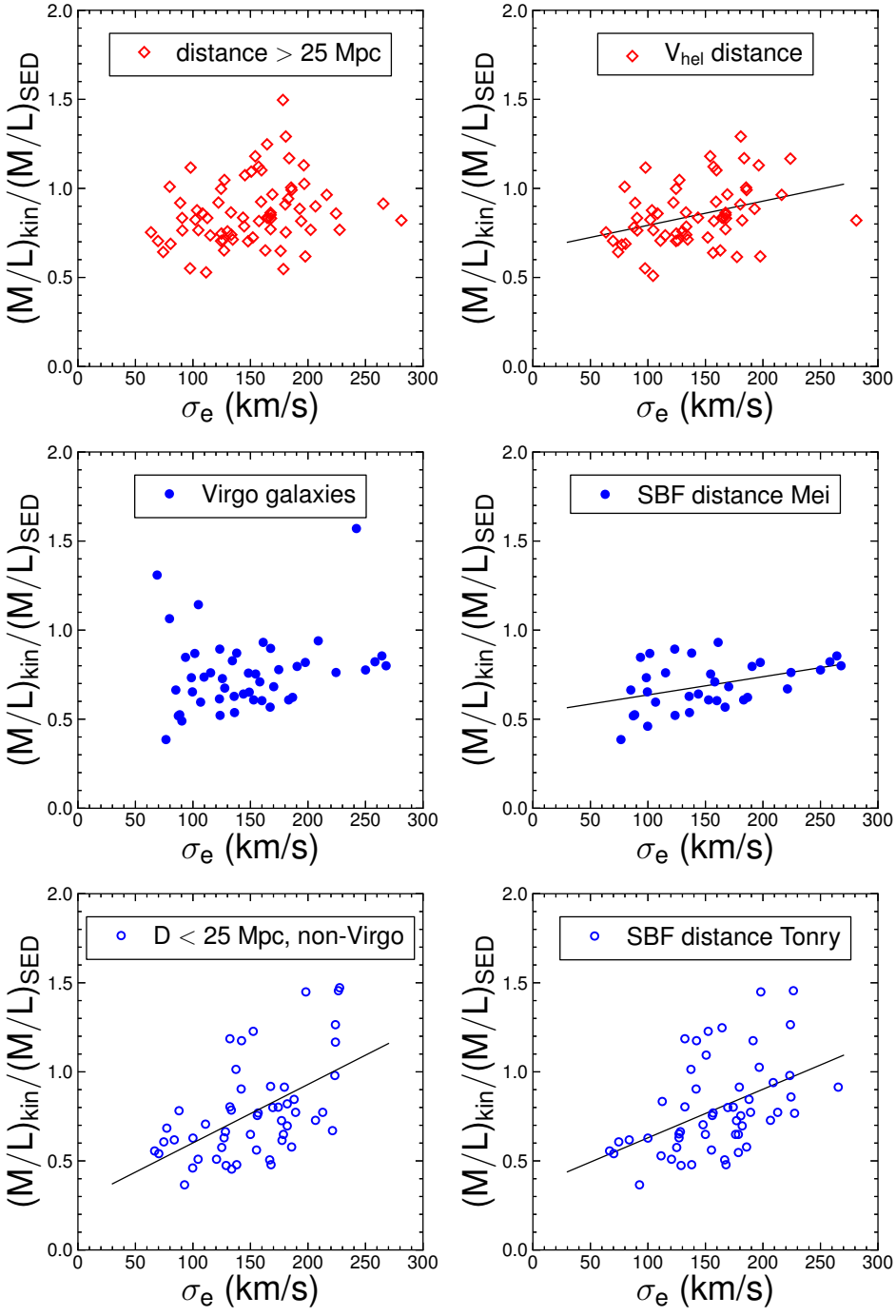
distance > 25 Mpc
V_hel distance
Virgo galaxies
SBF distance Mei
D < 25 Mpc, non-Virgo
SBF distance Tonry
(M/L)kin/(M/L)SED
σe (km/s)
0.0
0.5
1.0
1.5
2.0
0
50
100
150
200
250
300

Figure 2.9: The trend of the IMF mismatch parameter $\alpha = (M/L)_{\rm kin}/(M/L)_{\rm SED}$ with effective velocity dispersion for different sub-samples of galaxies. The left and right column show samples selected based on distance and distance measurement method, respectively. The distance selection criterion of 25 Mpc corresponds approximately to the transition from SBF distances to $V_{\rm hel}$ distances, avoiding the bias that is introduced by the availability of SBF distance measurements at this distance. The two panels in each row correspond to roughly the same galaxy selections. Top row: most galaxies at $D > 25$ Mpc have a redshift distance determination; middle row: most Virgo galaxies have an SBF distance from Mei et al. (2007); bottom row: most non-Virgo galaxies closer than 25 Mpc have an SBF distance from Tonry et al. (2001). Most of the IMF trend with velocity dispersion comes from the set of non-Virgo galaxies at $D < 25$ Mpc or, equivalently, from the set of galaxies with Tonry SBF distances. This is the same set that shows a distance dependence of the IMF mismatch parameter. Solid lines represent the best fit linear relation for all panels with a Pearson R^2 correlation of at least 0.12. The remaining two panels have a Pearson R^2 of 0.05. See Table 2.3 for all corresponding statistics.

There is a striking difference in the IMF trends with velocity dispersion between the two SBF distance sources that are used as input, Tonry et al. (2001) and Mei et al. (2007). The SBF method is believed to be the most accurate distance measure for close-by ETGs. The method is based on the assumption that in the observed region the stars sample a homogeneous distribution in space. Fluctuations in brightness are then caused by shot noise. The relative size of these fluctuations contains information about the average number of stars per point spread function. For ETGs that are further away this number of stars will be larger and the relative fluctuations in brightness will be smaller. Although the SBF method can be quite precise, it is an indirect way of measuring distance and may therefore be prone to unknown biases. If all stars would be equally bright then the method would be theoretically simple, but in reality different galaxies consist of different populations of stars, be it because of differences in age, metallicity or possibly the IMF of the galaxy. For this reason the SBF method is calibrated observationally as a function of colour.

The Tonry distance scale is calibrated as a function of (V-I) colour, by comparing with different distance estimates for groups. The Mei distance scale is calibrated as a function of $(g_{475} - z_{850})$ colour. Since the Mei sample consists of galaxies that belong to the Virgo Cluster, the SBF distance is calibrated as a function of colour requiring that different colour galaxies are homogeneously distributed in distance. Table 2.4 shows the R^2 correlation coefficients for the correlations between the spatial distribution of galaxies (in distance, right ascension, declination) and $g_{475} - z_{850}$ colour as well as between spatial distribution and the ATLAS^{3D} velocity dispersion. The colour-distance correlation was made to disappear by cal-

Galaxy Selection	number of galaxies	Pearson R^2 Spearman R^2	(α vs. D) p-value p-value	slope	Pearson R^2 Spearman R^2	(α vs. σ_e) p-value p-value	slope
Hβ + quality selection	171	0.08 0.12	0.0002 0.000003	0.0075	0.11 0.12	0.000008 0.000005	0.0016
D > 25 Mpc	70	0.006 0.008	0.54 0.46	0.0031	0.05 0.08	0.05 0.02	0.0009
Virgo	47	0.0005 0.001	0.88 0.82	-0.0062	0.05 0.06	0.13 0.10	0.0009
D < 25 Mpc, non-Virgo	52	0.11 0.12	0.01 0.01	0.0185	0.29 0.30	0.00003 0.00003	0.0033
V_{hel}	59	0.07 0.06	0.04 0.06	0.0080	0.12 0.14	0.006 0.004	0.0014
SBF Mei	34	0.04 0.01	0.28 0.57	-0.0145	0.17 0.16	0.01 0.02	0.0010
SBF Tonry	54	0.08 0.11	0.04 0.02	0.0112	0.21 0.27	0.0004 0.00007	0.0027

Table 2.3: Trend of the IMF mismatch parameter with both distance D (columns 3-5) and effective velocity dispersion σ_e (columns 6-8). Both trends are quantified by the Pearson R^2 coefficient, by the corresponding 2-tailed p-value for the null-hypothesis of no correlation and by the slope of the best linear fit. The Spearman R^2 and corresponding 2-tailed p-value are also given. Note that at a fixed slope, R^2 increases if the scatter decreases, thus "SBF Mei" and "V_{hel}" naturally have a higher R^2 coefficient. The first row corresponds to all high-quality galaxies, selected by having a non-zero "quality" label in Cappellari et al. (2013b) and an Hβ absorption with an equivalent width smaller than 2.3 Å. The next three rows are subsets of these high quality galaxies based on distance, where the galaxies with distances smaller than 25 Mpc have been split into Virgo galaxies and non-Virgo galaxies. The last three rows correspond to subsets defined by different distance determination methods: "V_{hel}" are galaxies for which the distance is determined from their heliocentric redshift velocity, "SBF Mei" refers to galaxies with a distance determination by Mei et al. (2007), "SBF Tonry" refers to distances by Tonry et al. (2001). The other two distance methods from Table 2.2 are not included, because both contain only 12 galaxies, too few to give meaningful statistics. Both the trend with D and the trend with σ_e are mostly due to the non-Virgo, $D < 25$ Mpc set or, equivalently, the sample of galaxies with a distance determination from Tonry et al. (2001). The trends with σ_e are also plotted in Figure 2.9.

	Distance	RA	DEC
g(475)-z(850) colour	0.008	0.00007	0.03
σ_e (ATLAS^{3D})	0.01	0.0009	0.003

Table 2.4: Pearson R^2 correlation coefficients between 3D spatial variables of the Virgo galaxies and colour as given by Mei et al. (2007) or velocity dispersion as given by Cappellari et al. (2013b). Galaxy colours do not correlate significantly with right ascension or declination. The colour - SBF magnitude relation is calibrated by requiring that the same holds in the radial direction. Because colour and σ_e are highly correlated, this removes the σ_e trend with distance as well.

ibrating the colour-dependent SBF distance, such that the distribution in this direction is as uniform as it is in the transverse directions. Colour and velocity dispersion are highly correlated. Table 2.4 shows that removing the colour-distance dependence for the Virgo galaxies has also automatically removed the σ_e-distance dependence.

This SBF distance calibration with colour is different for the Tonry dataset. Figure 2.10 shows the difference in distance modulus for the 26 galaxies that are part of both the Tonry et al. (2001) SBF catalog and the Mei et al. (2007) SBF catalog. Although one should be cautious in overinterpreting this data due to small number statistics, there are clear trends in the distance difference between the two data sets with both colour and effective velocity dispersion (as determined by ATLAS^{3D}). For high velocity dispersion the Tonry distance is systematically smaller than the Mei distance and vice versa. This means that for high σ_e the JAM method will systematically give a higher IMF mismatch parameter for the Tonry distance than for the Mei distance. This effect is about half of what is needed to fully explain the difference in (σ_e,α) slope in the middle-right and bottom-right panels of Figure 2.9, assuming the same correlation holds for the non-Virgo galaxies that do not have a Mei distance determination.

If we adjust the IMF mismatch parameter with simple scaling relations from Mei to Tonry for the set of galaxies that have a distance determination by both, the best-fit slope of this subset for the (σ_e,α) relation increases from 0.00090 to 0.00140, while the value of R^2 increases from 0.221 to 0.338. If we do the opposite for the high quality Tonry galaxies, Figure 2.9 (bottom right panel), using $\alpha_{new} = \alpha_{old} \cdot (1.156 - 7.591 \cdot 10^{-4} \cdot \sigma_e)$, the best-fit slope decreases from 0.0027 to 0.0022, while the value of R^2 decreases from 0.215 to 0.148. The calibration effect is significant, but not sufficient to completely explain the difference in (σ_e,α) trend between the two sets. Qualitatively the conclusion that there is an IMF trend seems to hold. However, one should keep in mind that this conclusion also de-

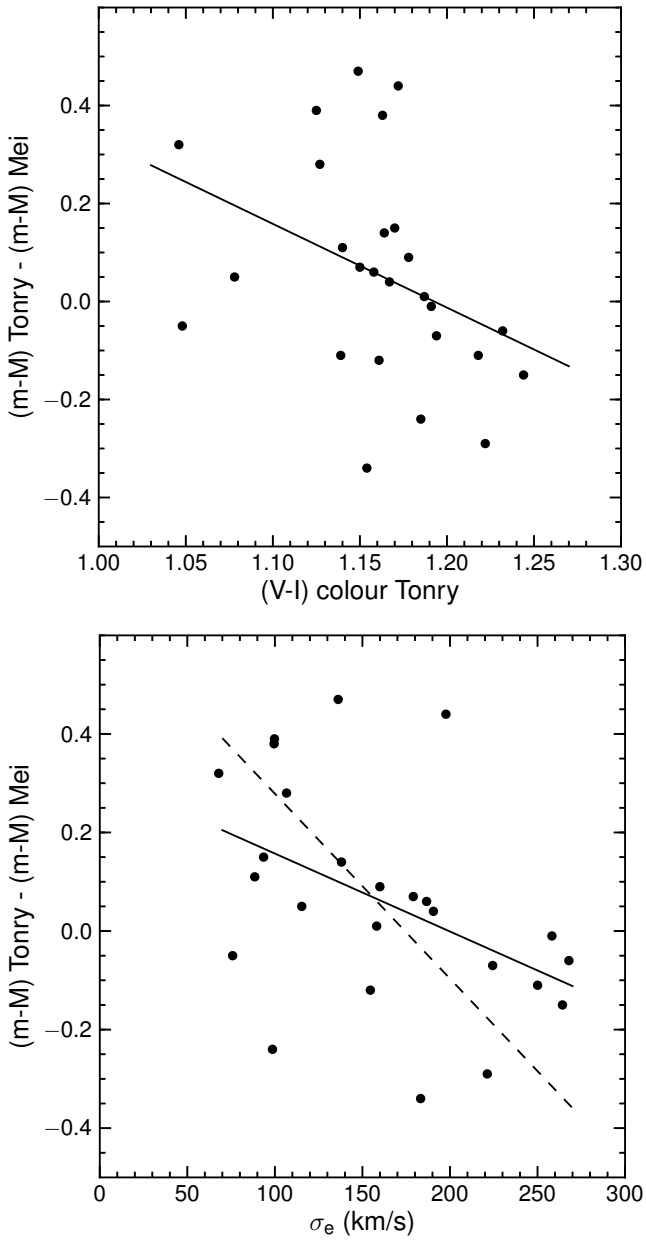

Figure 2.10: For the galaxies that have an SBF distance determination from both Tonry et al. (2001) and Mei et al. (2007), the difference in distance modulus is plotted as a function of V-I color from Tonry (top panel) and the effective velocity dispersion from ATLAS^{3D} (bottom panel). A trend in distance calibration is visible in both panels, with respective R^2 correlations of 0.14 and 0.20. The dashed line in the right panel represents the systematic bias that would be needed to completely explain the difference in (σ_e, α) trend between Tonry and Mei. The observed bias is roughly half of what is needed.

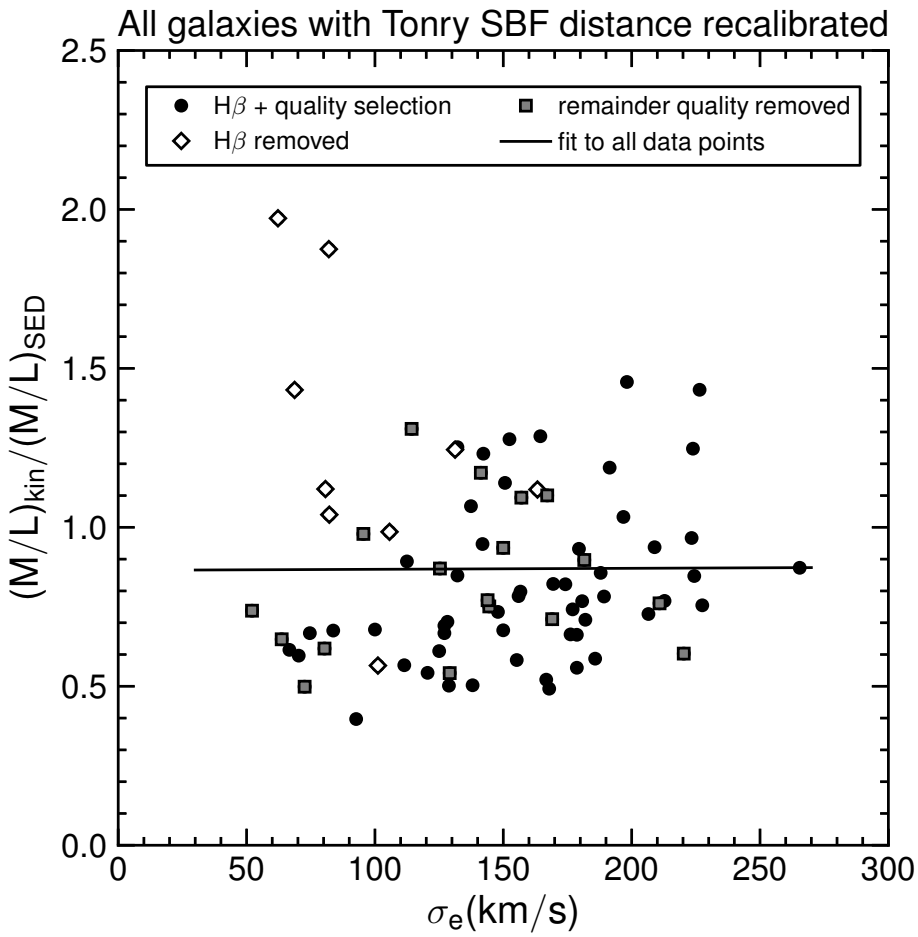

Figure 2.11: Trend of the IMF mismatch parameter $\alpha = (M/L)_{\rm kin}/(M/L)_{\rm SED}$ with effective velocity dispersion for all galaxies that have a Tonry et al. (2001) SBF distance in ATLAS$^{\rm 3D}$. Data points have been recalibrated to account for the σ_e dependent difference with Mei et al. (2007) SBF distances. The fit to all data points has an R^2 of 0.00002 and slope of 0.00003.

pends on the $H\beta$ selection effects discussed earlier. For example, the strongest trend of Figure 2.9 (bottom right panel) can be made to completely disappear by both recalibrating the Tonry SBF distance and including the ``lower quality JAM fit'' galaxies, see Figure 2.11. Moreover, in section 2.6 we showed that the effect of mass completeness of the galaxy sample on the inferred (σ_e,α) relation can be large.

2.8 Conclusions

We have asserted the evidence for a non-universal IMF by the ATLAS^{3D} Survey and the systematic trend of these IMF variations with the effective velocity dispersion of the Early Type Galaxies.

- We analysed the correlation between the kinematic mass to light ratio and the IMF mismatch parameter from Cappellari et al. (2012). We show that a similar correlation could arise from Gaussian measurement errors on the kinematic mass to light ratio of the order 30%, i.e. larger than anticipated (Figures 2.2, 2.3). However, the observed correlation is somewhat larger than expected from this Gaussian error simulation. The inferred IMF variation hence depends crucially on the precise understanding of the modelling and measurement errors. For this reason, secondary evidence in the form of a large trend of the inferred IMF with another astrophysical variable would be very helpful. The largest trend (at Pearson $R^2 = 0.11$) is found for velocity dispersion within an effective radius.

- Part of the trend of the IMF with velocity dispersion depends on a galaxy selection on $H\beta$ absorption, meant to exclude galaxies with a strong radial gradient in stellar populations (Figures 2.2, 2.4). Although this selection might be unavoidable due to the larger errors in the determinations of $M_{\rm SED}$ and $M_{\rm kin}$, one should keep in mind the bias that it produces, especially since these are mostly low velocity galaxies with a high IMF mismatch parameter, opposing the trend of the other galaxies.

- The IMF trend with velocity dispersion is not accompanied by an IMF trend with mass inferred from SED fitting (Figure 2.4). Thus, contrary to what one might expect (McGee et al. 2014), taken at face value, the ATLAS^{3D} results imply no significant changes in the shape of the observed galaxy stellar mass function (Figure 2.5).

- The ATLAS^{3D} Survey is selected to an absolute K-band magnitude M_K of -21.5. We estimate that this results in incompleteness for masses below

$2 \times 10^{10}\mathrm{M}_{\odot}$ (Figure 2.6) (higher than the low-end mass of $\sim 6 \times 10^{9}\mathrm{M}_{\odot}$ (Cappellari et al. 2011a)). Below this completeness limit the mass plane (MP) as defined by Cappellari et al. (2013b,a) is expected to be affected by completeness effects. The inferred trend between IMF and velocity dispersion is dependent on the precise selection cut-off at the low mass end used in the fit. Specifically, restricting the galaxy sample to the domain $M_{\mathrm{kin}} > 2 \times 10^{10}\mathrm{M}_{\odot}$ removes the IMF trend with velocity dispersion, whereas the trend is relatively unaffected for a similar sample selection on M_{SED} (Figure 2.7).

- Apart from a trend of the IMF mismatch parameter $\alpha = (M/L)_{\mathrm{kin}}/(M/L)_{\mathrm{SED}}$ with velocity dispersion, we also find a trend with distance (Figure 2.8). If the correlation between IMF and distance were genuine, then it would presumably be due to environment. However, we find no correlation between the IMF of nearest neighbours.

- Selecting galaxies based on the method that was used to measure their distance (distance is used as input in the kinematical fitting procedure) shows that both the IMF trend with distance and the IMF trend with velocity dispersion are concentrated in the subset of galaxies that have a distance determination from Tonry et al. (2001) (Figure 2.9). Equivalently, both trends are concentrated in the subset of galaxies that are closer than 25 Mpc and that do not belong to the Virgo Cluster[7]. Most galaxies in the Virgo Cluster have a distance determination from Mei et al. (2007). The subset of galaxies more distant than 25 Mpc shows no IMF trend with velocity dispersion[8].

- Part of the difference in the IMF trend with velocity dispersion between the ETGs with a distance determination from Tonry et al. (2001) and those with a distance determination from Mei et al. (2007) can be traced back to calibration differences of the SBF distance scale with colour (Figure 2.10). The empirical colour-calibration from Mei et al. (2007) automatically removes any correlation between distance and velocity dispersion for Virgo galaxies (Table 2.4). It also reduces the kinematically deduced IMF trend with velocity dispersion with respect to Tonry et al. (2001). Since this conclusion is reached by comparing the 26 galaxies that have a distance measurement by both Tonry et al. (2001) and Mei et al. (2007) it might be affected by small number statistics.

[7]The probability of an IMF-velocity dispersion correlation at least as large as that observed for the (non-Virgo, closer than 25 Mpc) galaxy subsample, from a random subsample of galaxies is 1.5%.

[8]The probability of an IMF-velocity dispersion correlation at least as small as that observed for the subsample of galaxies further than 25 Mpc, from a random subsample of galaxies is 12%.

The dependence of the IMF - σ relation on the mass cutoff suggests that it would be valuable to extend the dataset to a lower mass completeness limit (currently at $2 \times 10^{10} M_{\odot}$). This can rule out the possibility that selection effects contribute to the IMF dependence on velocity dispersion.

This study does not rule out the existence of IMF variations or the correlation of these with velocity dispersion, but it does point out several independent effects that can mimic IMF variations within the framework of the ATLAS^{3D} analysis. We need a better understanding and control over random- and systematic errors in ATLAS^{3D}-like analyses and ultimately we need precision agreement between the different experimental probes of the galactic scale IMF.

Acknowledgements

We thank Jarle Brinchmann, Konrad Kuijken, Ivo Labbe and Adam Muzzin for helpful discussions. We thank Sean McGee for a careful reading of the manuscript. We thank the referee for providing constructive comments and help in improving the contents of this paper. We gratefully acknowledge support from the European Research Council under the European Union's Seventh Framework Programme (FP7/2007-2013) / ERC Grant agreement 278594-GasAroundGalaxies.

There are 10^{11} stars in the galaxy. That used to be a huge number. But it's only a hundred billion. It's less than the national deficit! We used to call them astronomical numbers. Now we should call them economical numbers.

-- Richard Feynman[9]

[9] (Goodstein 1989)

3 Implications of a variable IMF for the interpretation of observations of galaxy populations

Based on:
Bart Clauwens, Joop Schaye, Marijn Franx
Implications of a variable IMF for the interpretation of observations of galaxy populations
Published in MNRAS

We investigate the effect of a metallicity-dependent stellar initial mass function (IMF), as deduced observationally by Martín-Navarro et al. (2015d), on the inferred stellar masses and star formation rates (SFRs) of a representative sample of 186,886 SDSS galaxies. Relative to a Chabrier IMF, for which we show the implied masses to be close to minimal, the inferred masses increase in both the low- and high-metallicity regimes due to the addition of stellar remnants and dwarf stars, respectively. The resulting galaxy stellar mass function (GSMF) shifts toward higher masses by 0.5 dex, without affecting the high-mass slope (and thus the need for effective quenching). The implied low-redshift SFR density increases by an order of magnitude. However, these results depend strongly on the assumed IMF parametrisation, which is not directly constrained by the observations. Varying the low-end IMF slope instead of the high-end IMF slope, while maintaining the same dwarf-to-giant ratio, results in a much more modest GSMF shift of 0.2 dex and a 10 per cent increase in the SFR density relative to the Chabrier IMF. A bottom-heavy IMF during the late, metal-rich evolutionary stage of a galaxy would help explain the rapid quenching and the bimodality in the galaxy population by on the one hand making galaxies less quenched (due to the continued formation of dwarf stars) and on the other hand reducing the gas consumption timescale. We conclude that the implications of the observational evidence for a variable IMF could vary from absolutely dramatic to mild but significant.

3.1 Introduction

The stellar initial mass function (IMF) describes the number distribution of stars as a function of stellar mass at the zero age main sequence. The IMF can not only help us understand physical processes inside molecular clouds, it is also a key ingredient for understanding astrophysical processes on larger scales. A top-heavy IMF will lead to more energetic stellar feedback, a higher metal production and more ionizing radiation, which could have an impact on the nature of the formed galaxies, the total star formation history, metal enrichment and on the re-ionization history of our Universe.

Although IMF studies have a rich history going back to the seminal work of Salpeter (1955), both in nearby galaxies through direct star counts and in more distant galaxies by more indirect methods, a consensus on the functional form of the IMF and its possible dependencies has not been reached. Observations aiming to measure galaxy stellar masses and star formation rates typically assume a Chabrier (2003) IMF (e.g. Moustakas et al. 2013; Bauer et al. 2013; Chang et al. 2015) or a similar Kroupa (2001) IMF (e.g. Kauffmann et al. 2003; Muzzin et al. 2013a). The same holds true for hydrodynamic simulations of galaxy formation (e.g. Hopkins et al. 2014; Schaye et al. 2015; Snyder et al. 2015). A different IMF, specifically an IMF that depends on one or more local astrophysical conditions, could have a dramatic impact on the interpretation of observations and the results of simulations.

Most nearby IMF measurements tend to support a universal Kroupa- or Chabrier-like IMF, see Kroupa (2002); Chabrier (2003); Kroupa et al. (2013); Kirk and Myers (2011); Bastian et al. (2011) and references therein, but there are many complications in determining the IMF from direct star counts, see e.g. Scalo (2005) and Weisz et al. (2013). Recently, Weisz et al. (2015) found a very small intrinsic scatter in the power-law slope of the high-end mass function for young resolved star clusters in M31, albeit at a higher value (1.45 ± 0.05) than the Kroupa slope (1.30) or the slope they infer for the Milky Way (1.15 ± 0.1), although this offset might be explained by dynamical depletion (Oh and Kroupa 2016). Conversely, a recent dynamical study of 29 Local Group Clusters by Zaritsky et al. (2014) concludes that there are clear variations in the cluster IMF. Indications for a nearby metallicity-dependent IMF come from stellar counts of two nearby metal-poor, old, ultra-faint dwarf galaxies by Geha et al. (2013), which are found to have a very top-heavy IMF, and from a study of galactic globular clusters by Marks et al. (2012), who report an increasingly top-heavy IMF with decreasing cluster metallicity and increasing cloud-core density.

IMF studies based on observations of more distant galaxies can be roughly di-

vided into two classes. The first class consists of dynamical methods that weigh the stellar content of a galaxy and compare this to the stellar mass obtained from spectral energy density (SED) fitting. Studies of the dynamical masses of SDSS galaxies by Dutton et al. (2013); Conroy and van Dokkum (2012); Tortora et al. (2013) report IMF trends with velocity dispersion or galaxy mass. However, a similar study of low-mass (around $10^9 M_\odot$) early-type galaxies (ETGs) by Tortora et al. (2016) reports the same average IMF normalisation for these low-mass ETGs as for the more massive ETGs. All these studies report relatively large variations in the IMF mass normalisation at fixed stellar mass, but it is not exactly clear to what extent these variations could be caused by assumptions on the dark matter profile, the anisotropy of stellar motions or the inclination of the observed galaxies. A major risk is confusion of dark matter and stellar matter. For this reason the centres of ETGs are the best targets as they are believed to be relatively devoid of dark matter.

The most ambitious attempt at measuring dynamical stellar masses of ETG centres has been undertaken by the ATLAS^{3D} team, who use integral field spectroscopy of 260 nearby ETGs. Cappellari et al. (2012, 2013b,a) report IMF variations that correlate with the stellar mass-to-light ratio inferred from SED modelling under the assumption of a universal IMF and also with the effective velocity dispersion of the ETGs, but not with age, metallicity or alpha-enhancement (McDermid et al. 2014). However, Clauwens et al. (2015) show that the inferred IMF variations could be caused by a slight underestimation of the modeling- and measurement errors. Random Gaussian errors in the total kinematic mass determination of the order 30% would give a trend that is very similar to the one reported in Cappellari et al. (2012). Recently, Li et al. (2016) tested the accuracy of stellar mass measurements with the JAM method used by Cappellari et al. (2012), by applying it to mock galaxies from the Illustris simulation and they report random modeling errors of 40% and biases that grow with diminishing resolution[1].

Strong gravitational lensing provides an independent way to measure dynamical stellar masses. In general such studies find a Kroupa-like IMF normalization for spiral galaxies (Brewer et al. 2012) and a normalization heavier than Kroupa for massive ETGs (Treu et al. 2010; Oguri et al. 2014; Barnabè et al. 2013), but the analysis of the nearest strong-lensing galaxy by Smith and Lucey (2013) does

[1]This 40% error is for the high-resolution test, which still has a lower resolution than is typical for ATLAS^{3D} observations. A similar analysis of mock galaxies at a higher resolution would be needed to disentangle the contributions of IMF variations and modelling- and measurement-errors to the observed variations in M_{*kin}/M_{*Salp} found by the ATLAS^{3D} Survey. A resolution-dependent bias could also possibly cause a trend of M_{*kin}/M_{*Salp} with distance, like the one reported in Clauwens et al. (2015).

not support this[2].

The second class of independent methods to determine the galaxy scale IMF relies on the observation of specific spectral features that discriminate between low- and high-mass stars. A comparison of the X-ray binary count studies of Dabringhausen et al. (2012) and Peacock et al. (2014) suggests a top-heavy IMF for ultracompact dwarf galaxies. Several spectral studies point at an enhanced fraction of low-mass stars in ETGs with respect to a standard Kroupa IMF. van Dokkum and Conroy (2012) and Conroy and van Dokkum (2012) find an IMF trend with alpha-enhancement, velocity dispersion and metallicity (in decreasing order of significance), compatible with results from Pastorello et al. (2014). Other studies (La Barbera et al. 2013; Martín-Navarro et al. 2015c,b) suggest a trend that is driven by velocity dispersion or stellar mass. Smith (2014) and Smith et al. (2015) show that there is disagreement between IMF results from spectral features and respectively kinematic- and strong lensing studies of the same galaxies.

Overall, IMF observations have not yet converged to a single view. The primary candidates for variables that correlate with IMF variations are metallicity and velocity dispersion. Some other candidates suggested by observations are dynamically determined density(Spiniello et al. 2015), star formation rate (Gunawardhana et al. 2011), luminosity (Hoversten and Glazebrook 2008), surface brightness (Meurer et al. 2009 and Lee et al. 2009, but see Boselli et al. 2009) and cosmic time (Davé 2008; Ferreras et al. 2015). Of course all these variables are also correlated with each other in a complicated way. An ambitious attempt at resolving these interdependencies is the IGIMF theory (Weidner et al. 2013; Recchi and Kroupa 2015) which builds an effective galactic scale IMF in a bottom-up manner from the IMFs of individual star clusters, that depend on metallicity, SFR and cloud core density. In this paper we will take a more agnostic top-down approach and consider IMF variations on a galactic scale.

Distilling a consistent view from the reported constraints on the IMF is difficult, since the observations are performed on different types of galaxies with different diagnostics, different systematics, different model dependencies, different assumptions, a sensitivity to different mass ranges of the IMF and even different IMF parametrisations. For example, some spectroscopic studies use the so-called bimodal IMF parametrisation from Vazdekis et al. (1996), for which the free parameter is the IMF slope above 0.6 $M_\odot$, whereas others use a parametrisation for which the IMF slope above 0.5 $M_\odot$ or 1.0 $M_\odot$ is kept fixed (Conroy and van Dokkum 2012). In addition, sometimes the low-mass cut-off is allowed to vary

[2]The strong-lensing measurement of this particular galaxy is expected to be less sensitive to dark matter, since the Einstein radius is roughly 25% of the effective radius, probing a region that is believed to be dominated by stars.

(Spiniello et al. 2015).

Still, the implications of IMF variations on derived galaxy properties could be large and are worth investigating. Previous work on the effect of IMF variations on inferred galaxy masses has focused specifically on the implications of an IMF trend with velocity dispersion. McGee et al. (2014) report a significantly shallower galaxy stellar mass function (GSMF) high-mass drop-off based on IMF-velocity dispersion trends observed by La Barbera et al. (2013); Ferreras et al. (2013); Spiniello et al. (2014). Conversely, Clauwens et al. (2015) report a nearly unchanged GSMF high-mass drop-off, based on the IMF observations by Cappellari et al. (2012).

In this paper we investigate the effects of the IMF trend with metallicity observed by Martín-Navarro et al. (2015d), although many of the main conclusions also hold in a broader context. We will not only focus on the effects on inferred galaxy masses, but also on the inferred star formation rates, which turn out to be very sensitive to the assumed IMF.

Martín-Navarro et al. (2015d) find a strong IMF dependency on metallicity, with high-metallicity regions containing more low-mass stars. They analyse integral field spectroscopic data from the CALIFA survey (Sánchez et al. 2012) for 24 ETGs in order to obtain radial IMF profiles, using the spectral indices $H_{\beta O}$, [MgFe]′ , Mg2Fe, NaD, $TiO_{2CALIFA}$ and TiO_1. A consistent IMF-metallicity trend is obtained for SDSS galaxy spectra that include near-IR IMF-sensitive features. Their sample shows a weaker IMF dependence on respectively age, velocity dispersion and [Mg/Fe]. The reported stronger trend with metallicity (Spearman rank correlation 0.82) rather than with [Mg/Fe] (Spearman rank correlation 0.21) is not necessarily in conflict with the results from Conroy and van Dokkum (2012) who find Spearman rank correlations of respectively 0.33 with metallicity and 0.81 with [Mg/Fe], because the sample of Martín-Navarro et al. (2015d) has a much wider range of metallicities, going as low as [M/H]≈ -0.4.

In this paper we investigate the implications that this strong metallicity dependence of the IMF, concretely equation 2 from Martín-Navarro et al. (2015d), would have on several galaxy diagnostics. Specifically, we concentrate on the implications for galaxy stellar masses, star formation rates and derived relations like the galaxy stellar mass function, the main sequence of star formation and the mass-metallicity relation. We do this by re-interpreting the observations of a representative sample of 186,886 SDSS redshift $z \sim 0.1$ galaxies. Although the presented results will be fully quantitative, our results should be viewed in a more qualitative way, due to the many uncertainties in measuring the IMF and the resulting diversity of the reported IMF measurements that have been discussed.

Although the physical mechanisms responsible for the formation of the IMF are not yet understood, metallicity, being a local property of the interstellar medium

with a strong influence on the cooling rate of the gas, is likely to have an influence on the mass function of stars. On the other hand, a locally metallicity-dependent IMF could have a large influence on galaxies as a whole. A reduction in the formation of high-mass stars with respect to low-mass stars in the late, high-metallicity, stage of a galaxy's evolution could have an accelerating effect on the quenching of star formation in the galaxy, due to less energetic stellar feedback. This could trigger a last burst of low-mass star formation that empties the cool gas reservoir more rapidly. The true star formation rate of the galaxy would be larger than the typically inferred SFR, which is only sensitive to high-mass star formation.

The remainder of this paper is organised as follows. Section 3.2 describes the method used to translate the metallicity-dependent IMF variations into stellar mass and SFR changes for a large sample of SDSS galaxies. The implications for the star formation main sequence, GSMF and the mass-metallicity relation are presented in sections 3.3, 3.4 and 3.5, respectively. Section 3.6 discusses the possible implications of a IMF-metallicity trend on the quenching of galaxies. For an overview of the main takeaways of this work, see section 3.7. Some limitations of our analysis are discussed in the Appendix. Throughout this work we adopt a solar abundance of $Z_{\odot} = 0.019$.

3.2 Method

3.2.1 The Vazdekis IMF

The IMF can be uniquely defined by its slope as a function of stellar mass. The IMF slope is defined as the slope in the plane of (log number of stars per log initial stellar mass) versus (log initial stellar mass), see Figure 3.1. It is customary to define this IMF slope to be positive for a descending curve.

Martín-Navarro et al. (2015d) report a strong trend of the IMF slope with metallicity, expressed in their equation 2:

$$\Gamma_b = 2.2(\pm 0.1) + 3.1(\pm 0.5) \times [M/H], \tag{3.1}$$

where $[M/H]$ is the logarithm of the metallicity with respect to solar[3] and Γ_b is the IMF slope above a stellar mass of 0.6 $M_{\odot}$ in the bimodal IMF parametrisation of Vazdekis et al. (1996)[4]. In this work we will refer to this IMF parametrisation

[3]Note that the inferred high-end IMF slope is quite high for solar metallicity ($\Gamma_b = 2.2$ for $Z = 0.019$) which is possibly in tension with local IMF measurements, although adopting a solar metallicity of $Z = 0.012$ lowers the inferred IMF slope to $\Gamma_b = 1.58$. $\Gamma_b = 1.3$ is reached for $Z = 0.010$.

[4]This high-end IMF slope is defined such that the Salpeter value is 1.35 (and not 2.35).

as the Vazdekis IMF. We show some examples of this IMF for different values of Γ_b in Figure 3.1. This Vazdekis IMF has a slope of zero below a stellar mass of 0.2 and a spline from 0.2 $M_\odot$ to 0.6 $M_\odot$. The spline is normalized such that the endpoints would be the same if the IMF of the two outer parts would be interpolated and matched at 0.4 $M_\odot$. The IMF is defined between 0.1 $M_\odot$ and 100 $M_\odot$. Equation 3.1 is a fit to spectroscopic IMF determinations from local CALIFA measurements, SDSS measurements and radial profile measurements of three ETGs by Martín-Navarro et al. (2015d). These three data sets use a similar spectroscopic IMF analysis on different sources and give consistent results, as can be seen from fig. 2 of Martín-Navarro et al. (2015d).

The aim of this paper is to apply this relation on a galaxy-by-galaxy basis to a large sample of SDSS galaxies and to investigate the potential consequences of such a metallicity-dependent IMF. We use the stellar metallicity measurements of Gallazzi et al. (2005) as input for the metallicity-dependent IMF. In doing so we implicitly assume that these metallicity measurements themselves are not dependent on the IMF. This will not be completely accurate, but it is a valid approximation, since the typically IMF-dependent metal line indices TiO and NaD are excluded from the metallicity measurement of Gallazzi et al. (2005). They concentrate on those indices that are best reproduced by the Bruzual and Charlot (2003) models with a fixed IMF[5]. A recent mass-metallicity relation measurement by González Delgado et al. (2014) with the CALIFA integral field spectrograph for a sample of 300 galaxies, ranging from ellipticals to late-type spirals, agrees well with the SDSS measurements by Gallazzi et al. (2005). At a given mass, the scatter in the metallicity is expected to be mostly intrinsic, rather than due to measurement uncertainties (see fig. 8 of Gallazzi et al. 2005).

The spectroscopic IMF determination of Martín-Navarro et al. (2015d) relies on the light being dominated by old stars. Therefore these measurements are done exclusively for ETGs. We will assume that the same relation holds also for star forming galaxies. Of course there is a possibility that a metallicity-IMF relation will manifest itself differently in star forming galaxies, but large differences are not expected, since the IMF is literally a property of the galaxy during star formation. Hence, for any given ETG, the measured IMF corresponds to the time when most of its stellar mass was build up, at which time it would be classified as a star forming galaxy. There is a possibility of a redshift dependence of equation 3.1, which could mean that it would be different for ETGs and star forming galaxies observed at redshift zero, but here we will assume that the IMF is solely determined by the local

[5]The metallicities measured by Martín-Navarro et al. (2015d) are expected to deviate slightly from those of Gallazzi et al. (2005). Generally the age-sensitive features (e.g. Hβ) have a slight sensitivity to the IMF (La Barbera et al. 2013), which results in slightly younger ages and thus slightly higher metallicities for a bottom-heavy IMF with respect to a Chabrier IMF.

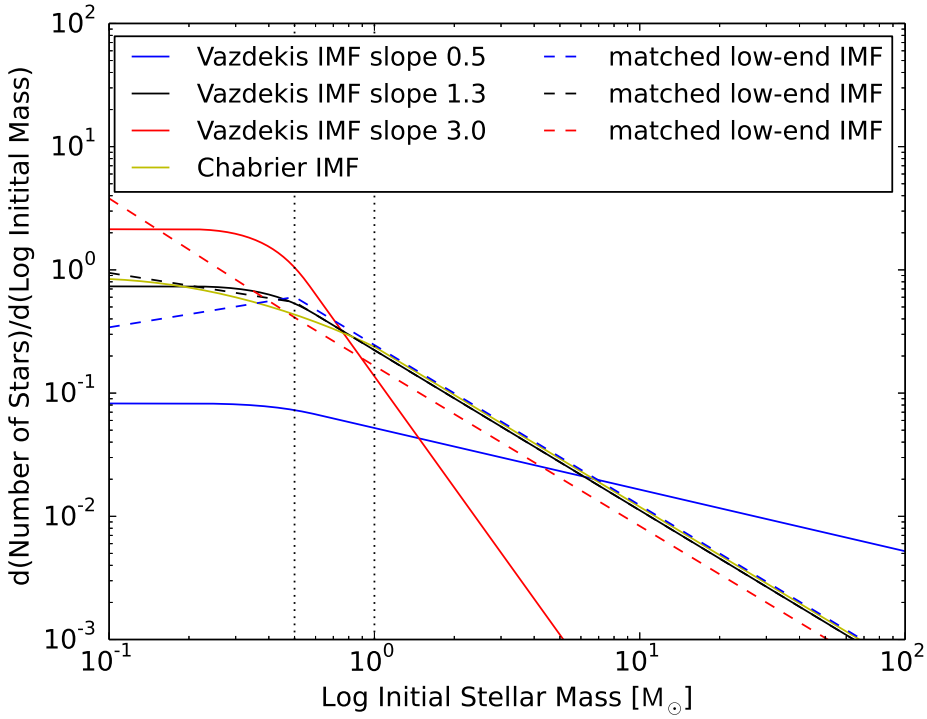

Figure 3.1: The IMF for the two parametrisations used throughout this work. The yellow solid line depicts the Chabrier IMF. The other solid lines are for the Vazdekis IMF (Vazdekis et al. 1996), which is parametrised by its high-end slope. The indicated IMF slopes for the blue-, black- and red curves correspond to a $[M/H]$ value in equation 3.1 of respectively -0.55, -0.29 and 0.26. Dashed lines show our corresponding low-end IMF, for which the slope below 0.5 $\mathrm{M}_{\odot}$ is the free parameter. Lines with the same colour are matched on the dwarf-to-giant ratio, equation 3.3, defined as the ratio of the mass in stars below 0.5 $\mathrm{M}_{\odot}$ with respect to the mass in stars below 1.0 $\mathrm{M}_{\odot}$. These mass regimes are indicated with the vertical dotted lines. The same dwarf-to-giant ratio, as measured from IMF sensitive spectral lines (Martín-Navarro et al. 2015d), can be accommodated by vastly different IMFs.

gas metallicity during star formation and does not depend directly on redshift. The measured stellar metallicity reflects this local gas metallicity during star formation.

Another simplifying assumption of our analysis is that we neglect metallicity gradients and characterise each galaxy by a single metallicity. This is justified by the fact that the IMF determinations of galaxy regions by Martín-Navarro et al. (2015d) lie on the same metallicity-dependent trend as that of complete SDSS galaxies. Another caveat is that the CALIFA ETG sample consists mostly of high-velocity dispersion galaxies. We assume that the reported IMF-metallicity trend for this sample is representative for all galaxies. We will see that the implications of this IMF trend for inferred galaxy properties are most prominent at high masses and therefore are not expected to be affected much by this assumption.

The two main galaxy properties that we want to adjust to a metallicity-dependent IMF are galaxy stellar mass and star formation rate. We use the SDSS masses and star formation rates from Chang et al. (2015) and the r-band weighted ages from Gallazzi et al. (2005) . We match on Plate ID, Fiber ID and modified julian date and select the galaxies with a well-defined metallicity and age in Gallazzi et al. (2005). This leaves a sample of 186,886 SDSS galaxies.

To recompute the galaxy masses, for each galaxy we compare the Cousins R-band mass-to-light ratio of a simple stellar population (SSP) with the given metallicity and age and a Chabrier IMF[6] to the mass-to-light ratio of a SSP with the same metallicity and age, but with the IMF implied by equation 3.1. We verified that the results are almost the same if we use the Johnson V-band or the SDSS r-band.

All results in this paper are obtained with the flexible stellar population synthesis (FSPS) code of Conroy and Gunn (2010), but where possible we verified that very similar results are obtained by using the tables from the MILES website. Metallicities are restricted to the range for which there are BaSTI isochrones (Pietrinferni et al. 2013), $-1.80 < log_{10}(Z/\mathrm{Z}_{\odot}) < 0.32$, for a solar metallicity of $\mathrm{Z}_{\odot} = 0.019$ (which is used throughout this paper). The FSPS spectra are generated for IMF slope values binned with a separation of $\delta\Gamma = 0.1$. Then the M/L_R values are interpolated in the 3-dimensional space of (log age, metallicity, IMF slope).

We apply equation 3.1 slightly outside the metallicity regime of the observa-

[6]The Chabrier IMF (Chabrier 2003) is defined as $\frac{d\,N}{d\,log_{10}(M/\mathrm{M}_{\odot})} = A_1\, exp[-\frac{(log_{10}(M/\mathrm{M}_{\odot})-log_{10}(0.079))^2}{2\times 0.69^2}]$ for $M < 1.0\,\mathrm{M}_{\odot}$ and $\frac{d\,N}{d\,log_{10}(M/\mathrm{M}_{\odot})} = A_2\,(M/\mathrm{M}_{\odot})^{-1.3}$ for $M > 1.0\,\mathrm{M}_{\odot}$, with N the number of stars and M the initial stellar mass. The normalisation constants A_1 and A_2 are fixed by the requirement that the IMF is continuous at $M = 1.0\,\mathrm{M}_{\odot}$ and that the total integral of initial mass in stars from $0.1\,\mathrm{M}_{\odot}$ to $100\,\mathrm{M}_{\odot}$ equals $1\,\mathrm{M}_{\odot}$. This IMF is very similar to the (Kroupa 2001) IMF and the "Canonical IMF" (Kroupa et al. 2013).

tions by Martín-Navarro et al. (2015d) ($-0.40 < log_{10}(Z/\mathrm{Z}_{\odot}) < 0.25$). The highest metallicity in Gallazzi et al. (2005) is $log_{10}(Z/\mathrm{Z}_{\odot}) = 0.417$. At the low-metallicity-end we extrapolate to $log_{10}(Z/\mathrm{Z}_{\odot}) = -0.60$ or equivalently a Vazdekis IMF slope of 0.34, and keep the IMF constant for lower metallicities. This extrapolation, necessitated by a lack of measurements for galaxies in the metallicity range $-1.80 < log_{10}(Z/\mathrm{Z}_{\odot}) < -0.40$, introduces a large uncertainty in the predictions for these low-metallicity galaxies. Equation 3.1 gives very shallow high-end IMF slopes for very metal-poor galaxies, thus much depends on the exact choice of the low-metallicity cut-off. Also, for shallow high-end IMF slopes, the results become quite sensitive to the precise high-mass cut-off that is used. For an IMF defined in between 0.1 $\mathrm{M}_{\odot}$ and 100 $\mathrm{M}_{\odot}$, half of the initial mass is created in stars heavier than 50 $\mathrm{M}_{\odot}$ for a high-end IMF slope of zero. In equation 3.1 this happens at $log_{10}(Z/\mathrm{Z}_{\odot}) = -0.71$. At our adopted low-metallicity cut-off of $log_{10}(Z/\mathrm{Z}_{\odot}) = -0.6$, 37% of the stellar mass is created in stars heavier than 50 $\mathrm{M}_{\odot}$. It is good to keep in mind that the IMF measurements of Martín-Navarro et al. (2015d) are still marginally consistent with a minimal high-end slope of 1.3 (Kroupa) for galaxies with $log_{10}(Z/\mathrm{Z}_{\odot}) < -0.29$, in which case there would be a bottom-heavy IMF for metal-rich galaxies, but no top-heavy IMF for metal-poor galaxies.

We may expect a top-heavy IMF for extremely low metallicities in theorised Population III stars, but the IMF in the intermediate metallicity regime is not well constrained. This metallicity regime is however probed by the IMF determination of Marks et al. (2012). They report an IMF dependence on metallicity for globular clusters that is qualitatively similar to Martín-Navarro et al. (2015d). Their fit of the metallicity-dependent high-end IMF slope reaches 0.05 for the lowest metallicities ($Z \approx -2.5\mathrm{Z}_{\odot}$), so even lower than our adopted minimum value of 0.34. Figure 3.2 shows the fraction of galaxies in our sample that fall below our adopted cut-off of the IMF-metallicity relation as a function of stellar mass for a Chabrier IMF. Below a mass of $10^{9.2}\mathrm{M}_{\odot}$ (from SED fitting with a Chabrier IMF) 50% of the galaxies have a metallicity lower than the cut-off. A simple extrapolation of equation 3.1 would therefore enhance the effect of a top-heavy IMF at low metallicities with respect to the results reported in this work for low masses.

3.2.2 The matched low-end IMF

Another implicit extrapolation of the IMF determination from spectral indices by Martín-Navarro et al. (2015d) is contained in the parametrisation used for the IMF. Although the free parameter of the Vazdekis et al. (1996) IMF parametrisation is the high-end IMF slope, this high-end slope is not directly measured. Martín-Navarro et al. (2015d) state that the IMF sensitive features more closely

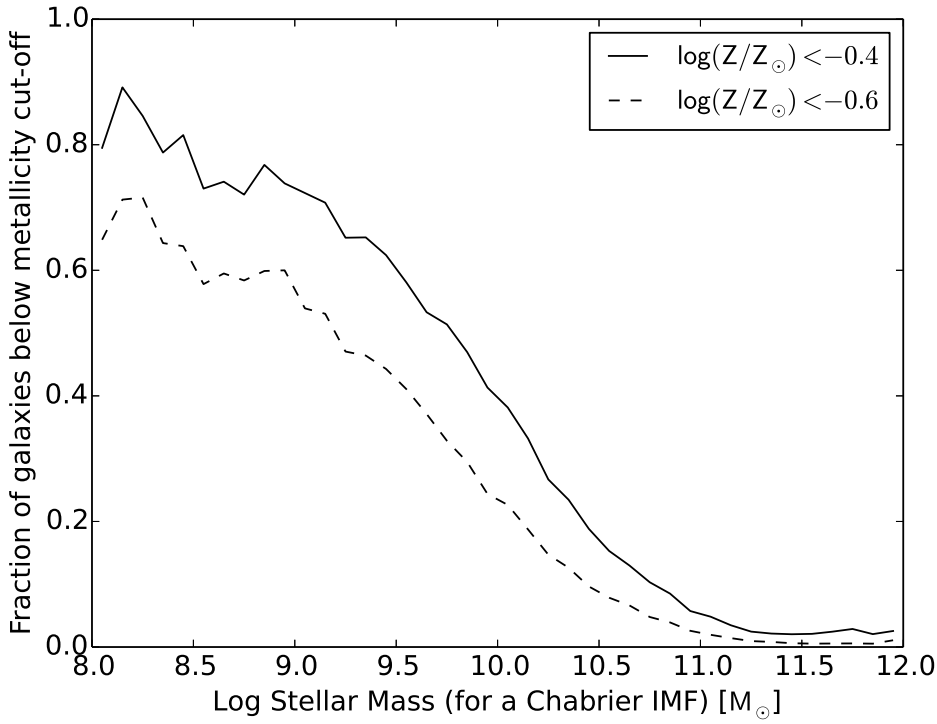

Figure 3.2: The dashed line shows the fraction of galaxies below our adopted low-metallicity cut-off of the IMF-metallicity relation, equation 3.1, at $log_{10}(Z/\mathrm{Z}_\odot) = -0.6$. For masses below $10^{9.2}\mathrm{M}_\odot$, more than 50% of the galaxies have a metallicity below this cut-off. The solid line shows the same fraction for the lowest metallicity in the sample of Martín-Navarro et al. (2015d).

trace the dwarf-to-giant ratio $F_{0.5}$, as defined in La Barbera et al. (2013):

$$F_{0.5} = \frac{\int_{0.1\mathrm{M}_\odot}^{0.5\mathrm{M}_\odot} M\Phi(M)dM}{\int_{0.1\mathrm{M}_\odot}^{100\mathrm{M}_\odot} M\Phi(M)dM}, \tag{3.2}$$

which denotes the initial mass fraction in stars below 0.5 $\mathrm{M}_\odot$. In fact, since most ETGs contain very few stars more massive than 1.0 $\mathrm{M}_\odot$, beyond this mass the inferred IMF is more sensitive to the parametrisation than to the direct observations. It would be interesting to see whether the use of an IMF parametrisation for which the low-mass end varies in the analysis of Martín-Navarro et al. (2015d), would indeed give similar results in terms of the trend between metallicity and $F_{0.5}$.

In this work, apart from the Vazdekis IMF parametrisation, we will also use an alternative `low-end' IMF parametrisation in which the IMF slope below $0.5\mathrm{M}_\odot$ is varied and the slope above $0.5\mathrm{M}_\odot$ is fixed at the standard Kroupa value of 1.3. Instead of matching the Vazdekis IMF slope to the low-end slope that yields the same $F_{0.5}$, we match the two IMF parametrisations by requiring the same value of $F_{0.5}/F_{1.0}$:

$$F_{0.5}/F_{1.0} = \frac{\int_{0.1\mathrm{M}_\odot}^{0.5\mathrm{M}_\odot} M\Phi(M)dM}{\int_{0.1\mathrm{M}_\odot}^{1.0\mathrm{M}_\odot} M\Phi(M)dM}\,. \tag{3.3}$$

Matching directly on $F_{0.5}$ would not eliminate the implicit extrapolation of the Vazdekis IMF to high masses.

For a shallow Vazdekis IMF slope, $F_{0.5}$ can become very small, but this does not mean that the stars below 0.5 $\mathrm{M}_\odot$ do not give a significant contribution to the *current* mass- or light-budget of the galaxy, since all the high-mass stars have turned into stellar remnants. Matching the two IMF parametrisations on $F_{0.5}/F_{1.0}$ more closely preserves the actually measured signal related to the dwarf-to-giant ratio. In principle one could choose to tune the mass parameter in F_M separately for each galaxy, depending on its age, but we chose to fix this value at 1.0 $\mathrm{M}_\odot$. The fact that the TiO_2 and TiO_1 indices in La Barbera et al. (2013) do not depend much on the SSP age below 10 Gyr (see their figure 4) shows that even for ETGs that have some stars with masses above 1.0 $\mathrm{M}_\odot$, these will not dominate the measured IMF signal.

Throughout this paper we will present results for the two IMF parametrisations described above, but one should keep in mind that any normalised linear combination of the two, distributing the metallicity-dependent dwarf-to-giant ratio variations over the low- and high-end IMF slopes, would also be in agreement with the data from Martín-Navarro et al. (2015d). Figure 3.1 shows some examples of IMFs for the two different parametrisations that are matched on $F_{0.5}/F_{1.0}$.

3.2.3 Star formation rates

In order to estimate the changes to the inferred star formation rates due to a variable IMF, we compare the magnitudes in several ultraviolet bands for a 100 Myr old constant star formation rate population, implemented with the help of the FSPS code. We do this for each galaxy in the sample, interpolating the metallicity between the discrete BaSTI values and the IMF slope on a 0.1 width grid. As SFR tracers we use the SDSS u-band, the GALEX FUV band and the total intensity of ionising radiation obtained from integrating the FSPS spectra up to 912.0 Å[7]. These three different bands are sensitive to star formation on different time scales. The FUV-band magnitude of a galaxy with a constant star forming rate levels off after about 100 Myr (although this is an IMF dependent statement), with H-alpha (which tracks the ionising luminosity) being sensitive to shorter time scales and the u-band to much longer time scales. Part of the high energy photons that are emitted by the young massive stars will be absorbed by dust and re-emitted in the infrared. For our purposes this is a second order effect. Assuming that the infrared output from dust is in equilibrium with the input in energetic radiation from massive young stars, it scales in a similar way with IMF changes as the UV emission.

Figure 3.3 shows how the luminosity in different bands of a 100 Myr old constant star formation rate population changes with respect to a Chabrier IMF as a function of the assumed Vazdekis slope. There is a slight dependence on the metallicity of the stellar population (the metallicity-IMF relation has not yet been implemented here). The SDSS-u, GALEX-FUV and total ionising luminosity show similar offsets. For a shallow Vazdekis IMF slope (i.e. a low metallicity) most star formation goes into massive stars and the different tracers can indicate, if interpreted using a Chabrier IMF, a SFR up to an order of magnitude too high. For a steep Vazdekis IMF slope (i.e. a high metallicity) mostly dwarf stars are formed and the luminosity in the given bands drops dramatically by up to three orders of magnitude. The difference between the FUV luminosity and the luminosity in ionising radiation also implies a calibration offset between the FUV-SFR and Hα-SFR that can exceed an order of magnitude[8].

For our sample of observed galaxies we adjust the SFR on a galaxy-by-galaxy basis by the inverse of the luminosity ratio of Figure 3.3. For each galaxy we use the Vazdekis IMF slope implied by the IMF-metallicity relation, equation 3.1. As a conservative estimate of the implied SFR change, we use the ratio of luminosities

[7]Using the number of ionising photons instead of the total energy in ionising photons gives indistinguishable results.

[8]A similar offset in the Hα-UV flux ratio appears in the IGIMF theory for low-SFR galaxies (Pflamm-Altenburg et al. 2009).

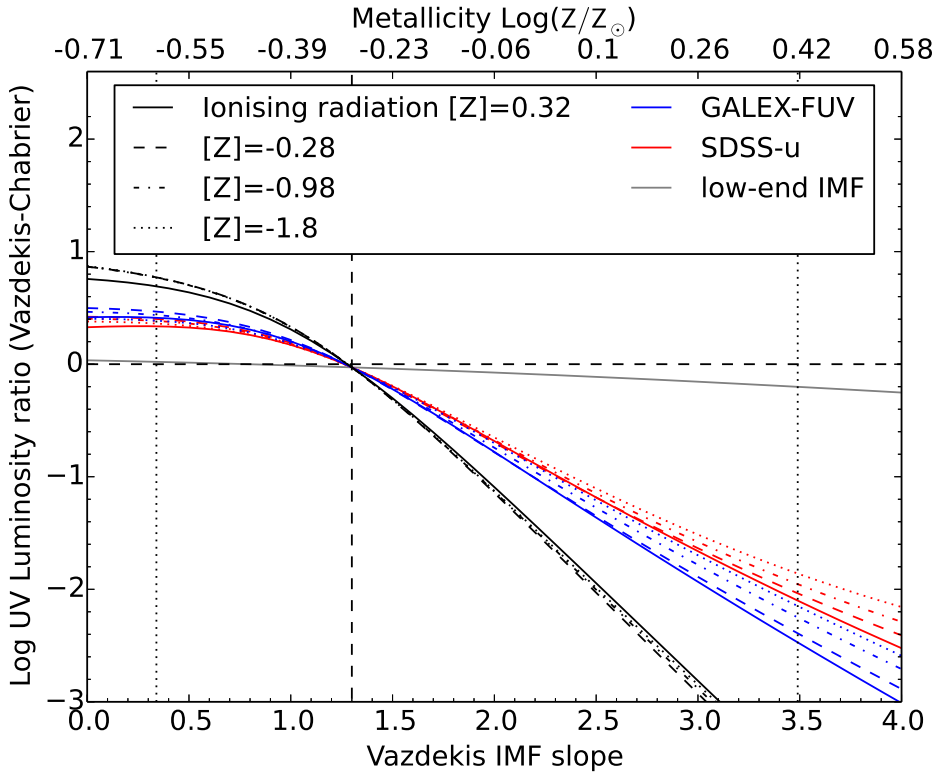

Figure 3.3: The luminosity ratio of a 100 Myr old constant star formation rate stellar population with a Vazdekis IMF with the given high-end slope and that of the same stellar population with a Chabrier IMF. The top horizontal axis gives the metallicities corresponding to the IMF slopes via equation 3.1. Different colours depict different bands: black for for the total luminosity in ionising radiation, blue for the GALEX-FUV band and red for the SDSS-u band. Different line styles depict different metallicities. The black dashed horizontal and vertical lines depict the Chabrier values and the black dotted vertical lines show the minimum and maximum values of the Vazdekis IMF slope that are used in this work. The implied correction to the star formation rate when switching from the Chabrier to the Vazdekis IMF is the inverse of this luminosity ratio. These implied SFR changes span orders of magnitude. The much smaller luminosity ratio between the low-end IMF and the Chabrier IMF is indicated by the solid grey curve. It does not depend on the choice of UV-band.

in the GALEX-FUV band.

For the `low-end' IMF parametrisation, shown in grey in Figure 3.3, the SFR changes are much smaller than for the `Vazdekis' case. Moreover, the implied changes are in this case nearly identical for the different bands and metallicities. This is because the `low-end' IMF changes the reservoir of stars that are formed below 0.5 $M_\odot$, while keeping the IMF slope above 0.5 $M_\odot$ fixed. Because dwarf stars with $M < 0.5 M_\odot$ give a negligible contribution to the luminosity in these bands, the only effect is that of a change in the overall normalization of the high-mass end of the IMF.

3.2.4 Stellar masses

Figure 3.4 shows the galaxy mass changes caused by a switch from a Chabrier IMF, depending on metallicity and r-band weighted age. The mass change is determined by the change in mass-to-light ratio in the Cousins R-band. Galaxies are represented by a simple stellar population. This is a much better approximation for the ETGs used in the IMF determination of Martín-Navarro et al. (2015d) than for actively star forming galaxies. This simplification of the star formation history is justified in the Appendix by comparing results from a SSP with those from a constant star formation history. Qualitative differences only show up for low-metallicity galaxies in the Vazdekis IMF parametrisation.

Figure 3.4 shows that for steep Vazdekis IMF slopes, or equivalently high metallicities, switching from a Chabrier IMF to a Vazdekis IMF can increase the inferred stellar mass by more than an order of magnitude due to an increase in the fraction of dwarf stars. Most of these metal-rich galaxies are old though, which results in a mass change of approximately 0.6 dex. For metal-poor galaxies, the increased fraction of stellar remnants can induce a mass increase of $0.2 - 0.65$ dex. For the low-end IMF the expected stellar mass changes are much smaller, ranging from -0.06 dex at low metallicities due to a shortage of dwarf stars to 0.29 dex at high metallicities due to an excess of dwarf stars. Mass changes for the low-end IMF are almost independent of age.

It is worth noting that for old galaxies a high-end IMF slope around 1.3, or equivalently a Chabrier-like IMF, minimizes the inferred stellar mass of the galaxy. This means that any variations in the high-end slope of the IMF away from Chabrier are bound to increase the inferred mass of the galaxy. A Chabrier IMF (or a similar Kroupa/Canonical IMF) balances the amount of mass locked up in dwarf stars on the one side and stellar remnants on the other side in such a way that the total of this invisible stellar mass is close to minimal at late times.

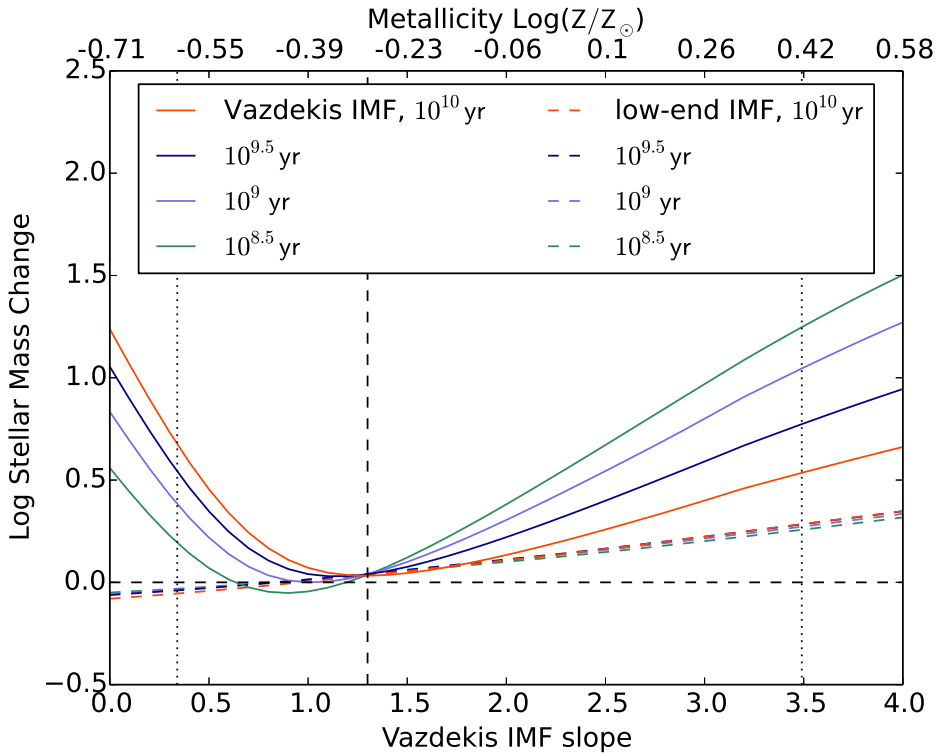

Figure 3.4: The implied stellar mass changes of galaxies resulting from switching from a Chabrier IMF to a metallicity-dependent IMF, equation 3.1, for a fixed observed luminosity. The double horizontal axis reflects this equation. The mass changes are based on the change in mass-to-light ratio in the Cousins R-band for a galaxy with a fixed age and metallicity. Different line colours represent different SSP ages. The dashed lines represent the low-end IMF parametrisations matched to the Vazdekis IMF on $F_{0.5}/F_{1.0}$, equation 3.3. The black dashed lines depict the Chabrier values and the black dotted vertical lines show the minimum and maximum values of the Vazdekis IMF slope used in this work. The stellar mass increase at high metallicities is due to dwarf stars. The slight stellar mass decrease for low metallicity and a low-end IMF is due to a shortage of dwarf stars. The Vazdekis IMF shows an increase in mass in this region due to stellar remnants. A similar plot for a constant star formation rate instead of a simple stellar population is shown in the Appendix, Figure 3.13.

3.3 Star Formation Main Sequence

Figure 3.5 shows the mass and SFR changes relative to a Chabrier IMF implied by the metallicity-dependent IMF from Martín-Navarro et al. (2015d), equation 3.1, for 186,886 SDSS galaxies. The top panel shows the results for the Vazdekis IMF parametrisation and the right panel shows the results for the low-end IMF parametrisation. The large difference between both panels clearly shows that the effects of the IMF change is more sensitive to the IMF parametrisation, rather than to the direct measurements of Martín-Navarro et al. (2015d).

The `Vazdekis IMF' panel shows two tails emanating from the (zero SFR change, zero mass change) point. The lower tail consists of low-metallicity galaxies, which have a shallow high-end IMF slope. This results in a negative SFR correction, since there are fewer dwarf stars formed than for a Chabrier IMF. The stellar mass correction for most of these galaxies is positive though, because of invisible mass locked up in stellar remnants. The maximum extent of this effect depends in part on the assumed cut-off in equation 3.1 below $log_{10}(Z/Z_{\odot}) = -0.6$. The upper tail consists of high-metallicity galaxies, which have a steep high-end IMF slope. These have more star formation in dwarf stars than for a Chabrier IMF, which results in an increase of the inferred star formation rate of up to two orders of magnitude. The increase in stellar mass is smaller, which means that the specific star formation rate (SSFR) is increased as well.

The effect for the `low-end' IMF parametrisation is much smaller (especially for the SFR) but still significant. In this case the whole effect can be understood in terms of how much mass is locked up in dwarf stars, since the IMF slope above 0.5 $M_{\odot}$ is kept fixed. Naively one might think that the specific star formation rate should remain unchanged in this case, since the percentage of extra dwarf stars formed in current star formation is the same as the percentage of extra dwarf stars locked up from older generations. This would be true if the SSFR were defined as the SFR divided by the total initial stellar mass formed, but it is instead defined with respect to the current stellar mass (Hopkins and Beacom 2008). The current total stellar mass is lower than the initial stellar mass, because of mass loss by intermediate-mass and massive stars. This means that for an IMF with relatively more dwarf stars, there is an extra relative `increase' of stellar mass with respect to the Chabrier case, caused by a diminished stellar mass loss (and thus a diminished difference between the initial stellar mass and the current stellar mass). This means that the change in stellar mass is larger than the change in SFR and thus that the SSFR decreases. The opposite happens in the case where the `low-end' IMF has fewer dwarf stars than the Chabrier IMF. This causes the pattern in the second panel of Figure 3.5, which shows the displacement of the galaxies in the mass-

SFR plane. The change in SFR is roughly two thirds of the change in mass.

Figure 3.5: The implied stellar mass change and star formation rate change with respect to observations that assume a Chabrier IMF for a sample of SDSS galaxies that obey the IMF-metallicity relation of Martín-Navarro et al. (2015d), equation 3.1, with metallicities from Gallazzi et al. (2005). The colour scale indicates the average log stellar mass of the galaxies in each pixel. Some typical metallicity values are indicated with arrows. The black dotted line depicts a constant specific star formation rate. The top panel assumes the Vazdekis IMF parametrisation for which the free parameter is the high-end IMF slope. The bottom panel assumes our low-end IMF parametrisation, for which the free parameter is the low-end IMF slope. Both panels show large changes, but the 'Vazdekis' case has much more drastic consequences, with star formation rate changes of over two orders of magnitude. At a given metallicity, any normalised linear combination of these two IMFs would be in agreement with the IMF measurements from line indices by Martín-Navarro et al. (2015d).

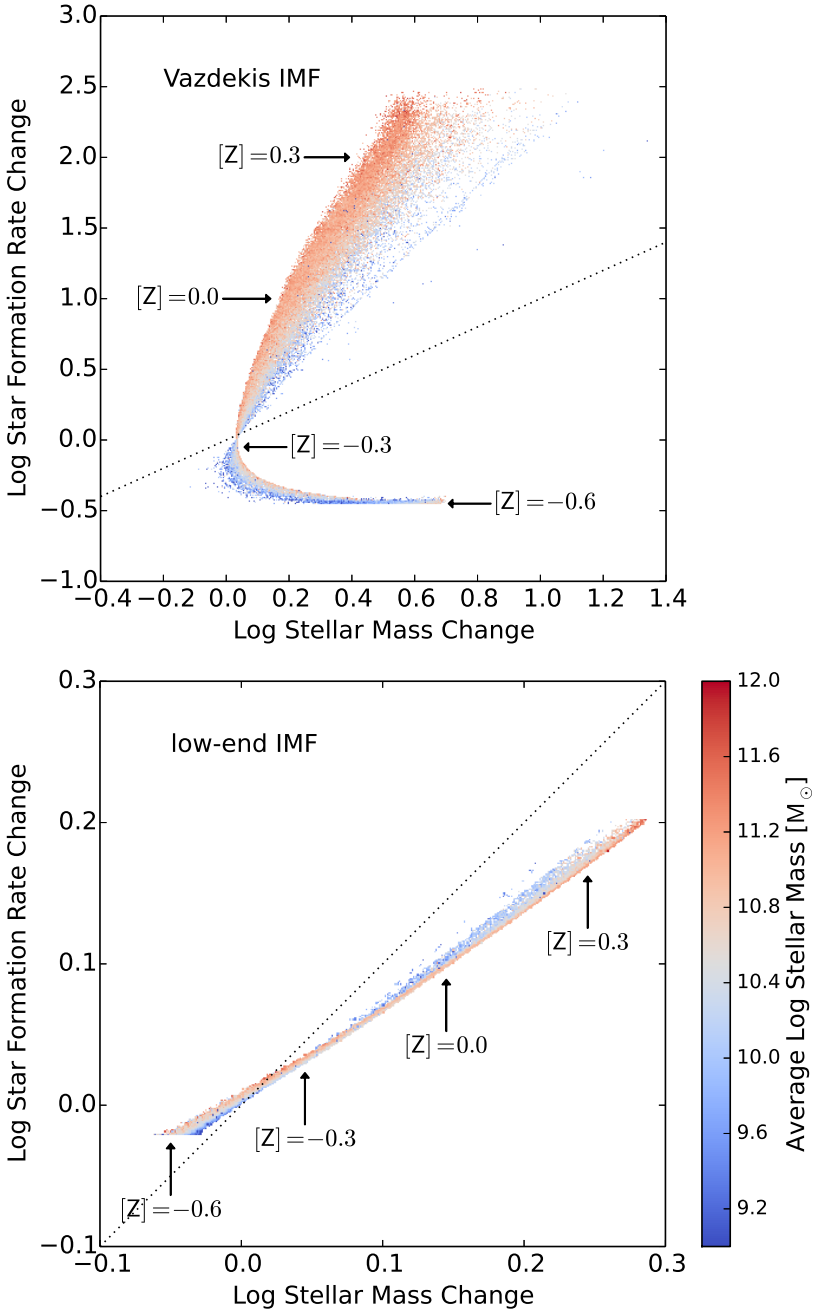
Vazdekis IMF
[Z] =0.3
[Z] =0.0
[Z] =−0.3
[Z] =−0.6
Log Star Formation Rate Change
Log Stellar Mass Change
low-end IMF
[Z] =0.3
[Z] =0.0
[Z] =−0.3
[Z] =−0.6
Log Star Formation Rate Change
Log Stellar Mass Change
Average Log Stellar Mass [M⊙]

Figure 3.6: The inferred star formation rate as a function of inferred stellar mass for different IMFs. The top panel shows the matched sample of SDSS galaxies with metallicities from Gallazzi et al. (2005) and masses and star formation rates from Chang et al. (2015), assuming a Chabrier IMF. The middle panel shows the results for the metallicity-dependent Vazdekis IMF, as described in Figure 3.5. The bottom panel shows the effect of a low-end metallicity-dependent IMF. For ease of comparison, the medians of the matched sample with the Chabrier IMF have been plotted in black in all panels: dashed lines denote the median for all galaxies and solid lines denote the median for all star-forming galaxies (defined as those galaxies with a SSFR larger than $10^{-11.5}/\mathrm{yr}$, indicated with a red dashed line). White lines in the top panel show the medians for the complete sample from Chang et al. (2015). In the middle and bottom panels the white lines show the medians of the underlying distributions. The excellent agreement between the white and black solid lines in the top panel shows that our selection on galaxies for which stellar metallicities are available, does not introduce a bias. The red solid line in the top panel demarcates the boundary below which the star formation rates should be regarded as upper bounds. The region below the red solid line in the middle panel is contaminated by these upper bounds. The middle panel shows that the metallicity-dependent Vazdekis IMF has a large influence on the mass-SFR relation, while the low-end metallicity-dependent IMF in the bottom panel has only a small effect. Any normalised linear combination of these two cases would be in agreement with the IMF measurements from line indices by Martín-Navarro et al. (2015d).

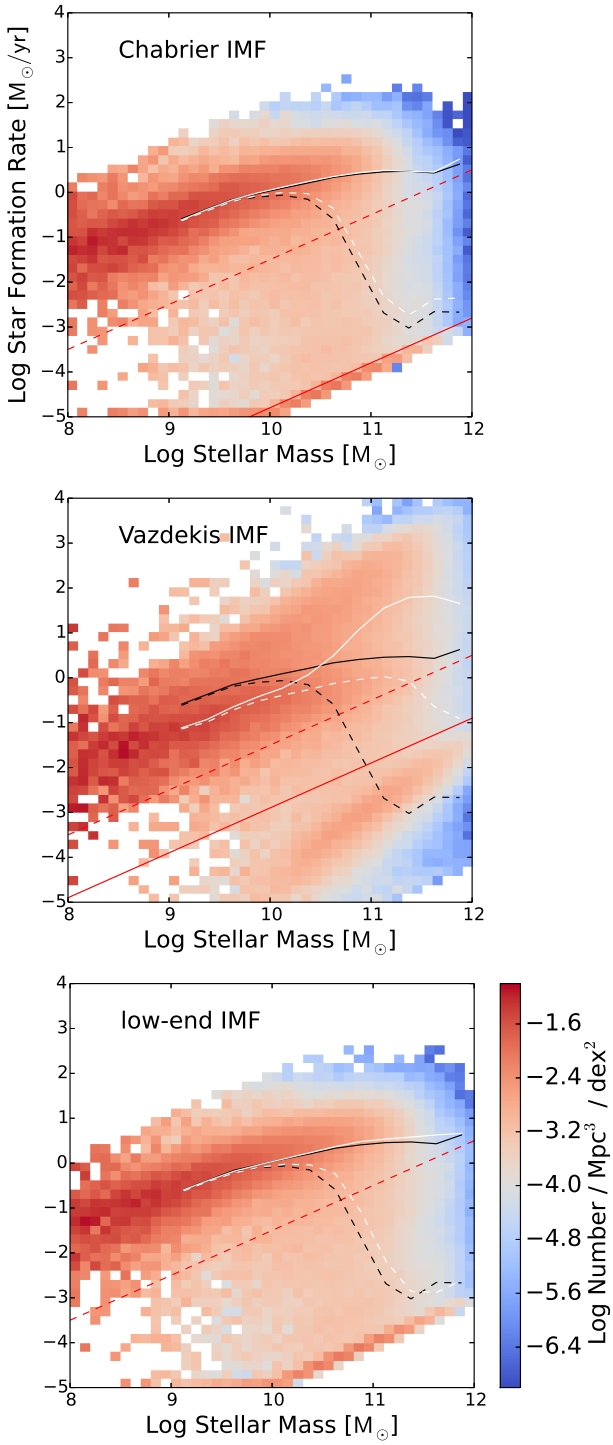
Chabrier IMF
Vazdekis IMF
low-end IMF
Log Star Formation Rate [M⊙/yr]
Log Stellar Mass [M⊙]
Log Number / Mpc³ / dex²
−1.6
−2.4
−3.2
−4.0
−4.8
−5.6
−6.4

Figure 3.6 shows the effect of the metallicity-dependent IMF on the star formation main sequence. The top panel shows the mass-SFR relation for the selection of 186,886 galaxies out of the 858,365 SDSS galaxies of Chang et al. (2015) that have a well-defined metallicity and age determination by Gallazzi et al. (2005). The running median SFR of star-forming galaxies with $SSFR > 10^{-11.5}$/yr, black solid line, coincides with that for the complete Chang et al. (2015) sample (solid white line). Therefore, we expect no significant selection effects for the main sequence. The running median for the complete sample (black and white dashed lines) shows a slight underrepresentation of quiescent galaxies in our sample with respect to the complete Chang et al. (2015) sample. The colour scale in Figure 3.6 represents the number of galaxies per Mpc^3, per dex stellar mass, per dex SFR. Individual galaxies have been weighted by $1/V_{max}$ from Chang et al. (2015), correcting for the maximum volume in which the given galaxy would be selected. The whole sample has been rescaled by 858,365/186,886, neglecting the aforementioned slight underrepresentation of quiescent galaxies in our sample.

The middle and bottom panels show the effect of the metallicity-dependent dwarf-to-giant ratio for respectively a Vazdekis IMF parametrisation and a low-end IMF parametrisation, as described in section 3.2. The Vazdekis IMF has a dramatic influence on the star formation main sequence (compare the black and white solid lines in the middle panel). Below a mass of $\sim 10^{10.5}\mathrm{M}_\odot$ the dominant effect is from metal-poor galaxies which lower the median inferred SFR by ~ 0.5 dex relative to a Chabrier IMF. Above this mass the dominant effect is from metal-rich galaxies which increase the median SFR, effectively extending the SSFR main sequence up to a stellar mass of $\sim 10^{12}\mathrm{M}_\odot$ and making it more linear. We used a running median to represent the typical galaxy at each mass. The true average SFR at low masses is actually increased, because of an increase in the scatter.

The increased scatter in this plot could indicate that the underlying metallicity-IMF relation or the Vazdekis parametrisation of the IMF is wrong, because in general a more precise description will cause a decrease in the observed scatter. This is not necessarily the case though. Apart from measurement or modelling errors in the metallicity, the increased scatter could also be an intrinsic property of the galaxy population. For a galaxy population that truly follows the assumed Vazdekis IMF-metallicity trend, the middle panel would indicate the total star formation, but the top panel would still indicate the effective high-mass star formation. It is possible that the high-mass star formation is better behaved than the total star formation. For a varying IMF these two quantities are no longer directly linked to each other, but it is the high-mass star formation that determines the stellar feedback. It could well be that this causes the high-mass star formation to be regulated, whereas the increased dwarf star formation for metal-rich galaxies

could create a runaway process of star formation that is less regulated and therefore shows a larger galaxy-by-galaxy variation at a given mass. We will discuss this possibility in section 3.6.

The bottom panel shows results for the low-end IMF parametrisation. For this parametrisation there is almost no effect at low masses and at high masses the star formation main-sequence is prolonged to slightly higher masses. The effect on the median for star forming galaxies is especially small, since individual galaxies are displaced almost parallel to lines of constant SSFR, along the main sequence, see also Figure 3.5. In practice one could construct an IMF parametrisation in between the two options described here, for which part of the observed trend of the IMF sensitive line indices would be caused by a changing low-end IMF slope and part would be caused by a changing high-end slope. The effects on the mass-SFR plot would fall somewhere in between the middle and bottom panels of Figure 3.6. Qualitatively this means an extension of the star formation main sequence together with a possible lowering of the median SFR at low masses, but quantitatively the magnitude of this effect is not well constrained by current observations.

Figure 3.7 shows the inferred low-redshift SFR densities of the Universe as a function of galaxy mass. The effect of a low-end metallicity-dependent IMF is quite small, shifting the star formation to higher masses by about 0.2 dex. The implied increase of the total SFR density of galaxies more massive than $10^9 M_\odot$ is a factor of 1.11. For the Vazdekis IMF this is a factor of 16.6. The effect is much stronger, with a large peak of dwarf star formation around $M_{*,SSP} \approx 10^{11.3} M_\odot$.

3.4 Galaxy Stellar Mass Function

Figure 3.8 shows the mass change due to the change from a Chabrier IMF to a metallicity-dependent IMF for our sample of galaxies as a function of the original Chabrier stellar mass. The median mass increase for the Vazdekis IMF is larger than that for a Salpeter IMF, which might be in tension with some of the mass measurements from strong lensing and from dynamics. This suggests that at least a fraction of the IMF-metallicity trend measured by Martín-Navarro et al. (2015d) should be provided for by a change in the low-end slope of the IMF. For the Vazdekis IMF the mass change at low masses is due to stellar remnants while at high masses it is due to dwarf stars. Nevertheless, the overall effect is insensitive to mass, with a large scatter at all masses. Thus, metallicity-dependent IMF changes do not necessarily create a clear trend of $M_{*true}/M_{*Chabrier}$ with $M_{*Chabrier}$, where the latter is obtained through SED fitting. The low-end IMF parametrisation gives smaller mass changes, but it does produce a clear trend of $M_{*true}/M_{*Chabrier}$ with $M_{*Chabrier}$, with a progressively larger IMF-induced

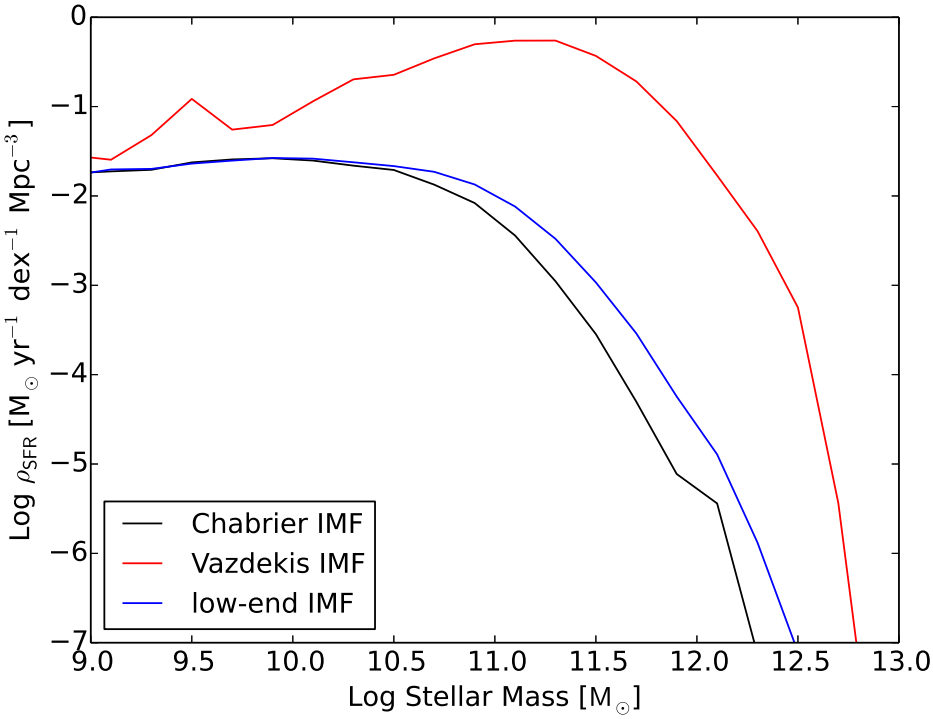

Figure 3.7: The inferred star formation rate density as a function of the inferred stellar mass for the sample of SDSS galaxies with different IMFs. The black line shows the original estimate for a Chabrier IMF. The red line corresponds to the metallicity-dependent Vazdekis IMF and the blue line corresponds to the metallicity-dependent low-end IMF. The increased number of dwarf stars for metal-rich galaxies causes a very large increase in the inferred SFR, which peaks around a mass of $10^{11.3}\mathrm{M}_\odot$ for the Vazdekis IMF. For the low-end IMF the effect is much more subtle.

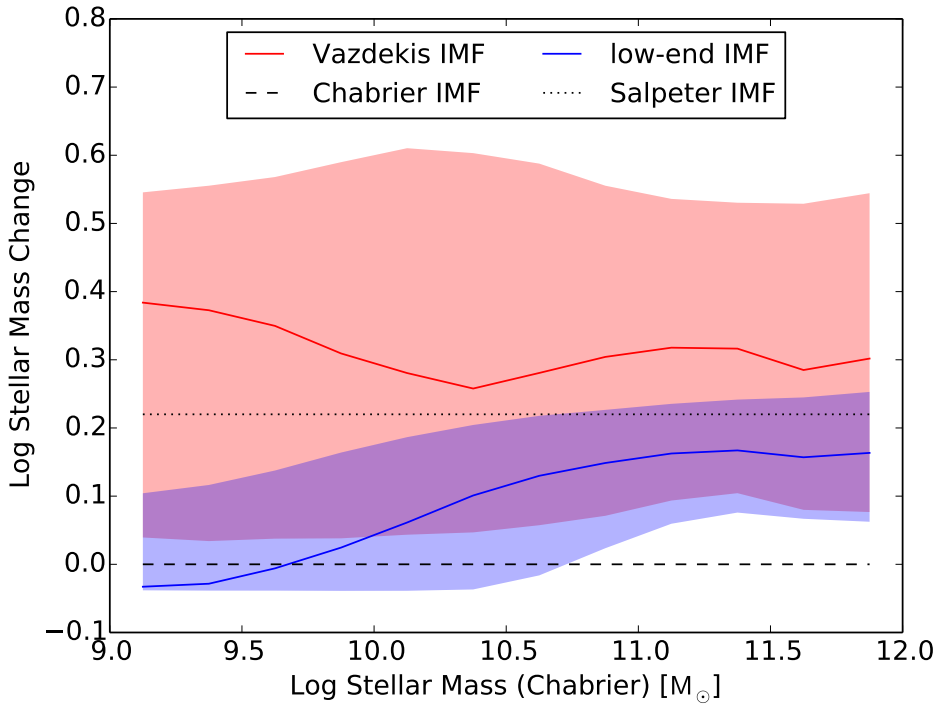

Figure 3.8: The difference in stellar mass estimates between a metallicity-dependent IMF and a Chabrier IMF as a function of the stellar mass inferred for a Chabrier IMF for the sample of 186,886 SDSS galaxies. The red line and shaded region show the median and the 10%-90% region for the Vazdekis IMF. Blue corresponds to the low-end IMF. The black dashed and dotted lines depict the Chabrier and Salpeter IMFs respectively.

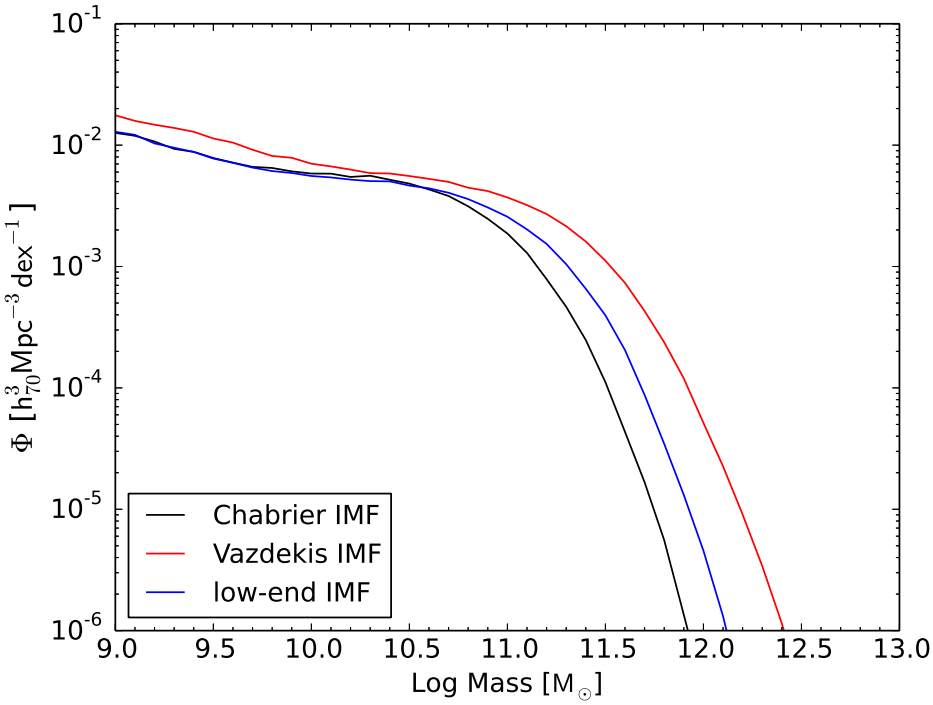

Figure 3.9: The galaxy stellar mass function inferred from observations of Moustakas et al. (2013) for several IMFs: Chabrier (black), metallicity-dependent Vazdekis IMF (red) and metallicity-dependent low-end IMF (blue). For both metallicity-dependent IMFs the knee of the mass function shifts to higher masses, but the steepness of the drop-off is hardly affected.

mass correction towards higher masses.

In figure 3.9 we show the effect on the galaxy stellar mass function inferred from the observations of Moustakas et al. (2013). Galaxies are scattered as a function of mass according to the exact distribution underlying Figure 3.8. For galaxies below a mass of $10^9 M_\odot$ we extrapolate the Moustakas mass function with a slope of 0.41 and we apply the mass changes corresponding to the lowest 0.1 wide mass bin at $10^9 M_\odot$. For both IMF parametrisations the knee of the mass function shifts to a higher mass, but the steepness of the high-mass drop-off is not affected much. The abrupt nature of this drop-off is generally believed to be caused by the feedback of active galactic nuclei (AGN). This AGN feedback should be very effective at quenching high-mass galaxies in order to prevent more massive galaxies from forming. A metallicity-dependent IMF does not remove the need for such an efficient quenching mechanism at high masses, it only shifts the mass at which this quenching occurs, which can also be seen in Figure 3.6. The IMF changes also

imply a change in the total stellar mass density of the Universe. The total stellar mass density in galaxies above $10^9 M_\odot$ increases by a factor 1.33 for the low-end IMF and by a factor 2.31 for the Vazdekis IMF.

In this work we focus on low-redshift observations, but the implications of a metallicity-IMF trend at higher redshifts could be very significant. A more top-heavy IMF at higher redshifts, implied by lower metallicities, would affect the relation between the total star formation rate density implied by direct SFR measurements at these redshifts and that from comparing the galaxy stellar mass function at different redshifts. At high redshifts the true star formation rate would be smaller than that inferred from SFR measurements with a Chabrier IMF. The star formation rate density, deduced from comparing neighbouring redshift slices of the galaxy stellar mass function, interpreted with a Chabrier IMF, would also be too high. In the case of a `low-end' IMF, the offsets in both SFR density determinations are the same, since they are caused by the same overestimation of mass locked in invisible dwarf stars with masses smaller than $0.5 M_\odot$. The consistency between both SFR density determinations is thus not affected. For a Vazdekis IMF, the direct SFR density measurement is more sensitive to the IMF change than the SFR density estimate from comparing GSMFs, because it is more sensitive to the highest mass stars. In this case we thus expect a smaller increase in stellar mass in the Universe from comparing GSMFs than that implied by direct SFR observations, if both are interpreted with a Chabrier IMF.

3.5 Metals

We used the stellar mass-metallicity measurements of Gallazzi et al. (2005) as input for the metallicity-dependent IMF. However, a metallicity-dependent IMF will alter the stellar masses of these observed galaxies and will therefore change the mass-metallicity relation. Figure 3.10 shows the effect that this has for both the Vazdekis IMF and the low-end IMF. Solid white lines in both panels show the running median metallicity for the Vazdekis (top panel) and low-end (bottom panel) IMFs, while the black curve indicates the median metallicity for a universal Chabrier IMF. In both cases the mass-metallicity relation is steeper at high mass for the metallicity-dependent IMF than for the Chabrier IMF. We used the same weighting with $1/V_{max}$ as in Figure 3.6.

The behaviour at low metallicity is different for the two parametrisations. In the Vazdekis case we see a clear shift to higher masses for $Z < Z_\odot$. At the low-metallicity end this shift is caused by a progressively more top-heavy IMF for lower metallicities and the resulting mass gain is comprised of stellar remnants. We did not extrapolate the IMF metallicity trend, equation 3.1, below $log_{10}(Z/Z_\odot) =$

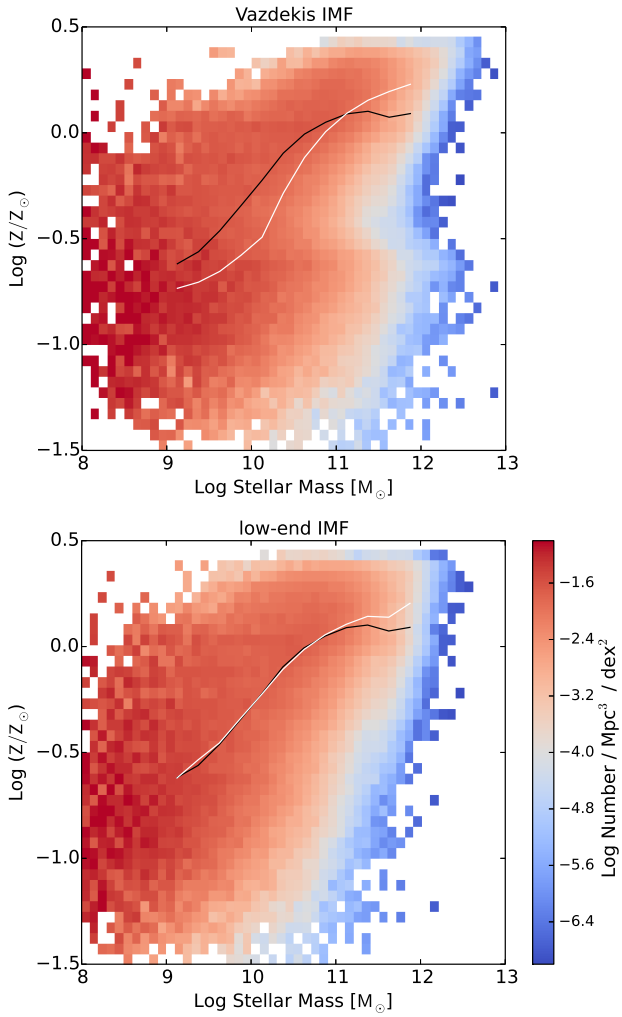

Figure 3.10: The effect of a metallicity-dependent IMF on the inferred stellar mass-metallicity relation from Gallazzi et al. (2005). The top and bottom panels show the results for respectively the Vazdekis and the low-end IMF parametrisations. White solid lines indicate the running median and the black solid line indicates the running median for a universal Chabrier IMF. In both panels the mass-metallicity relation shows considerably less flattening at high masses for the variable IMF. In the 'Vazdekis IMF' panel there is a clear feature of galaxies shifting to the right at $log_{10}(Z/Z_\odot) \approx -0.6$. The reason that this shift remains constant below $log_{10}(Z/Z_\odot) = -0.6$ is that we do not extrapolate the IMF-metallicity relation, equation 3.1, below this metallicity, which is a somewhat arbitrary choice. This mass shift is due to stellar remnants that are created by a presumably more top-heavy IMF at low metallicities. The 'low-end' panel does not have this feature. The effect of extrapolating below $log_{10}(Z/Z_\odot) = -0.6$ in this panel would be a slight shift to the left instead of to the right.

-0.6, otherwise this shift to the right in the top panel of figure 3.10 would get more prominent toward lower metallicities, as can be seen in Figure 3.4.

The mass-metallicity relation inferred from the low-end IMF is much less sensitive to this extrapolation and the effect goes in the opposite direction. Since in this case the high-end IMF slope is kept fixed, the net effect of extrapolating to lower metallicities would be to have an IMF that is increasingly deficient in $M < 0.5\mathrm{M}_{\odot}$ stars. The resulting galaxies would be less massive than suggested by SED fitting with a Chabrier IMF. This would shift the galaxies in the right panel of figure 3.10 at metallicities below $log_{10}(Z/\mathrm{Z}_{\odot}) = -0.6$ slightly to the left. This effect is much less drastic than for the Vazdekis case as it is clearly bounded from below by having no stars below 0.5 $\mathrm{M}_{\odot}$, whereas in the Vazdekis case the ratio of observed stars over remnants is not bounded.

Figure 3.11 shows the metal mass released over the lifetime of a simple stellar population as a function of metallicity. In order to construct this we used the metallicity-dependent yield tables for individual stars of different masses from Portinari et al. (1998) and Marigo (2001). There are two ways in which the metal release of a simple stellar population depends on metallicity. First, through a metallicity dependence of the metals released by individual stars, but the more significant contribution comes from the metallicity dependence of the IMF, especially for the Vazdekis IMF. In this case, a galaxy would presumably start out on the left, with a low metallicity, a top-heavy IMF and a high metal output. During the lifetime of a galaxy on average its metallicity will grow and as a result it will shift to the right in this graph, towards a more bottom-heavy IMF and a lower metal output. Apart from a boost in the metal release, the early top-heavy IMF will leave not much evidence, because these metal producing stars will have been turned into stellar remnants. The metal output inferred from the integrated contribution of SFR observations at higher redshifts over time would not change drastically though, since these SFR observations effectively measure the formation rate of high-mass stars. These are exactly the stars that produce the metals.

The same situation applies to ionising radiation, because the bulk of the ionising radiation and metals are produced by the same massive stars. In principle reionisation would get a head start due to an early top-heavy IMF. For redshifts where we have representative Hα-based SFR measurements, the IMF-metallicity relation should not change the implied ionising photon production much, but for higher redshifts the IMF effect on reionisation can potentially be large.

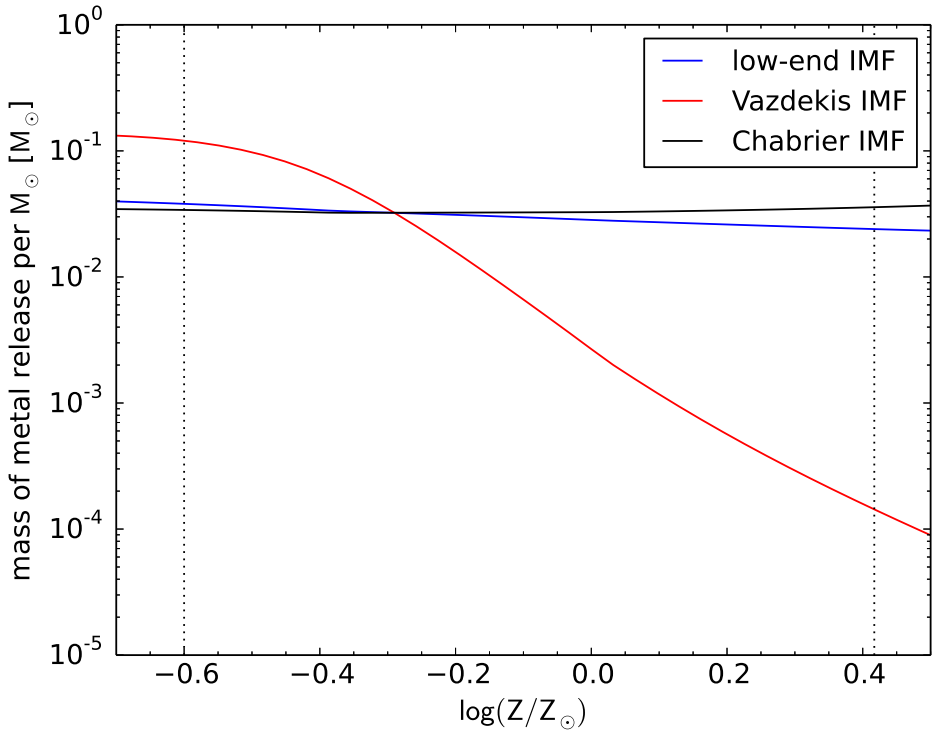

Figure 3.11: The total metal mass released by a simple stellar population over its lifetime as a function of metallicity for the metallicity-dependent Vazdekis IMF, the corresponding low-end IMF and the Chabrier IMF. The metal release for different stellar masses and stellar stages are taken from Portinari et al. (1998) and Marigo (2001). The trends are primarily due to changes in the IMF with metallicity and to a lesser extent due to a metallicity-dependence in the metal output of individual stars. Dotted vertical lines show the minimum and maximum values of the metallicity used in this work.

3.6 Rapid Galaxy Quenching

The distribution of galaxies in a colour-magnitude plot is observed to follow a bimodal pattern (e.g. Strateva et al. 2001; Bell et al. 2004), with most galaxies being classified as either a `red sequence' or a `blue cloud' galaxy. The red sequence is comprised of red, mostly elliptical galaxies and the blue cloud is comprised of blue, mostly spiral galaxies. Galaxies that fall in between those categories are called `green valley' galaxies. They are believed to be mostly galaxies that are currently quenching, making the transition from the blue cloud to the red sequence (e.g. Trayford et al. 2016).

A similar classification of galaxies can be made based on stellar mass and specific star formation rate, although this may depend on the type of SFR estimator used. A short-time SFR indicator like Hα may be inherently more bursty, so a quiescent galaxy based on the Hα SFR may not be quiescent based on the u-band SFR. Regardless of this ambiguity in defining a green valley galaxy, in general relatively few galaxies are in this `in between' state. This suggests that the quenching of a typical galaxy is a fast process. Also, especially at high masses, quenching needs to be very effective to explain the sharp drop-off in the number density of high-mass galaxies beyond the knee of the galaxy mass function.

A bottom-heavy IMF at the late stages of galaxy evolution could help speed up the last phase of the quenching process, because it produces less feedback per unit mass of stars formed and because it shortens the gas consumption time scale inferred from the observed galaxy properties. Figure 3.5 shows that a metallicity-dependent IMF can cause the inferred SFR to increase by of up to 2.5 orders of magnitude relative to a Chabrier IMF (although the implied SFR changes are much smaller if the IMF changes apply to the low-end IMF slope rather than the high-end IMF slope). The implied gas consumption timescale[9], $\tau_{gas} = 1.33(M_{HI} + M_{H_2})/SFR$, i.e. the timescale for the galaxy to run out of its current cold gas reserve, scales with the inverse of the SFR and will thus be significantly shortened. On the other hand, the expected stellar feedback for a galaxy with such a bottom-heavy IMF will not change much, because the observed SFR already effectively represents the SFR in high-mass stars.

A late time bottom-heavy IMF for massive present-day galaxies would help to explain the bimodal distribution of galaxies in another way. It would make the quenched galaxies effectively less quenched, because most of their star formation is in dwarf stars, the star formation rates implied by the observations would be higher. The requirements on the efficiency of the feedback process that is responsible for preventing gas accretion and for the ejection of gas lost by evolved stars would thus

[9]The factor of 1.33 captures the contribution from helium.

Table 3.1: The first column gives some typical stellar mass values for a universal Chabrier IMF. The second column gives the corresponding median stellar mass for a metallicity-dependent Vazdekis IMF, from Figure 3.8. The third column gives the corresponding halo mass from Behroozi et al. (2010). The fourth column gives the median total HI plus H_2 gas mass from Bahé et al. (2016) and references therein. The starred measurement indicates a slight extrapolation beyond $M_\star \approx 11.3 M_\odot$. There is at least a 0.5 dex uncertainty in this median gas mass value. The fifth and sixth columns give the median SFR for a Chabrier respectively Vazdekis IMF from Figure 3.6. The seventh column gives the halo gas accretion rate at the given halo mass from Correa et al. (2015). The accretion rates in the middle two lines are very close to the implied SFR for the Vazdekis IMF. The eighth and ninth columns give the median gas consumption timescales for respectively a Chabrier and Vazdekis IMF, calculated from the corresponding star formation rates and the hydrogen gas mass (column four), including a correction for helium. The Chabrier IMF implies a nearly constant median gas consumption timescale across 1.5 dex in mass, whereas the median gas consumption timescale for a Vazdekis IMF decreases by a factor 32 over this mass range.

$log_{10}(M_\star)$ Chabrier [$M_\odot$]	$log_{10}(M_\star)$ Vazdekis [$M_\odot$]	log_{10} (M_{Halo}) [$M_\odot$]	log_{10} (M_{HI+H_2}) [$M_\odot$]	SFR Chabrier [$M_\odot$/yr]	SFR Vazdekis [$M_\odot$/yr]	halo gas accretion rate [$M_\odot$/yr]	gas consumption time Chabrier [yr]	gas consumption time Vazdekis [yr]
10.0	10.3	11.6	9.2	1.0	1.0	2.5	2.1×10^9	2.1×10^9
10.5	10.8	12.1	9.5	1.8	7.1	8.0	2.3×10^9	5.9×10^8
11.0	11.3	13.1	9.5	2.5	50	79	1.7×10^9	8.4×10^7
11.5	11.8	14.9	9.4*	2.5	50	1×10^4	1.3×10^9	6.7×10^7

be reduced.

The higher SFRs imply shorter gas consumption timescales. Previous work on the effect of a variable IMF on gas consumption timescales has been done by Pflamm-Altenburg and Kroupa (2009) in the context of the IGIMF model. They report a gas consumption timescale of 3 Gyr, that does not depend on the neutral gas mass for dwarf irregular and large disk galaxies alike. Table 3.1 lists the median values for the gas consumption timescale implied by the SFR changes and the measurements of total HI plus H_2 gas from the GASS and COLD GASS surveys (Catinella et al. 2010; Saintonge et al. 2011). For a universal Chabrier IMF the median gas consumption timescale is almost constant over the mass range from $10^{10} M_\odot$ to $10^{11.5} M_\odot$ at a value of $\approx 2 \times 10^9$ yr. Over the same mass range a metallicity-dependent Vazdekis IMF implies a progressively shorter median gas consumption timescale for more massive galaxies, with a decrease by a factor of 32 to a value of 67 million years for the most massive galaxies. If this star formation were to be sustained for longer periods, it would require an efficient refueling of the cool gas reservoir of 50 $M_\odot$/yr (in which case the refueling rate equals the star formation rate). We can compare this rate to the rate of gas accretion onto the halo. For this we use the stellar mass-halo mass relation from Behroozi et al. (2010) to determine the halo mass (where we always use the Chabrier IMF) and

the corresponding halo gas accretion rate from Correa et al. (2015). At a stellar mass of $10^{10}M_{\odot}$, the accretion onto the halo is about a factor 2.5 larger than the median SFR, both for a universal Chabrier IMF and for the Vazdekis IMF. For the Chabrier IMF this ratio becomes progressively larger for larger masses, but for the Vazdekis IMF it first drops, around the knee of the galaxy mass function, where the halo gas accretion rate is just marginally larger than the SFR, before rising again at the high-mass end.

In conclusion, the increased SFR, relative to Chabrier, for the metallicity-dependent Vazdekis IMF may require large cooling flows onto the galaxy, of the same order as the gas accretion rate onto the halo, and would imply very short gas consumption timescales. The large gas accretion rates may be inconsistent with X-ray observations of galaxy clusters (e.g. Peterson et al. 2003). Combining the high-end metallicity-dependent IMF changes with changes to the low-end slope would reduce the magnitude of these effects. They would imply a speedup of the quenching process, especially around the knee of the galaxy stellar mass function.

3.7 Conclusions

In this paper we have investigated the consequences of a metallicity-dependent IMF, as measured for SDSS galaxies and elliptical annuli of CALIFA galaxies by Martín-Navarro et al. (2015d). We use the stellar mass and SFR measurements of Chang et al. (2015) and the stellar metallicity measurements of Gallazzi et al. (2005). We assume that each of our 186,886 SDSS galaxies follows the exact IMF-metallicity relation given by equation 3.1 (Martín-Navarro et al. 2015d).

The measurement of IMF-specific spectral lines in ETGs by Martín-Navarro et al. (2015d) is effectively sensitive to the current dwarf-to-giant ratio, equation 3.3. It is insensitive to the IMF slope for stellar masses $M \gg 1.0M_{\odot}$, because of a sparseness of stars in this mass range in the observed ETGs and because of the relative insensitivity of the used line indices to stars in this mass range. The implications of this varying IMF for the masses and star formation rates of observed galaxies are however very dependent on the high-end IMF. For this reason we investigate two extreme cases. First, we use the IMF parametrisation of Martín-Navarro et al. (2015d), for which the high-end IMF slope is varied and the low-end slope is held fixed. We refer to this case as the `Vazdekis IMF'. Second, we use a `low-end' IMF parametrisation, for which the high-end slope is fixed at the Chabrier value and the slope below 0.5 $M_{\odot}$ is varied. Our main conclusions are as follows:

- When we match both IMF parametrisations on the current dwarf-to-giant ratio, the same observations lead to completely different IMFs (Fig. 3.1).

- The trend between the high-end IMF slope and metallicity can imply large changes in the SFR inferred from observations, depending on the SFR tracer. Compared to a Chabrier IMF, the implied bottom-heavy SFR can be up to three orders of magnitude larger for the most metal-rich galaxies, with a calibration offset between the observed FUV-SFR and the Hα-SFR of up to an order of magnitude. The top-heavy IMF for metal-poor galaxies can reduce the inferred SFR by up to 0.8 dex. When we vary the low-end IMF slope instead of the high-end slope, the same IMF-metallicity trend causes much smaller SFR changes ranging from -0.02 dex to 0.20 dex and no FUV-Hα SFR calibration offsets (Fig. 3.3).

- The stellar mass changes implied by the IMF-metallicity trend are also much smaller when the low-end IMF slope is varied (-0.06 dex $< \Delta log_{10}(M_\star) <$ 0.29 dex) than when the high-end IMF slope is varied (-0.06 dex $< \Delta log_{10}(M_\star) <$ 1.25 dex). A combination of a metallicity-dependent variation of the low-end and high-end IMF slope would cause a behaviour that is in between these two extremes (Fig. 3.4).

- The high-end slope of 1.3 for a Chabrier IMF (or a similar Kroupa/Canonical IMF) minimizes the total mass of old galaxies. Changing the high-end slope will always increase the inferred mass of the galaxy by either locking up more mass in dwarf stars or in stellar remnants (Fig. 3.4).

- The implied combined mass-SFR changes for our sample of 186,886 SDSS galaxies are shown in Figure 3.5. When the high-end IMF slope is varied, metal-rich galaxies will become more massive and their SSFR will increase by up to two orders of magnitude. When changing the low-end IMF slope, the increase in mass is combined with a slight decrease in the SSFR.

- Figure 3.6 shows the effect of a variable IMF on the star forming main sequence. The effect for the low-end IMF is mild, because most galaxies are displaced along the sequence. When changing the high-end slope the effect is large, especially at the high-mass end. The star-forming main sequence is effectively prolonged up to a stellar mass of $10^{12}M_\odot$. In between $10^9M_\odot$ and $10^{10}M_\odot$ the median SFR becomes lower, but the same does not hold for the average SFR, due to an increased scatter.

- Increases in the total low-redshift SFR density range from a factor of 1.11 for the low-end IMF to a factor of 16.6 for the Vazdekis IMF, with a larger SFR contribution from galaxies around a mass of $10^{11.3}M_\odot$ (Fig. 3.7).

- If the metallicity-dependent IMF variations only affect the low-end slope, then they will produce a clear trend of the IMF-dependent mass change with SED-fitting mass (using a Chabrier IMF for the SED fit) (Fig. 3.8). For $M \gtrsim 10^{11}\mathrm{M}_{\odot}$ a small fraction of galaxies will be more massive than for a Salpeter IMF. High-end IMF slope variations produce a larger mass change, possibly in tension with dynamic mass measurements, but no clear trend with Chabrier SED mass.

- Independent of the IMF parametrisation, the IMF-metallicity trend will produce a shift of the galaxy stellar mass function to higher masses, without changing the steepness of the high-mass dropoff much, see Figure 3.9. This means that these IMF variations do not remove the need for an efficient quenching mechanism for high-mass galaxies, but they shift the mass at which this happens upwards by 0.2 to 0.5 dex. The implied total stellar mass density of the Universe increases by a factor of 1.3 to 2.3.

- The IMF-metallicity trend implies a steeper stellar mass-metallicity relation for $M \sim 10^{11}\mathrm{M}_{\odot}$ (Fig. 3.10).

- If the high-end IMF slope is more shallow for metal-poor galaxies, then this would produce a large change in the metal mass released per unit mass of stars formed over the lifetime of a galaxy. Figure 3.11 shows that this metal production could be three orders of magnitude higher in the early metal-poor stage of a galaxy than in the late metal-rich stage. This strong evolution makes it impossible to give a good estimate of the total metal production of any galaxy as this might be dominated by the early stages and depends crucially on the exact mass and metallicity evolution of the galaxy. The total metal production deduced from the Hα-SFR evolution of the Universe is not expected to change much though, since Hα directly traces the massive metal-producing stars.

- If the high-end IMF slope is shallower for metal-poor galaxies, then this will increase the production of ionising photons for metal-poor galaxies in the early Universe. This would imply an increased production of ionising photons for high redshifts that are not probed directly by Hα observations, which would have an effect on models for the reionisation of the Universe.

- A bottom-heavy IMF during the late, metal-rich stage of galaxy evolution could help to explain the observed bimodality in galaxy properties: the observation that most galaxies can be classified as `blue cloud' or `red sequence' galaxies and only very few galaxies are observed in the intermediate `green valley' stage. On the one hand, `quenched' galaxies would be less quenched,

because their true star formation rate would be higher than for a Chabrier IMF, due to the `invisible' formation of dwarf stars. On the other hand, the quenching time of these galaxies would be lower, due to the much shorter implied gas consumption timescale. If gas cooling onto the galaxy is regulated in part by stellar feedback, then a more bottom-heavy IMF at higher metallicity could initiate a runaway process of low-mass star formation, because these low-mass stars do not provide feedback.

- Metallicity-dependent changes to the high-end IMF slope imply gas consumption timescales that become progressively shorter for more massive galaxies, down to 67 million years at $10^{11.5}M_{\odot}$, whereas for a universal Chabrier IMF this gas consumption timescale is approximately constant at $\approx 2 \times 10^{9}$yr. Around the knee of the GSMF these IMF changes require a cooling flow onto the galaxy of about 7 to 50 $M_{\odot}$/yr in order to sustain the SFR. These values are only slightly below the expected gas accretion rate onto the halo, see Table 3.1.

In conclusion, the implications of the observational evidence for a variable IMF for the low-redshift Universe could vary from absolutely dramatic to mild but significant, depending on the assumed IMF parametrisation.

Acknowledgements

We would like to thank Chris Barber, Ignacio Martín-Navarro, Alexandre Vazdekis and Francesco La Barbera for valuable contributions. We gratefully acknowledge support from the European Research Council under the European Union's Seventh Framework Programme (FP7/2007-2013) / ERC Grant agreement 278594-GasAroundGalaxies.

3.8 Appendix

In section 3.2 we described the method by which we calculate new masses and star formation rates for galaxies with an IMF different than the one used in the original mass and SFR determination. The most precise way to do this would be by redoing the whole SED fitting procedure for every galaxy, assuming a metallicity-dependent IMF. In this work we have used a simpler method to recalibrate the stellar masses and star formation rates, because at the moment we believe the errors to be dominated by uncertainties in the IMF measurements and in the stellar metallicity measurements and by a large dependency on the assumed IMF parametrisation. As a first order correction to the masses we compare mass-to-light ratios in

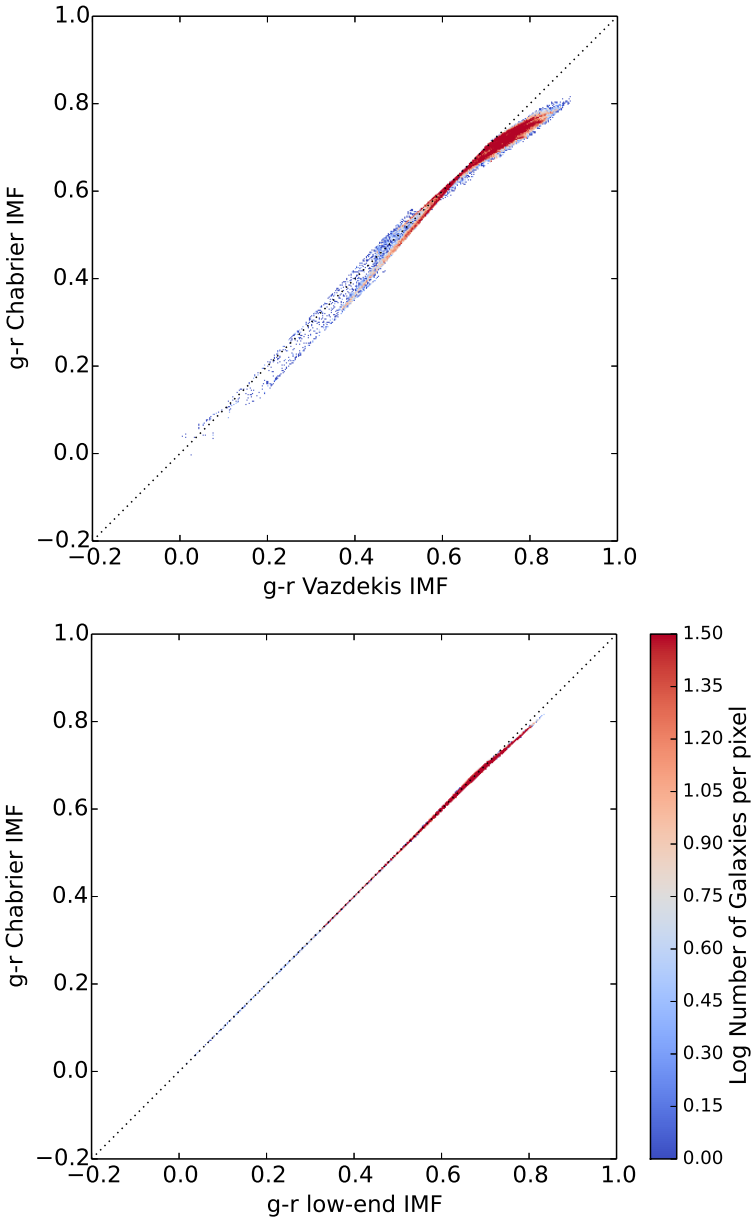

Figure 3.12: Dustless SDSS g-r colour of the varying IMF versus the colour of a Chabrier IMF for the complete sample of galaxies used in this work. The left panel show the Vazdekis IMF and the right panel shows the low-end IMF. The black dotted line indicates a one-to-one relation. A large deviation from this would mean a breakdown of our method to recalibrate stellar masses to a changed IMF. In the 'low-end' case the colours are almost unchanged, because the dwarf stars do not contribute much to the overall light. Also in the 'Vazdekis' case the colour changes are quite small.

the Cousins R-band for a simple stellar population with an r-band weighted age and metallicity given by Gallazzi et al. (2005) and a varying IMF to the mass-to-light ratio of a SSP with the same age and metallicity, but a Chabrier IMF. An alternative method would be to match on colour and some combination of age and metallicity. The problem with matching on colour is that it is very susceptible to dust. Still, we expect our method to break down once the dustless colour of the varied IMF SSP is very different from that of the Chabrier SSP, because a large change in dustless colour would also imply a large change in the true observed colour.

For this reason we plot the dustless SDSS g-r colours of our complete galaxy sample in figure 3.12. For the low-end IMF parametrisation there is almost no change in colour. This parametrisation only changes the IMF below 0.5 $M_{\odot}$. These stars do not contribute much to the overall light and as a consequence changing the low-end IMF has a negligeable effect on the dustless colour. Also for the Vazdekis IMF parametrisation the changes in dustless colours are quite small.

Another simplification lies in the fact that we use a simple stellar population, which is a good approximation for ETGs but not for star forming galaxies. For a star forming galaxy the used SSP is a simplification with respect to a constant star formation history or an exponential one, but the used r-band luminosity weighted age is skewed towards more recent star formation, as opposed to a mass-weighted age, through a large dependency of luminosity on mass. Typically the r-band luminosity weighted age is about half of the true average stellar age for a Chabrier constant star formation rate older than 10^8yr. In order to estimate the error in the IMF dependent mass change introduced by our simplification of the star formation history we plot the expected mass changes for a constant star formation history in Figure 3.13. This should be compared with Figure 3.4. The labeled ages are r-band luminosity weighted ages. As a function of IMF slope also the ratio between the r-band weighted age and the age of the start of star formation changes. This ratio becomes increasingly larger for an increasingly top-heavy IMF, which causes the cut-off of the Vazdekis IMF lines at the left. Here the implied age to the start of the constant star formation would be more than the age of the universe. The assumption of a SSP has no drastic consequences. For a low-end IMF parametrisation the results are almost indistinguishable. For a Vazdekis IMF parametrisation with a super-Chabrier slope, a constant star formation rate increases the expected dex mass shifts by 15%-25%. For a sub-Chabrier IMF slope the effect is more complicated. Here, a constant star formation history is only possible for low r-band weighted ages. The implied mass changes will be up to 0.15 dex lower than for a SSP. In some cases this may make the galaxy lighter than Chabrier instead of heavier, with a lightest mass change of -0.17 dex.

We conclude that our method is a good first order approximation of the ex-

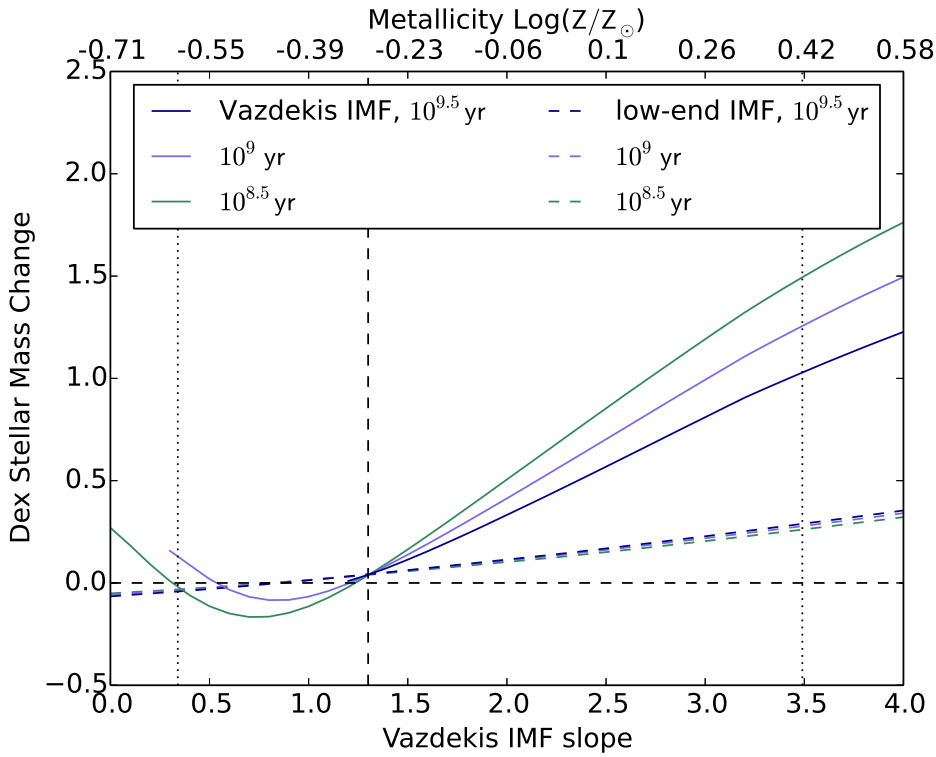

Figure 3.13: Same as figure 3.4, but for a constant star formation history instead of a simple stellar population. This plot is meant to estimate the error made in using a SSP for all galaxies. The different colours denote different r-band weighted ages. The solid lines stop at the left when the implied start of constant star formation would be the same as the age of the Universe.

pected mass differences implied by a metallicity-dependent IMF. A more precise treatment, using a varying IMF in SED fitting could be beneficial, but at the moment this is not expected to be the main source of systematic or random errors. Moreover SED fitting itself also suffers from an age-metallicity degeneracy and a degeneracy in the fitted star formation history. For example Torrey et al. (2015a) find that SED fitting mock galaxies from the Illustris simulation with the FAST code delivers more accurate stellar masses when the metallicity for all galaxies is kept fixed.

Opinionis enim commenta delet dies, naturae iudicia confirmat.
Time destroys the figments of the imagination, while confirming the judgments of nature.

-- Marcus Tullius Cicero[10]

[10](Cicero 45 B.C.)

4 A large difference in the progenitor masses of active and passive galaxies in the EAGLE simulation

Based on:
Bart Clauwens, Marijn Franx, Joop Schaye
A large difference in the progenitor masses of active and passive galaxies in the EAGLE simulation
Published in MNRAS Letters

Cumulative number density matching of galaxies is a method to observationally connect descendent galaxies to their typical main progenitors at higher redshifts and thereby to assess the evolution of galaxy properties. The accuracy of this method is limited due to galaxy merging and scatter in the stellar mass growth history of individual galaxies. Behroozi et al. (2013) have introduced a refinement of the method, based on abundance matching of observed galaxies to the Bolshoi dark-matter-only simulation. The EAGLE cosmological hydro-simulation is well suited to test this method, because it reproduces the observed evolution of the galaxy stellar mass function and the passive fraction. We find agreement with the Behroozi et al. (2013) method for the complete sample of main progenitors of $z = 0$ galaxies, but we also find a strong dependence on the current star formation rate. Passive galaxies with a stellar mass up to $10^{10.75}\mathrm{M}_{\odot}$ have a completely different median mass history than active galaxies of the same mass. This difference persists if we only select central galaxies. This means that the cumulative number density method should be applied separately to active and passive galaxies. Even then, the typical main progenitor of a $z = 0$ galaxy already spans two orders of magnitude in stellar mass at $z = 2$.

4.1 Introduction

Observations provide properties of samples of galaxies at different redshifts. Inferring the typical evolution of individual galaxies from these observations is non-trivial, since it involves linking representative progenitor- and descendant-galaxies. This link is not directly observable, since every galaxy is normally only observed at

one instance in time.

Once we have the ideal cosmological simulation that reproduces the evolution of all properties of galaxy samples across cosmic time, we can retrieve typical galaxy evolution tracks from this. However, at the moment, the space of possible simulations is many-dimensional and not well constrained by physics from first principles. Changes in one of the modelling assumptions can affect many predictions in a complicated way. Vice versa, the comparison of simulation predictions and observations does not easily translate into a required change in the model ingredients. For that reason, apart from comparing galaxy samples in observations and simulations, it is important to attempt to infer the typical evolution of individual galaxy properties as much as possible directly from observations.

Cumulative number density matching of galaxies across redshift is a promising method to achieve this. In its original form it does not need any simulation input. The cumulative number density at a given redshift and mass is defined as the comoving number density of galaxies with a stellar mass larger than or equal to the given mass. Main progenitors are then selected at a constant cumulative number density. The underlying assumption is that galaxies evolve conjointly, building up stellar mass in a similar way, without changing rank order (based on stellar mass or velocity dispersion).

This method, originating from the work of Loeb and Peebles (2003), has been employed by Papovich et al. (2011) and Lundgren et al. (2014) to study stellar mass and star formation rate (SFR) evolution out to $z \approx 8$, by van Dokkum et al. (2010) and Patel et al. (2013) to study the evolution of the structural parameters of massive galaxies out to $z \approx 3$, by van Dokkum et al. (2013) and Morishita et al. (2015) to study the stellar density profile evolution of Milky-Way-like and massive galaxies since $z \approx 3$ and by Finkelstein et al. (2015) to predict the abundance of bright $z \approx 9$ galaxies.

Cumulative number density matching is not expected to be a perfect method for inferring the evolution of galaxies, because it neglects galaxy mergers and because rank order may not be conserved. The viability of the method has therefore been investigated by Leja et al. (2013), applied forward in time to the descendants of $z \approx 3$ galaxies, based on the Guo et al. (2011) semi-analytic model of galaxy formation. They find that a constant cumulative number density is a good first order approximation for these descendants. Behroozi et al. (2013) apply the method backwards in time to the main progenitors of $z = 0$ galaxies. They use by construction a representative history of the galaxy stellar mass function (GSMF), based on the abundance matching of observed galaxies to the Bolshoi dark-matter-only simulation. They find that a constant cumulative density is a poor prescription for matching main progenitors and they give a recipe to account for the increase in the running median cumulative number density towards higher redshifts that re-

sults from merging: $(0.16\Delta z)$ dex. This equation applies to a large range of galaxy masses and redshifts up to 8. Other recent studies have been undertaken by Torrey et al. (2015b) based on the Illustris hydrodynamic simulation as well as by Mundy et al. (2015), Henriques et al. (2015) and Terrazas et al. (2016) for different semi-analytic methods.

In this work we investigate the accuracy of the cumulative number density matching technique by comparing to results of the EAGLE hydrodynamic simulation (Schaye et al. 2015; Crain et al. 2015). EAGLE is arguably the first hydrodynamic simulation that has an accurate enough evolution of the GSMF (Furlong et al. 2015) and a representative enough passive/active galaxy population (Schaye et al. 2015; Trayford et al. 2016) to address this question in some detail.

4.2 Simulation

We follow the main progenitors of redshift zero galaxies in the $(100\ \mathrm{Mpc})^3$ sized EAGLE simulation RefL100N1504. This simulation has been calibrated to the $z = 0$ GSMF and mass-size relation. It has an initial gas particle mass of $1.8 \times 10^6\ \mathrm{M}_\odot$ and a maximum gravitational force softening of 700 pc. We use the public data release described in McAlpine et al. (2016). Following De Lucia and Blaizot (2007), the main progenitor is defined as the progenitor with the most massive integrated history.

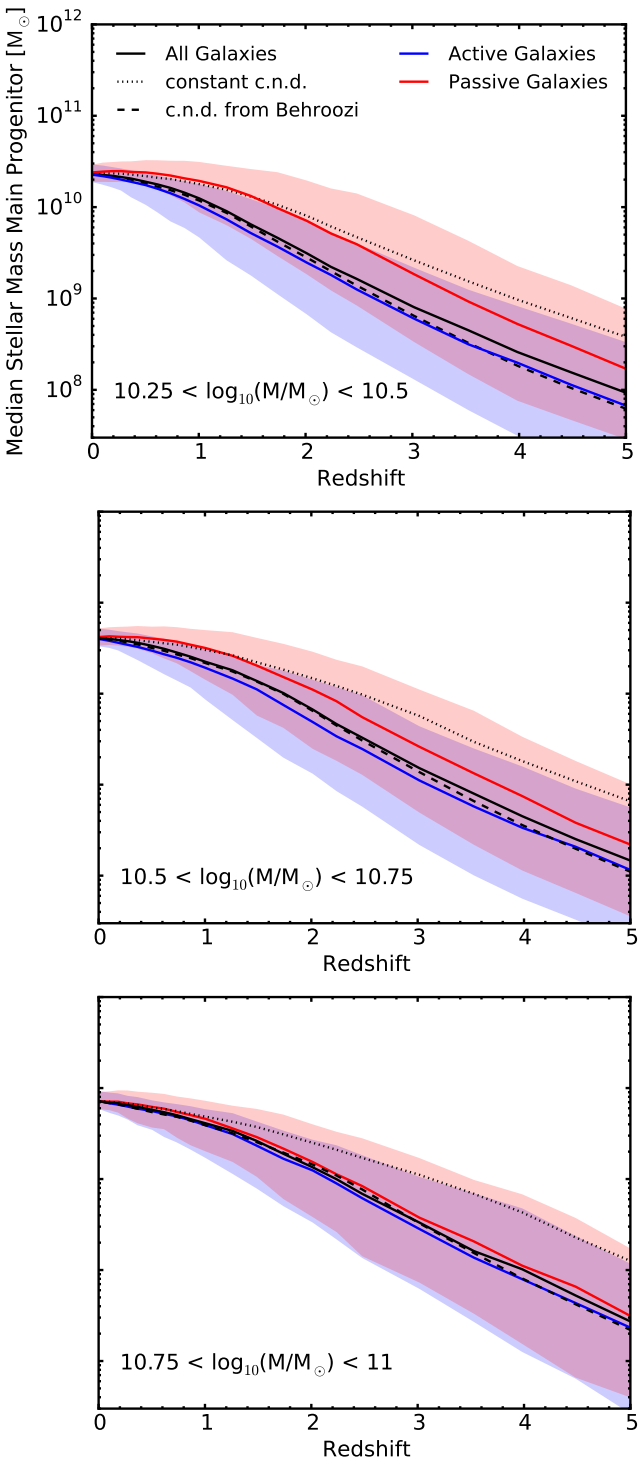
Median Stellar Mass Main Progenitor [M⊙]
All Galaxies
constant c.n.d.
c.n.d. from Behroozi
Active Galaxies
Passive Galaxies
10.25 < log10(M/M⊙) < 10.5
10.5 < log10(M/M⊙) < 10.75
10.75 < log10(M/M⊙) < 11
Redshift

Figure 4.1: The history of the median main progenitor stellar mass in the EAGLE simulation for three 0.25 dex wide mass bins, selected at $z = 0$. The solid black curve denotes the true median main progenitor mass. The dotted black curve shows the stellar mass at a constant cumulative number density. The dashed black curve follows the stellar mass at an exponentially evolving cumulative number density as suggested by Behroozi et al. (2013). Solid blue and red curves denote the true median main progenitor masses for the subsets of $z = 0$ active respectively passive galaxies. The shaded regions denote the corresponding $10^{\text{th}} - 90^{\text{th}}$ percentiles.

4.3 Results

Fig. 4.1 shows the median mass history of main progenitors in three 0.25 dex wide mass bins at $z = 0$. For all mass bins (also those not shown at lower and higher masses) a constant cumulative number density (dotted black curve) significantly overestimates the true median main progenitor mass (solid black curve) in the simulation. Typically there is already an 0.5 dex difference in mass at $z = 2$. We confirm that this offset is adequately captured by the prescription of Behroozi et al. (2013) of increasing the cumulative number density by $(0.16\Delta z)$ dex (compare solid and dashed black curves). The fact that the EAGLE hydrodynamic simulation gives the same median main progenitor mass history as the abundance matching technique of Behroozi et al. (2013), shows that this is mainly a property of the dark matter halo merger tree, provided that the history of the GSMF is accurately captured by the simulation.

However, hydrodynamic processes do determine what kind of galaxy can be expected to be found in what kind of halo. The technique of finding representative main progenitors via cumulative number density matching assumes that galaxies of a certain mass share a common history. We know from observations that the redshift zero galaxy population is bimodal, with clear active (star forming) and passive galaxy populations (e.g. Strateva et al. 2001). We expect that the history of a typical passive galaxy differs from that of a typical active galaxy, remaining closer to its current stellar mass.

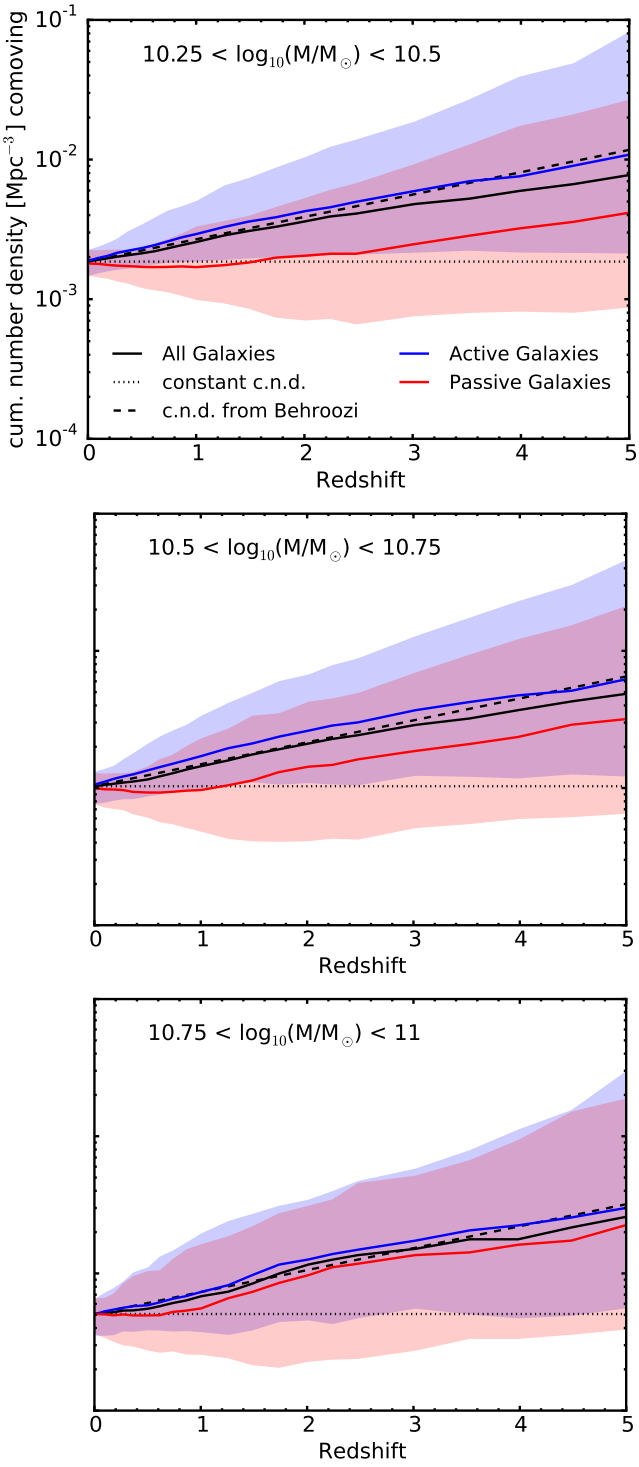
10.25 < log10(M/M⊙) < 10.5
10.5 < log10(M/M⊙) < 10.75
10.75 < log10(M/M⊙) < 11
cum. number density [Mpc−3] comoving
Redshift
All Galaxies
constant c.n.d.
c.n.d. from Behroozi
Active Galaxies
Passive Galaxies

Figure 4.2: The cumulative number density of main progenitors. All selections are the same as in Fig. 4.1. The median main progenitor mass of the $z = 0$ passive galaxies (solid red lines) tends to follow a constant cumulative number density at low redshift and an exponential increase in the cumulative number density parallel to the Behroozi et al. (2013) prescription at higher redshifts.

Indeed, in the EAGLE simulation the current active/passive status of a galaxy (defined using a sSFR cut at 10^{-11}/yr), is highly predictive for its median main progenitor mass history. The blue and red curves in Fig. 4.1 show the median main progenitor mass of the $z = 0$ active, respectively passive, galaxy populations. The three mass bins cover the interesting region that goes from no difference between active/passive at $10.75 < log_{10}(M/\mathrm{M}_{\odot}) < 11$ and higher, via a significant difference at Milky Way-like masses $10.5 < log_{10}(M/\mathrm{M}_{\odot}) < 10.75$, towards a large difference at $10.25 < log_{10}(M/\mathrm{M}_{\odot}) < 10.5$ and lower. These differences can be of the same order as those between a constant cumulative number density and the Behroozi et al. (2013) prescription, roughly 0.5 dex at $z = 2$. The $10^{\mathrm{th}} - 90^{\mathrm{th}}$ percentile blue and red shaded regions show that there is also a large variation in main progenitor masses. A recent study by Terrazas et al. (2016) reports a comparable 0.35 dex difference at $z = 2$ between the median main progenitor masses of active and passive $10.7 < log_{10}(M/\mathrm{M}_{\odot}) < 10.9$ galaxies in the semi-analytic model of Henriques et al. (2015).

Fig. 4.2 shows the median cumulative number density for the same galaxy samples as in Fig. 4.1. At a given redshift, the comoving cumulative density refers to the number density of galaxies with a stellar mass larger than or equal to the median main progenitor mass of the indicated galaxy sample, which is selected at $z = 0$. We see that the median main progenitor of the active galaxies follows the exponential cumulative number density increase of Behroozi et al. (2013), but the median main progenitor of the passive galaxies first evolves along a track of constant cumulative number density up to $z \sim 1.5$, after which it follows the same exponential trend as the main progenitors of active galaxies, albeit at an offset which would correspond to a more massive active galaxy at redshift zero.

This behaviour can be explained by comparing the evolution of the sSFR of the main progenitors of the active versus passive $z = 0$ galaxy selections. Fig. 4.3 shows the ratio of the average sSFRs of the passive and active galaxy selections in different $z = 0$ mass bins. We see that the main progenitors of passive galaxies have a reduced sSFR with respect to the main progenitors of active galaxies up to $z \approx 1.25$ for the highest-mass bin and up to $z \approx 2.5$ for the lowest-mass bin. Higher-mass passive galaxies have on average quenched later. Although not all the stellar mass

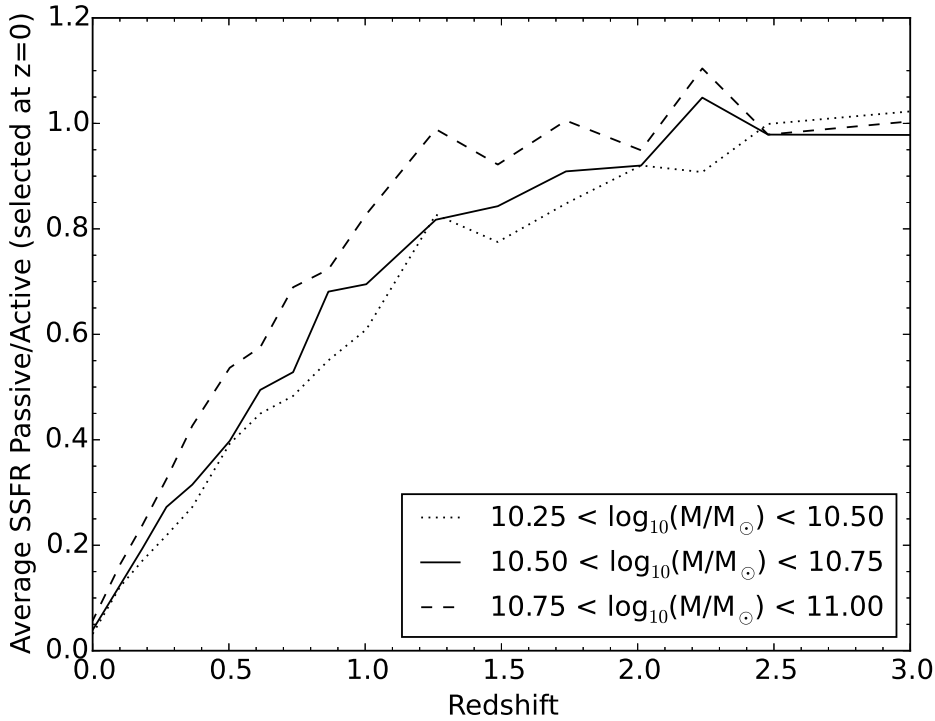

Figure 4.3: The average specific star formation rate of the main progenitors of the passive $z = 0$ galaxy sample divided by that of the active galaxy sample, as a function of redshift. The three curves are for three different, 0.25 dex wide, stellar mass bins.

growth can be attributed to the sSFR of the main progenitor, since dry mergers also contribute, the integrated effect of this sSFR difference between the active and passive samples plays a large part in driving the difference in median main progenitor mass and the corresponding difference in cumulative number density. The redshift range over which the passive main progenitors in Fig. 4.2 follow a constant cumulative number density roughly agrees with the redshift range in Fig. 4.3 for which the sSFR is reduced. In this same redshift range EAGLE matches the observed passive fraction as a function of galaxy stellar mass quite well (see Fig. 6, Furlong et al. 2015).

In order to get a better insight into the difference between the true main progenitor galaxy sample and that obtained with different cumulative number density matching techniques, Fig. 4.4 shows a snapshot at redshift 2 of the two most relevant galaxy properties: the stellar mass and the sSFR, for the main progenitors of galaxies with Milky Way-like masses at redshift zero. The top panel shows the significant difference between the constant cumulative number density technique and that obtained by using the real median cumulative number density, which gives results that are very similar to the Behroozi et al. (2013) prescription. The bottom panel shows the difference when using the real median cumulative number density for active and passive galaxies separately. At $z = 2$ the stellar mass range of the main progenitors, which was 0.25 dex at redshift zero, already spans several orders of magnitude. Since the EAGLE galaxies follow a relatively tight stellar mass versus dark matter mass relation, the same applies to the halo mass. Hence, any technique that does not sample a representative spread in stellar mass, will select a rather unrepresentative sample of main progenitors. Moreover, for such a wide distribution, the median and the mean stellar mass will differ substantially.

Depending on which galaxy property is studied, one might need a different cumulative number density matching technique. For example, a study like that of van Dokkum et al. (2013), which uses a cumulative number density matching technique to observationally assess the radial stellar mass buildup of Milky Way-like galaxies, would benefit from using a cumulative number density based on the average stellar mass, or even better, including a representative variation in mass.

Apart from discriminating between the progenitors of active and passive galaxies, an obvious other selection criterion is on satellite- versus central galaxies. Fig. 4.5 (top panel) shows that selecting only the main progenitors of central galaxies gives a similar dependence on the active/passive state as for all galaxies in Fig. 4.2, so the difference in mass between the main progenitors of active and passive galaxies is not mainly caused by the quenching of satellite galaxies. Fig. 4.5 (bottom panel) shows however that the main progenitors of passive satellites tend to be more massive than those of passive centrals. This difference could be due to earlier quenching of satellite galaxies and/or the stripping of stars from satellite

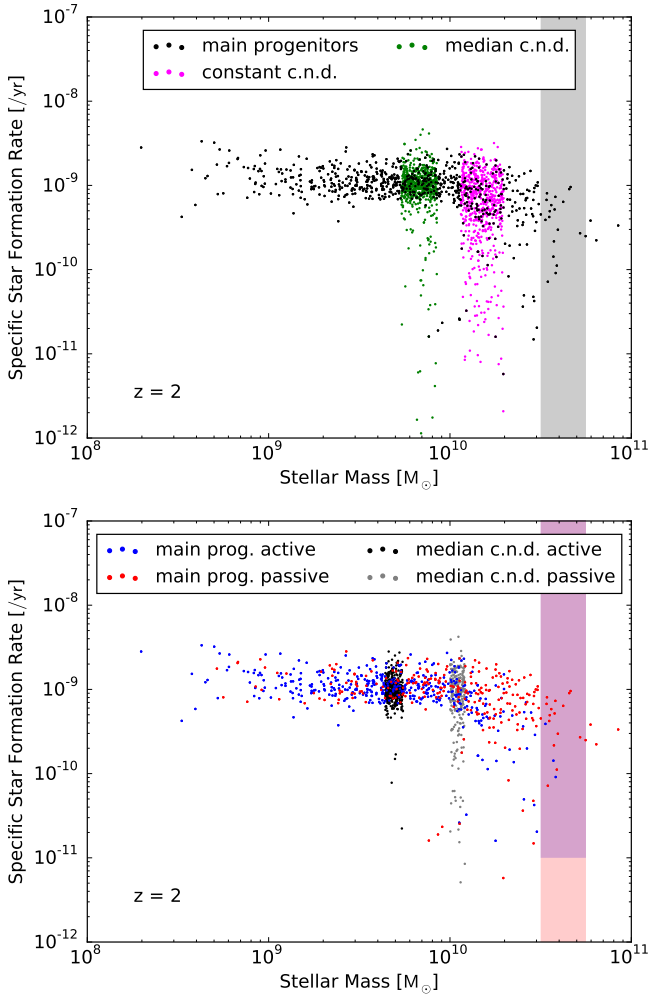

Figure 4.4: The specific star formation rate versus stellar mass of the main progenitors at a redshift of 2 of the galaxy sample selected at redshift zero to have a stellar mass of $10.5 < log_{10}(M/\mathrm{M}_\odot) < 10.75$ (indicated by the grey band). In the top panel, black dots denote the true main progenitors, magenta dots denote the galaxy sample that would be selected at $z = 2$ based on a constant median cumulative number density and green dots denote the galaxy sample that would be selected using the true median main progenitor stellar mass, which gives similar results as the prescription of Behroozi et al. (2013). In the bottom panel a redshift zero selection is made on active/passive galaxies, denoted by the blue/red bands. Blue and red dots denote the true main progenitors of the active respectively passive galaxies. Black and grey dots denote the galaxy sample that would be selected at $z = 2$ using the correct median main progenitor mass separately for the active and passive sample.

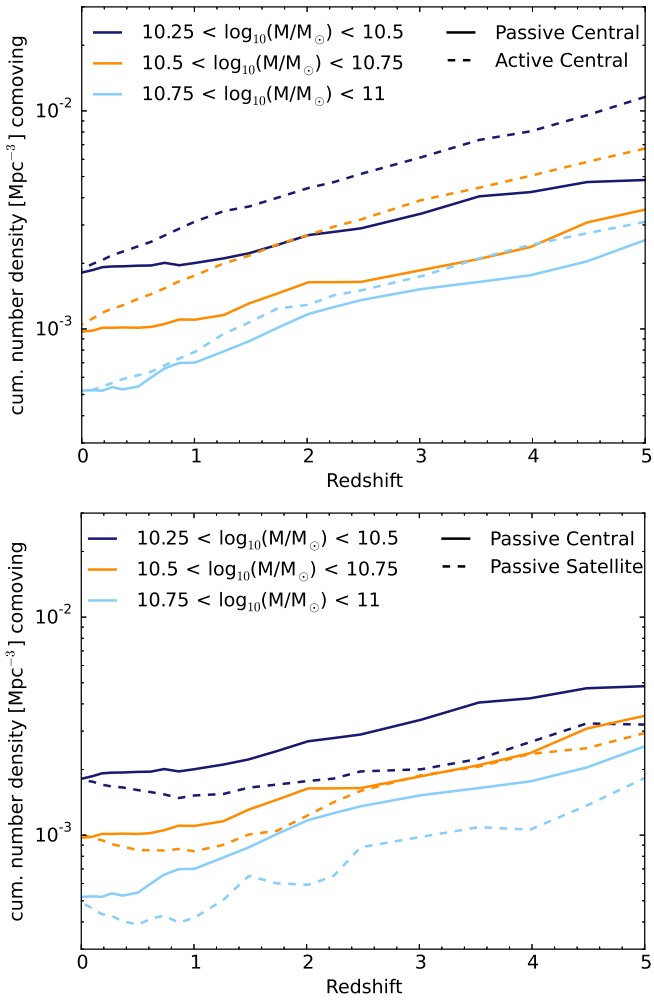

Figure 4.5: The median cumulative number density of the main progenitors of $z = 0$ galaxies in different mass bins (indicated by different colours), separately for passive and active centrals (top panel) and for passive centrals and satellites (bottom panel). The top panel shows a similar difference between active and passive cumulative number densities for central galaxies as Fig. 4.2 showed for all galaxies. The bottom panel shows that the main progenitors of passive satellites tend to be more massive than those of passive centrals of the same mass.

galaxies. There is no similar difference in mass between the main progenitors of active centrals and satellites (not shown).

Our results indicate that the progenitor masses are systematically offset for passive galaxies by an amount similar to the correction calculated by Behroozi et al. (2013). In addition, the properties of the progenitors are systematically correlated over time (e.g. SFR and hence central density, Sersic profile, etc.). This means that, in the absence of a procedure to correct for these correlations, the method has only limited applicability. At the highest masses ($n < 5 \times 10^{-4} \times 10^{0.16z}\,\mathrm{Mpc}^{-3}$) the method works best.

4.4 Conclusions

We use the EAGLE hydrodynamical simulation to study the accuracy of the cumulative number density matching technique in creating a representative sample of main progenitor galaxies as a function of redshift. The EAGLE simulation is well suited to study this question, because it reproduces the evolution of the galaxy stellar mass function and has a representative population of passive and active galaxies. Our main findings are as follows:

- Using a constant cumulative number density prescription to find typical main progenitors of redshift zero galaxies neglects mergers and significantly overestimates the median progenitor mass. The error is ≈ 0.5 dex at $z = 2$ for galaxies in the stellar mass range $10^{10}\mathrm{M}_{\odot} < M < 10^{11}\mathrm{M}_{\odot}$ and ≈ 0.25 dex for $M > 10^{11}\mathrm{M}_{\odot}$ (Fig. 4.1).

- The prescription of Behroozi et al. (2013) to increase the cumulative number density by 0.16 dex per Δz accurately captures the evolution of the median main progenitor stellar mass. As Behroozi et al. (2013) used a dark mater only simulation, this shows that the evolution of the median main progenitor mass is mainly set by the properties of the halo merger tree (Fig. 4.2).

- The main progenitor masses of $z = 0$ galaxies that are less massive than $10^{10.75}\mathrm{M}_{\odot}$ critically depend on the current star formation rate. At $z = 2$ the median main progenitor mass of passive galaxies ($sSFR < 10^{-11}$/yr at $z = 0$) is ≈ 0.5 dex higher than that of active galaxies (Figs. 4.1,4.2).

- The difference between the median main progenitor mass of active and passive galaxies (or equivalently the difference in median cumulative number density) increases gradually up to $z \approx 2$. Out to this same redshift we see a reduced average sSFR for the main progenitors of passive galaxies compared to those of active galaxies (Fig. 4.3).

- The mass difference between the main progenitors of passive and active galaxies persists if we only select central galaxies (Fig. 4.5).
- The large difference between main progenitor masses of passive and active galaxies calls for an inclusion of an sSFR distinction in the cumulative number density matching technique.
- The spread in main progenitor masses already spans several orders of magnitude at $z = 2$ (Fig. 4.4). Therefore, it is imperative to include the variation in the main progenitor stellar masses (or cumulative number densities) in observational studies that use the cumulative number density matching technique. For such a wide distribution the average (e.g. main progenitor density profile) is expected to be different from the median.
- The main progenitors of passive satellites tend to be more massive than those of passive centrals in the same $z = 0$ mass range (Fig. 4.5). A similar distinction between the main progenitor masses of active centrals and active satellites does not exist.

Hence, the cumulative number density matching technique should discriminate between the main progenitors of active and passive galaxies in order to obtain a reasonable accuracy. Exactly how to implement this is not clear. One could base such a method on a simulation like EAGLE and device a main progenitor selection scheme based on both stellar mass and sSFR. This would however negate the initial appeal of the method: that it only depends on observations (and on the dark matter merger tree in the case of the Behroozi et al. 2013 method).

Acknowledgements

We gratefully acknowledge support from the European Research Council under the European Union's Seventh Framework Programme (FP7/2007-2013) / ERC Grant agreement 278594-GasAroundGalaxies.

Yet Am-Tep was still troubled by the question ``why?" What deep forces control the behaviour of the world, and why do they sometimes burst forth in violent and seemingly incomprehensible ways? He shared his questions with his grandson, but there were no answers.

...

A century passed by, and then a millennium, and there still were no answers.

-- Roger Penrose[1]

[1](Penrose 2004)

5 The average structural evolution of massive galaxies can be reliably estimated using cumulative galaxy number densities

Based on:
Bart Clauwens, Marijn Franx, Joop Schaye
A large difference in the progenitor masses of active and passive galaxies in the EAGLE simulation
Published in MNRAS Letters

Galaxy evolution can be studied observationally by linking progenitor and descendant galaxies through an evolving cumulative number density selection. This procedure can reproduce the expected evolution of the median stellar mass from abundance matching. However, models predict an increasing scatter in main progenitor masses at higher redshifts, which makes galaxy selection at the median mass unrepresentative. Consequently, there is no guarantee that the evolution of other galaxy properties deduced from this selection are reliable. Despite this concern, we show that this procedure approximately reproduces the evolution of the average stellar density profile of main progenitors of $M \approx 10^{11.5}\mathrm{M}_{\odot}$ galaxies, when applied to the EAGLE hydrodynamical simulation. At $z \gtrsim 3.5$ the aperture masses disagree by about a factor two, but this discrepancy disappears when we include the expected scatter in cumulative number densities. The evolution of the average density profile in EAGLE broadly agrees with observations from UltraVISTA and CANDELS, suggesting an inside-out growth history for these massive galaxies over $0 \lesssim z \lesssim 5$. However, for $z \lesssim 2$ the inside-out growth trend is stronger in EAGLE. We conclude that cumulative number density matching gives reasonably accurate results when applied to the evolution of the mean density profile of massive galaxies.

5.1 Introduction

An interesting challenge for the study of galaxy evolution is to find a method to distill the evolution of a typical galaxy from that of the total observed galaxy population. One way to do this, is to rank the observed galaxies at each redshift ac-

cording to their stellar mass and then assign a unique cumulative number density (hereafter CND) to each galaxy, defined as the comoving number density (Mpc^{-3}) of galaxies at that redshift that are more massive than the given galaxy. The simplest assumption is then that galaxies evolve along a constant CND. This method has been used to study, among other things, the evolution of stellar masses, star formation rates and stellar density profiles of Milky Way-like and massive galaxies (Loeb and Peebles 2003; van Dokkum et al. 2010; Papovich et al. 2011; van Dokkum et al. 2013; Patel et al. 2013; Lundgren et al. 2014; Morishita et al. 2015).

However, the assumption of a constant CND is a very crude approximation to the expected evolution in a ΛCDM cosmology, which is inherently stochastic in nature and cannot conserve galaxy numbers due to merging. Behroozi et al. (2013, hereafter B13) give a more accurate prediction for the expected evolution of the CND, which accounts for mergers. This prediction has been applied to observations by Marchesini et al. (2014) and Vulcani et al. (2016) to study, among other properties, the stellar mass, star formation rate and environments of the main progenitors of massive galaxies. Papovich et al. (2015) use a similar method to study the evolution of the stellar density profiles of main progenitors of both massive and Milky Way-mass galaxies.

B13 base their prediction for the evolution of the median CND on abundance matching of observed galaxies to halos in the Bolshoi dark matter simulation. The median is taken at each redshift and represents the typical main progenitor. They find a significant increase of the median CND of ≈ 0.16 dex per Δz when tracing main progenitors[1] and a much smaller redshift dependence when tracing descendants[2]. They also find a large scatter (≈ 0.7 dex) around this median CND that increases with Δz.

The expected evolution of the median number density of the progenitors/descendants can be accounted for when applied to observations (Marchesini et al. 2014; Papovich et al. 2015; Vulcani et al. 2016). The large scatter is more problematic, because it potentially defeats the purpose of the method to reliably identify progenitors/descendants. It would be more accurate to also sample the scatter in the CND. However, when sampling such a wide distribution of galaxy masses, there are many galaxies to choose from and thus also many ways in which to choose galaxies with the wrong properties. This would not matter if there were no additional independent correlations between the properties of descendants and progenitors. It is however possible that, for example, progenitors of similar stellar mass with more/less centrally concentrated density profiles tend to form more/less

[1]B13 have made their exact results available at http://code.google.com/p/nd-redshift/.

[2]One should keep in mind that, for descendants, the median CND is defined only with respect to the surviving galaxies and might evolve more steeply when the merged galaxies are included in the median.

massive descendants. The assumption that the evolution of galaxy properties can be reliably estimated from a stellar mass-selected galaxy sample, might hold to a differing degree for different galaxy properties.

For this reason it is important to test the CND matching technique on semi-analytic models and hydrodynamical simulations of galaxy formation in a context where these additional independent correlations might appear. In a previous paper (Clauwens et al. 2016) we reported such a correlation between the $z = 0$ star formation rate of Milky way-mass galaxies and the stellar mass of their main progenitors in the EAGLE hydrodynamical simulation (Schaye et al. 2015; Crain et al. 2015): main progenitors of passive galaxies tend to be a factor 2.5 more massive at $z = 2$ than main progenitors of active galaxies with the same stellar mass.

In this paper we investigate the extent to which CND matching can retrieve the stellar density profiles of the main progenitors of massive galaxies out to $z = 5$ in the EAGLE simulation. We base our galaxy selection on the observational work of Hill et al. (2017) and we conclude with a direct comparison of simulation and observations.

Other works that analyse the performance of CND matching in semi-analytic models and hydrodynamic simulations include Leja et al. (2013); Torrey et al. (2015b, 2017); Mundy et al. (2015); Henriques et al. (2015); Terrazas et al. (2016); Jaacks et al. (2016); van de Voort (2016); Wellons and Torrey (2017). One advantage of using the EAGLE simulation for our analysis, is that it matches the observed evolution of the galaxy stellar mass function (GSMF) quite well (Furlong et al. 2015). Therefore, the B13 prescription, which is based on the observed GSMF through abundance matching, is expected to work for the EAGLE simulation, at least in retrieving the median stellar mass evolution.

5.2 Method

For this work we use the $(100\,\mathrm{Mpc})^3$ sized reference run of the EAGLE hydrodynamical simulation: Ref-L100N1504. All the used data is publicly available (McAlpine et al. 2016). The simulation includes radiative cooling and heating, and stochastic feedback from active galactic nuclei and stars (the latter depending on the local density and metallicity). The simulation has been calibrated to reproduce the current GSMF and galaxy sizes. The effective resolution is set by an initial gas particle mass of $1.6 \times 10^6 \mathrm{M}_\odot$, a maximal gravitational force softening of 700 pc and an effective temperature pressure floor of 8000 K for the interstellar medium (Schaye and Dalla Vecchia 2008). This means that by design the simulation does not give cold thin disks. The minimal disk height is roughly 1 proper kpc (pkpc). In some cases we will give results on a 1 pkpc scale, but keep in mind that this

is stretching the domain of applicability of the simulation. Certainly these results will be much less robust then those on scales of 3 pkpc and larger.

We base the galaxy selection in EAGLE on the observational work of Hill et al. (2017), who use stacked observations from UltraVISTA and CANDELS out to $z = 5$ to study the structural evolution of the progenitors of massive galaxies. Their descendants are selected at $0.2 < z < 0.5$ to have a stellar mass of $10^{11.5}\mathrm{M}_{\odot}$. Main progenitor stacks are made in redshift intervals out to $z = 5$ along the evolving CND prescribed by B13.

In EAGLE we select all the galaxies at $z = 0.37$ that have a stellar mass of $11.4 < \mathrm{Log}(M/\mathrm{M}_{\odot}) < 11.6$ within a 70 pkpc 3D aperture, comparable with the 75 pkpc 3D aperture aimed for in the observations. This gives a sample of 24 descendant galaxies. Throughout this paper we will use the 3D stellar aperture masses within 1, 3, 5, 20 and 70 pkpc as a coarse sampling of the stellar density profiles.

We follow the main progenitor evolution of the aperture masses for both the true main progenitors of these 24 galaxies and for the 24 galaxies closest to the median CND from B13. Lastly, we make a `fiducial' selection of 24 galaxies for which the expected variance in the main progenitor CNDs is taken into account. For this we fit an evolving lognormal distribution of CNDs, based on the 68^{th} percentile range given by B13. We sample the lognormal distribution at regular cumulative probabilities (multiples of 1/25). Recently Torrey et al. (2017) and Wellons and Torrey (2017) also advocated the use of a lognormal distribution of CNDs.

Figure 5.1: The evolving average stellar mass within a fixed 3D proper aperture. The apertures for the red curves in the top, middle and bottom panels are 1,3 and 5 pkpc, respectively. Black curves denote the aperture masses within 70 pkpc, which are the same in all panels. Blue curves denote the difference between inner and outer apertures (black and red). Different line styles denote different evolving galaxy selections within the EAGLE simulation. The true main progenitor evolution is depicted by solid curves. Dashed curves represent a selection based on the expected B13 median CND, whereas dotted curves represent the 'fiducial' selection, which also includes the scatter in the CND evolution from B13. In all panels the 'B13' curves agree remarkably well with the 'main progenitors', with an increasing discrepancy towards higher redshifts. The agreement for the 'fiducial' curves is even better.

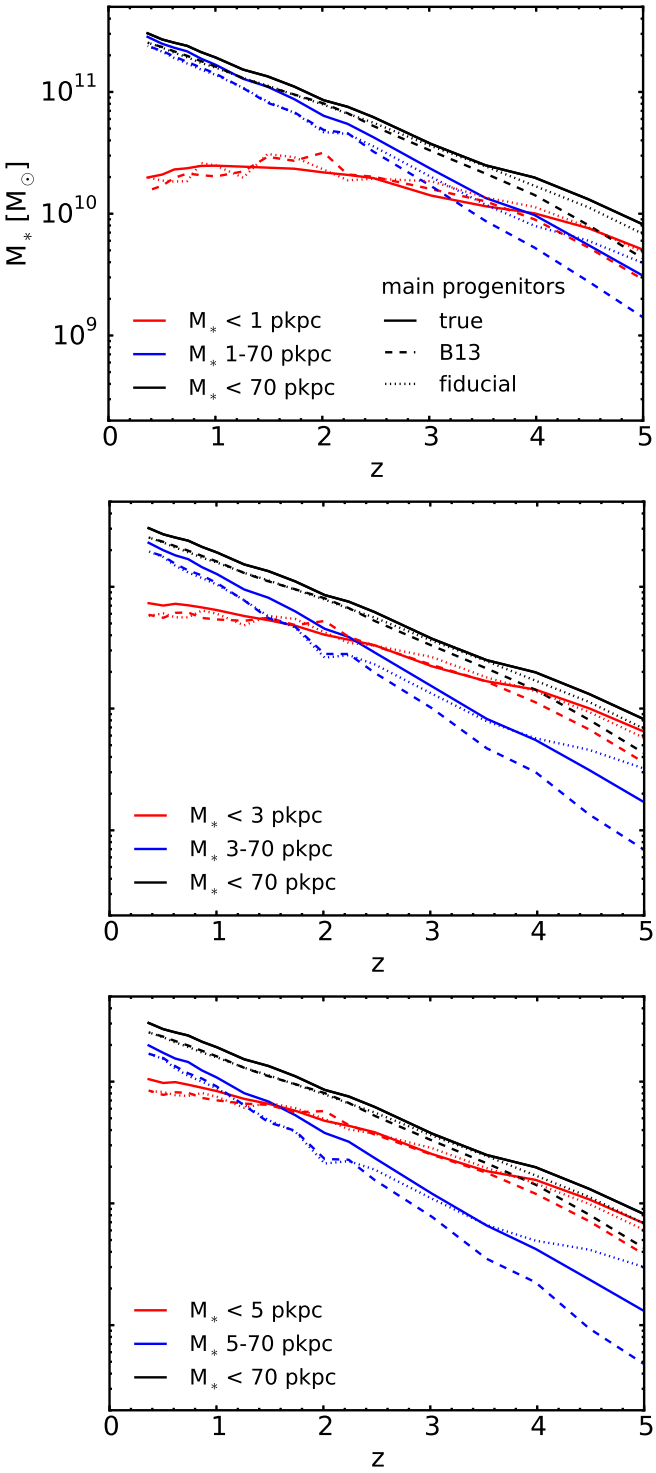
10^{11}
10^{10}
10^{9}
M_* [$M_\odot$]
M_* < 1 pkpc
M_* 1-70 pkpc
M_* < 70 pkpc
main progenitors
true
B13
fiducial
0
1
2
3
4
5
z
M_* < 3 pkpc
M_* 3-70 pkpc
M_* < 70 pkpc
z
M_* < 5 pkpc
M_* 5-70 pkpc
M_* < 70 pkpc
z

5.3 Results

Figure 5.1 compares the evolution of the average aperture masses for the true main progenitors in EAGLE to the evolution obtained with the `B13' selection and the `fiducial' selection. We use average masses rather than median masses because this is equivalent to what one gets from stacking observations. Remarkably, the `B13' aperture mass evolution (dashed curves) agrees well with the main progenitor aperture mass evolution (solid curves) for all apertures. The agreement is especially good below $z \approx 3.5$. Above this redshift the difference between the main progenitor and the `B13' mass within a 70 pkpc aperture increases to ≈ 0.3 dex. A similar divergence appears for the smaller apertures.

At $z \gtrsim 2.5$ the `fiducial' aperture masses (dotted curves) are more accurate than the `B13' aperture masses (dashed curves). Qualitatively we can understand this because the higher the redshift, the larger the scatter in the true main progenitor masses, and the more important it becomes to model this scatter accurately.

The average density profile of the main progenitors of $M_* = 10^{11.5}\mathrm{M}_\odot$ galaxies is thus well approximated in EAGLE by using the `B13' method. Assuming that the real Universe resembles the EAGLE simulation in this regard, this means that stacking galaxy images along the B13 CND is a reliable way to estimate the average growth of the density profile of galaxies with this mass. An important question is whether the average density profile is representative of the individual galaxies that compose the stack.

Figure 5.2 shows the 10%-90% range of the main progenitor stellar masses in the 3 pkpc aperture (blue shaded area). The `B13' method (red shaded area), by construction, does not try to match this and indeed does not. The `fiducial' method (green shaded area) reproduces the scatter in the 3 pkpc aperture mass at higher redshifts. The scatter in the 1,5 and 70 pkpc apertures is also reproduced (not shown).

Figure 5.3 shows the evolution of the median galaxy stellar mass fraction within a 3 pkpc radius (blue curve). This fraction evolves from ≈ 0.74 at $z = 5$ to ≈ 0.22 at $z = 0.37$, clearly indicative of an inside-out growth history. Similar inside-out behaviour is observed for the other apertures (not shown). The fraction for the 1 pkpc and 5 pkpc apertures evolves from ≈ 0.36 to ≈ 0.05 and from ≈ 0.81 to ≈ 0.33 respectively. The `B13' method (red curve) slightly overestimates this inside-out growth trend for individual galaxies, as does the `fiducial' method (green curve). However the `fiducial' method succeeds better in reproducing the scatter at high redshifts (indicated by the 10%-90% shaded regions).

The evolution of the average stellar density profile is dominated by the most

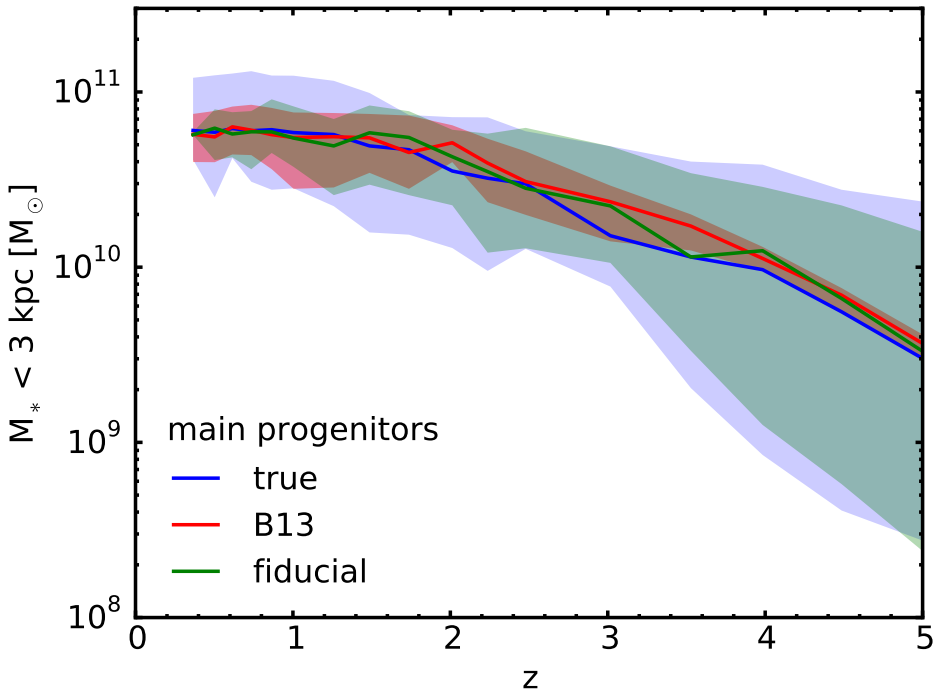

Figure 5.2: The evolving median stellar mass within a 3 pkpc 3D radius. Solid lines show the evolving medians and shaded regions show the 10%-90% percentiles. The main progenitor selection is shown in blue, the 'B13' selection in red and the 'fiducial' selection is shown in green. Plots for 1 or 5 pkpc apertures look qualitatively similar (not shown) with a more extended 10%-90% range for the 1 pkpc aperture. The 'fiducial' selection reproduces the true spread in progenitor aperture masses at high redshifts.

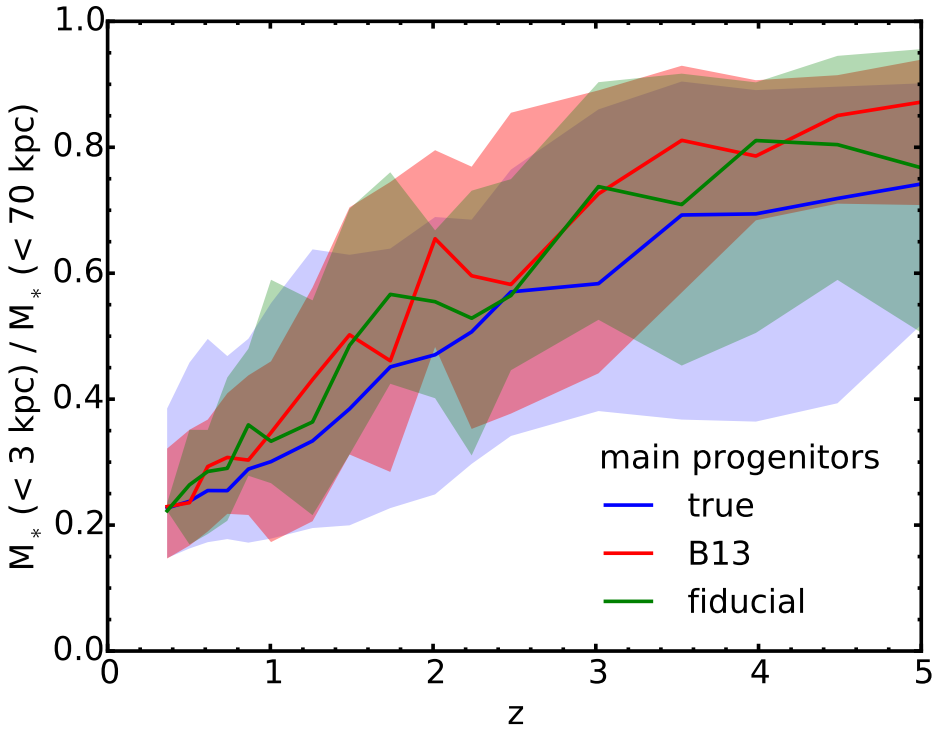

Figure 5.3: The fraction of stellar mass that resides in the central 3 pkpc as a function of redshift. Solid lines denote the median and shaded regions denote the 10%-90% range for the same galaxy selections as in Figs. 5.1 and 5.2. Both methods reproduce the general trend, but slightly overestimate the fraction at all redshifts. The 'fiducial' method reproduces the scatter at high redshift better than the 'B13' method.

massive main progenitors at each redshift. This evolution is estimated well by the `B13' method, despite the fact that the galaxies in the `B13' selection are neither representative of the true main progenitors' mass (Fig. 5.2) nor of their evolution (Fig. 5.3). The `fiducial' method improves on all these points, but might be difficult to implement observationally, because it requires deeper observations (typically an order of magnitude fainter at $z = 5$). However, when the objective is to retrieve the average growth of the stellar profile density, we expect the sampling of scatter in mass at the high-mass end to be of much greater importance than that at the low-mass end. Thus, a galaxy selection similar to our `fiducial' model, but with a low mass cut could be a viable alternative.

5.4 Comparison with observations

Up to this point we have used the EAGLE simulation to validate the use of a CND matching technique based on B13 to retrieve the history of the stellar density profile of massive galaxies. In this section we will directly compare EAGLE to observations obtained with this technique.

Figure 5.4 compares the evolution of aperture masses in EAGLE with those obtained by Hill et al. (2017). The observations comprise stacks of UltraVISTA (Data Release 3, not yet public) (McCracken et al. 2012; Muzzin et al. 2013b) and CANDELS (Brammer et al. 2012; Skelton et al. 2014) images. These stacks are fitted with a Sérsic profile and then de-projected, in order to compare them to the 3D aperture masses in EAGLE. For details see Hill et al. (2017). We have tried to keep the analysis of the simulation and observations as similar as possible.

Both the simulation and observations are evaluated along the evolving median CND of B13 that corresponds to a stellar mass of $10^{11.5}\mathrm{M}_{\odot}$ at $z = 0.35$. The observational errors take into account the uncertainty in the Sérsic parameters, in the SED-fitted masses from photometry, in the photometric redshifts, and cosmic variance. Both the SED-fitting and the EAGLE simulation assume a Chabrier IMF. The stellar mass in EAGLE does not include stars that reside in other subhalos (e.g. satellite galaxies). Similarly, in the observations, satellite galaxies and interlopers are masked. The total stellar mass in EAGLE is measured within a 3D aperture of 70 pkpc. In the observations the total stellar mass of the stack is taken to be the sum of the individual catalogue galaxy masses from SED-fitting. A single M/L ratio is assumed for the stack such that the total stellar mass resides within a 75 pkpc 3D deprojected aperture. This might induce an error in cases where the catalogue mass includes stellar light from outside 75 pkpc or in cases where stellar light within 75 pkpc is lost in the noise. M/L gradients, which could contribute at the ≈ 0.2 dex level, are not taken into account, whereas in EAGLE these are

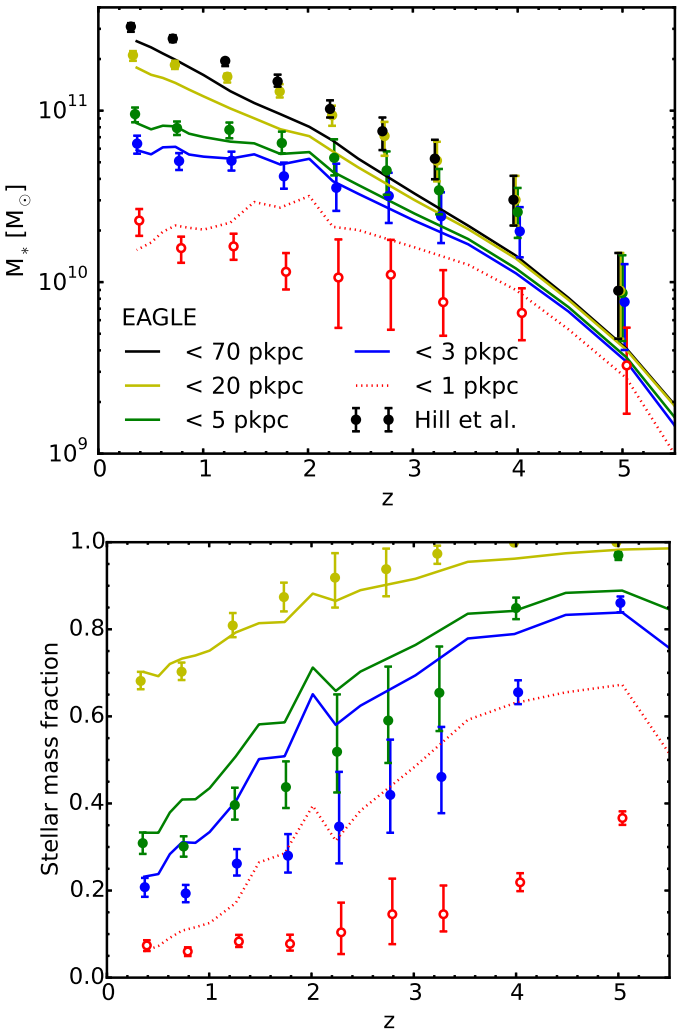

Figure 5.4: A comparison of the evolution of the aperture masses in the EAGLE simulation (curves) to the observations from Hill et al. (2017) (data points). Galaxies are selected both in the simulation and in the observations at the median CND from B13. This CND corresponds to a total stellar mass of $10^{11.5}\mathrm{M}_\odot$ at $z = 0.35$ in the observations (black data points) and to a slightly lower mass in EAGLE (black curve). Different colours denote the stellar mass within different 3D apertures. The red dashed curves and open data points should be treated with caution because they are probing a regime that is unresolved. In the bottom panel the masses are normalised to the total stellar mass at each redshift in order to show the inside-out growth trend. The error bars in the bottom panel are from Sérsic fitting. In the top panel the error bars also include uncertainties in the SED-fitted masses from photometry, uncertainties in photometric redshifts and cosmic variance. Overall there is good agreement between the simulation and observations. Both indicate an inside-out growth history over $0 \lesssim z \lesssim 5$. However, at $z \lesssim 2$ the inside-out growth trend in EAGLE is more prominent than observed.

included intrinsically, as the simulation directly traces stellar mass.

Finally, caution should be taken in interpreting the results for the stellar mass within the 1 pkpc aperture (red dashed lines and open data points). In EAGLE this is close to the resolution limit of the simulation. In the observations, for most galaxies the central pkpc is below the resolution limit and hence the mass within this aperture is mostly driven by the Sérsic fit.

Figure 5.4 shows overall agreement between observations and simulation. The difference between EAGLE and observations in the total stellar mass at the B13 CNDs (black curve and data points) diverges to approximately a factor of 2 at high redshifts, albeit at 1σ level at $z = 5$. For the 1 pkpc aperture (red dashed curve and open data points) the trend over the entire redshift range is similar, but EAGLE shows a declining 1 pkpc aperture mass for $0 \lesssim z \lesssim 2$. A comparison with Figure 5.1 (top panel) shows that this is mainly a feature of the B13 selection and not of the true main progenitors. Both simulation and observations show an inside-out growth history over $0 \lesssim z \lesssim 5$, indicated by the declining stellar mass fraction within the smaller apertures towards lower redshifts in the bottom panel. For $0 \lesssim z \lesssim 2$ the observations hint at a less pronounced inside-out growth trend than the EAGLE simulation.

In future an improvement on the comparison of the stellar density profile growth in observations and simulation can be made by taking into account M/L gradients in the observations or by making virtual observations of the simulation and comparing light profiles directly. If the growth is aimed to be representative of main progenitor growth then improvements can be made by also sampling the scatter in stellar mass at high redshifts (our fiducial method).

5.5 Conclusions

We used the EAGLE hydrodynamical simulation to determine whether the growth of the stellar density profile of the main progenitors of $M_* = 10^{11.5}\mathrm{M}_\odot$ galaxies can be reliably estimated with the cumulative number density (CND) matching technique. Our conclusions are as follows.

- The average stellar mass growth within 1, 3 and 5 pkpc 3D apertures is well approximated by selecting galaxies that follow the evolving CND of B13 (Fig. 5.1). This suggests that using the `B13' method to account for merging is a reasonable way to study the radially dependent build-up of stellar mass for these massive galaxies. The expected errors in the aperture masses grow to a factor of ≈ 2 at $z = 5$.

- The CND method can be improved by also sampling the expected scatter in the main progenitor stellar masses. We assume a lognormal form for this scatter, fitted to the 68^{th}-percentile range of B13. This `fiducial' method reduces the error in the retrieved aperture masses by a factor of ≈ 2, especially at high redshifts, where the expected scatter in main progenitor stellar masses is large (Fig. 5.1).

- Although the `B13' method succeeds in reproducing the average stellar mass growth within different apertures, it reproduces neither the scatter in these aperture masses (Fig. 5.2) nor the scatter in the central concentration of stellar mass (Fig. 5.3). The fact that the average aperture masses are reproduced is somewhat of a coincidence, since it is the average for a selection of galaxies that is neither representative in mass nor in the evolution of the true main progenitor sample.

- Sampling the scatter in stellar mass with the `fiducial' method yields results that are more representative of the true main progenitors' aperture masses (Fig. 5.2) and central stellar concentrations (Fig. 5.3).

Finally, we compared the evolution of 1, 3, 5 and 20 pkpc 3D mean aperture masses in EAGLE to the stacked UltraVISTA and CANDELS observations from Hill et al. (2017) (Fig. 5.4). Both in the simulation and in the observations we sample the galaxies along the evolving B13 median CND. Overall the simulation and observations agree remarkably well. Both indicate an inside-out stellar growth history over $0 \lesssim z \lesssim 5$. However, in EAGLE most of the relative inside-out growth happens for $z \lesssim 2.5$, whereas in the observations the inside-out aspect of the growth is more prominent at $z \gtrsim 2.5$.

Acknowledgements

This work was supported by the Netherlands Organisation for Scientific Research (NWO), through VICI grant 639.043.409 and by the European Research Council under the European Union's Seventh Framework Programme (FP7/2007- 2013) / ERC Grant agreement 278594-GasAroundGalaxies.

When you struggle to reach for something you don't know, that's where most of the interesting stuff is.

-- Herbie Hancock[3]

[3] (Hancock 2004)

6 The three phases of galaxy formation

Based on:
Bart Clauwens, Marijn Franx, Joop Schaye, Richard G. Bower
The three phases of galaxy formation
Submitted to MNRAS, arXiv:1711.00030

We investigate the origin of the Hubble sequence by analysing the evolution of the kinematic morphologies of central galaxies in the EAGLE cosmological simulation. By separating each galaxy into disk and spheroidal stellar components and tracing their evolution along the merger tree, we find that the morphology of galaxies follows a common evolutionary trend. We distinguish three phases of galaxy formation. These phases are determined primarily by mass, rather than redshift. For $M_* \lesssim 10^{9.5}\mathrm{M}_\odot$ galaxies grow in a disorganised way, resulting in a morphology that is dominated by random stellar motions. This phase is dominated by in-situ star formation, partly triggered by mergers. In the mass range $10^{9.5}\mathrm{M}_\odot \lesssim M_* \lesssim 10^{10.5}\mathrm{M}_\odot$ galaxies evolve towards a disk-dominated morphology, driven by in-situ star formation. The central spheroid (i.e. the bulge) at $z = 0$ consists mostly of stars that formed in-situ, yet the formation of the bulge is to a large degree associated with mergers. Finally, at $M_* \gtrsim 10^{10.5}\mathrm{M}_\odot$ growth through in-situ star formation slows down considerably and galaxies transform towards a more spheroidal morphology. This transformation is driven more by the buildup of spheroids than by the destruction of disks. Spheroid formation in these galaxies happens mostly by accretion at large radii of stars formed ex-situ (i.e. the halo rather than the bulge).

6.1 Introduction

Low-redshift galaxies have a wide range of morphologies, ranging from pure stellar disks, to disks with increasingly massive central stellar bulges, to elliptical galaxies. This morphological diversity is traditionally classified according to the Hubble sequence. We can decompose most galaxies into a rotationally supported stellar disk

and a spheroid, which is supported to a large degree by random, mostly radial, stellar orbits. This decomposition is motivated by the fact that classical bulges are very similar to elliptical galaxies without an accompanying disk, suggesting a similar formation mechanism. The main difference is that there is an offset between their mass-size relations (e.g. Gadotti 2009).

Galaxy morphology is tightly linked to other galaxy properties. More massive galaxies are generally less disky and, at a fixed mass, star forming galaxies tend to be disk dominated while quiescent galaxies are typically bulge dominated (e.g. Gadotti 2009; Bluck et al. 2014; Whitaker et al. 2015). Above 10^{10}M$_{\odot}$ the stellar mass in the low-redshift Universe is roughly equally divided between ellipticals, classical bulges and disks (Gadotti 2009). There is good evidence that high-redshift galaxies are built from these same morphological components with a qualitatively similar dependency on star formation and mass. Tacchella et al. (2015) find that most massive galaxies at $z \approx 2$ have fully grown and quenched bulges in their cores and van Dokkum et al. (2014) state that: `the presence of a dense core is a non-negotiable requirement for stopping star formation in massive galaxies'.

Observationally a distinction is made between classical bulges and pseudobulges (Kormendy 1993; Wyse et al. 1997). Classical bulges are dispersion dominated while pseudobulges (which can be disky, boxy/peanut shaped or nuclear bars) are rotationally dominated. Our focus will be on the dispersion dominated classical bulges, which account for a factor > 4 more in mass (Gadotti 2009).

There are many possible scenarios for bulge formation. Here we will briefly summarise the main ideas. Pseudobulges can form through secular processes (e.g. Kormendy and Kennicutt 2004) such as bar formation, followed by a buckling instability that transforms the bar into a peanut shaped pseudobulge (e.g. Raha et al. 1991; Pohlen et al. 2003; Guedes et al. 2013; Pérez et al. 2017). Classical bulges can form from diverse processes such as the collapse of primordial gas clouds (Eggen et al. 1962), disk instabilities (e.g. De Lucia et al. 2011), clump migration to the galaxy centre in violently unstable gas rich disks at high redshift (e.g. Noguchi 1999; Bournaud et al. 2007; Elmegreen et al. 2009; Perez et al. 2013), gas funneling to the centre in marginally unstable disks at high redshift (Krumholz et al. 2017), misallligned accretion (Sales et al. 2012; Aumer et al. 2013) and mergers (e.g. Aguerri et al. 2001; Aumer et al. 2013; Hopkins et al. 2010; De Lucia et al. 2011).

Mergers can influence bulge growth and overall morphological changes in diverse ways. Hernquist (1989) finds that tidal effects during mergers may induce instabilities that can funnel a large amount of gas into the central region of a galaxy, thereby inducing a starburst which creates a spheroidal component. In order to prevent too much bulge formation, stellar feedback is needed to remove low angular momentum gas, also during merger induced starbursts (e.g. Governato et al.

2009, 2010; Brook et al. 2011, 2012; Christensen and Brooks 2015; Zjupa and Springel 2017). This may not be sufficient and AGN feedback might be needed for a further supression. Disks can be destroyed by a major merger, but they can also regrow afterwards (e.g. Governato et al. 2009; De Lucia et al. 2011; Sparre and Springel 2017). For massive galaxies AGN feedback may be needed to prevent disk regrowth in order to form realistic ellipticals (e.g. Genel et al. 2015; Dubois et al. 2016; Sparre and Springel 2017). Generally, gas-poor (dry) mergers are thought to spin down galaxies, while gas rich (wet) mergers spin them up (e.g. Naab et al. 2014; Lagos et al. 2017a), although Penoyre et al. (2017) find that in the Illustris simulation this distinction has little influence. Finally, the time at which the merger takes place also matters. Late mergers are thought to give rise to a diffuse halo (Brook et al. 2011; Pillepich et al. 2015).

Mergers are the prime suspect for transforming disk galaxies into galaxies with large bulges and elliptical galaxies. However, this is not a settled matter. Lofthouse et al. (2017) conclude from observations at $z \approx 2$ that major mergers are not the dominant mechanism for spheroid creation, because only one in five blue spheroids at this redshift shows morphological disturbances. Sales et al. (2012) argue that in the GIMIC simulation (Crain et al. 2009), speroid formation does not rely on mergers, because it takes place even when most stars form in-situ, as opposed to having been accreted after forming ex-situ (i.e. in a galaxy other than the main progenitor). Furthermore, Rodriguez-Gomez et al. (2017) state that in the Illustris simulation mergers play no role in morphology below $10^{11}\mathrm{M}_{\odot}$, because accreted stellar fractions and mean merger gas fractions are indistinguishable between spheroidal and disk-dominated galaxies.

There are different ways to determine the morphology or bulge-to-total ratio (B/T) of a galaxy from observations. Usually the B/T ratio is determined photometrically, based on a decomposition of the light profile into a disk and a bulge component. The disk and bulge components are then generally assumed to have fixed S□rsic indices of $n = 1$ and $n = 4$ respectively (e.g. Bluck et al. 2014), but sometimes these indices are allowed to vary (e.g. Gadotti 2009; Sachdeva et al. 2017). The bulge can also be determined kinematically as a non-rotationally supported component. When similar methods are applied to galaxy simulations, in general photometric bulge determination leads to lower B/T ratios than kinematic bulge determination (Scannapieco et al. 2010) and these differences can be large. In the Illustris cosmological simulation the median B/T difference between both methods becomes larger than 0.5 for galaxy masses below $10^{10.6}\mathrm{M}_{\odot}$ (Bottrell et al. 2017), thus classifying galaxies as disky based on their light profile even when the kinematics show no ordered rotation.

In this work we investigate the evolution of kinematic morphologies (thus de-

rived from stellar motions) of galaxies in the EAGLE cosmological simulation (Schaye et al. 2015; Crain et al. 2015), with emphasis on the central bulge component. Oser et al. (2010) emphasized the two-phase nature of the formation of massive galaxies, whose inner regions are formed first and in-situ, while the stars in the outer parts are mainly formed ex-situ and were accreted later. Here, we investigate the provenance of in-situ/ex-situ stars in different kinematic galaxy components and we try to determine to what extent mergers are responsible for the morphological transformations of EAGLE galaxies. This will lead to a three-phase picture of galaxy formation, where low-mass galaxies are kinematically hot (i.e. spheroidal/puffy) even though most of their stars are formed in-situ, intermediate-mass galaxies also grow mostly through in-situ star formation but are kinematically cold (i.e. disky), and the growth of massive galaxies is dominated by accretion of stars formed ex-situ, making them more spheroidal.

Although EAGLE lacks the resolution to confidently reproduce the smallest observed bulges, it has overcome the largest hurdle: the overcooling problem. Overcooling would produce too massive and dense central stellar concentrations at high redshift, akin to bulges. EAGLE does well in this regard. It approximately reproduces the observed evolution of the galaxy stellar mass function (Furlong et al. 2015) and galaxy sizes, with passive galaxies being smaller at fixed mass (Furlong et al. 2017). Conclusions about the origin of galaxy morphology drawn from simulations that do not match the evolution of the mass function and the size-mass relation could be misleading, since the physical processes that determine a galaxy's stellar mass and size are also thought to determine its morphology. The galaxies in EAGLE also agree relatively well with the observed passive fraction as a function of mass (Schaye et al. 2015; Trayford et al. 2017). Furthermore, the galaxies have representative rotation curves (Schaller et al. 2015). It is thus a useful cosmological simulation to study the origin of morphology changes and bulge formation.

We build on earlier work related to the angular momentum of EAGLE galaxies. Zavala et al. (2016) find that $z = 0$ galaxy morphology is correlated with a loss of angular momentum at late times, both in the stellar component and in the inner dark matter component, due to mergers. Lagos et al. (2017b) find that galaxies with low angular momentum can be either the result of merger activity or of early star formation quenching in the absence of mergers. Lagos et al. (2017a) find that dry mergers tend to reduce the total stellar angular momentum while wet mergers tend to increase it, with a dependency on the alignment of the spin vectors of the merger pair. Finally, Correa et al. (2017) show that the kinematic morphology of EAGLE galaxies is closely related to mass and colour, with blue cloud galaxies having predominantly a disky structure and red sequence galaxies a spheroidal morphology.

We will shortly introduce the EAGLE simulation in section **??**. Section 6.3 describes our method for determining the kinematic morphology of a galaxy. We apply this to determine the morphological evolution of EAGLE galaxies in section 6.4. Section 6.5 focuses on the origin of stars in the stellar bulge and halo. Section 6.6 investigates the effects of mergers and in-situ star formation on the overall morphology of galaxies, while section 6.7 isolates the contribution of mergers on bulge and spheroid formation. For a summary of our main conclusions and a discussion of the three phases of galaxy formation, see section 6.8.

6.2 The EAGLE simulation

Our results are based on the $(100\,\mathrm{Mpc})^3$ sized reference run (Ref-L100N1504) of the EAGLE hydrodynamical simulation (Schaye et al. 2015; McAlpine et al. 2016). The simulation includes radiative cooling and heating (Wiersma et al. 2009a), star formation (Schaye and Dalla Vecchia 2008), stellar mass loss (Wiersma et al. 2009b), stochastic stellar feedback (Dalla Vecchia and Schaye 2012) (which depends on the local density and metallicity in order to prevent the overproduction of bulge-like dense stellar cores at high redshift due to numerical radiative losses) and stochastic feedback from active galactic nuclei. The simulation parameters are calibrated to the $z = 0$ galaxy stellar mass function and mass-size relation. The effect of the various parameters and the calibration choices are described in detail in Crain et al. (2015). The initial gas particle mass is $1.6 \times 10^6 \mathrm{M}_\odot$. The maximal gravitational force softening is 700 pc and a pressure floor is implemented for the interstellar medium in order to prevent spurious fragmentation (Schaye and Dalla Vecchia 2008).

The simulation relies on subgrid physics for unresolved processes at small scales and low temperatures in the interstellar medium. This means that the simulation by design does not give cold thin disks. The minimum resolved scale is about 1 kpc, which means that the simulation is best suited to study bulges at the larger end of the mass-size spectrum and the transformation of disk galaxies to elliptical galaxies. However, in appendix 6.9 we show that a comparison of the $(25\,\mathrm{Mpc})^3$ sized reference run (RefL0025N376) and the recalibrated run at a factor 8 higher mass resolution (RecalL0025N0752) suggests a good convergence of our results for $M_* \gtrsim 10^9 \mathrm{M}_\odot$.

In this work we adopt a kinematic definition for a classical bulge as the spheroidal, dispersion dominated component within 5 proper kpc (pkpc). We will study central galaxies at $z = 0$ and their main progenitors at higher redshifts (which are expected, but not required to be central galaxies). For satellites additional processes such as ram pressure stripping and strong tidal forces might induce morphological

changes, complications that we aim to avoid in this work.

6.3 Kinematic morphology

In this work we use a kinematic morphology indicator, rather than a photometric one. The kinematic morphology of a galaxy is generally condensed into a single indicator such as a bulge-to-total ratio (B/T), disk-to-total ratio (D/T) or a kinematic morphology parameter κ_{rot} (e.g. Scannapieco et al. 2010; Sales et al. 2010, 2012; Zavala et al. 2016; Bottrell et al. 2017; Correa et al. 2017), with varying prescriptions for each indicator. In this work we use a simple prescription similar to the one applied to the GIMIC simulation by Crain et al. (2010) and to the Illustris simulation by Bottrell et al. (2017).

First we determine for each galaxy the direction of total stellar angular momentum of all stellar particles within the stellar half-mass radius, denoted as $\hat{Z}$. Then we project the angular momentum of individual stellar particles $\vec{j}$ onto the $\hat{Z}$-direction and normalise it by the total angular momentum $|\vec{j}|$ of the given particle. The resulting variable $j_Z/|\vec{j}|$ denotes the amount of corotation for each stellar particle with the central half of the galaxy. Stellar particles that corotate with the stellar disk have $j_Z/|\vec{j}| = 1$, stellar particles that counter-rotate have $j_Z/|\vec{j}| = -1$ and stellar particles with random directions of angular momentum (a pure non-rotating spheroid) are distributed uniformly between -1 and 1 (which is the reason why we chose this definition).

Fig. 6.1 shows the distribution of this `angular momentum alignment' parameter versus radius for three typical galaxies, a disk galaxy (top left panel), a disk+bulge galaxy (top middle panel) and an elliptical galaxy (top right panel). Each point corresponds to a stellar particle and its colour indicates its formation redshift. There is a clear visual distinction between the stellar disk component (stars with $j_Z/|\vec{j}| \approx 1$), which tends to be younger, and the spheroidal component (uniformly distributed $j_Z/|\vec{j}|$) which consists of older stars. In order to disentangle both components in a robust way, we define the `spheroidal component' with mass S to be twice the mass of counter-rotating stars (with $j_Z/|\vec{j}| < 0$) (Crain et al. 2010). The stellar disk mass, D, is defined as the total mass, T, minus the spheroidal component S. In rare cases where more than half of the stellar mass is counter-rotating we set $S = T, D = 0$.

We use the ratio S/T to quantify the stellar morphology of each galaxy. It varies from low to high (specific values are included in the top panels of Fig. 6.1) ranging from disk galaxies, via disk+bulge galaxies to elliptical galaxies. We specifically denote this as S/T instead of the more common B/T ratio, because there is no distinction based on radius and the spheroidal component includes both the

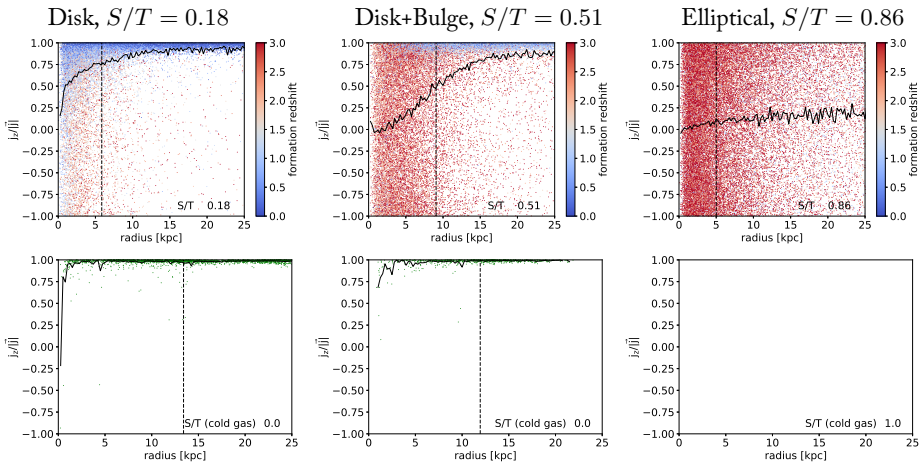

Figure 6.1: The kinematic structure of three typical EAGLE galaxies with different kinematic morphologies ranging from a disk structure (top left panel) to a disk+bulge structure (top middle) and an elliptical structure (top right). All three galaxies (f.l.t.r. GalaxyID 8772511, 8960069, 10645724) are at $z = 0$ and have similar stellar masses, $\log_{10}(T/\mathrm{M}_\odot) = 10.56, 10.60, 10.70$ respectively. Each dot denotes a stellar particle, colour coded by the redshift at which it was formed. The horizontal axis denotes the 3D distance from the centre. The stellar half-mass radius is denoted by the vertical black dashed line. The vertical axis shows the alignment of the angular momentum of a given stellar particle ($\vec{j}$) with the angular momentum direction of the galaxy ($\hat{Z}$), where $\hat{Z}$ denotes the direction of the total angular momentum of all star particles within the stellar half-mass radius. With this definition purely corotating particles have $j_Z/|\vec{j}| = 1$ and purely counterrotating particles have $j_Z/|\vec{j}| = -1$. In this graph, a random distribution of angular momenta would have a constant point density in the vertical direction. We decompose each galaxy into two components, a 'spheroidal' component with mass (S) equal to twice the mass of all particles $j_Z/|\vec{j}| < 0$ and a 'disk component' (D) which comprises the rest of the total stellar mass (T). In this way the kinematic structure of each galaxy is characterised by a single ratio S/T, which is 0.18, 0.51 and 0.86 respectively for these galaxies. The solid black curve in each panel denotes the running average of $j_Z/|\vec{j}|$ as a function of radius. In the top middle panel this goes from 0 at small radii, corresponding to a truly random angular momentum distribution to a value of close to 1 at large radi, corresponding to a pure disk. The bottom panels show the same diagnostics for the star-forming gas particles in the same three galaxies, but using the same direction for $\hat{Z}$ as in the top row. The right galaxy has no star-forming gas.

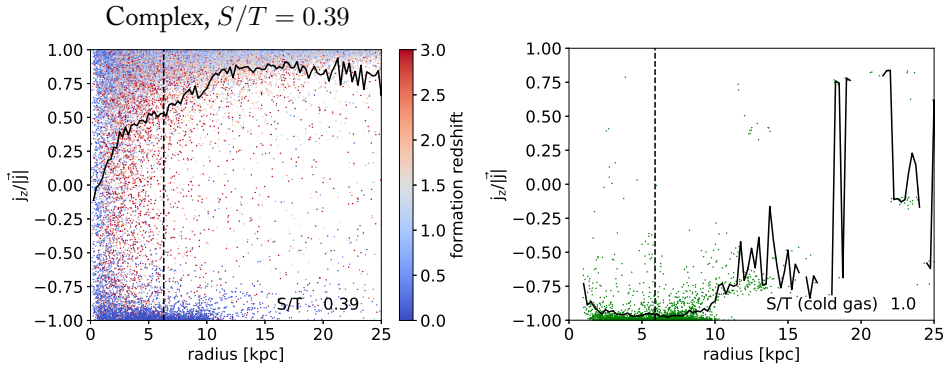

Figure 6.2: The same diagnostics as in Fig. 6.1 for GalaxyID 18281742 at $z = 0$ which has a stellar mass of $\log_{10}(T/\mathrm{M}_\odot) = 10.71$. This galaxy has a more exotic kinematic structure. The right panel shows a star-forming gas disk which is counterrotating with respect to the stars. In the left panel we see a counterrotating young stellar disk together with an extended corotating disk that consists of stars of varying ages and there is a hint of a bulge. The S/T ratio does not discriminate between a classical bulge, a counterrotating disk or a counterrotating bar, but it does capture the kinematic content of the majority of galaxies that are more akin to the ones in Fig. 6.1.

bulge and halo, although in many cases the spheroidal component is more centrally concentrated than the disk component. The difference with the B/T-ratio from Bottrell et al. (2017) lies in the calculation of the $\hat{Z}$ direction. Bottrell et al. (2017) use all stellar particles within ten half-mass radii. We use all stellar particles within one half-mass radius. We do this because the total stellar angular momentum can be dominated by structures at large radii (for example due to recent mergers) which could lead to a misclassification of the direction of rotation of the stellar disk. For a significant fraction of galaxies, the direction of the total stellar angular momentum varies with radius. The results thus depend on the choice of radius. The advantage of our prescription with respect to prescriptions based on kinetic energy (e.g. Sales et al. 2010, 2012; Correa et al. 2017) is that the decomposition into a disk component and a spheroidal component is not sensitive to small variations in this $\hat{Z}$-direction. In fact for a hypothetical galaxy with a pure disk component and a purely random spheroidal component, the S/T ratio will remain the same as long as the $\hat{Z}$-direction points to within 90° of the disk direction, because all disk stars will have a positive $j_Z/|\vec{j}|$ and all spheroid stars will remain uniformly distributed.

Of course a good portion of galaxies have more complicated structures than just a disk and a spheroid. When plotting the total angular momenta (instead of just the $\hat{Z}$-component), they show signs of for example bars or misaligned accre-

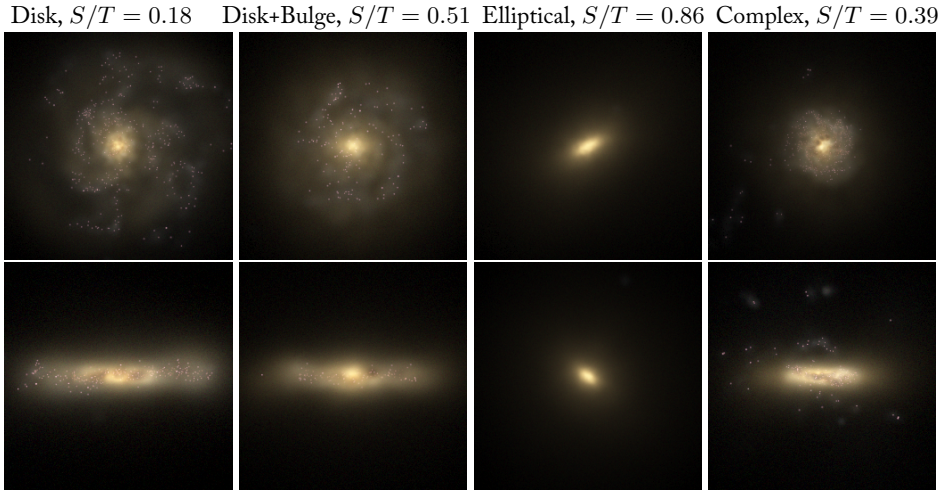

Figure 6.3: Mock gri-images for the four galaxies from Figs. 6.1 and 6.2. The images are 60 by 60 pkpc large. See Trayford et al. (2015) and McAlpine et al. (2016) for details. The top row shows the face-on views for GalaxyID 8772511, 8960069,10645724 and 18281742 respectively. The bottom row shows the corresponding edge-on views. The images for the first three galaxies agree by eye with the morphology that we deduced from the angular momenta of the stellar particles, representing a disk, disk+bulge and an elliptical galaxy respectively. The fourth galaxy would be classied by eye as a simple disk galaxy. Its counterrotating star-forming gas-disk is not apparent in the image.

tion (Sales et al. 2012), but our simple decomposition catches the essence of the major kinematic morphology transformations that occur in the EAGLE simulation. Fig. 6.2 shows an example of a galaxy with a more complicated structure. The left panel shows that the youngest stars form a disk of 20 kpc diameter that is counter-rotating with respect to main disk, which is composed of older stars. The right panel shows that the star forming gas corresponds to this young counter-rotating disk. This galaxy has an S/T ratio of 0.39, where in reality there is almost no hot spheroidal component, but instead two disks. This shows that in some cases the interpretation is not as simple as suggested by Fig. 6.1.

The bottom row of Fig. 6.1 also shows the distribution of the cold star forming gas for our three example galaxies. Typically the angular momenta of star forming gas particles are very well aligned, starting at small radii (as in the left and middle bottom panels) yielding `star forming gas S/T' ratios of ≈ 1. Note that for the gas we still use the same $\hat{Z}$-direction defined by the stars within the half-mass radius. The elliptical galaxy (right bottom panel) has no star forming gas left.

Fig. 6.3 shows mock gri-images for the four galaxies from Figs. 6.1, 6.2. The visual morphology corresponds well with our classification based on the S/T ra-

tio. Keep in mind that our S/T ratio is mass weighted. Disk stars are typically younger than spheroid stars, see Fig. 6.1. A luminosity-weighted S/T ratio for these galaxies would thus be smaller and the visual impression will thus be diskier than suggested by the mass-weighted S/T. We understand that for comparison with observations our definition of S/T is not ideal as it would be hard to extract this ratio from observations, for which less detailed kinematic information is available. A direct comparison with observations is not the purpose of this work though. Our aim is to gain physical insight into the formation of speroid and disk components in the simulation. For this, the S/T ratio, which is based on detailed kinematic information, is well suited.

We do not retrieve pure stellar disks with $S/T \approx 0.0$ (although this ratio is common for the star forming gas), whereas galaxies with very small bulge-to-disk ratios are thought to be fairly common (e.g. Kormendy et al. 2010). At the other end we interpret the elliptical galaxy from Figs. 6.1, 6.3 as having a 14% disk component ($S/T = 0.86$), whereas this galaxy would probably be classified photometrically as a pure elliptical galaxy. However, observations of ETG's that include stellar kinematics (e.g. Emsellem et al. 2011) point towards varying degrees of rotational support for these galaxies. The 14% surplus of stars over a uniform distribution in Fig. 6.1 is concentrated at $j_Z/|\vec{j}| \approx 1$.

In addition to the S/T ratio for the entire galaxy, we will use the S/T ratio for stars within 5 pkpc of the galaxy's centre and for stars outside 5 pkpc. This splits the `spheroidal' component into a `stellar bulge' and a `stellar halo' respectively and the disk component into an `inner disk' and an `outer disk'.

6.4 Morphology evolution

Fig. 6.4 shows the relation between the stellar S/T ratio and stellar mass for central galaxies in the RefL0100N1504 simulation at different redshifts. At all redshifts this relation follows a similar trend. Low-mass galaxies ($T \lesssim 10^{9.5}\mathrm{M}_\odot$) are mostly spheroidal. Around the mass of the Milky Way most galaxies are disky and massive galaxies ($T \gtrsim 10^{11}\mathrm{M}_\odot$) tend to be elliptical. The kinematic morphology of galaxies in EAGLE is primarily a function of stellar mass rather than redshift, although there are minor additional trends with redshift. At low redshifts ($z \lesssim 1$) the mass-morphology relation is a bit less pronounced and there is more scatter towards disky (low S/T) galaxies at low masses.

A convergence test of these results is included in appendix 6.9, Fig. 6.10. In short, these results are well converged in a `weak convergence' sense (Schaye et al. 2015), meaning that the results are consistent at higher resolution when the subgrid model is recalibrated to the present-day galaxy stellar mass function and mass-

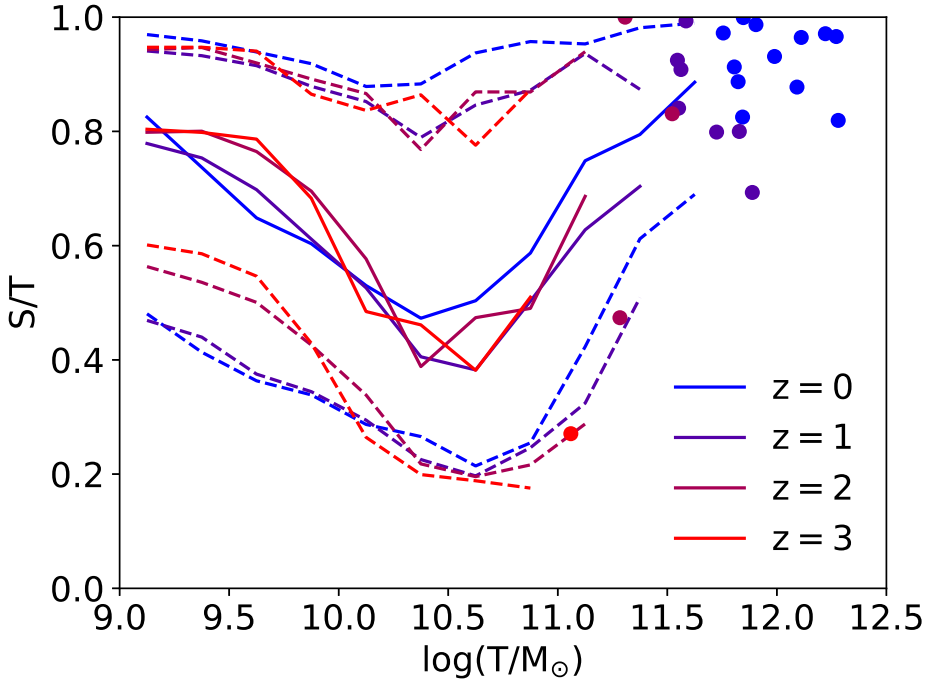

Figure 6.4: The kinematic morphology of central galaxies, specifically the spheroid-to-total stellar mass ratio, as a function of stellar mass for different redshifts (colours). Solid curves denote running medians and dashed curves denote 10%-90% ranges. For mass bins with fewer than 10 galaxies, individual galaxies are shown as coloured dots. Although there are minor differences between the different redshifts, the overall picture is very similar. At low and high masses galaxies are mostly spheroidal (high S/T). In between, at $T \approx 10^{10.5}\mathrm{M}_{\odot}$, galaxies are mostly disky (low S/T). This trend is slightly stronger at high redshift than at low redshift.

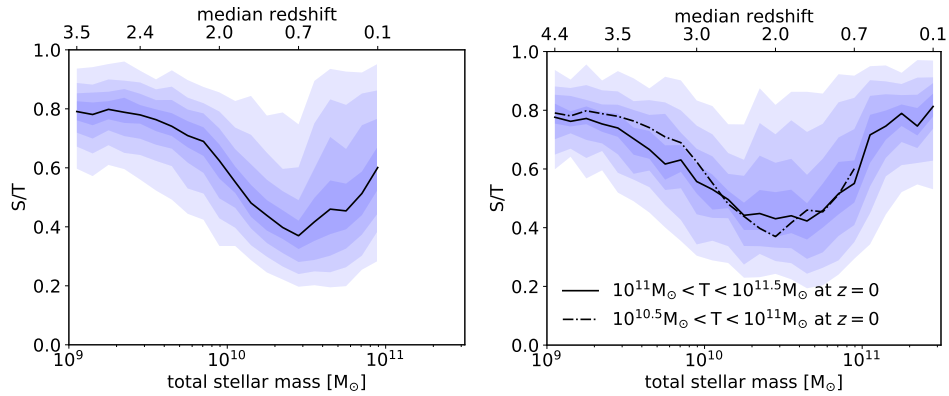

Figure 6.5: The left panel shows the evolution of the stellar kinematics for the main progenitors of central galaxies with a total stellar mass $10.5 < \log_{10}(T/\mathrm{M}_\odot) < 11$ at $z = 0$. The vertical axis denotes the mass ratio of the 'spheroidal' component with respect to the 'total' stellar mass for these progenitors. The horizontal axis denotes the stellar mass of the main progenitors. The median redshift of these progenitors at different masses is indicated by the top horizontal axis. The solid black curve indicates the median of the distribution and the colours represent percentiles in 10% increments. Most of these galaxies share a common kinematic evolution, starting out at high S/T ratios at $T \lessapprox 3 \times 10^9 \mathrm{M}_\odot$, subsequently becoming diskier towards $T \approx 3 \times 10^{10} \mathrm{M}_\odot$, after which the trend reverses and galaxies become increasingly less disky. The right panel shows the same diagnostics for central galaxies selected to have $11 < \log_{10}(T/\mathrm{M}_\odot) < 11.5$ at $z = 0$. The solid curve from the left panel is repeated as a dash-dotted curve for reference. The trend for these galaxies is remarkably similar, although the cosmic timing is very different (compare the top horizontal axes).

size relation. This recalibration is needed to obtain the same effective efficiency of feedback processes at large scales when the transition between sub- and super-grid physics changes.

Instead of considering galaxy morphology for the whole population, we will now focus on the evolution of galaxy morphology along the merger tree, thus following the main progenitors[1] of massive galaxies backwards in time. Ultimately our goal is to understand when and why morphological transformations take place. A question best answered by following the evolution of these galaxies directly.

Fig. 6.5 shows the evolution of the S/T ratio for the main progenitors of galaxies in the $z = 0$ mass range $10.5 < \log_{10}(T/\mathrm{M}_\odot) < 11$ (left panel) and $11 < \log_{10}(T/\mathrm{M}_\odot) < 11.5$ (right panel). The median redshift as a function of

[1]Main progenitors are loosely speaking the most massive progenitors, although in the case of a merger with a mass ratio close to unity, the choice of main progenitor is somewhat arbitrary. We use the prescription of De Lucia and Blaizot (2007) to select the progenitor with the `most massive integrated history', see Qu et al. (2017).

mass is shown using the top axis. Although these galaxies span an order of magnitude in mass at $z = 0$, they follow a very similar trend (compare the black solid and dash dotted curves in the right panel), as expected from the lack of significant evolution found in Fig. 6.4. Galaxies start out with a spheroidal kinematic structure at low masses. In between $10^{9.5}\mathrm{M}_\odot$ and $10^{10.5}\mathrm{M}_\odot$ they build up a prominent disk, resulting in a decrease of the S/T ratio. At $T > 10^{10.5}\mathrm{M}_\odot$ the S/T ratio increases again, indicating a conversion from disky galaxies to spheroidal galaxies.

Perhaps surprisingly, we thus find that that low-mass ($T \lesssim 10^{9.5}\mathrm{M}_\odot$) central galaxies (Fig. 6.4) and the low-mass main progenitors of massive $z = 0$ central galaxies (Fig. 6.5) tend to have a spheroidal (or otherwise non-disky) morphology. One might think that this could be due to the artificial pressure floor which inhibits the formation of cold, thin (i.e. scale height $\ll 1$ kpc) disks. However, we find no direct relation to the galaxy sizes, as would be expected if a puffy gas disk would be the root cause. In fact the median half-mass radius of the main progenitors remains constant over the mass range $10^9\mathrm{M}_\odot < T < 10^{10.3}\mathrm{M}_\odot$ (not shown), whereas the transformation from elliptical to disk galaxies is practically complete over this mass range. Similarly, the overall mass-size relation in EAGLE is very flat at these masses, see Fig. 9 of Schaye et al. (2015). Also, we find that the star forming gas particles tend to have a disky distribution also at small radii (as is the case for the example galaxies in Fig. 6.1 but also for many lower mass galaxies), indicating that the cause for the spheroidal morphology is likely not the pressure-floor induced puffiness of the cool gas disk.

Recently El-Badry et al. (2017) have found similar results for $z = 0$ galaxies in the FIRE-2 simulation. The FIRE-2 simulation has a much higher resolution than EAGLE for low mass galaxies and it includes cooling of the interstellar matter down to 10 K. They found that the HI gas shows much more corotation than the stars for galaxies in the wide stellar mass range $10^{6.3}\mathrm{M}_\odot < T < 10^{11.1}\mathrm{M}_\odot$. They also found that the gas fails to form a disk below $10^8\mathrm{M}_\odot$ and they furthermore found no signs of stellar disks for 15 out of their 17 galaxies with $T < 10^{9.5}\mathrm{M}_\odot$.

Simons et al. (2015) observe a similar transition based on the kinematics determined from nebular emission lines for a morphological blind selection of emission line galaxies at $z < 0.375$. They define $10^{9.5}\mathrm{M}_\odot$ as the `mass of disk formation', because above this mass most galaxies are rotation dominated disks, while below this mass a large fraction of galaxies show no kinematic signs of disk rotation. However, Fisher and Drory (2011) find the opposite trend based on a photometric B/T decomposition of the light profiles of galaxies in the local (11 Mpc) Universe. They find an increasing fraction of bulgeless galaxies with decreasing mass.

El-Badry et al. (2017) argue that the reduced rotational support in their low-mass galaxies is due to stellar feedback driving non-circular motions in the gas, in

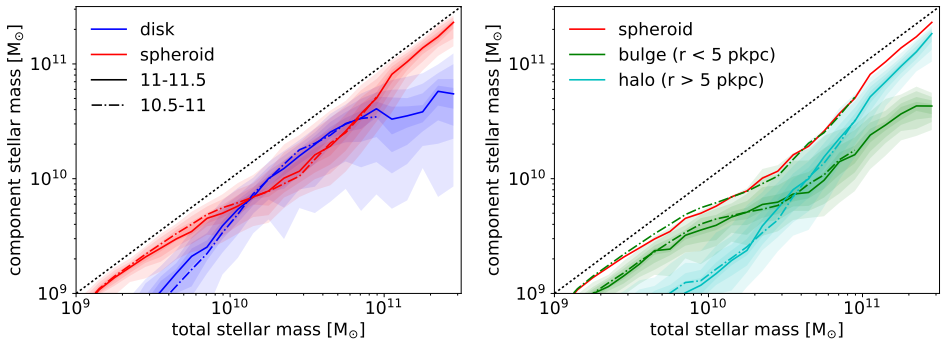

Figure 6.6: The left panel shows the evolution of the 'disk' mass component (blue) and the 'spheriodal' mass component (red) for the main progenitors of central galaxies. Solid and dash-dotted curves represent the same $z = 0$ mass ranges as in the right panel of Fig. 6.5. The curves show running medians. We have indicated percentile ranges in 10% shade increments only for the solid curve selection, but the ranges for the dash-dotted selection are very similar. The sum of the 'disk' and 'spheroid' components by definition equals the total mass (dotted black line). The two selections give very similar results. Galaxies start out witha spheroidal morphology, but the disk component grows fast, overtaking the spheroidal component just above $10^{10}\mathrm{M}_{\odot}$. At large mass scales the spheroidal component catches up and it dominates at $10^{11.5}\mathrm{M}_{\odot}$. The right panel splits the 'spheroid' component (repeated in red) into two radial bins. We define the stellar bulge (in green) as the hot component within 5 pkpc of the galaxy centre and we define the stellar halo (in cyan) as the hot component outside 5 pkcp. This distinction demonstrates that the rise in the hot component at large masses is mostly due to the growth of a hot stellar halo at large radii. However, the bulge component keeps increasing over the whole mass range.

combination with heating by the UV background which supresses the acretion of high angular momentum gas.

We found that the fraction of low-mass galaxies that have a disky morphology decreases somewhat with redshift (see Fig. 6.4). At high redshifts we expect effects from the possibly more violent, disorganised growth of galaxies which we discussed in the introduction: the collapse of primordial gas clouds (Eggen et al. 1962), clump migration in violently unstable disks (e.g. Noguchi 1999; Bournaud et al. 2007; Elmegreen et al. 2009; Perez et al. 2013), strong gas flows to the centre in marginally unstable disks (e.g. Krumholz et al. 2017) and misaligned accretion (e.g. Sales et al. 2012; Aumer et al. 2013). Moreover, the merger rates are much higher at these redshifts (e.g. Genel et al. 2009; Qu et al. 2017).

Fig. 6.6 (left panel) shows the evolution of the masses of the disk and spheroid components of the main progenitors. We see that during the period of rapid disk growth ($10^{9.5}\mathrm{M}_{\odot} \lesssim T \lesssim 10^{10.5}\mathrm{M}_{\odot}$), the spheroidal component does grow in mass, albeit at a reduced rate. At the high-mass end the growth of the disk com-

ponent flattens out, but the average disk mass still increases slightly. Although on average we do not see a destruction of disk mass, there will certainly be individual massive galaxies for which this is the case. For massive ($\approx 10^{11.5}\mathrm{M}_{\odot}$) galaxies the spheroidal component clearly dominates, with the 10^{th} percentile of the spheroidal component being more massive than the 90^{th} percentile of the disk component. The relative scatter in disk masses is larger than the relative scatter in the spheroid masses.

In the right panel of Fig. 6.6 we split the spheroidal component into a bulge and halo, i.e. inside and outside 5 pkpc respectively. This shows that the low-mass progenitors are dominated by a bulge, while bulge growth slows down considerably at $T \approx 10^{9.75}\mathrm{M}_{\odot}$ and makes place for a fast growth of the halo component at $T \gtrsim 10^{10.3}\mathrm{M}_{\odot}$. However, the mean bulge mass continues to grow during the period of rapid disk growth and subsequent halo growth. Roughly 24% of the bulge mass of a $10^{10.5}\mathrm{M}_{\odot}$ galaxy was on average in place at $10^{9.5}\mathrm{M}_{\odot}$, before the epoch of rapid disk growth. At $10^{11}\mathrm{M}_{\odot}$ this percentage has dropped to 7%, although a good portion of the bulge growth above $10^{10.5}\mathrm{M}_{\odot}$ takes place in galaxies with extensive halos, for which the bulge may not be perceived as a separate component. This is certainly the case for the ellipticals at the massive end.

6.5 The origin of bulge stars

The stars that make up a present-day galaxy have either been formed in its main progenitor (in-situ) or have been formed in another progenitor (ex-situ) and have subsequently been accreted during a merger. Disk stars are expected to have mainly formed in-situ. For the bulge and the halo components it is less obvious where their stars formed. These components could be the result of:

1. various secular processes in the absence of mergers (in-situ),
2. the disruption of stellar disks by mergers (in-situ)
3. merger induced gas flows and subsequent star formation (in-situ),
4. accretion of stars during mergers (ex-situ).

In this section we aim to estimate the contribution of process (iv) in the EAGLE simulation: direct bulge/halo formation from accreted stars. In section 6.7 we will focus on the total merger contribution to bulge/halo formation, processes (ii), (iii) and (iv). Any remaining non-merger related bulge/halo formation will be attributed by definition to process (i) which includes the potential disruption of stellar disks by non-merger induced mechanisms as well as the non-merger induced direct formation of stars in a spheroidal component.

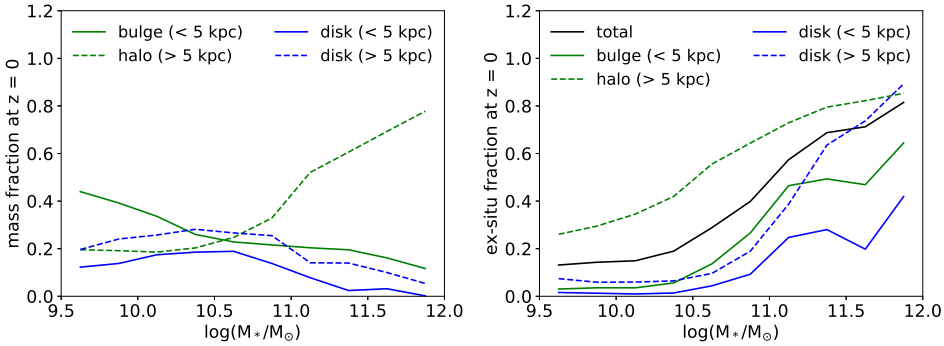

Figure 6.7: The left panel shows the median stellar mass fractions of four kinematic stellar components of central galaxies at $z = 0$. The spheroidal component is split into a bulge' (solid green curve) and a 'halo' (dashed green curve) as in the right panel of Fig. 6.6. The disk is similarly split at a radius of 5 kpc, giving an 'inner disk' component (solid blue curve) and an 'outer disk' component (dashed blue curve). Note that the horizontal axes in Figs. 6.5 and 6.6 corresponded to the mass of the main progenitors, which corresponded to high redshifts for low masses, whereas in this figure the horizontal axis corresponds to $z = 0$ only. The picture is however qualitatively similar. At low masses the bulge dominates, at high masses the halo dominates and in between the disk has its largest contribution. The right panel shows, for each component separately, the median mass fraction of stars belonging to that component that has been accreted (rather than formed in-situ). The black solid curve gives the median ex-situ mass fraction for the total galaxy. For $T \lesssim 10^{10.5}\mathrm{M}_\odot$ the disk, as well as the bulge, are almost entirely made up of in-situ formed stars, whereas the halo has a large contribution from ex-situ formed stars. At larger masses also the bulge and disk components contain more ex-situ formed stars.

The left panel of fig. 6.7 shows the makeup of $z = 0$ galaxies as a function of mass in terms of bulge, halo and disk components. The disk components are most prominent around and below the knee of the galaxy stellar mass function, $T \lesssim 10^{10.75}\mathrm{M}_{\odot}$ (where most of the stellar mass in the universe resides). At higher masses the halo component dominates while at $T \lesssim 10^{10}\mathrm{M}_{\odot}$ the bulge component dominates the mass budget. This is all in qualitative agreement with the trend we saw for the main progenitors at high redshift in Fig. 6.6.

We now aim to calculate the fraction of stars for all of those morphological components that have an ex-situ origin. Remember that our decomposition into a hot/disk component is statistical in the sense that stellar particles with $j_Z/|\vec{j}| > 0$ are not uniquely assigned to be in either component. It is therefore not possible to trace the provenance of the stars in each component directly. We can, however, circumvent this problem by first doing an S/T decomposition for the in-situ and ex-situ formed stars separately (both inside and outside 5 pkpc). We then obtain masses for eight components (combinations of in-situ/ex-situ, spheroid/disk, inside/outside 5 kpc) from which we can calculate the ex-situ fractions. The right panel of Fig. 6.7 shows the medians of these mass fractions for all central $z = 0$ galaxies.

For $T \lesssim 10^{10.5} M_{\odot}$ the contribution from ex-situ formed stars to the bulge is very small ($\lesssim$ 10%) (as it is for the disk). This means that these bulges were not formed directly from stars that were accreted during mergers, process (iv). The halo does have a prominent contribution from ex-situ stars, even for low-mass systems. At the massive end ($T \gtrsim 10^{11} M_{\odot}$) where the overall ex-situ content of galaxies rises (solid black curve), all components contain a larger fraction of ex-situ formed stars. For the disk components we should not overinterpret this finding though, because these are ex-situ fractions for components that themselves constitute only a minor fraction of the total stellar mass budget of these massive galaxies, as is evident from the left panel of Fig. 6.7.

6.6 The effects of star formation and mergers on morphology

In the previous section we investigated the importance of the direct formation of bulges and halos from stars accreted during mergers. This does not include the indirect effect that mergers might have in triggering morphological changes. In this section we first investigate the effect of mergers and in-situ star formation on the overall kinematic morphology S/T, before isolating the effect on the buildup of the individual morphological components in section 6.7.

We investigate the changes in kinematic morphology between consecutive snap-

shots along the merger tree and relate those to the merger activity and in-situ star formation. We use all main progenitors of central galaxies in the mass range $10^{10.5}\mathrm{M}_\odot < T < 10^{12}\mathrm{M}_\odot$ at $z = 0$. The time resolution of this analysis is roughly 0.7 Gyr, although the time between consecutive snapshots is not completely constant. This is a convenient time step, because it is small compared to the ages of the galaxies, but long enough to capture the main effect of a merger on the morphology of a galaxy (except for cases where the merger happens close to the snapshot time). In principle we use all snapshots, although at very high redshifts few main progenitors will be in the mass range under consideration.

Fig. 6.8 shows how the rates of kinematic morphology changes, $\Delta(S/T)/\Delta t$, relate to the stellar mass growth rates of galaxies (top row), to the mass growth rates through in-situ star formation ($\Delta M_{\mathrm{insitu}}/(T\Delta t)$ middle row) and to the mass growth rate through accretion of ex-situ formed stars ($\Delta M_{\mathrm{exsitu}}/(T\Delta t)$) which we use as a proxy for merger activity (bottom row). For each time step we define $\Delta M_{\mathrm{exsitu}}/T$ as the fraction of stellar mass at the later snapshot that has been accreted after the earlier snapshot. We normalise this by the time difference, Δt, between the two snapshots to obtain a rate per Gyr. In this calculation, the mass of the star particles, which is not constant due to stellar mass loss, is evaluated at the later snapshot (both for ΔM and for T). The in-situ mass fraction is calculated in a similar way. It includes all stars that have been formed since the earlier snapshot, thus also the stars that formed during a merger[2]. We have split the sample into mass bins (columns) that represent the main progenitor stellar mass at the earliest of the two consecutive snapshots. This gives a much clearer picture than splitting by redshift (not shown).

Below $10^{10.5}\mathrm{M}_\odot$ galaxies tend to become more disky when they experience fast mass growth (downward trend in the first two panels of the top row), which is consistent with Fig. 6.5. This push towards a disky kinematic structure is clearly caused by the in-situ star formation, as is evident from the strong downward trend in the first two panels of the middle row of Fig. 6.8, although mergers try to push the galaxies in the opposite direction towards a spheroidal kinematic structure (mostly the second panel of the bottom row).

Above $10^{10.5}\mathrm{M}_\odot$ the trend is reversed. Galaxies tend to become more spheroidal as they grow in mass (upward trend in the last two panels of the top row). The trend weakens at the highest masses because these galaxies are already mostly spheroidal. This transformation is driven by merger activity (upward trend in the last two panels of the bottom row) with a negligible contribution to the morphology changes by

[2]Technically it also includes stars that formed in a merger companion after the earlier snapshot and just before accretion. These should ideally be classified as ex-situ stars. This happens due to the finite time resolution but constitutes an insignificant fraction of the total $\Delta M_{\mathrm{insitu}}$ budget.

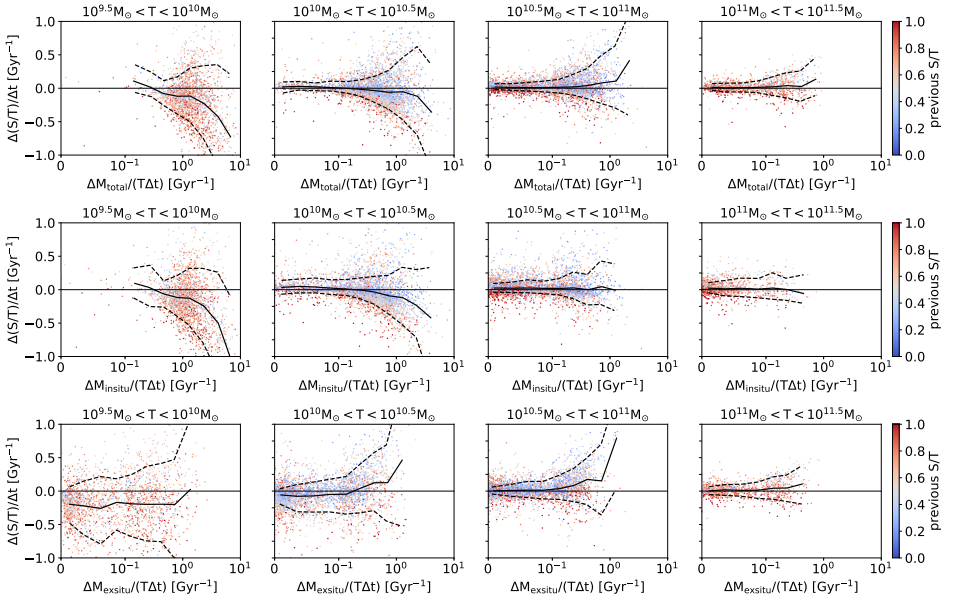

Figure 6.8: The change in kinematic structure between consecutive snapshots, denoted by the change in the S/T ratio per Gyr, as a function of respectively the relative stellar mass growth per Gyr (top row), the mass growth through in-situ star formation (middle row) and the mass growth through accretion of stars (bottom row). Each column corresponds to a different main progenitor mass range (evaluated at the earliest snapshot) as indicated above each panel. This figure contains all main progenitors of central galaxies at $z = 0$ in the mass range $10^{10.5}\mathrm{M}_\odot < T < 10^{12}\mathrm{M}_\odot$. Each main progenitor appears multiple times over multiple panels (once for each snapshot for which it falls in the assigned mass range). The galaxies are colour-coded by the S/T ratio at the earliest snapshot. In each panel the running average is denoted by a solid curve and the 10%-90% range by dashed curves. The horizontal axis is linear below 10^{-1} and logarithmic above that. The top row shows that in the mass range $10^{9.5}\mathrm{M}_\odot \lesssim T \lesssim 10^{10.5}\mathrm{M}_\odot$ mass growth leads on average to a more disky kinematic structure (decreasing S/T), while in the range $10^{10.5}\mathrm{M}_\odot \lesssim T \lesssim 10^{11.5}\mathrm{M}_\odot$ mass growth leads to a more spheroidal kinematic structure (increasing S/T). The middle row shows that the strong trend for growing galaxies to become more disky below $\approx 10^{10.5}\mathrm{M}_\odot$ is a direct result of the in-situ star formation activity. The bottom row shows that merger activity on average leads to a more spheroidal kinematic structure.

in-situ star formation (negligible trend in the last two panels of the middle row). The lack of a pronounced trend with the in-situ mass growth above $10^{10.5}\mathrm{M}_{\odot}$ could be due in part to the fact that the relative growth rate through in-situ star formation at these masses does not reach the high values that are responsible for most of the trend at lower masses. The importance of in-situ and ex-situ growth for morphology change thus shows a strong dependence on the mass of the main progenitor[3].

The reason that morphological changes can be decomposed into changes induced by mergers and by in-situ star formation, is that the in-situ and ex-situ mass growth of galaxies is mostly unrelated. They are positively correlated, meaning that galaxies of a given mass with a higher merger activity tend to have a higher in-situ star formation rate, but this is a small effect. The Spearman R^2 coefficient between $\Delta(M_{\mathrm{insitu}}/(T\Delta t))$ and $\Delta(M_{\mathrm{exsitu}}/(T\Delta t)$ varies from 0.13 to 0.17 for the different 0.5 dex wide mass bins, which means, loosely speaking, that they are for 85% unaware of each other's existence and peak at different (≈ 0.7 Gyr) time steps. This is in qualitative agreement with observations from CANDELS at $z \approx 2$ which indicate that only 3% of the star formation budget in $T > 10^{10}\mathrm{M}_{\odot}$ galaxies is triggered by major mergers (Lofthouse et al. 2017) and with observations from GAMA that only show enhanced star formation in primary merger galaxies for short duration (< 0.1 Gyr) star formation indicators and find a reduced star formation rate in secondary galaxies (Davies et al. 2015).

We show a figure analogous to Fig. 6.8 in Appendix 6.10 (Fig. 6.11), but for S/T changes within 5 pkpc, thus relating to bulge formation. The trends are the same as for Fig. 6.8. Below $10^{10.5}\mathrm{M}_{\odot}$ in-situ star formation builds up a central disk, above this mass mergers dominate and push the central region towards a bulge structure.

6.7 The merger contribution to spheroid and disk formation rates

In this section we look at the total effect that mergers have on spheroid formation. Fig. 6.9 (top row) shows the dependence of the spheroid growth rate, $\Delta S/(T\Delta t)$, on merger activity[4], $\Delta M_{\mathrm{exsitu}}/(T\Delta t)$. This measure for merger activity includes

[3]The same probably holds for central galaxies that are not main progenitors of $z = 0$ galaxies. We have specifically investigated main progenitors, because we are interested in long-lasting changes in morphology that are not wiped out by the disappearance of galaxies during mergers.

[4]In the calculation of $\Delta S/T$, we take for T the average T of both snapshots. This is done because in rare cases during a merger T can be artificially low, due to a misidentification of which stellar particle belongs to which subhalo. If T is very small, $\Delta S/T$ blows up. Furthermore we reject time

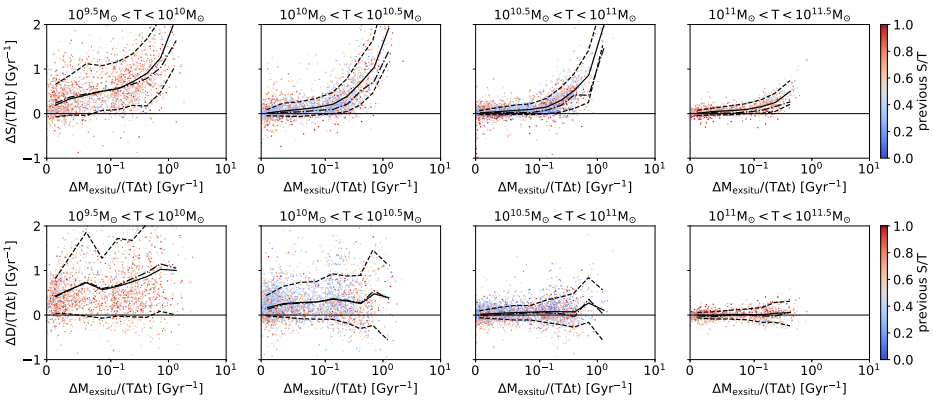

Figure 6.9: The dependence of spheroid growth (top row) and disk growth (bottom row) on merger activity. The top row is the same as the bottom row of Fig. 6.8, but now the vertical axis denotes $\Delta S/(T\Delta t)$ instead of $\Delta(S/T)/\Delta t$. This isolates the growth rate of the spheroid component instead of the morphological change rate. Note that the horizontal axes are linear up to 0.1 and logarithmic beyond that. The solid curves denote running averages, dashed curves denote the 10%-90% range and the dash-dotted curves denote the running averages for the bulge growth rate $(\Delta S/T)_{<5\mathrm{kpc}}/\Delta t$ (the underlying distribution inside 5 kpc is not shown, but is very similar). In all top panels the relative growth rate of the spheroid depends strongly on merger activity. Time steps with little to no accretion of stars, on average show little to no growth of the spheroid (solid curve) or the bulge (dash-dotted curve). The bottom row shows the same diagnostics, but then for the growth rate of the disk (solid curves denote the running averages of the underlying distribution, dashed curves denote the 10%-90% range and the dash-dotted curves denote the running averages for the disk within 5 kpc). Disk growth shows a small dependency on merger activity. The curves are rising in the left part of the panels, where the accreted stellar mass rates are very small. It could well be that these 'tiny' mergers trace the smooth accretion of gas. On average we do not see evidence for the destruction of disks by mergers (the solid and dash-dotted curves in the bottom panels are not declining towards the right).

mergers of all resolved mass ratios. For all mass ranges (columns) the average growth rate of the spheroid (solid black curve) increases strongly with merger activity and approaches zero during periods of low merger activity. This means that most of the spheroid formation is triggered by mergers.

We use the total ex-situ mass accretion rate as our proxy for merger activity instead of the more commonly used merger ratio and classification into minor and major mergers, because we expect the growth rate of the spheroid to not only depend on the merger ratio of the most prominent merger, but also on the number of mergers that occur during a ≈ 0.7 Gyr time step. Nevertheless, the horizontal axis in Fig. 6.9 can be roughly translated into a merger ratio. $\Delta M_{\rm exsitu}/(T\Delta t) \approx 0.1$ Gyr^{-1} is equivalent to a single merger with a mass ratio 1:13 within 0.7 Gyr. Similarly a rate of 0.3 Gyr^{-1} corresponds to a single merger with a mass ratio 1:3.7 within 0.7 Gyr. The contribution at $\Delta M_{\rm exsitu}/(T\Delta t) > 0.3$ Gyr^{-1} can thus roughly be attributed to major mergers. The contribution at 0.1 Gyr$^{-1} < \Delta M_{\rm exsitu}/(T\Delta t) < 0.3$ Gyr^{-1} can roughly be attributed to minor mergers and the contribution at $\Delta M_{\rm exsitu}/(T\Delta t) < 0.1$ Gyr^{-1} can be attributed to `tiny' mergers, which in some works is referred to as the `smooth accretion' of stars. The average spheroid growth rates (solid curves in the top row) mostly rise in response to stellar accretion rates in the `minor and major' merger regime, especially above 10^{10}M$_\odot$. The same is true for the bulge growth rates (dash-dotted curves in the top row).

From the trends in the top row of Fig. 6.9 we can estimate the percentages of the spheroid- and bulge formation rates that are associated with mergers. This represents the combined effect of items (ii), (iii) and (iv) from section 6.5. First we estimate the secular contribution to spheroid formation, item (i) from section 6.5, by dividing the spheroid growth rate in the absence of mergers by the average growth rate: $\langle \Delta S/(T\Delta t)\rangle_{\Delta M_{\rm exsitu}/(T\Delta t)<0.025\ {\rm Gyr}^{-1}}/\langle \Delta S/(T\Delta t)\rangle$. The denominator of this fraction is given by the 2$^{\rm nd}$ column of Table 6.1 and the numerator is given by the left-most points of the solid curves in the top row of Fig. 6.9. The merger contribution to spheroid formation is then simply defined as 1 minus the secular contribution and is listed in the 3$^{\rm rd}$ column of Table 6.1. This merger contribution includes growth due to ex-situ formed (i.e. accreted) stars, stars formed in-situ during merger events and stars displaced from the disk to the spheroid component. It includes `tiny' mergers with very small mass ratios. We also estimate the approximate contribution of `minor plus major' and `major' mergers (3$^{\rm rd}$ column, in parentheses). For these estimates we use a cut at $\Delta M_{\rm exsitu}/(T\Delta t) < 0.1$ Gyr^{-1} and $\Delta M_{\rm exsitu}/(T\Delta t) < 0.3$ Gyr^{-1} respectively in

steps for which T drops by more than two-thirds. This only alters the percentages in Table 6.1 by at most 2%.

Table 6.1: The estimated contribution of mergers (of any mass ratio) to the rate of spheroid formation (3rd column) and bulge formation (5th column) in different main progenitor mass bins (1st column). We include a mass bin 0.5 dex smaller than in Figs. 6.8 and 6.9. The 2nd column gives the average rate of relative spheroid mass growth in the different mass bins. See the main text for an explanation of how we use this, together with the solid curves in the top row of Fig. 6.9, to estimate the total merger contribution to spheroid formation (3rd column) and the approximate contribution of 'minor + major' and 'major' mergers (3rd column, in parentheses). The 4th and 5th columns repeat the same procedure for the bulge (i.e. the spheroid inside 5 kpc; corresponding to the dash-dotted curves in the top row of Fig. 6.9). Overall we see that the merger contributions to spheroid and bulge growth are very large, especially above $10^{10}\mathrm{M}_{\odot}$. Major, minor and tiny mergers all contribute to a similar degree.

$\log_{10}(T/\mathrm{M}_{\odot})$	$\langle \Delta S/(T\Delta t)\rangle$	merger contribution to spheroid formation rate	$\langle \Delta S/(T\Delta t)\rangle_{<5\mathrm{kpc}}$	merger contribution to bulge formation rate
	Gyr^{-1}	all (minor+major, major)	Gyr^{-1}	all (minor+major, major)
9-9.5	1.39	>51% (∼39%, ∼25%)	1.43	>47% (∼33%, ∼19%)
9.5-10	0.57	>67% (∼46%, ∼28%)	0.55	>57% (∼36%, ∼21%)
10-10.5	0.16	>91% (∼76%, ∼46%)	0.10	>95% (∼82%, ∼55%)
10.5-11	0.08	>82% (∼65%, ∼33%)	0.05	>82% (∼74%, ∼41%)
11-11.5	0.08	>92% (∼64%, ∼21%)	0.04	>76% (∼64%, ∼20%)

the numerator. The listed merger contributions are rough estimates. On the one hand they could be biased low, because in cases where the merger happens close to the snapshot time, the merger-triggered growth might be spread out over three consecutive snapshots, in which case we would miss part of it. On the other hand the estimates for the contributions of `minor+major' and `major' mergers could be biased high if multiple mergers occur between consecutive snapshots. We use the same procedure in an aperture of 5 pkpc to estimate the merger contribution to bulge formation (using the 4th column of Table 6.1 and the dash-dotted curves in Fig. 6.9, resulting in the percentages listed in the 5th column of Table 6.1).

The lower limits on the merger contribution to bulge and spheroid (i.e. bulge+halo) formation are quite similar. Above $10^{10}\mathrm{M}_{\odot}$, $\gtrsim 80\%$ of the bulge- or spheroid formation rate is associated with mergers (of any mass ratio). Major mergers contribute $\sim 20\% - 55\%$, minor mergers $25\% - 45\%$ and `tiny' mergers $5\% - 30\%$. Below $10^{10}\mathrm{M}_{\odot}$ the total merger contribution drops, but it is still in the 50% range. Comparing this to the fraction of bulge stars that have an ex-situ origin (right panel of Fig. 6.7), we find that a large part of the bulge forms from either (iii) messy, merger induced episodes of central star formation or from (ii) the disruption of stellar disks by mergers. We thus see that mergers, although not responsible for the direct supply of bulge stars, do trigger the formation of bulges and dominate the transition to elliptical morphologies at high masses in the EAGLE simulation.

Table 6.2: The estimated contribution of mergers (of any mass ratio) to the rate of disk formation (3rd column) and inner disk formation within 5 kpc (5th column) in different main progenitor mass bins (1st column). The diagnostics are the same as for Table 6.1, but for the disk component, D, instead of the spheroidal component, S (thus using the bottom row of Fig. 6.8). For the three mass bins with negligible disk growth/destruction no merger contribution percentage is given. During the main period of disk growth ($10^{9.5}\mathrm{M}_\odot \gtrsim T \gtrsim 10^{10.5}\mathrm{M}_\odot$) the disk grows mostly independently from merger activity, but on average mergers (mostly tiny mergers) do have a slight positive effect on the disk growth rate. For $T \lesssim 10^{9.5}\mathrm{M}_\odot$ the disk grows preferentially during mergers. The same is true for $T \gtrsim 10^{10.5}\mathrm{M}_\odot$, although in this case there is almost no disk growth. The inner disk behaves similarly to the total disk. The main difference is the slight destruction on average of the inner disk for $T \gtrsim 10^{11}\mathrm{M}_\odot$

$\log_{10}(T/\mathrm{M}_\odot)$	$\langle \Delta D/(T\Delta t)\rangle$	merger contribution to disk formation rate	$\langle \Delta D/(T\Delta t)\rangle_{<5\mathrm{kpc}}$	merger contribution to inner disk formation rate
	Gyr^{-1}	all (minor+major, major)	Gyr^{-1}	all (minor+major, major)
9-9.5	0.66	>65% (∼43%, ∼22%)	0.68	>69% (∼46%, ∼25%)
9.5-10	0.66	>35% (∼18%, ∼11%)	0.69	>41% (∼22%, ∼12%)
10-10.5	0.24	>30% (∼15%, ∼5%)	0.23	>42% (∼22%, ∼6%)
10.5-11	0.04	>53% (∼29%, ∼10%)	0.008	-
11-11.5	0.005	-	-0.02	-

The bottom row of Fig. 6.9 shows the effect that mergers have on the disk formation rate. Overall the trend is upward, but small, indicating that disk formation is on average slightly enhanced during periods of merger activity. The bottom-left panel shows the largest upward trend, hinting that in the lower mass range (corresponding to higher redshifts) the rate of disk formation is enhanced during periods of merger activity. Table 6.2 gives the merger contributions to the disk formation rate (calculated in the same way as the merger contributions to spheroid formation). We see that for $10^9\mathrm{M}_\odot < T < 10^{9.5}\mathrm{M}_\odot$ (which does not have a panel in Fig. 6.9) the disk growth rate rises strongly during merger activity (as does the spheroid growth rate from Table 6.1, which is much larger in this mass bin). This indicates that galaxy growth in this main progenitor mass range does not occur in an orderly fashion, but is a rather messy affair. Roughly half of the mass growth is associated with mergers and most of it ends up in the spheroidal component. Note that in our definition of S, the spheroid is not necessarily a smooth elliptical structure, but can also be a more complex clumpy structure, as long as it does not have a very well-defined sense of rotation.

In the mass range $10^{9.5}\mathrm{M}_\odot < T < 10^{10.5}\mathrm{M}_\odot$, the mass range in which disks come to dominate (see Figs. 6.5 and 6.6), the disks grows in a more orderly fashion, mostly independently from mergers. From the 3th and 5th columns of Table 6.1 we see that $\gtrsim 35\%$ of the disk growth in this mass range can be attributed to mergers,

of which half is due to `tiny' mergers or the associated smooth accretion of gas.

For $T > 10^{10.5}\mathrm{M}_{\odot}$ the disk formation rate drops dramatically (see the 2$^{\mathrm{nd}}$ and 4$^{\mathrm{th}}$ column of Table 6.2). The sporadic disk formation occurs on large radii and becomes more correlated with merger activity. Perhaps surprisingly, the average effect of mergers on disk growth is positive, indicating that on average mergers do not result in the net destruction of stellar disks. In fact, if we look at the right parts of the solid curves in the bottom row of Fig. 6.9, major mergers on average do not result in negative values of ΔD in any mass bin. For $T > 10^{11}\mathrm{M}_{\odot}$ the inner disks are on average slightly destroyed, but this does not seem to be connected to merger activity. The morphological transformation of massive galaxies in EAGLE is thus more driven by the buildup of spheroids than by the destruction of disks.

The strong trend of morphology with mass at the massive end, which is present in the overall galaxy population at $z \lesssim 2$ (Fig. 6.4) and in the evolution of the progenitors of today's massive galaxies (Fig. 6.5), is thus caused by the strong reduction of in-situ star formation rates around the knee of the galaxy stellar mass function (i.e. $T \approx 10^{10.7}\mathrm{M}_{\odot}$). In the absence of significant in-situ star formation, galaxies mainly grow through mergers, causing a transformation towards elliptical morphologies. This morphological transformation is thus a direct result of the quenching of star formation in massive galaxies. Bower et al. (2017) find that in EAGLE the strong quenching around the knee of the galaxy stellar mass function is caused by feedback from the central black hole. For $T \lesssim 10^{10.5}\mathrm{M}_{\odot}$ stellar feedback causes bouyant outflows of hot gas. However, for $T \gtrsim 10^{10.5}\mathrm{M}_{\odot}$ the hydrostatic gas corona becomes so hot that the gas heated by stellar feedback is no longer buoyant. The subsequent buildup of gas in the centre triggers rapid growth of the central black hole, which eventually, disrupts the supply of cold gas and quenches the star formation. Any other quenching mechanism that kicks in at these masses (as is required by the observed galaxy stellar mass function) would presumably have a similar effect on galaxy morphologies, when combined with the effect of mergers, unless the quenching mechanism itself has a strong direct effect on stellar orbits.

6.8 Conclusions

We have investigated the kinematic morphological evolution of the stellar component of central galaxies in the EAGLE cosmological simulation. We use a simple prescription based on the angular momenta of the stellar particles to separate each galaxy into a `spheroidal' and a `disk' component (see Figs. 6.1 and 6.3), where the mass of the former is taken to be twice the mass of counterrotating stars. The morphology of each galaxy is characterised by the ratio of the mass in

the `spheroidal' component ($S$) and the total stellar mass ($T \equiv M_*$). Note that this mass-weighted $S/T$ ratio is generally higher than a luminosity-weighted ratio (which corresponds to the visual appearance), since stars in the `disk' component tend to be younger than stars in the `spheroidal' component. We separate the `spheroidal' component into a `stellar bulge' (within 5 pkpc) and a `stellar halo' (outside 5 pkpc). We study the evolution of these components for the overall population of central galaxies with $M_* > 10^9 \mathrm{M}_\odot$ and we follow the evolution along the merger tree, for the main progenitors of central galaxies in the $z = 0$ mass range $10^{10.5}\mathrm{M}_\odot < M_* < 10^{12}\mathrm{M}_\odot$. We draw the following conclusions:

- The kinematic morphologies of central galaxies depend strongly on stellar mass, with little additional dependence on redshift (Fig. 6.4). This mass dependence is the same for the main progenitors of $z = 0$ central galaxies (Fig. 6.5). These galaxies follow a similar kinematic evolution, quite independently from their $z = 0$ descendant mass. Galaxies tend to start out with a high S/T ratio at $M_* \lesssim 10^{9.5}\mathrm{M}_\odot$, build up a stellar disk an display a decreasing S/T ratio towards $M_* \approx 10^{10.5} M_\odot$, after which the S/T ratio starts to rise again. The redshift at which galaxies go through these phases depends strongly on their $z = 0$ mass.

- Throughout the whole evolution, the average stellar bulge component keeps growing in mass. Approximately a quarter of the bulge mass of a $10^{10.5}\mathrm{M}_\odot$ galaxy was in place at $M_* = 10^{9.5}\mathrm{M}_\odot$, before the epoch of rapid disk growth (Fig. 6.6).

- The mass growth at high masses ($M_* \gtrsim 10^{10.5}\mathrm{M}_\odot$) is dominated by the growth of the stellar halo (Fig. 6.6).

- The stellar bulges of $z = 0$ galaxies with mass $M_* \lesssim 10^{10.5}\mathrm{M}_\odot$ consist almost entirely of stars that were formed in-situ. The stellar halo, on the other hand, has a large contribution from stars that were accreted during mergers (Fig. 6.7).

- Morphological changes are mainly caused by in-situ star formation for galaxies in the mass range $10^{9.5}\mathrm{M}_\odot \lesssim M_* \lesssim 10^{10.5}\mathrm{M}_\odot$ (at the time of star formation) and are mainly associated with merger activity for $M_* \gtrsim 10^{10.5}\mathrm{M}_\odot$ (Fig. 6.8).

- For $M_* > 10^{10}\mathrm{M}_\odot$ mergers (including all mass ratios) contribute $\gtrsim 80\%$ to the formation rate of bulges (Table 6.1, top row of Fig. 6.9). This percentage represents the combined effect of the accretion of stars formed ex-situ, the disruption of stellar disks and merger-triggered star formation in a

spheroidal component. We estimate that $20\% - 55\%$ is due to major mergers, $25\% - 45\%$ is due to minor mergers and $5\% - 15\%$ is due to `tiny' mergers with very small merger ratios. The merger contribution to bulge formation, especially the contribution from major mergers, is largest in the $10^{10}\mathrm{M}_{\odot} < M_{*} < 10^{10.5}\mathrm{M}_{\odot}$ mass bin and becomes a bit smaller towards higher masses.

- For $M_{*} > 10^{10}\mathrm{M}_{\odot}$ mergers of all mass ratios contribute $\gtrsim 80\%$ to the formation of spheroids (i.e. bulges+halos), of which $20\% - 50\%$ is due to major mergers, $30\% - 45\%$ due to minor mergers and $15\% - 30\%$ due to 'tiny' mergers (Table 6.1, top row of Fig. 6.9).

- Most of the mass of the disk component is formed independently from mergers, but mergers do have a slight net positive effect on the disk growth rate (Table 6.2, bottom row of Fig. 6.9). On average mergers thus do not destroy disks. The morphological transformation of massive galaxies is mainly due to the formation of spheroids. Note, however, that our definition of a disk is purely kinematic: a spheroidal galaxy with net rotation could have a substantial `disk' component.

- For $M_{*} \lesssim 10^{9.5}\mathrm{M}_{\odot}$ the main progenitor galaxies grow preferentially via in-situ star formation during episodes of enhanced merger activity and form mainly a spheroidal, or more complex non-rotationally supported, structure (Tables 6.1 and 6.2, Fig. 6.6).

In conclusion, we find that galaxy formation in EAGLE can be classified into three phases, based on galaxy stellar mass. First, an early phase ($M_{*} \lesssim 10^{9.5}\mathrm{M}_{\odot}$) of disorganised in-situ star formation associated with merger activity, which results in a spheroidal (or more complex, non-rotationally supported) morphology. Second, a phase ($10^{9.5}\mathrm{M}_{\odot} \lesssim M_{*} \lesssim 10^{10.5}\mathrm{M}_{\odot}$) of organised in-situ star formation, resulting in a disky morphology. Third, a late phase ($M_{*} \gtrsim 10^{10.5}\mathrm{M}_{\odot}$) in which mergers trigger the transformation from disk-dominated galaxies to bulge-dominated or elliptical galaxies. The last phase is increasingly driven by the accretion of stars formed ex-situ.

Testing this three phase picture observationally is beyond the scope of this work. In order to investigate whether real galaxies go through similar phases as EAGLE galaxies, one could compare to slit-spectroscopy or IFU surveys, applying the same selection criteria and using virtual observations.

Acknowledgements

We thank Camila Correa and Scott Trager for reading the manuscript and providing comments. This work was supported by the Netherlands Organisation for Scientific Research (NWO), through VICI grant 639.043.409. We made use of he DiRAC Data Centric system at Durham University, operated by the Institute for Computational Cosmology on behalf of the STFC DiRAC HPC Facility (www.dirac.ac.uk). This equipment was funded by BIS National E-infrastructure capital grant ST/K00042X/1, STFC capital grants ST/H008519/1 and ST/K00087X/1, STFC DiRAC Operations grant ST/K003267/1 and Durham University. DiRAC is part of the National E-Infrastructure. RGB acknowledges the support of STFC consolidated grant ST/L00075X/1.

6.9 Appendix A

Figure 6.10 shows the convergence with the numerical resolution of the S/T ratio for the population of central galaxies as a function of stellar mass, Fig. 6.4. We compare results from the $(25\ \mathrm{Mpc})^3$ sized reference run (RefL0025N0376), which has the same resolution as the $(100\ \mathrm{Mpc})^3$ sized main simulation run (RefL0100N1504), with the $(25\ \mathrm{Mpc})^3$ sized recalibrated run (RecalL0025N0376), which has an 8 times higher mass resolution (or 2 times higher spatial resolution). This is a test of weak-convergence (Schaye et al. 2015) as the parameters of the subgrid physics have been recalibrated to the present-day galaxy stellar mass function and mass-size relation. A recalibration is needed because a change in the resolution also affects the division between sub- and super-grid physics. The purpose of recalibrating is to make the large-scale effects of feedback processes the same at the higher resolution. The convergence in Fig. 6.10 is good. Results for the morphology evolution of the main progenitors of massive galaxies can not be tested for convergence in the same way, because the $(25\ \mathrm{Mpc})^3$ sized simulation box does not contain enough massive galaxies. However, the good convergence of our morphology measure for the overall population suggests that results can also be trusted for these main progenitors.

6.10 Appendix B

Fig. 6.11 shows the same diagnostics as Fig. 6.8 for the inner 5 pkpc. We include it here instead of in the main text, because these figures turn out to be very similar. This means that the effects of mergers and in-situ star formation on the evolution

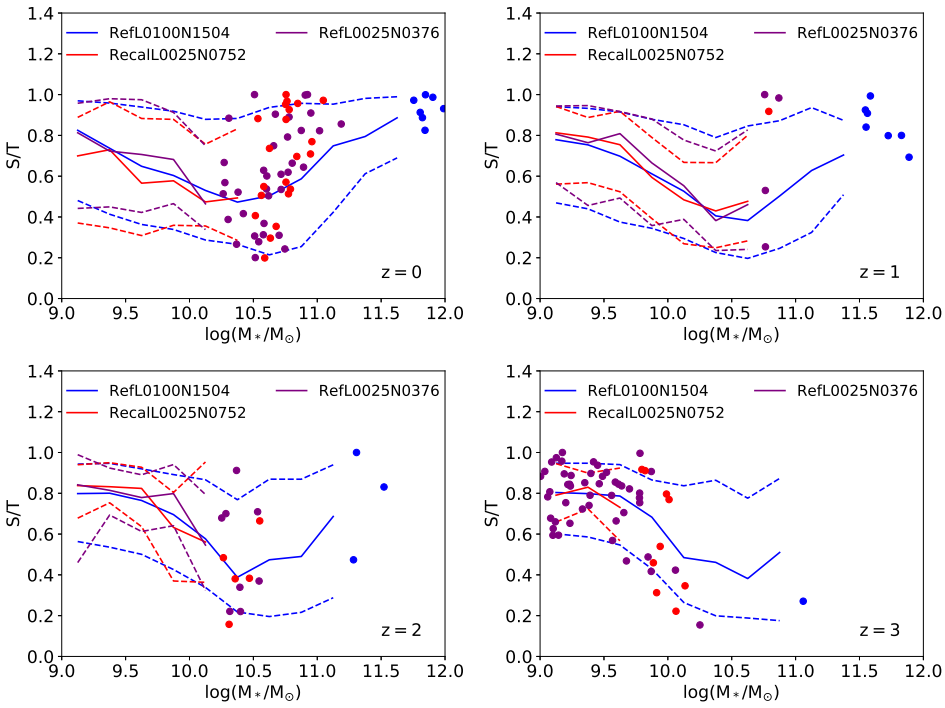

Figure 6.10: Weak convergence test of the mass dependence of the S/T ratio for the population of central galaxies at different redshifts. Different panels show different redshifts. In each panel the running median (solid curve) and 10%-90% range (dashed curves) is shown for three different simulation runs (colours). Blue corresponds to the original $(100\ \mathrm{Mpc})^3$ reference run, as shown in Fig. 6.4. Purple and red correspond respectively to the $(25\ \mathrm{Mpc})^3$ reference run and the $(25\ \mathrm{Mpc})^3$ recalibrated run at 8 times higher mass resolution and 2 times higher spatial resolution. individual galaxies are shown as coloured dots for mass bins that contain fewer than 10 galaxies. A comparison of the blue and purple curves mainly tests cosmic variance. These boxes differ by a factor 64 in volume, but use the same resolution. A comparison of the red and purple curves is a test of 'weak convergence' with the numerical resolution (see Schaye et al. 2015, for a discussion). For all redshifts the convergence is excellent, although at the lowest masses and lowest redshifts there is a tendency for galaxies in the higher-resolution RecalL0025N0752 (red) to be slightly more disky.

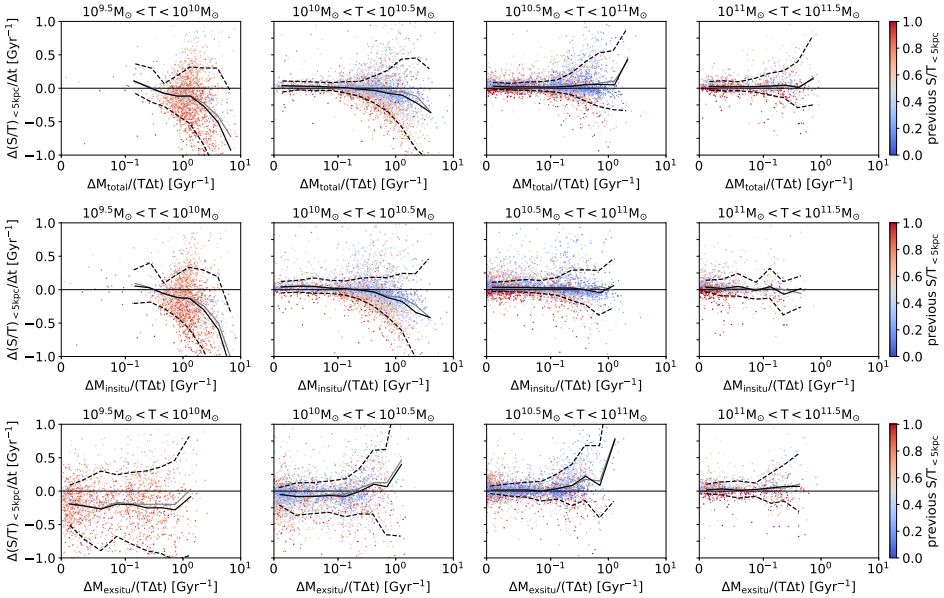

Figure 6.11: As Fig. 6.8 for the kinematic changes in the inner 5 pkpc (which separates bulge formation from bulge+halo formation). The running averages from Fig. 6.8 are repeated as solid grey curves. In all panels there is a good agreement between the kinematic changes within 5 kpc (solid black curves) and those for the whole galaxy (solid grey curves). This means that the dependence of the inner kinematic changes on merger activity are very similar to that for the whole galaxy.

of the kinematic morphology in the centres of galaxies (< 5 pkpc) are very similar to the effects they have on the galaxies as a whole.

7 | Samenvatting in het Nederlands

7.1 De vorming van sterrenstelsels

7.1.1 Sterrenstelsels

Sterrenstelsels zijn enorme conglomeraties van werelden, die bestaan uit biljoenen sterren en planeten en zo mogelijk nog meer levende wezens die hun planeet, hun zonnestelsel of hun sterrenstelsel `thuis' noemen. Voor ons, sterrenkundigen, zijn sterrenstelsels echter slechts testdeeltjes die de structuur van het Heelal uitlichten op de grootste schalen. Het zijn vage lichtvlekken in de nachtelijke hemel waarvan we een mooie foto proberen te nemen. Nadat we veel van deze foto's hebben bestudeerd, komen deze sterrenstelsels langzaam tot leven. In onze verbeelding worden sterrenstelsels levende wezens, die gas in- en uitademen en nieuw weefsel vormen in de vorm van sterren en planeten.

Deze wezens groeien op in een harde wereld van eten of gegeten worden. Zelfs als hun omgeving hen niet verslindt dan nog speelt het een belangrijke rol in hun ontwikkeling. Echter, nog belangrijker voor de ontwikkeling van een sterrenstelsel zijn interne processen. Deze processen spelen zich af in de stellaire geboorte wolken, in individuele sterren of zelfs in de individuele atomen waaruit een sterrenstelsel bestaat. We proberen deze processen beter te begrijpen door virtuele sterrenstelsels te creëren die als een soort van laboratorium ratten in onze grootste supercomputers leven.

Ondanks het feit dat onze perceptie van sterrenstelsel steeds verfijnder wordt, worden zij in veel van onze wetenschappelijke figuren gereduceerd tot datapunten in een enorme puntenwolk, wat je zou kunnen beschouwen als een versimpeling. Ongetwijfeld komt onze eigen Melkweg in vele vergelijkbare figuren voor in vele uithoeken van het Heelal, zonder dat iemand zich daar druk maakt over ons leven hier op aarde. Voor dit proefschrift zullen sterrenstelsels deze verfijnde, doch

hoogst versimpelde, mentale plaatjes zijn, los van emotionele lading of een echt gevoel van plaats, tijd of verbondenheid. Dit komt deels door een gebrek aan verbeeldingskracht, maar voornamelijk door een gebrek aan informatie.

7.1.2 De bouwstenen van sterrenstelsels

De precisie waarmee we alles behalve de meest dichtstbijzijnde sterrenstelsels waarnemen stelt ons niet in staat om de individuele sterren, die het licht van een sterrenstelsel produceren, te tellen, noch laat onze korte levensduur ons toe om deze sterrenstelsels te zien evolueren. We moeten vertrouwen op een scala aan technieken en modellen om deze informatie te distilleren uit wat ons gegeven is door de nachtelijke hemel. Hieronder zal ik een korte samenvatting geven van de successen van de wetenschappelijke gemeenschap in het ontrafelen van de bouwstenen van sterrenstelsels zowel in de ruimte als in de tijd. Dit is geen gebalanceerde beschrijving van alle factoren die bijdragen aan de evolutie van sterrenstelsels. Ik zal vooral ingaan op de belangrijkste concepten die nodig zijn voor een begrip van hoofdstukken 2 t/m 6 van dit proefschrift.

Sterren

We denken dat sterrenstelsels bestaan uit vele componenten, te weten een halo van heet gas, koude wolken van moleculair gas, een donkere-materie halo en massieve (centrale) zwarte gaten, maar er is slechts één component die cruciaal is voor een alleenstaande, door zwaartekracht gebonden structuur om te classificeren als een sterrenstelsel: het moet vele sterren bevatten. Waarnemingen laten zien dat `veel' alles kan betekenen van ongeveer 10^3 tot 10^{12} sterren. Er zijn veel meer lichtgewicht of middelzware sterrenstelsels dan dat er massieve sterrenstelsels zijn, maar alsnog bevinden de meeste sterren zich in massieve sterrenstelsels. Onze zon is hierop geen uitzondering, aangezien de Melkweg ongeveer 2.5×10^{11} sterren bevat.

Niet alle sterren worden gelijk geboren. Ze hebben een verscheidenheid aan intrinsieke eigenschappen zoals massa, hoekmoment, metalliciteit[1] en leeftijd en afgeleide eigenschappen zoals, grootte, lichtkracht en temperatuur. Veruit de belangrijkste eigenschap is de massa van een ster. Sterren worden geboren met een grote range aan massa's ($0.08\mathrm{M}_\odot \lesssim M \lesssim 120\mathrm{M}_\odot$)[2] welke hun uiterlijk en hun lot bepaalt.

[1] De metalliciteit van een ster, gaswolk of ander astronomisch object is de fractie van elementen zwaarder dan helium. Zuurstof wordt, binnen de astronomie, dus gezien als een metaal. De exacte definitie van metalliciteit loopt uiteen, afhankelijk van de manier waarop deze waargenomen wordt.

[2] De gebruikelijke eenheid voor massa in de astronomie is zonsmassa's, $\mathrm{M}_\odot = 1.99 \times 10^{30}$kg.

Lichte sterren leiden een rustig en lang leven, terwijl zware sterren fel schijnen, hun brandstof snel opbranden en sterven in massieve explosies die grote hoeveelheden aan heet, metaal-rijk gas injecteren in de interstellaire ruimte. Het verschil in energie uitstoting tussen lage- en hoge massa sterren is enorm. De lichtkracht van een ster schaalt ruwweg met de 3.5^{e} macht van zijn massa, wat betekent dat de lichtkracht per massa eenheid schaalt met de 2.5^{e} macht van de massa. Er is slechts een eindige hoeveelheid energie die vrij kan komen uit een eenheid aan stellaire massa, voordat een ster begint aan zijn laatste fase. Hoe sneller een ster zijn energie opbrandt des te sneller zal dit einde komen. De levensduur van een ster is dus grofweg proportioneel met de -2.5^{e} macht van de massa. Dit betekent dat een ster die 10 keer zwaarder is, ongeveer 3000 keer feller zal schijnen (met een hetere blauwe kleur), maar een levensduur zal hebben die ongeveer 300 keer korter is. In de praktijk betekent dit dat het licht van een sterrenstelsel gedomineerd wordt door jonge, massieve sterren, zolang deze aanwezig zijn. Wanneer deze massieve sterren verdwijnen zal een sterrenstelsel rood worden en minder fel schijnen. Zelfs voor sterrenstelsels die niet langer actief sterren vormen, zal het meeste licht komen van de zwaarste, nog aanwezige sterren. Deze sterren kunnen slechts een klein deel van de massa van een sterrenstelsel uitmaken, aangezien een aanzienlijk deel van de stellaire massa opgesloten kan zijn in dwergsterren en in de overblijfsels van de overleden massieve sterren zoals neutronen sterren en zwarte gaten.

Het tempo waarmee sterren energie en metalen terug geven aan de gaswolken waaruit zij geboren zijn hangt dus sterk af van de massa van deze sterren. We noemen dit proces `stellaire feedback'. Sterren worden geboren in zeer koude ($\approx$ 30 K) en dichte wolken van moleculair gas. Deze feedback, die kan bestaan uit licht, stellaire winden, kosmische straling of supernova explosies, kan deze stellaire geboorte wolken opwarmen of wegblazen en daarmee het tempo waarmee nieuwe sterren vormen reguleren. Zonder stellaire feedback kunnen hydrodynamische simulaties niet voorkomen dat ster-vorming escaleert, maar deze feedback kan ook lokaal ster-vorming stimuleren door de interstellaire materie samen te drukken in schokgolven en het kan ster-vorming op latere tijdstippen stimuleren door de interstellaire materie te verrijken met metalen, die zorgdragen voor een effectieve koeling van het interstellaire gas.

Waarnemingen van het lokale deel van het Heelal, het deel waarin we de sterren kunnen tellen (e.g. de Melkweg, haar globulaire clusters, jonge clusters in Andromeda) laten zien dat de verdeling van ster massa's bij geboorte hetzelfde is in verschillende omgevingen. We noemen deze verdeling van de massa's waarmee sterren geboren worden de initiële massa functie (IMF). Zie paragraaf 3.2 voor een precieze definitie en Fig. 3.1 voor de vorm van de IMF in het lokale Heelal, zoals deze bepaald is door Chabrier (2003). Voor lange tijd sinds de introductie van de IMF door Salpeter (1955), is de consensus, gedreven door waarnemingen,

dat de IMF universeel is. Dit betekent dat hij hetzelfde is in het hele Heelal en dus niet afhangt van de eigenschappen van de stellaire geboorte wolken.

Een universeel IMF is handig voor het modelleren van ster populaties en sterrenstelsels. Over het algemeen is de aanname dat de stellaire opbouw van een sterrenstelsel een superpositie is van meerdere simpele stellaire populaties (SSPs): populaties met een enkele metalliciteit en leeftijd, geëvolueerd vanuit een universeel IMF. Observationele methodes voor het matchen van spectra van sterrenstelsels gaan over het algemeen uit van een enkele metalliciteit en een simpele functionele vorm voor de superpositie van verschillende stellaire leeftijden. In hydrodynamische simulaties stelt typisch elk virtueel ster-deeltje een simpele stellaire populatie voor. De stellaire opbouw van een sterrenstelsel wordt dan gegeven door een superpositie van vele ster-deeltjes, die elk een andere leeftijd en metalliciteit kunnen hebben.

Echter, in het laatste decennium wordt de universaliteit van het IMF in twijfel getrokken door interpretaties van een scala aan waarnemingen. Vele teams hebben geprobeerd het IMF op galactische schalen of in extreme omgevingen te bepalen. Hierbij gebruiken zij diverse creatieve methodes, anders dan het direct tellen van sterren. Er zijn nu vele claims van waargenomen IMF variaties, wat bijdraagt aan een interessant en levendig vakgebied. Echter de diverse claims zijn vaak moeilijk met elkaar te verenigen. De meest invloedrijke bijdragen zijn van van Dokkum and Conroy (2012) & Conroy and van Dokkum (2012) en van Cappellari et al. (2012).

Van Dokkum and Conroy (2012) , Conroy and van Dokkum (2012) schatten het IMF van vroeg-type[3] sterrenstelsels door precieze modellen van absorptie lijnen te fitten aan het geïntegreerde licht van deze sterrenstelsels, inclusief lijnen die een andere sterkte hebben in dwerg sterren dan in reuzen sterren.

Cappellari et al. (2012) gebruiken een compleet andere methode om het IMF te bepalen. Zij proberen het centrale deel van nabije, vroeg-type sterrenstelsels te wegen door de bewegingen van de sterren te modelleren. Vervolgens schrijven zij het surplus aan gravitationele massa, bovenop wat verwacht wordt van sterren, een centraal zwart gat en donkere materie, toe aan `onzichtbare' sterren.

Beide groepen concluderen, losjes gezegd, dat sterrenstelsels met hoge snelheid dispersies (wat overeenkomt met hoge massa's) neigen naar een IMF met een surplus aan `onzichtbare' sterren ten opzichte van een Chabrier IMF. Bij van Dokkum and Conroy (2012); Conroy and van Dokkum (2012) is dit surplus toe te schrijven aan dwerg sterren. Bij Cappellari et al. (2012) is het toe te schrijven aan dwerg sterren of aan de overblijfsels van massieve sterren. Beide studies lijken

[3]De term `vroeg-type' wordt grofweg inwisselbaar gebruikt met `elliptisch' of `sferisch'. `Laat-type' is vergelijkbaar met `schijf' or `spiraal'. Zie de subsectie `morfologische componenten' voor een korte introductie in de classificatie van sterrenstelsels gebaseerd op morfologie en/of kleur.

op de oppervlakte overeen te komen. Echter, deze overeenkomst verdwijnt bij een vergelijk in detail. Secties 2.1 en 3.1 geven een meer gedetailleerde discussie van de huidige staat aangaande waarnemingen die geïnterpreteerd kunnen worden als bewijs voor IMF variaties.

De botsing van sterrenstelsels

Het kost veel tijd om een sterrenstelsel te groeien. Voor de meeste sterrenstelsels kost het de leeftijd van het Heelal om hen te groeien tot aan hun huidige grootte en massa. Deze groei neemt deels plaats in isolatie van andere sterrenstelsels. Gas koelt af en wordt gevangen door de zwaartekracht van een sterrenstelsel. Over het algemeen vormt het daar een draaiende schijf van koud gas waaruit sterren geboren worden. Deze ster-vorming kan geleidelijk plaats vinden of het kan plaats vinden in episodes van verhoogde ster-vorming afgelost met episodes waarin feedback tijdelijk de ster-vorming reduceert. Waarnemingen van de mate van ster-vorming als een functie van de massa van een sterrenstelsel laten zien dat ster-vorming goed gereguleerd is. Dat wil zeggen, het is gereguleerd tot het moment dat een sterrenstelsel stopt met het vormen van nieuwe sterren. Deze nauwe relatie tussen de massa en ster-vorming snelheid van een sterrenstelsel wordt genoemd de `ster-vorming hoofdreeks' (Brinchmann et al. 2004; Salim et al. 2007). Deze relatie geld niet alleen nu, maar ook in het vroege Heelal (zij het met een andere normalisatie). Er is echter ook een compleet andere manier waarop sterrenstelsels kunnen groeien. Ze kunnen groeien door op elkaar te botsen. Dit proces, waarbij typisch een minder massief sterrenstelsel gevangen wordt in het zwaartekrachtsveld van een massiever stelsel, waarna beide sterrenstelsels samensmelten, wordt een `merger' genoemd.

Mergers kunnen een effect hebben op de vorm van een sterrenstelsel. Mergers van twee sterrenstelsels met een vergelijkbare massa kunnen een geordende, draaiende stellaire schijf veranderen in een meer willekeurige sferische vorm. Fig. 1.1 laat twee sterrenstelsels zien die aan het mergen zijn. Mergers kunnen ook een direct effect hebben op het gas tussen de sterren, de interstellaire materie, aangezien dit gas daadwerkelijk botst (in tegenstelling tot de sterren die gewoon langs elkaar vliegen). Dit kan zorgen voor een compressie van het gas, gevolgd door afkoeling en een fase van verhoogde ster-vorming. Een sterrenstelsel kan dus tijdens een merger in massa toenemen door oude sterren in te vangen of door nieuwe sterren te vormen. Dit laatste, verhoogde ster-vorming als gevolg van een merger, moet voldoen aan dezelfde waargenomen beperking op de fluctuaties in de ster-vorming snelheid die ook geldt voor sterrenstelsels in isolatie, te weten de ster-vorming hoofdreeks.

Een typisch sterrenstelsel maakt veel mergers mee tijdens zijn leven. Het volgen van een sterrenstelsel terug in de tijd is alleen mogelijk op een letterlijke manier

voor sterrenstelsels in een kosmologische simulatie, waarvoor we toegang hebben tot de gehele historie. Als we een typisch sterrenstelsel terug in de tijd volgen, vertakt het zich in vele kleinere `progenitor' sterrenstelsels, de bouwstenen waaruit het uiteindelijke sterrenstelsel is opgebouwd. De stamboom van een sterrenstelsel, aldus verkregen, heet ook wel de `merger tree'. In deze stamboom definiëren we de meest massieve aftakking als de hoofdtak, die bestaat uit `main progenitor' sterrenstelsels (op elk tijdstip is slechts één progenitor de main progenitor). In de meeste gevallen is deze main progenitor duidelijk het meest prominente sterrenstelsel die de basis vormde voor het huidige sterrenstelsel. Echter, in het zeldzame geval dat twee sterrenstelsels van gelijke massa mergen, is de keuze welk sterrenstelsel de main progenitor is enigszins willekeurig. Onder de evolutie van sterrenstelsels wordt over het algemeen verstaan de evolutie van de eigenschappen van de main progenitor. Alle andere progenitors verdwijnen op een gegeven moment, doordat ze opgeslokt worden door de main progenitor.

Het tempo waarmee sterrenstelsels van uiteenlopende massa's mergen, ofwel de `merger rate', wordt relatief goed begrepen binnen de ΛCDM[4] kosmologie. Sterrenstelsels worden gedomineerd in massa door een koude donkere-materie component. Deze component is minder geconcentreerd dan de gewone materie, aangezien het zijn energie niet kan uitstralen en dus niet kan afkoelen en samenklonteren, omdat donkere materie, zover we weten, alleen interactie heeft via zwaartekracht. We denken dat elk sterrenstelsel zich bevindt in een donkere materie halo. Precies om de reden dat donkere materie alleen op zwaartekracht reageert, is het veel makkelijker te simuleren. Simulaties (e.g. Genel et al. 2009) laten zien dat donkere-materie halos deels vormen door continue accretie en deels door mergers in een `bottom-up' manier. Lichte halos mergen gemiddeld eerder dan zware halos. Het belangrijke punt hier is dat de vorming van donkere-materie halos zich weinig aantrekt van de normale materie die zich in deze halos bevindt. Binnen de ΛCDM kosmologie zijn de merger rates dus direct af te leiden uit simpele principes. Ze zijn niet onderhevig aan de vele onzekerheden die ons begrip van de veel complexere `normale' materie plagen. De grootste onzekerheid in de afleiding van de merger rates van sterrenstelsels binnen de ΛCDM kosmologie komt van de vertaling van de massa van donkere-materie halo's naar de stellaire massa van de sterrenstelsels die zich hierin bevinden. Niet alle donkere materie halo's bevatten dezelfde fractie aan stellaire massa. Een donkere-materie merger

[4]Dit is het huidige kosmologische model, welke aangenomen wordt voor alle `observabelen' zoals intrinsieke helderheden van sterrenstelsels, groottes, leeftijden, massa's en ster-vorming snelheden, met de uitzondering van ruwe data zoals schijnbare helderheden en spectraal-lijn ratios. Λ representeert `donkere energie' of de kosmologische constante geïntroduceerd door Einstein. Het zorgt voor een versnelde expansie van het huidige Heelal. CDM staat voor `cold dark matter' oftewel `koude donkere materie', de dominante vorm van gravitationele massa in het Heelal.

massa-ratio kan dus niet direct vertaald worden in een sterrenstelsel merger massa-ratio. Een manier om dit probleem te omzeilen is door aan te nemen dat, op elk moment in de tijd, de stellaire massa van de waargenomen sterrenstelsels monotoon geprojecteerd kan worden op de theoretische donkere materie halo populatie, zodat het meest massieve sterrenstelsel in een gegeven volume zich bevindt in de meest massieve donkere materie halo, etc. Voor massieve sterrenstelsels betekent dit dat een relatief breed interval van halo massa's correspondeert met een relatief smal interval van stellaire massa's. Mergers tussen deze sterrenstelsels hebben dus een massa-ratio dichter bij één als deze massa-ratio gedefinieerd wordt met betrekking tot stellaire massa in plaats van donkere-materie massa. Merger rates en ratios kunnen ook waargenomen worden, door botsende sterrenstelsels en sterrenstelsels die tekenen van recente mergers vertonen, te tellen, maar dit is vrij inexact, omdat het afhangt van aannames aangaande de tijd die een merger in beslag neemt en de mate waarin mergers leiden tot waarneembare morfologische afwijkingen.

Morfologische componenten

Sterrenstelsels komen in verschillende vormen en maten. Sommige sterrenstelsels hebben een zeer georganiseerde structuur, een platte ronddraaiende schijf, terwijl andere sterremstelsels een chaotisch uiterlijk hebben, wellicht midden in een merger episode zitten, of een sferische morfologie hebben waarbij de sterren op zeer radiële, in plaats van circulaire, banen bewegen. De meeste stellaire massa in het Universum kan echter toegeschreven worden aan twee morfologische componenten: schijven en sferoïden. Het merendeel van de huidige sterrenstelsels classificeren óf als een pure schijf, zie Fig. 1.2, óf als een schijf met een centrale sferoïde (een bulge), zie Fig. 1.3, óf als een pure sferoïde (een elliptisch sterrenstelsel), zie Fig. 1.4.

Waarnemingen laten zien dat de morfologie van een sterrenstelsel nauw verbonden is aan zijn kleur. De kleur-distributie van sterrenstelsels is ruwweg bimodaal. Sterrenstelsels worden, op basis van hun kleur, geclassificeerd in `blauwe wolk' sterrenstelsels en `rode reeks' sterrenstelsels (Strateva et al. 2001; Bell et al. 2004). Blauwe-wolk sterrenstelsels vormen actief sterren en hebben overwegend een schijf-achtige morfologie. Hun licht wordt gedomineerd door massieve jonge sterren. Rode-reeks sterrenstelsels vormen niet of nauwelijks sterren meer en hebben overwegend een sferische morfologie. Hun licht wordt gedomineerd door oudere sterren van middelmatige massa. De centrale sferoïden van schijf stelsels (bulges) zijn over het algemeen ook rood. Zij bestaan voornamelijk uit oude sterren en laten weinig tekenen van ster-vorming zien.

Er zijn slechts weinig sterrenstelsels die tussen de `blauwe wolk' en de `rode reeks' vallen in de zogenaamde `groene vallei'. Dit betekent dat de overgang van

de blauwe wolk naar de rode reeks relatief snel moet verlopen. Één van de belangrijkste uitdagingen in het onderzoek naar de vorming van sterrenstelsels is om een representatieve populatie van sterrenstelsels te creëren, binnen de gecontroleerde omgeving van een kosmologische simulatie, die deze bimodaliteit deelt.

Sectie 6.1 geeft een meer gedetailleerd overzicht van de morfologische componenten van sterrenstelsels, van de manier waarop deze bepaald worden en van hun potentiële vormings-mechanismen.

7.2 Dit proefschrift

7.2.1 Hoofdstuk 2: Een analyse van het bewijs van ATLAS^{3D} voor een variabele initiële massa functie

Cappellari et al. (2012) bepalen IMF variaties door het centrale deel van 260 nabije vroeg-type sterrenstelsels te wegen. Deze sterrenstelsels zijn waargenomen met de SAURON integral field spectograph op de William Herschel Telescope. Dit geeft ons, na het verwerken van de ruwe data, een twee-dimensionale afbeelding, waarin elke pixel een verdeling van de stellaire snelheden in de kijkrichting bevat. Cappellari et al. (2012) modelleren deze stellaire bewegingen onder de aanname dat ze in dynamisch evenwicht zijn en de onderliggende massa verdeling traceren. Van deze, kinematisch bepaalde, massa trekken ze de verwachte donkere materie massa af. Zodoende bepalen zij de gravitationele stellaire massa in het centrale deel van deze sterrenstelsels. Onafhankelijk hiervan bepalen ze een `fotometrische' stellaire massa, door modellen van galactische spectra te fitten aan het geïntegreerde licht van deze galactische centra. Deze modellen bouwen een galactisch spectrum op als een som over de spectra van individuele sterren, waarvoor zij een universeel IMF aannemen. Verschillen tussen de gravitationele stellaire massa en de fotometrische stellaire massa worden vervolgens toegeschreven aan IMF variaties.

Dit is een riskante procedure, omdat verschillen in de twee massa bepalingen ook het gevolg kunnen zijn van een scala aan waarneem- en model-onzekerheden. Een onderschatting van deze onzekerheden zal leiden tot een overschatting van de intrinsieke IMF variaties.

Dit hoofdstuk onderzoekt deze onzekerheden. We laten zien dat de resultaten van Cappellari et al. (2012) grotendeels gerepliceerd kunnen worden door een universeel IMF aan te nemen in combinatie met grotere model-onzekerheden. Verder onderzoeken we compleetheid effecten en selectie effecten. We rapporteren een onverwachte trend van de afgeleide IMF variaties met de afstand tot de aarde en we leiden af hoe de voorgestelde IMF variaties, indien echt, de massa verdeling van de waargenomen populatie aan sterrenstelsels in het Heelal zouden

veranderen[5].

7.2.2 Hoofdstuk 3: Implicaties van een variabel IMF voor de interpretatie van waarnemingen van populaties van sterrenstelsels

Martín-Navarro et al. (2015d) bepalen de IMF in galactische deelgebieden, gebaseerd op de analyse van IMF-gevoelige spectraal-lijnen in de CALIFA survey. Hun sample bevat een grote diversiteit aan metalliciteiten en zij rapporteren een sterke metalliciteits-afhankelijkheid van het door hun bepaalde IMF.

In dit hoofdstuk onderzoeken we wat de voorgestelde metalliciteits-afhankelijkheid van de IMF zou betekenen voor de interpretatie van waargenomen eigenschappen van sterrenstelsels. We passen de voorgestelde IMF toe op een sterrenstelsel-voor-sterrenstelsel basis op een sample van 186,886 sterrenstelsels uit de Sloan Digital Sky Survey. We laten zien dat de implicaties voor de ster-vorming hoofdreeks, de galactische stellaire massa functie en de massa-metalliciteit relatie sterk afhangen van aannames over de functionele vorm van de IMF en uiteenlopen van mild, doch significant, tot zeer omvangrijk.

Bovendien onderzoeken we een scenario waarin ster-vorming in de late, metaalrijke, fase van de evolutie van een sterrenstelsel, gedomineerd wordt door dwerg sterren. Dit kan helpen de bimodaliteit in de waargenomen populatie van sterrenstelsels te verklaren door, aan de ene kant, de ster-vorming snelheid van deze `dode' sterrenstelsels te vergroten (en dus tevens de intrinsieke bimodaliteit in stervorming snelheden te verminderen) en, aan de andere kant, de gas consumptie tijd te verlagen, resulterend in een snellere overgang van de `blauwe wolk' naar de `rode reeks'.

7.2.3 Hoofdstuk 4: Een groot verschil in de progenitor massa's van actieve en passieve sterrenstelsels in de EAGLE simulatie

Een belangrijke vraag aangaande de vorming van sterrenstelsels is hoe, uit de waargenomen evolutie van de populatie van sterrenstelsels, de typische evolutie van individuele sterrenstelsels te distilleren. Als we hiervoor een precieze methode hadden, zou het ons enorm helpen om de opbouw van sterrenstelsels te traceren en de hieraan gerelateerde evolutie van hun eigenschappen zoals grootte, metalliciteit,

[5]De getalsmatige dichtheid van sterrenstelsels als een functie van stellaire massa, gecorrigeerd voor compleetheid effecten, wordt ook wel de `galactische stellaire massa functie' (GSMF) genoemd. Deze wordt gekarakteriseerd door een steile daling boven $\approx 10^{10.75} M_{\odot}$. De meeste stellaire massa in het Heelal bevindt zich net hieronder.

morfologie en ster-vorming activiteit te begrijpen. Helaas bestaat zo een precieze methode niet. We moeten vertrouwen op versimpelde aannames. Over het algemeen gebruiken we een methode genaamd `cumulative number density matching', welke aanneemt dat main progenitors geïdentificeert kunnen worden op basis van hun cumulatieve[6] getals-dichtheid.

De prestatie van deze methode kan alleen gecontroleerd worden binnen een kosmologische simulatie, waarvoor we toegang hebben tot de gehele merger tree vanaf het begin der tijden. Ik had het geluk dat tijdens mijn tijd als promotie student, de EAGLE kosmologische simulatie het licht zag (Schaye et al. 2015). Dit is, naar mijn mening, de eerste kosmologische simulatie die voldoende overeenstemt met het waargenomen Heelal om hem met vertrouwen toe te passen op dit probleem.

We vinden dat, in de EAGLE simulatie, de mediaan van de stellaire massa van de main progenitors in het vroege heelal sterk afhangt van de ster-vorming activiteit van de huidige sterrenstelsels (geselecteerd in een vast massa interval). Dit is het geval voor huidige sterrenstelsels met een massa tot aan $10^{10.75}\mathrm{M}_{\odot}$.

Als het zelfde geldt voor het echte Heelal dan beperkt dit drastisch de toepasbaarheid van de `cumulative number density matching' methode, in ieder geval in zijn huidige vorm. Bovendien is het moeilijk een extensie van het model voor te stellen dat dit probleem vermijdt zonder uit te gaan van input uit een kosmologische simulatie/model (wat het belangrijkste pluspunt van de methode teniet zou doen: dat het alleen afhangt van waarnemingen en robuuste donkere-materie simulaties).

7.2.4 Hoofdstuk 5: De gemiddelde structurele evolutie van massieve sterrenstelsels kan op een betrouwbare manier bepaald worden op basis van cumulatieve getals-dichtheden van sterrenstelsels.

In het vorige hoofdstuk hebben we gezien dat de `cumulative number density matching' methode verwacht wordt onbetrouwbaar te zijn voor massa's lager dan $10^{10.75}\mathrm{M}_{\odot}$ vanwege een groot verschil in de progenitor massa's van actieve- en passieve sterrenstelsels. Voor massievere sterrenstelsels komt dit probleem niet voor en kunnen we verwachten dat de methode goed werkt.

Echter, voor deze massieve sterrenstelsels is er nog steeds een grote variatie

[6]Cumulatief refereert hier aan de stellaire massa, hoewel andere variabelen zoals snelheids-dispersie ook gebruikt worden. De cumulatieve getals-dichtheid van een gegeven sterrenstelsel op een gegeven kosmische tijdstip is gedefinieerd als de getals-dichtheid van sterrenstelsels die een stellaire massa hebben groter dan het gegeven sterrenstelsel, op hetzelfde tijdstip, binnen een, met de kosmische uitdijing meebewegend, volume (Mpc^{-3}).

in main progenitor massa's. Dit maakt het noodzakelijk om de methode apart te toetsen voor iedere eigenschap van een sterrenstelsel. De mediaan/gemiddelde eigenschap van de echte main progenitor sample (met een brede massa distributie) is niet noodzakelijkerwijs hetzelfde als de mediaan/gemiddelde eigenschap van een sample van sterrenstelsels die geselecteerd zijn op de `median cumulative number density' (met een smalle massa distributie).

We laten zien dat, ondanks deze complicatie, de cumulative number density matching techniek redelijk goed werkt als deze toegepast wordt op de evolutie van de dichtheids-profielen van massieve sterrenstelsels in EAGLE. Dit kan verbeterd worden door ook de verwachte spreiding in main progenitor massa's te modelleren, gebaseerd op donkere-materie simulaties.

Verder passen we de methode toe op waarnemingen van UltraVISTA en CANDELS tot aan[7] $z = 5$. We leiden af dat massieve sterrenstelsels van binnen uit gegroeid zijn sinds $z = 5$. Sinds $z = 2$ is deze trend bescheiden. Hier is de evolutie van de waargenomen dichtheids-profielen gelijkvormiger dan in de EAGLE simulatie, met een vergelijkbare relatieve groei op alle afstanden van het galactische centrum.

7.2.5 Hoofdstuk 6: De drie fases in de vorming van sterrenstelsels

Alhoewel de morfologie van sterrenstelsels uitgebreid bestudeerd is en we waargenomen sterrenstelsels in zeer specifieke morfologische types kunnen indelen, zijn de processen die de morfologie van een sterrenstelsel bepalen niet goed begrepen. Stellaire schijven vormen uit koude gas schijven, maar kosmologische simulaties laten zien dat hun grootte sterk afhangt van de implementatie van verscheidene feedback processen en dus, op het moment, niet vanuit simpele principes afgeleid kan worden. Voor sferoïden is er geen tekort aan hypothetische vormingsmechanismen, maar op het moment is het niet duidelijk welke mechanismen waar en wanneer dominant zijn.

In dit hoofdstuk bestuderen we de veranderingen in morfologie van sterrenstelsels in de EAGLE simulatie, met de nadruk op de vorming van sferoïden. Feedback processen in EAGLE zijn gekalibreerd om de lage-roodverschuiving massa-grootte relatie te reproduceren. De waargenomen groottes van stellaire schijven worden dus in goede benadering gereproduceerd (Schaye et al. 2015). Bovendien bevat de simulatie een representatieve populatie van massieve, rode, elliptische sterrenstelsels (Correa, Schaye, Clauwens et al. 2017). EAGLE is dus een bruikbare

[7] z staat voor de roodverschuiving van het waargenomen licht. Roodverschuiving $z = 5$ verwijst naar waarnemingen van sterrenstelsels gezien op een tijd dat het Heelal een factor $z + 1 = 6$ kleiner was (of een factor $6^3 = 216$ in volume).

test-omgeving om de morfologie van sterrenstelsels te bestuderen.

We traceren de morfologische opbouw van de main progenitors van sterrenstelsels met een stellaire massa van $10^{10.5}\mathrm{M}_{\odot} < M_{*} < 10^{12}\mathrm{M}_{\odot}$. Hieruit concluderen we dat de vorming van sterrenstelsels in EAGLE een proces is dat drie fases kent. Op lage massa's ($M_{*} \lesssim 10^{9.5}\mathrm{M}_{\odot}$) groeien sterrenstelsels op een chaotische manier, voornamelijk in, door mergers veroorzaakte, ster-vorming episodes die resulteren in sferische morfologiën. In de massa range $10^{9.5}\mathrm{M}_{\odot} \lesssim M_{*} \lesssim 10^{10.5}\mathrm{M}_{\odot}$ evolueren de sterrenstelsels op een meer geordende manier en bouwen zij een prominente stellaire schijf op door in-situ ster-vorming. Tijdens deze fase blijven de centrale bulges groeien. Zij bestaan voornamelijk uit sterren die in-situ gevormd zijn, maar alhoewel de bulges dus maar voor een insignificant deel bestaan uit sterren die tijdens mergers ingevangen zijn, is de groei van deze bulges wel degelijk toe te schrijven aan merger activiteit. Voor $M_{*} \gtrsim 10^{10.5}\mathrm{M}_{\odot}$ gaan sterrenstelsels hun laatste fase in. De in-situ ster-vorming wordt sterk gereduceerd, terwijl schijfgedomineerde sterrenstelsels veranderen in sferoïde-gedomineerde sterrenstelsels, onder de invloed van mergers.

Bibliography

D. Adams. *The Hitch Hiker's Guide to the Galaxy: A Trilogy in Four Parts*. Hitchhiker's Guide to the Galaxy Series. Heinemann, 1986. ISBN 9780434009206.

J. A. L. Aguerri, M. Balcells, and R. F. Peletier. Growth of galactic bulges by mergers. I. Dense satellites. *A&A*, 367:428--442, February 2001. doi: 10.1051/0004-6361:20000441.

M. Aumer, S. D. M. White, T. Naab, and C. Scannapieco. Towards a more realistic population of bright spiral galaxies in cosmological simulations. *MNRAS*, 434:3142--3164, October 2013. doi: 10.1093/mnras/stt1230.

R. Bacon, Y. Copin, G. Monnet, B. W. Miller, J. R. Allington-Smith, M. Bureau, C. M. Carollo, R. L. Davies, E. Emsellem, H. Kuntschner, R. F. Peletier, E. K. Verolme, and P. T. de Zeeuw. The SAURON project - I. The panoramic integral-field spectrograph. *MNRAS*, 326:23--35, September 2001. doi: 10.1046/j.1365-8711.2001.04612.x.

Y. M. Bahé, R. A. Crain, G. Kauffmann, R. G. Bower, J. Schaye, M. Furlong, C. Lagos, M. Schaller, J. W. Trayford, C. Dalla Vecchia, and T. Theuns. The distribution of atomic hydrogen in EAGLE galaxies: morphologies, profiles, and H I holes. *MNRAS*, 456:1115--1136, February 2016. doi: 10.1093/mnras/stv2674.

M. Barnabè, C. Spiniello, L. V. E. Koopmans, S. C. Trager, O. Czoske, and T. Treu. A low-mass cut-off near the hydrogen burning limit for Salpeter-like initial mass functions in early-type galaxies. *MNRAS*, 436:253--258, November 2013. doi: 10.1093/mnras/stt1727.

N. Bastian, K. R. Covey, and M. R. Meyer. Looking for Systematic Variations in the Stellar Initial Mass Function. In C. Johns-Krull, M. K. Browning, and A. A. West, editors, *16th Cambridge Workshop on Cool Stars, Stellar Systems, and the Sun*, volume 448 of *Astronomical Society of the Pacific Conference Series*, page 361, December 2011.

A. E. Bauer, A. M. Hopkins, M. Gunawardhana, E. N. Taylor, I. Baldry, S. P. Bamford, J. Bland-Hawthorn, S. Brough, M. J. I. Brown, M. E. Cluver, M. Colless, C. J. Conselice, S. Croom, S. Driver, C. Foster, D. H. Jones, M. A. Lara-Lopez, J. Liske, Á. R. López-Sánchez, J. Loveday, P. Norberg, M. S. Owers, K. Pimbblet, A. Robotham, A. E. Sansom, and R. Sharp. Galaxy And Mass Assembly (GAMA): linking star formation histories and stellar mass growth. *MNRAS*, 434:209--221, September 2013.

doi: 10.1093/mnras/stt1011.

P. S. Behroozi, C. Conroy, and R. H. Wechsler. A Comprehensive Analysis of Uncertainties Affecting the Stellar Mass-Halo Mass Relation for $0 < z < 4$. *ApJ*, 717:379--403, July 2010. doi: 10.1088/0004-637X/717/1/379.

P. S. Behroozi, D. Marchesini, R. H. Wechsler, A. Muzzin, C. Papovich, and M. Stefanon. Using Cumulative Number Densities to Compare Galaxies across Cosmic Time. *ApJ*, 777:L10, November 2013. doi: 10.1088/2041-8205/777/1/L10.

E. F. Bell, C. Wolf, K. Meisenheimer, H.-W. Rix, A. Borch, S. Dye, M. Kleinheinrich, L. Wisotzki, and D. H. McIntosh. Nearly 5000 Distant Early-Type Galaxies in COMBO-17: A Red Sequence and Its Evolution since z˜1. *ApJ*, 608:752--767, June 2004. doi: 10.1086/420778.

A. F. L. Bluck, J. T. Mendel, S. L. Ellison, J. Moreno, L. Simard, D. R. Patton, and E. Starkenburg. Bulge mass is king: the dominant role of the bulge in determining the fraction of passive galaxies in the Sloan Digital Sky Survey. *MNRAS*, 441:599--629, June 2014. doi: 10.1093/mnras/stu594.

A. Boselli, S. Boissier, L. Cortese, V. Buat, T. M. Hughes, and G. Gavazzi. High-mass Star Formation in Normal Late-type Galaxies: Observational Constraints to the Initial Mass Function. *ApJ*, 706:1527--1544, December 2009. doi: 10.1088/0004-637X/706/2/1527.

C. Bottrell, P. Torrey, L. Simard, and S. L. Ellison. Galaxies in the Illustris simulation as seen by the Sloan Digital Sky Survey - II. Size-luminosity relations and the deficit of bulge-dominated galaxies in Illustris at low mass. *MNRAS*, 467:2879--2895, May 2017. doi: 10.1093/mnras/stx276.

F. Bournaud, B. G. Elmegreen, and D. M. Elmegreen. Rapid Formation of Exponential Disks and Bulges at High Redshift from the Dynamical Evolution of Clump-Cluster and Chain Galaxies. *ApJ*, 670:237--248, November 2007. doi: 10.1086/522077.

R. G. Bower, J. Schaye, C. S. Frenk, T. Theuns, M. Schaller, R. A. Crain, and S. McAlpine. The dark nemesis of galaxy formation: why hot haloes trigger black hole growth and bring star formation to an end. *MNRAS*, 465:32--44, February 2017. doi: 10.1093/mnras/stw2735.

G. B. Brammer, P. G. van Dokkum, M. Franx, M. Fumagalli, S. Patel, H.-W. Rix, R. E. Skelton, M. Kriek, E. Nelson, K. B. Schmidt, R. Bezanson, E. da Cunha, D. K. Erb, X. Fan, N. Förster Schreiber, G. D. Illingworth, I. Labbé, J. Leja, B. Lundgren, D. Magee, D. Marchesini, P. McCarthy, I. Momcheva, A. Muzzin, R. Quadri, C. C. Steidel, T. Tal, D. Wake, K. E. Whitaker, and A. Williams. 3D-HST: A Wide-field Grism Spectroscopic Survey with the Hubble Space Telescope. *ApJS*, 200:13, June 2012. doi: 10.1088/0067-0049/200/2/13.

B. J. Brewer, A. A. Dutton, T. Treu, M. W. Auger, P. J. Marshall, M. Barnabè, A. S. Bolton, D. C. Koo, and L. V. E. Koopmans. The SWELLS survey - III. Disfavouring 'heavy' initial mass functions for spiral lens galaxies. *MNRAS*, 422:3574--3590, June 2012. doi: 10.1111/j.1365-2966.2012.20870.x.

J. Brinchmann, S. Charlot, S. D. M. White, C. Tremonti, G. Kauffmann, T. Heckman, and J. Brinkmann. The physical properties of star-forming galaxies in the low-redshift Universe. *MNRAS*, 351:1151--1179, July 2004. doi: 10.1111/j.1365-2966.2004.07881.

x.

C. B. Brook, F. Governato, R. Roškar, G. Stinson, A. M. Brooks, J. Wadsley, T. Quinn, B. K. Gibson, O. Snaith, K. Pilkington, E. House, and A. Pontzen. Hierarchical formation of bulgeless galaxies: why outflows have low angular momentum. *MNRAS*, 415: 1051--1060, August 2011. doi: 10.1111/j.1365-2966.2011.18545.x.

C. B. Brook, G. Stinson, B. K. Gibson, R. Roškar, J. Wadsley, and T. Quinn. Hierarchical formation of bulgeless galaxies - II. Redistribution of angular momentum via galactic fountains. *MNRAS*, 419:771--779, January 2012. doi: 10.1111/j.1365-2966.2011.19740.x.

G. Bruzual and S. Charlot. Stellar population synthesis at the resolution of 2003. *MNRAS*, 344:1000--1028, October 2003. doi: 10.1046/j.1365-8711.2003.06897.x.

M. Cappellari. Measuring the inclination and mass-to-light ratio of axisymmetric galaxies via anisotropic Jeans models of stellar kinematics. *MNRAS*, 390:71--86, October 2008. doi: 10.1111/j.1365-2966.2008.13754.x.

M. Cappellari. Anisotropic Jeans models of stellar kinematics: second moments including proper motions and radial velocities. *ArXiv e-prints*, November 2012.

M. Cappellari, E. Emsellem, D. Krajnović, R. M. McDermid, N. Scott, G. A. Verdoes Kleijn, L. M. Young, K. Alatalo, R. Bacon, L. Blitz, M. Bois, F. Bournaud, M. Bureau, R. L. Davies, T. A. Davis, P. T. de Zeeuw, P.-A. Duc, S. Khochfar, H. Kuntschner, P.-Y. Lablanche, R. Morganti, T. Naab, T. Oosterloo, M. Sarzi, P. Serra, and A.-M. Weijmans. The ATLAS^{3D} project - I. A volume-limited sample of 260 nearby early-type galaxies: science goals and selection criteria. *MNRAS*, 413:813--836, May 2011a. doi: 10.1111/j.1365-2966.2010.18174.x.

M. Cappellari, E. Emsellem, D. Krajnović, R. M. McDermid, P. Serra, K. Alatalo, L. Blitz, M. Bois, F. Bournaud, M. Bureau, R. L. Davies, T. A. Davis, P. T. de Zeeuw, S. Khochfar, H. Kuntschner, P.-Y. Lablanche, R. Morganti, T. Naab, T. Oosterloo, M. Sarzi, N. Scott, A.-M. Weijmans, and L. M. Young. The ATLAS^{3D} project - VII. A new look at the morphology of nearby galaxies: the kinematic morphology-density relation. *MNRAS*, 416:1680--1696, September 2011b. doi: 10.1111/j.1365-2966.2011.18600.x.

M. Cappellari, R. M. McDermid, K. Alatalo, L. Blitz, M. Bois, F. Bournaud, M. Bureau, A. F. Crocker, R. L. Davies, T. A. Davis, P. T. de Zeeuw, P.-A. Duc, E. Emsellem, S. Khochfar, D. Krajnović, H. Kuntschner, P.-Y. Lablanche, R. Morganti, T. Naab, T. Oosterloo, M. Sarzi, N. Scott, P. Serra, A.-M. Weijmans, and L. M. Young. Systematic variation of the stellar initial mass function in early-type galaxies. *Nature*, 484: 485--488, April 2012. doi: 10.1038/nature10972.

M. Cappellari, R. M. McDermid, K. Alatalo, L. Blitz, M. Bois, F. Bournaud, M. Bureau, A. F. Crocker, R. L. Davies, T. A. Davis, P. T. de Zeeuw, P.-A. Duc, E. Emsellem, S. Khochfar, D. Krajnović, H. Kuntschner, R. Morganti, T. Naab, T. Oosterloo, M. Sarzi, N. Scott, P. Serra, A.-M. Weijmans, and L. M. Young. The ATLAS^{3D} project - XX. Mass-size and mass-σ distributions of early-type galaxies: bulge fraction drives kinematics, mass-to-light ratio, molecular gas fraction and stellar initial mass function. *MNRAS*, 432:1862--1893, July 2013a. doi: 10.1093/mnras/stt644.

M. Cappellari, N. Scott, K. Alatalo, L. Blitz, M. Bois, F. Bournaud, M. Bureau, A. F.

Crocker, R. L. Davies, T. A. Davis, P. T. de Zeeuw, P.-A. Duc, E. Emsellem, S. Khochfar, D. Krajnović, H. Kuntschner, R. M. McDermid, R. Morganti, T. Naab, T. Oosterloo, M. Sarzi, P. Serra, A.-M. Weijmans, and L. M. Young. The ATLAS^{3D} project - XV. Benchmark for early-type galaxies scaling relations from 260 dynamical models: mass-to-light ratio, dark matter, Fundamental Plane and Mass Plane. *MNRAS*, 432:1709--1741, July 2013b. doi: 10.1093/mnras/stt562.

B. Catinella, D. Schiminovich, G. Kauffmann, S. Fabello, J. Wang, C. Hummels, J. Lemonias, S. M. Moran, R. Wu, R. Giovanelli, M. P. Haynes, T. M. Heckman, A. R. Basu-Zych, M. R. Blanton, J. Brinchmann, T. Budavári, T. Gonçalves, B. D. Johnson, R. C. Kennicutt, B. F. Madore, C. D. Martin, M. R. Rich, L. J. Tacconi, D. A. Thilker, V. Wild, and T. K. Wyder. The GALEX Arecibo SDSS Survey - I. Gas fraction scaling relations of massive galaxies and first data release. *MNRAS*, 403: 683--708, April 2010. doi: 10.1111/j.1365-2966.2009.16180.x.

G. Chabrier. Galactic Stellar and Substellar Initial Mass Function. *PASP*, 115:763--795, July 2003. doi: 10.1086/376392.

Y.-Y. Chang, A. van der Wel, E. da Cunha, and H.-W. Rix. Stellar Masses and Star Formation Rates for 1M Galaxies from SDSS+WISE. *ApJS*, 219:8, July 2015. doi: 10.1088/0067-0049/219/1/8.

C. Christensen and A. Brooks. The impact of feedback on merger-driven bulge growth. In *American Astronomical Society Meeting Abstracts*, volume 225 of *American Astronomical Society Meeting Abstracts*, page 437.08, January 2015.

M.T. Cicero. *De Natura Deorum (vol. 2)*. Cambridge University Press (1880 edition), 45 B.C.

B. Clauwens, J. Schaye, and M. Franx. An assessment of the evidence from ATLAS^{3D} for a variable initial mass function. *MNRAS*, 449:4091--4104, June 2015. doi: 10.1093/mnras/stv603.

B. Clauwens, M. Franx, and J. Schaye. A large difference in the progenitor masses of active and passive galaxies in the EAGLE simulation. *MNRAS*, 463:L1--L5, November 2016. doi: 10.1093/mnrasl/slw137.

C. Conroy and J. E. Gunn. FSPS: Flexible Stellar Population Synthesis. Astrophysics Source Code Library, October 2010.

C. Conroy and P. G. van Dokkum. The Stellar Initial Mass Function in Early-type Galaxies From Absorption Line Spectroscopy. II. Results. *ApJ*, 760:71, November 2012. doi: 10.1088/0004-637X/760/1/71.

C. Conroy, A. A. Dutton, G. J. Graves, J. T. Mendel, and P. G. van Dokkum. Dynamical versus Stellar Masses in Compact Early-type Galaxies: Further Evidence for Systematic Variation in the Stellar Initial Mass Function. *ApJ*, 776:L26, October 2013. doi: 10.1088/2041-8205/776/2/L26.

C. A. Correa, J. S. B. Wyithe, J. Schaye, and A. R. Duffy. The accretion history of dark matter haloes - II. The connections with the mass power spectrum and the density profile. *MNRAS*, 450:1521--1537, June 2015. doi: 10.1093/mnras/stv697.

C. A. Correa, J. Schaye, B. Clauwens, R. G. Bower, R. A. Crain, M. Schaller, T. Theuns, and A. C. R. Thob. The relation between galaxy morphology and colour in the EAGLE simulation. *ArXiv e-prints*, April 2017.

R. A. Crain, T. Theuns, C. Dalla Vecchia, V. R. Eke, C. S. Frenk, A. Jenkins, S. T. Kay, J. A. Peacock, F. R. Pearce, J. Schaye, V. Springel, P. A. Thomas, S. D. M. White, and R. P. C. Wiersma. Galaxies-intergalactic medium interaction calculation - I. Galaxy formation as a function of large-scale environment. *MNRAS*, 399:1773--1794, November 2009. doi: 10.1111/j.1365-2966.2009.15402.x.

R. A. Crain, I. G. McCarthy, C. S. Frenk, T. Theuns, and J. Schaye. X-ray coronae in simulations of disc galaxy formation. *MNRAS*, 407:1403--1422, September 2010. doi: 10.1111/j.1365-2966.2010.16985.x.

R. A. Crain, J. Schaye, R. G. Bower, M. Furlong, M. Schaller, T. Theuns, C. Dalla Vecchia, C. S. Frenk, I. G. McCarthy, J. C. Helly, A. Jenkins, Y. M. Rosas-Guevara, S. D. M. White, and J. W. Trayford. The EAGLE simulations of galaxy formation: calibration of subgrid physics and model variations. *MNRAS*, 450:1937--1961, June 2015. doi: 10.1093/mnras/stv725.

J. Dabringhausen, P. Kroupa, J. Pflamm-Altenburg, and S. Mieske. Low-mass X-Ray Binaries Indicate a Top-heavy Stellar Initial Mass Function in Ultracompact Dwarf Galaxies. *ApJ*, 747:72, March 2012. doi: 10.1088/0004-637X/747/1/72.

C. Dalla Vecchia and J. Schaye. Simulating galactic outflows with thermal supernova feedback. *MNRAS*, 426:140--158, October 2012. doi: 10.1111/j.1365-2966.2012.21704.x.

R. Davé. The galaxy stellar mass-star formation rate relation: evidence for an evolving stellar initial mass function? *MNRAS*, 385:147--160, March 2008. doi: 10.1111/j.1365-2966.2008.12866.x.

L. J. M. Davies, A. S. G. Robotham, S. P. Driver, M. Alpaslan, I. K. Baldry, J. Bland-Hawthorn, S. Brough, M. J. I. Brown, M. E. Cluver, M. J. Drinkwater, C. Foster, M. W. Grootes, I. S. Konstantopoulos, M. A. Lara-López, Á. R. López-Sánchez, J. Loveday, M. J. Meyer, A. J. Moffett, P. Norberg, M. S. Owers, C. C. Popescu, R. De Propris, R. Sharp, R. J. Tuffs, L. Wang, S. M. Wilkins, L. Dunne, N. Bourne, and M. W. L. Smith. Galaxy And Mass Assembly (GAMA): the effect of close interactions on star formation in galaxies. *MNRAS*, 452:616--636, September 2015. doi: 10.1093/mnras/stv1241.

G. De Lucia and J. Blaizot. The hierarchical formation of the brightest cluster galaxies. *MNRAS*, 375:2--14, February 2007. doi: 10.1111/j.1365-2966.2006.11287.x.

G. De Lucia, F. Fontanot, D. Wilman, and P. Monaco. Times, environments and channels of bulge formation in a Lambda cold dark matter cosmology. *MNRAS*, 414:1439--1454, June 2011. doi: 10.1111/j.1365-2966.2011.18475.x.

Y. Dubois, S. Peirani, C. Pichon, J. Devriendt, R. Gavazzi, C. Welker, and M. Volonteri. The HORIZON-AGN simulation: morphological diversity of galaxies promoted by AGN feedback. *MNRAS*, 463:3948--3964, December 2016. doi: 10.1093/mnras/stw2265.

A. A. Dutton, A. V. Macciò, J. T. Mendel, and L. Simard. Universal IMF versus dark halo response in early-type galaxies: breaking the degeneracy with the Fundamental Plane. *MNRAS*, 432:2496--2511, July 2013. doi: 10.1093/mnras/stt608.

O. J. Eggen, D. Lynden-Bell, and A. R. Sandage. Evidence from the motions of old stars that the Galaxy collapsed. *ApJ*, 136:748, November 1962. doi: 10.1086/147433.

K. El-Badry, E. Quataert, A. Wetzel, P. F. Hopkins, D. R. Weisz, T. K. Chan, A. Fitts, M. Boylan-Kolchin, D. Kereš, C.-A. Faucher-Giguère, and S. Garrison-Kimmel. Gas kinematics, morphology, and angular momentum in the FIRE simulations. *ArXiv e-prints*, May 2017.

B. Elmegreen, F. Bournaud, and D. Elmegreen. Bulge Formation by the Coalescence of Giant Clumps in Primordial Disk Galaxies. In *American Astronomical Society Meeting Abstracts #213*, volume 41 of *Bulletin of the American Astronomical Society*, page 496, January 2009.

E. Emsellem, G. Monnet, and R. Bacon. The multi-gaussian expansion method: a tool for building realistic photometric and kinematical models of stellar systems I. The formalism. *A&A*, 285:723--738, May 1994.

E. Emsellem, M. Cappellari, D. Krajnović, K. Alatalo, L. Blitz, M. Bois, F. Bournaud, M. Bureau, R. L. Davies, T. A. Davis, P. T. de Zeeuw, S. Khochfar, H. Kuntschner, P.-Y. Lablanche, R. M. McDermid, R. Morganti, T. Naab, T. Oosterloo, M. Sarzi, N. Scott, P. Serra, G. van de Ven, A.-M. Weijmans, and L. M. Young. The ATLAS^{3D} project - III. A census of the stellar angular momentum within the effective radius of early-type galaxies: unveiling the distribution of fast and slow rotators. *MNRAS*, 414: 888--912, June 2011. doi: 10.1111/j.1365-2966.2011.18496.x.

I. Ferreras, F. La Barbera, I. G. de la Rosa, A. Vazdekis, R. R. de Carvalho, J. Falcón-Barroso, and E. Ricciardelli. Systematic variation of the stellar initial mass function with velocity dispersion in early-type galaxies. *MNRAS*, 429:L15--L19, February 2013. doi: 10.1093/mnrasl/sls014.

I. Ferreras, C. Weidner, A. Vazdekis, and F. La Barbera. Further evidence for a time-dependent initial mass function in massive early-type galaxies. *MNRAS*, 448:L82--L86, March 2015. doi: 10.1093/mnrasl/slv003.

S. L. Finkelstein, R. E. Ryan, Jr., C. Papovich, M. Dickinson, M. Song, R. S. Somerville, H. C. Ferguson, B. Salmon, M. Giavalisco, A. M. Koekemoer, M. L. N. Ashby, P. Behroozi, M. Castellano, J. S. Dunlop, S. M. Faber, G. G. Fazio, A. Fontana, N. A. Grogin, N. Hathi, J. Jaacks, D. D. Kocevski, R. Livermore, R. J. McLure, E. Merlin, B. Mobasher, J. A. Newman, M. Rafelski, V. Tilvi, and S. P. Willner. The Evolution of the Galaxy Rest-frame Ultraviolet Luminosity Function over the First Two Billion Years. *ApJ*, 810:71, September 2015. doi: 10.1088/0004-637X/810/1/71.

D. B. Fisher and N. Drory. Demographics of Bulge Types within 11 Mpc and Implications for Galaxy Evolution. *ApJ*, 733:L47, June 2011. doi: 10.1088/2041-8205/733/2/L47.

M. Furlong, R. G. Bower, T. Theuns, J. Schaye, R. A. Crain, M. Schaller, C. Dalla Vecchia, C. S. Frenk, I. G. McCarthy, J. Helly, A. Jenkins, and Y. M. Rosas-Guevara. Evolution of galaxy stellar masses and star formation rates in the EAGLE simulations. *MNRAS*, 450:4486--4504, July 2015. doi: 10.1093/mnras/stv852.

M. Furlong, R. G. Bower, R. A. Crain, J. Schaye, T. Theuns, J. W. Trayford, Y. Qu, M. Schaller, M. Berthet, and J. C. Helly. Size evolution of normal and compact galaxies in the EAGLE simulation. *MNRAS*, 465:722--738, February 2017. doi: 10.1093/mnras/stw2740.

D. A. Gadotti. Structural properties of pseudo-bulges, classical bulges and elliptical galaxies: a Sloan Digital Sky Survey perspective. *MNRAS*, 393:1531--1552, March 2009.

doi: 10.1111/j.1365-2966.2008.14257.x.

A. Gallazzi, S. Charlot, J. Brinchmann, S. D. M. White, and C. A. Tremonti. The ages and metallicities of galaxies in the local universe. *MNRAS*, 362:41--58, September 2005. doi: 10.1111/j.1365-2966.2005.09321.x.

M. Geha, T. M. Brown, J. Tumlinson, J. S. Kalirai, J. D. Simon, E. N. Kirby, D. A. VandenBerg, R. R. Muñoz, R. J. Avila, P. Guhathakurta, and H. C. Ferguson. The Stellar Initial Mass Function of Ultra-faint Dwarf Galaxies: Evidence for IMF Variations with Galactic Environment. *ApJ*, 771:29, July 2013. doi: 10.1088/0004-637X/771/1/29.

S. Genel, R. Genzel, N. Bouché, T. Naab, and A. Sternberg. The Halo Merger Rate in the Millennium Simulation and Implications for Observed Galaxy Merger Fractions. *ApJ*, 701:2002--2018, August 2009. doi: 10.1088/0004-637X/701/2/2002.

S. Genel, S. M. Fall, L. Hernquist, M. Vogelsberger, G. F. Snyder, V. Rodriguez-Gomez, D. Sijacki, and V. Springel. Galactic Angular Momentum in the Illustris Simulation: Feedback and the Hubble Sequence. *ApJ*, 804:L40, May 2015. doi: 10.1088/2041-8205/804/2/L40.

R. M. González Delgado, R. Cid Fernandes, R. García-Benito, E. Pérez, A. L. de Amorim, C. Cortijo-Ferrero, E. A. D. Lacerda, R. López Fernández, S. F. Sánchez, N. Vale Asari, J. Alves, J. Bland-Hawthorn, L. Galbany, A. Gallazzi, B. Husemann, S. Bekeraite, B. Jungwiert, A. R. López-Sánchez, A. de Lorenzo-Cáceres, R. A. Marino, D. Mast, M. Mollá, A. del Olmo, P. Sánchez-Blázquez, G. van de Ven, J. M. Vílchez, C. J. Walcher, L. Wisotzki, B. Ziegler, and C. collaboration920. Insights on the Stellar Mass-Metallicity Relation from the CALIFA Survey. *ApJ*, 791:L16, August 2014. doi: 10.1088/2041-8205/791/1/L16.

D Goodstein. Richard P. Feynman, Teacher. *Physics Today*, 42, number 2:70--75, February 1989.

F. Governato, C. B. Brook, A. M. Brooks, L. Mayer, B. Willman, P. Jonsson, A. M. Stilp, L. Pope, C. Christensen, J. Wadsley, and T. Quinn. Forming a large disc galaxy from a $z < 1$ major merger. *MNRAS*, 398:312--320, September 2009. doi: 10.1111/j.1365-2966.2009.15143.x.

F. Governato, C. Brook, L. Mayer, A. Brooks, G. Rhee, J. Wadsley, P. Jonsson, B. Willman, G. Stinson, T. Quinn, and P. Madau. Bulgeless dwarf galaxies and dark matter cores from supernova-driven outflows. *Nature*, 463:203--206, January 2010. doi: 10.1038/nature08640.

J. Guedes, L. Mayer, M. Carollo, and P. Madau. Pseudobulge Formation as a Dynamical Rather than a Secular Process. *ApJ*, 772:36, July 2013. doi: 10.1088/0004-637X/772/1/36.

M. L. P. Gunawardhana, A. M. Hopkins, R. G. Sharp, S. Brough, E. Taylor, J. Bland-Hawthorn, C. Maraston, R. J. Tuffs, C. C. Popescu, D. Wijesinghe, D. H. Jones, S. Croom, E. Sadler, S. Wilkins, S. P. Driver, J. Liske, P. Norberg, I. K. Baldry, S. P. Bamford, J. Loveday, J. A. Peacock, A. S. G. Robotham, D. B. Zucker, Q. A. Parker, C. J. Conselice, E. Cameron, C. S. Frenk, D. T. Hill, L. S. Kelvin, K. Kuijken, B. F. Madore, B. Nichol, H. R. Parkinson, K. A. Pimbblet, M. Prescott, W. J. Sutherland, D. Thomas, and E. van Kampen. Galaxy and Mass Assembly (GAMA): the star formation rate dependence of the stellar initial mass function. *MNRAS*, 415:1647--1662,

August 2011. doi: 10.1111/j.1365-2966.2011.18800.x.

Q. Guo, S. White, M. Boylan-Kolchin, G. De Lucia, G. Kauffmann, G. Lemson, C. Li, V. Springel, and S. Weinmann. From dwarf spheroidals to cD galaxies: simulating the galaxy population in a ΛCDM cosmology. *MNRAS*, 413:101--131, May 2011. doi: 10.1111/j.1365-2966.2010.18114.x.

H. Hancock. The ethics of jazz, harvard lecture series, norton lectures, 2004.

B. M. B. Henriques, S. D. M. White, P. A. Thomas, R. Angulo, Q. Guo, G. Lemson, V. Springel, and R. Overzier. Galaxy formation in the Planck cosmology - I. Matching the observed evolution of star formation rates, colours and stellar masses. *MNRAS*, 451: 2663--2680, August 2015. doi: 10.1093/mnras/stv705.

L. Hernquist. Tidal triggering of starbursts and nuclear activity in galaxies. *Nature*, 340: 687--691, August 1989. doi: 10.1038/340687a0.

A. R. Hill, A. Muzzin, M. Franx, B. Clauwens, C. Schreiber, D. Marchesini, M. Stefanon, I. Labbe, G. Brammer, K. Caputi, J. Fynbo, B. Milvang-Jensen, R. E. Skelton, P. van Dokkum, and K. E. Whitaker. The Mass, Color, and Structural Evolution of Today's Massive Galaxies Since $z \approx 5$. *ApJ*, 837:147, March 2017. doi: 10.3847/1538-4357/aa61fe.

A. M. Hopkins and J. F. Beacom. Erratum: ``On the Normalization of the Cosmic Star Formation History" (<A href="/abs/2006ApJ...651..142H">ApJ, 651, 142 [2006]</A>). *ApJ*, 682:1486--1486, August 2008. doi: 10.1086/589809.

P. F. Hopkins, K. Bundy, D. Croton, L. Hernquist, D. Keres, S. Khochfar, K. Stewart, A. Wetzel, and J. D. Younger. Mergers and Bulge Formation in ΛCDM: Which Mergers Matter? *ApJ*, 715:202--229, May 2010. doi: 10.1088/0004-637X/715/1/202.

P. F. Hopkins, D. Kereš, J. Oñorbe, C.-A. Faucher-Giguère, E. Quataert, N. Murray, and J. S. Bullock. Galaxies on FIRE (Feedback In Realistic Environments): stellar feedback explains cosmologically inefficient star formation. *MNRAS*, 445:581--603, November 2014. doi: 10.1093/mnras/stu1738.

E. A. Hoversten and K. Glazebrook. Evidence for a Nonuniversal Stellar Initial Mass Function from the Integrated Properties of SDSS Galaxies. *ApJ*, 675:163-187, March 2008. doi: 10.1086/524095.

J. Jaacks, S. L. Finkelstein, and K. Nagamine. Connecting the Dots: Tracking Galaxy Evolution Using Constant Cumulative Number Density at $3 < z < 7$. *ApJ*, 817:174, February 2016. doi: 10.3847/0004-637X/817/2/174.

G. Kauffmann, T. M. Heckman, S. D. M. White, S. Charlot, C. Tremonti, J. Brinchmann, G. Bruzual, E. W. Peng, M. Seibert, M. Bernardi, M. Blanton, J. Brinkmann, F. Castander, I. Csábai, M. Fukugita, Z. Ivezic, J. A. Munn, R. C. Nichol, N. Padmanabhan, A. R. Thakar, D. H. Weinberg, and D. York. Stellar masses and star formation histories for 10^5 galaxies from the Sloan Digital Sky Survey. *MNRAS*, 341:33--53, May 2003. doi: 10.1046/j.1365-8711.2003.06291.x.

H. Kirk and P. C. Myers. Young Stellar Groups and Their Most Massive Stars. *ApJ*, 727: 64, February 2011. doi: 10.1088/0004-637X/727/2/64.

J. Kormendy. Kinematics of extragalactic bulges: evidence that some bulges are really disks. In H. Dejonghe and H. J. Habing, editors, *Galactic Bulges*, volume 153 of *IAU Symposium*, page 209, 1993.

J. Kormendy and R. C. Kennicutt, Jr. Secular Evolution and the Formation of Pseudobulges in Disk Galaxies. *ARA&A*, 42:603--683, September 2004. doi: 10.1146/annurev.astro.42.053102.134024.

J. Kormendy, N. Drory, R. Bender, and M. E. Cornell. Bulgeless Giant Galaxies Challenge Our Picture of Galaxy Formation by Hierarchical Clustering. *ApJ*, 723:54--80, November 2010. doi: 10.1088/0004-637X/723/1/54.

P. Kroupa. On the variation of the initial mass function. *MNRAS*, 322:231--246, April 2001. doi: 10.1046/j.1365-8711.2001.04022.x.

P. Kroupa. The Initial Mass Function of Stars: Evidence for Uniformity in Variable Systems. *Science*, 295:82--91, January 2002. doi: 10.1126/science.1067524.

P. Kroupa, C. Weidner, J. Pflamm-Altenburg, I. Thies, J. Dabringhausen, M. Marks, and T. Maschberger. *The Stellar and Sub-Stellar Initial Mass Function of Simple and Composite Populations*, page 115. 2013. doi: 10.1007/978-94-007-5612-0_4.

M. R. Krumholz, B. Burkhart, J. C. Forbes, and R. M. Crocker. A Unified Model for Galactic Discs: Star Formation, Turbulence Driving, and Mass Transport. *ArXiv e-prints*, May 2017.

F. La Barbera, I. Ferreras, A. Vazdekis, I. G. de la Rosa, R. R. de Carvalho, M. Trevisan, J. Falcón-Barroso, and E. Ricciardelli. SPIDER VIII - constraints on the stellar initial mass function of early-type galaxies from a variety of spectral features. *MNRAS*, 433: 3017--3047, August 2013. doi: 10.1093/mnras/stt943.

C. d. P. Lagos, A. R. H. Stevens, R. G. Bower, T. A. Davis, S. Contreras, N. D. Padilla, D. Obreschkow, D. Croton, J. W. Trayford, C. Welker, and T. Theuns. The catastrophic effect of mergers on the angular momentum and morphology of galaxies in EAGLE. *ArXiv e-prints*, January 2017a.

C. d. P. Lagos, T. Theuns, A. R. H. Stevens, L. Cortese, N. D. Padilla, T. A. Davis, S. Contreras, and D. Croton. Angular momentum evolution of galaxies in EAGLE. *MNRAS*, 464:3850--3870, February 2017b. doi: 10.1093/mnras/stw2610.

J. C. Lee, A. Gil de Paz, C. Tremonti, R. C. Kennicutt, Jr., S. Salim, M. Bothwell, D. Calzetti, J. Dalcanton, D. Dale, C. Engelbracht, S. J. J. G. Funes, B. Johnson, S. Sakai, E. Skillman, L. van Zee, F. Walter, and D. Weisz. Comparison of Hα and UV Star Formation Rates in the Local Volume: Systematic Discrepancies for Dwarf Galaxies. *ApJ*, 706:599-613, November 2009. doi: 10.1088/0004-637X/706/1/599.

J. Leja, P. van Dokkum, and M. Franx. Tracing Galaxies through Cosmic Time with Number Density Selection. *ApJ*, 766:33, March 2013. doi: 10.1088/0004-637X/766/1/33.

H. Li, R. Li, S. Mao, D. Xu, R. J. Long, and E. Emsellem. Assessing the Jeans Anisotropic Multi-Gaussian Expansion method with the Illustris simulation. *MNRAS*, 455:3680--3692, February 2016. doi: 10.1093/mnras/stv2565.

A. Loeb and P. J. E. Peebles. Cosmological Origin of the Stellar Velocity Dispersions in Massive Early-Type Galaxies. *ApJ*, 589:29--34, May 2003. doi: 10.1086/374349.

E. K. Lofthouse, S. Kaviraj, C. J. Conselice, A. Mortlock, and W. Hartley. Major mergers are not significant drivers of star formation or morphological transformation around the epoch of peak cosmic star formation. *MNRAS*, 465:2895--2900, March 2017. doi: 10.1093/mnras/stw2895.

B. F. Lundgren, P. van Dokkum, M. Franx, I. Labbe, M. Trenti, R. Bouwens, V. Gonzalez, G. Illingworth, D. Magee, P. Oesch, and M. Stiavelli. Tracing the Mass Growth and Star Formation Rate Evolution of Massive Galaxies from z ˜ 6 to z ˜ 1 in the Hubble Ultra-Deep Field. *ApJ*, 780:34, January 2014. doi: 10.1088/0004-637X/780/1/34.

D. Marchesini, A. Muzzin, M. Stefanon, M. Franx, G. G. Brammer, C. Z. Marsan, B. Vulcani, J. P. U. Fynbo, B. Milvang-Jensen, J. S. Dunlop, and F. Buitrago. The Progenitors of Local Ultra-massive Galaxies Across Cosmic Time: From Dusty Star-bursting to Quiescent Stellar Populations. *ApJ*, 794:65, October 2014. doi: 10.1088/0004-637X/794/1/65.

P. Marigo. Chemical yields from low- and intermediate-mass stars: Model predictions and basic observational constraints. *A&A*, 370:194--217, April 2001. doi: 10.1051/0004-6361:20000247.

M. Marks, P. Kroupa, J. Dabringhausen, and M. S. Pawlowski. Evidence for top-heavy stellar initial mass functions with increasing density and decreasing metallicity. *MNRAS*, 422:2246--2254, May 2012. doi: 10.1111/j.1365-2966.2012.20767.x.

I. Martín-Navarro, F. L. Barbera, A. Vazdekis, J. Falcón-Barroso, and I. Ferreras. Radial variations in the stellar initial mass function of early-type galaxies. *MNRAS*, 447:1033--1048, February 2015a. doi: 10.1093/mnras/stu2480.

I. Martín-Navarro, F. La Barbera, A. Vazdekis, A. Ferré-Mateu, I. Trujillo, and M. A. Beasley. The initial mass function of a massive relic galaxy. *MNRAS*, 451:1081--1089, July 2015b. doi: 10.1093/mnras/stv1022.

I. Martín-Navarro, P. G. Pérez-González, I. Trujillo, P. Esquej, A. Vazdekis, H. Domínguez Sánchez, G. Barro, G. Bruzual, S. Charlot, A. Cava, I. Ferreras, N. Espino, F. La Barbera, A. M. Koekemoer, and A. J. Cenarro. The Stellar Initial Mass Function at $0.9 < z < 1.5$. *ApJ*, 798:L4, January 2015c. doi: 10.1088/2041-8205/798/1/L4.

I. Martín-Navarro, A. Vazdekis, F. La Barbera, J. Falcón-Barroso, M. Lyubenova, G. van de Ven, I. Ferreras, S. F. Sánchez, S. C. Trager, R. García-Benito, D. Mast, M. A. Mendoza, P. Sánchez-Blázquez, R. González Delgado, C. J. Walcher, and The CALIFA Team. IMF-Metallicity: A Tight Local Relation Revealed by the CALIFA Survey. *ApJ*, 806:L31, June 2015d. doi: 10.1088/2041-8205/806/2/L31.

S. McAlpine, J. C. Helly, M. Schaller, J. W. Trayford, Y. Qu, M. Furlong, R. G. Bower, R. A. Crain, J. Schaye, T. Theuns, C. Dalla Vecchia, C. S. Frenk, I. G. McCarthy, A. Jenkins, Y. Rosas-Guevara, S. D. M. White, M. Baes, P. Camps, and G. Lemson. The EAGLE simulations of galaxy formation: Public release of halo and galaxy catalogues. *Astronomy and Computing*, 15:72--89, April 2016. doi: 10.1016/j.ascom.2016.02.004.

H. J. McCracken, B. Milvang-Jensen, J. Dunlop, M. Franx, J. P. U. Fynbo, O. Le Fèvre, J. Holt, K. I. Caputi, Y. Goranova, F. Buitrago, J. P. Emerson, W. Freudling, P. Hudelot, C. López-Sanjuan, F. Magnard, Y. Mellier, P. Møller, K. K. Nilsson, W. Sutherland, L. Tasca, and J. Zabl. UltraVISTA: a new ultra-deep near-infrared survey in COSMOS. *A&A*, 544:A156, August 2012. doi: 10.1051/0004-6361/201219507.

R. M. McDermid, M. Cappellari, K. Alatalo, E. Bayet, L. Blitz, M. Bois, F. Bournaud, M. Bureau, A. F. Crocker, R. L. Davies, T. A. Davis, P. T. de Zeeuw, P.-A.

Duc, E. Emsellem, S. Khochfar, D. Krajnović, H. Kuntschner, R. Morganti, T. Naab, T. Oosterloo, M. Sarzi, N. Scott, P. Serra, A.-M. Weijmans, and L. M. Young. Connection between Dynamically Derived Initial Mass Function Normalization and Stellar Population Parameters. *ApJ*, 792:L37, September 2014. doi: 10.1088/2041-8205/792/2/L37.

S. L. McGee, R. Goto, and M. L. Balogh. The stellar mass function and efficiency of galaxy formation with a varying initial mass function. *MNRAS*, 438:3188--3204, March 2014. doi: 10.1093/mnras/stt2426.

S. Mei, J. P. Blakeslee, P. Côté, J. L. Tonry, M. J. West, L. Ferrarese, A. Jordán, E. W. Peng, A. Anthony, and D. Merritt. The ACS Virgo Cluster Survey. XIII. SBF Distance Catalog and the Three-dimensional Structure of the Virgo Cluster. *ApJ*, 655:144--162, January 2007. doi: 10.1086/509598.

G. R. Meurer, O. I. Wong, J. H. Kim, D. J. Hanish, SUNGG, and SINGG. Evidence for a Non-Uniform Initial Mass Function in the Local Universe. In *American Astronomical Society Meeting Abstracts #213*, volume 41 of *Bulletin of the American Astronomical Society*, page 443.06, January 2009.

T. Morishita, T. Ichikawa, M. Noguchi, M. Akiyama, S. G. Patel, M. Kajisawa, and T. Obata. From Diversity to Dichotomy, and Quenching: Milky-Way-like and Massive Galaxy Progenitors at $0.5 < z < 3.0$. *ApJ*, 805:34, May 2015. doi: 10.1088/0004-637X/805/1/34.

J. R. Mould, J. P. Huchra, W. L. Freedman, R. C. Kennicutt, Jr., L. Ferrarese, H. C. Ford, B. K. Gibson, J. A. Graham, S. M. G. Hughes, G. D. Illingworth, D. D. Kelson, L. M. Macri, B. F. Madore, S. Sakai, K. M. Sebo, N. A. Silbermann, and P. B. Stetson. The Hubble Space Telescope Key Project on the Extragalactic Distance Scale. XXVIII. Combining the Constraints on the Hubble Constant. *ApJ*, 529:786--794, February 2000. doi: 10.1086/308304.

J. Moustakas, A. L. Coil, J. Aird, M. R. Blanton, R. J. Cool, D. J. Eisenstein, A. J. Mendez, K. C. Wong, G. Zhu, and S. Arnouts. PRIMUS: Constraints on Star Formation Quenching and Galaxy Merging, and the Evolution of the Stellar Mass Function from z = 0-1. *ApJ*, 767:50, April 2013. doi: 10.1088/0004-637X/767/1/50.

C. J. Mundy, C. J. Conselice, and J. R. Ownsworth. Tracing galaxy populations through cosmic time: a critical test of methods for connecting the same galaxies between different redshifts at $z < 3$. *MNRAS*, 450:3696--3707, July 2015. doi: 10.1093/mnras/stv860.

A. Muzzin, D. Marchesini, M. Stefanon, M. Franx, H. J. McCracken, B. Milvang-Jensen, J. S. Dunlop, J. P. U. Fynbo, G. Brammer, I. Labbé, and P. G. van Dokkum. The Evolution of the Stellar Mass Functions of Star-forming and Quiescent Galaxies to z = 4 from the COSMOS/UltraVISTA Survey. *ApJ*, 777:18, November 2013a. doi: 10.1088/0004-637X/777/1/18.

A. Muzzin, D. Marchesini, M. Stefanon, M. Franx, B. Milvang-Jensen, J. S. Dunlop, J. P. U. Fynbo, G. Brammer, I. Labbé, and P. van Dokkum. A Public K_s -selected Catalog in the COSMOS/ULTRAVISTA Field: Photometry, Photometric Redshifts, and Stellar Population Parameters. *ApJS*, 206:8, May 2013b. doi: 10.1088/0067-0049/206/1/8.

T. Naab, L. Oser, E. Emsellem, M. Cappellari, D. Krajnović, R. M. McDermid, K. Alat-

alo, E. Bayet, L. Blitz, M. Bois, F. Bournaud, M. Bureau, A. Crocker, R. L. Davies, T. A. Davis, P. T. de Zeeuw, P.-A. Duc, M. Hirschmann, P. H. Johansson, S. Khochfar, H. Kuntschner, R. Morganti, T. Oosterloo, M. Sarzi, N. Scott, P. Serra, G. v. d. Ven, A. Weijmans, and L. M. Young. The ATLAS^{3D} project - XXV. Two-dimensional kinematic analysis of simulated galaxies and the cosmological origin of fast and slow rotators. *MNRAS*, 444:3357--3387, November 2014. doi: 10.1093/mnras/stt1919.

M. Noguchi. Early Evolution of Disk Galaxies: Formation of Bulges in Clumpy Young Galactic Disks. *ApJ*, 514:77--95, March 1999. doi: 10.1086/306932.

M. Oguri, C. E. Rusu, and E. E. Falco. The stellar and dark matter distributions in elliptical galaxies from the ensemble of strong gravitational lenses. *MNRAS*, February 2014. doi: 10.1093/mnras/stu106.

S. Oh and P. Kroupa. Dynamical ejections of massive stars from young star clusters under diverse initial conditions. *A&A*, 590:A107, May 2016. doi: 10.1051/0004-6361/201628233.

L. Oser, J. P. Ostriker, T. Naab, P. H. Johansson, and A. Burkert. The Two Phases of Galaxy Formation. *ApJ*, 725:2312--2323, December 2010. doi: 10.1088/0004-637X/725/2/2312.

C. Papovich, S. L. Finkelstein, H. C. Ferguson, J. M. Lotz, and M. Giavalisco. The rising star formation histories of distant galaxies and implications for gas accretion with time. *MNRAS*, 412:1123--1136, April 2011. doi: 10.1111/j.1365-2966.2010.17965.x.

C. Papovich, I. Labbé, R. Quadri, V. Tilvi, P. Behroozi, E. F. Bell, K. Glazebrook, L. Spitler, C. M. S. Straatman, K.-V. Tran, M. Cowley, R. Davé, A. Dekel, M. Dickinson, H. C. Ferguson, S. L. Finkelstein, E. Gawiser, H. Inami, S. M. Faber, G. G. Kacprzak, L. Kawinwanichakij, D. Kocevski, A. Koekemoer, D. C. Koo, P. Kurczynski, J. M. Lotz, Y. Lu, R. A. Lucas, D. McIntosh, N. Mehrtens, B. Mobasher, A. Monson, G. Morrison, T. Nanayakkara, S. E. Persson, B. Salmon, R. Simons, A. Tomczak, P. van Dokkum, B. Weiner, and S. P. Willner. ZFOURGE/CANDELS: On the Evolution of M* Galaxy Progenitors from z = 3 to 0.5. *ApJ*, 803:26, April 2015. doi: 10.1088/0004-637X/803/1/26.

N. Pastorello, D. A. Forbes, C. Foster, J. P. Brodie, C. Usher, A. J. Romanowsky, J. Strader, and J. A. Arnold. The SLUGGS survey: exploring the metallicity gradients of nearby early-type galaxies to large radii. *MNRAS*, 442:1003--1039, August 2014. doi: 10.1093/mnras/stu937.

S. G. Patel, P. G. van Dokkum, M. Franx, R. F. Quadri, A. Muzzin, D. Marchesini, R. J. Williams, B. P. Holden, and M. Stefanon. HST/WFC3 Confirmation of the Inside-out Growth of Massive Galaxies at $0 < z < 2$ and Identification of Their Star-forming Progenitors at z ~ 3. *ApJ*, 766:15, March 2013. doi: 10.1088/0004-637X/766/1/15.

M. B. Peacock, S. E. Zepf, T. J. Maccarone, A. Kundu, A. H. Gonzalez, B. D. Lehmer, and C. Maraston. Evidence for a Constant Initial Mass Function in Early-type Galaxies Based on Their X-Ray Binary Populations. *ApJ*, 784:162, April 2014. doi: 10.1088/0004-637X/784/2/162.

Z. Penoyre, B. P. Moster, D. Sijacki, and S. Genel. The origin and evolution of fast and slow rotators in the Illustris simulation. *MNRAS*, 468:3883--3906, July 2017. doi: 10.1093/mnras/stx762.

R. Penrose. *The Road to Reality - A Complete guide to the Laws of the Universe*. Jonathan Cape, 2004. ISBN 0-224-04447-8.

I. Pérez, I. Martínez-Valpuesta, T. Ruiz-Lara, A. de Lorenzo-Caceres, J. Falcón-Barroso, E. Florido, R. M. González Delgado, M. Lyubenova, R. A. Marino, S. F. Sánchez, P. Sánchez-Blázquez, G. van de Ven, and A. Zurita. Observational constraints to boxy/peanut bulge formation time. *MNRAS*, 470:L122--L126, September 2017. doi: 10.1093/mnrasl/slx087.

J. Perez, O. Valenzuela, P. B. Tissera, and L. Michel-Dansac. Clumpy disc and bulge formation. *MNRAS*, 436:259--265, November 2013. doi: 10.1093/mnras/stt1563.

J. R. Peterson, S. M. Kahn, F. B. S. Paerels, J. S. Kaastra, T. Tamura, J. A. M. Bleeker, C. Ferrigno, and J. G. Jernigan. High-Resolution X-Ray Spectroscopic Constraints on Cooling-Flow Models for Clusters of Galaxies. *ApJ*, 590:207--224, June 2003. doi: 10.1086/374830.

J. Pflamm-Altenburg and P. Kroupa. The Fundamental Gas Depletion and Stellar-Mass Buildup Times of Star-Forming Galaxies. *ApJ*, 706:516--524, November 2009. doi: 10.1088/0004-637X/706/1/516.

J. Pflamm-Altenburg, C. Weidner, and P. Kroupa. Diverging UV and Hα fluxes of star-forming galaxies predicted by the IGIMF theory. *MNRAS*, 395:394--400, May 2009. doi: 10.1111/j.1365-2966.2009.14522.x.

A. Pietrinferni, S. Cassisi, M. Salaris, and S. Hidalgo. The BaSTI Stellar Evolution Database: models for extremely metal-poor and super-metal-rich stellar populations. *A&A*, 558:A46, October 2013. doi: 10.1051/0004-6361/201321950.

A. Pillepich, P. Madau, and L. Mayer. Building Late-type Spiral Galaxies by In-situ and Ex-situ Star Formation. *ApJ*, 799:184, February 2015. doi: 10.1088/0004-637X/799/2/184.

M. Pohlen, M. Balcells, R. Lütticke, and R.-J. Dettmar. Evidence for a large stellar bar in the Low Surface Brightness galaxy UGC 7321. *A&A*, 409:485--490, October 2003. doi: 10.1051/0004-6361:20031091.

L. Portinari, C. Chiosi, and A. Bressan. Galactic chemical enrichment with new metallicity dependent stellar yields. *A&A*, 334:505--539, June 1998.

Y. Qu, J. C. Helly, R. G. Bower, T. Theuns, R. A. Crain, C. S. Frenk, M. Furlong, S. McAlpine, M. Schaller, J. Schaye, and S. D. M. White. A chronicle of galaxy mass assembly in the EAGLE simulation. *MNRAS*, 464:1659--1675, January 2017. doi: 10.1093/mnras/stw2437.

N. Raha, J. A. Sellwood, R. A. James, and F. D. Kahn. A dynamical instability of bars in disk galaxies. *Nature*, 352:411, August 1991. doi: 10.1038/352411a0.

S. Recchi and P. Kroupa. The chemical evolution of galaxies with a variable integrated galactic initial mass function. *MNRAS*, 446:4168--4175, February 2015. doi: 10.1093/mnras/stu2338.

V. Rodriguez-Gomez, L. V. Sales, S. Genel, A. Pillepich, J. Zjupa, D. Nelson, B. Griffen, P. Torrey, G. F. Snyder, M. Vogelsberger, V. Springel, C.-P. Ma, and L. Hernquist. The role of mergers and halo spin in shaping galaxy morphology. *MNRAS*, 467:3083--3098, May 2017. doi: 10.1093/mnras/stx305.

S. Sachdeva, K. Saha, and H. P. Singh. Growth of Bulges in Disk Galaxies Since z $\approx$ 1.

ApJ, 840:79, May 2017. doi: 10.3847/1538-4357/aa6c61.

A. Saintonge, G. Kauffmann, C. Kramer, L. J. Tacconi, C. Buchbender, B. Catinella, S. Fabello, J. Graciá-Carpio, J. Wang, L. Cortese, J. Fu, R. Genzel, R. Giovanelli, Q. Guo, M. P. Haynes, T. M. Heckman, M. R. Krumholz, J. Lemonias, C. Li, S. Moran, N. Rodriguez-Fernandez, D. Schiminovich, K. Schuster, and A. Sievers. COLD GASS, an IRAM legacy survey of molecular gas in massive galaxies - I. Relations between H_2, H I, stellar content and structural properties. *MNRAS*, 415:32--60, July 2011. doi: 10.1111/j.1365-2966.2011.18677.x.

L. V. Sales, J. F. Navarro, J. Schaye, C. Dalla Vecchia, V. Springel, and C. M. Booth. Feedback and the structure of simulated galaxies at redshift z= 2. *MNRAS*, 409:1541--1556, December 2010. doi: 10.1111/j.1365-2966.2010.17391.x.

L. V. Sales, J. F. Navarro, T. Theuns, J. Schaye, S. D. M. White, C. S. Frenk, R. A. Crain, and C. Dalla Vecchia. The origin of discs and spheroids in simulated galaxies. *MNRAS*, 423:1544--1555, June 2012. doi: 10.1111/j.1365-2966.2012.20975.x.

S. Salim, R. M. Rich, S. Charlot, J. Brinchmann, B. D. Johnson, D. Schiminovich, M. Seibert, R. Mallery, T. M. Heckman, K. Forster, P. G. Friedman, D. C. Martin, P. Morrissey, S. G. Neff, T. Small, T. K. Wyder, L. Bianchi, J. Donas, Y.-W. Lee, B. F. Madore, B. Milliard, A. S. Szalay, B. Y. Welsh, and S. K. Yi. UV Star Formation Rates in the Local Universe. *ApJS*, 173:267--292, December 2007. doi: 10.1086/519218.

E. E. Salpeter. The Luminosity Function and Stellar Evolution. *ApJ*, 121:161, January 1955. doi: 10.1086/145971.

S. F. Sánchez, R. C. Kennicutt, A. Gil de Paz, G. van de Ven, J. M. Vílchez, L. Wisotzki, C. J. Walcher, D. Mast, J. A. L. Aguerri, S. Albiol-Pérez, A. Alonso-Herrero, J. Alves, J. Bakos, T. Bartáková, J. Bland-Hawthorn, A. Boselli, D. J. Bomans, A. Castillo-Morales, C. Cortijo-Ferrero, A. de Lorenzo-Cáceres, A. Del Olmo, R.-J. Dettmar, A. Díaz, S. Ellis, J. Falcón-Barroso, H. Flores, A. Gallazzi, B. García-Lorenzo, R. González Delgado, N. Gruel, T. Haines, C. Hao, B. Husemann, J. Iglésias-Páramo, K. Jahnke, B. Johnson, B. Jungwiert, V. Kalinova, C. Kehrig, D. Kupko, Á. R. López-Sánchez, M. Lyubenova, R. A. Marino, E. Mármol-Queraltó, I. Márquez, J. Masegosa, S. Meidt, J. Mendez-Abreu, A. Monreal-Ibero, C. Montijo, A. M. Mourão, G. Palacios-Navarro, P. Papaderos, A. Pasquali, R. Peletier, E. Pérez, I. Pérez, A. Quirrenbach, M. Relaño, F. F. Rosales-Ortega, M. M. Roth, T. Ruiz-Lara, P. Sánchez-Blázquez, C. Sengupta, R. Singh, V. Stanishev, S. C. Trager, A. Vazdekis, K. Viironen, V. Wild, S. Zibetti, and B. Ziegler. CALIFA, the Calar Alto Legacy Integral Field Area survey. I. Survey presentation. *A&A*, 538:A8, February 2012. doi: 10.1051/0004-6361/201117353.

J. Scalo. Fifty years of IMF variation: the intermediate-mass stars. In E. Corbelli, F. Palla, and H. Zinnecker, editors, *The Initial Mass Function 50 Years Later*, volume 327 of *Astrophysics and Space Science Library*, page 23, January 2005.

C. Scannapieco, D. A. Gadotti, P. Jonsson, and S. D. M. White. An observer's view of simulated galaxies: disc-to-total ratios, bars and (pseudo-)bulges. *MNRAS*, 407:L41--L45, September 2010. doi: 10.1111/j.1745-3933.2010.00900.x.

M. Schaller, C. S. Frenk, R. G. Bower, T. Theuns, A. Jenkins, J. Schaye, R. A. Crain, M. Furlong, C. Dalla Vecchia, and I. G. McCarthy. Baryon effects on the internal

structure of ΛCDM haloes in the EAGLE simulations. *MNRAS*, 451:1247--1267, August 2015. doi: 10.1093/mnras/stv1067.

J. Schaye and C. Dalla Vecchia. On the relation between the Schmidt and Kennicutt-Schmidt star formation laws and its implications for numerical simulations. *MNRAS*, 383:1210--1222, January 2008. doi: 10.1111/j.1365-2966.2007.12639.x.

J. Schaye, R. A. Crain, R. G. Bower, M. Furlong, M. Schaller, T. Theuns, C. Dalla Vecchia, C. S. Frenk, I. G. McCarthy, J. C. Helly, A. Jenkins, Y. M. Rosas-Guevara, S. D. M. White, M. Baes, C. M. Booth, P. Camps, J. F. Navarro, Y. Qu, A. Rahmati, T. Sawala, P. A. Thomas, and J. Trayford. The EAGLE project: simulating the evolution and assembly of galaxies and their environments. *MNRAS*, 446:521--554, January 2015. doi: 10.1093/mnras/stu2058.

R. C. Simons, S. A. Kassin, B. J. Weiner, T. M. Heckman, J. C. Lee, J. M. Lotz, M. Peth, and K. Tchernyshyov. A transition mass in the local Tully-Fisher relation. *MNRAS*, 452:986--997, September 2015. doi: 10.1093/mnras/stv1298.

R. E. Skelton, K. E. Whitaker, I. G. Momcheva, G. B. Brammer, P. G. van Dokkum, I. Labbé, M. Franx, A. van der Wel, R. Bezanson, E. Da Cunha, M. Fumagalli, N. Förster Schreiber, M. Kriek, J. Leja, B. F. Lundgren, D. Magee, D. Marchesini, M. V. Maseda, E. J. Nelson, P. Oesch, C. Pacifici, S. G. Patel, S. Price, H.-W. Rix, T. Tal, D. A. Wake, and S. Wuyts. 3D-HST WFC3-selected Photometric Catalogs in the Five CANDELS/3D-HST Fields: Photometry, Photometric Redshifts, and Stellar Masses. *ApJS*, 214:24, October 2014. doi: 10.1088/0067-0049/214/2/24.

R. J. Smith. Variations in the initial mass function in early-type galaxies: a critical comparison between dynamical and spectroscopic results. *MNRAS*, 443:L69--L73, September 2014. doi: 10.1093/mnrasl/slu082.

R. J. Smith and J. R. Lucey. A giant elliptical galaxy with a lightweight initial mass function. *MNRAS*, 434:1964--1977, September 2013. doi: 10.1093/mnras/stt1141.

R. J. Smith, P. Alton, J. R. Lucey, C. Conroy, and D. Carter. The IMF-sensitive 1.14-μm Na I doublet in early-type galaxies. *MNRAS*, 454:L71--L75, November 2015. doi: 10.1093/mnrasl/slv132.

G. F. Snyder, P. Torrey, J. M. Lotz, S. Genel, C. K. McBride, M. Vogelsberger, A. Pillepich, D. Nelson, L. V. Sales, D. Sijacki, L. Hernquist, and V. Springel. Galaxy morphology and star formation in the Illustris Simulation at z = 0. *MNRAS*, 454:1886--1908, December 2015. doi: 10.1093/mnras/stv2078.

M. Sparre and V. Springel. The unorthodox evolution of major merger remnants into star-forming spiral galaxies. *MNRAS*, 470:3946--3958, October 2017. doi: 10.1093/mnras/stx1516.

C. Spiniello, S. Trager, L. V. E. Koopmans, and C. Conroy. The stellar IMF in early-type galaxies from a non-degenerate set of optical line indices. *MNRAS*, 438:1483--1499, February 2014. doi: 10.1093/mnras/stt2282.

C. Spiniello, M. Barnabè, L. V. E. Koopmans, and S. C. Trager. Are the total mass density and the low-mass end slope of the IMF anticorrelated? *MNRAS*, 452:L21--L25, September 2015. doi: 10.1093/mnrasl/slv079.

I. Strateva, Ž. Ivezić, G. R. Knapp, V. K. Narayanan, M. A. Strauss, J. E. Gunn, R. H. Lupton, D. Schlegel, N. A. Bahcall, J. Brinkmann, R. J. Brunner, T. Budavári, I. Csabai,

F. J. Castander, M. Doi, M. Fukugita, Z. Győry, M. Hamabe, G. Hennessy, T. Ichikawa, P. Z. Kunszt, D. Q. Lamb, T. A. McKay, S. Okamura, J. Racusin, M. Sekiguchi, D. P. Schneider, K. Shimasaku, and D. York. Color Separation of Galaxy Types in the Sloan Digital Sky Survey Imaging Data. *AJ*, 122:1861--1874, October 2001. doi: 10.1086/323301.

I. Stravinsky. *Poetics of Music in the Form of Six Lessons*. Harvard University Press, 1942. ISBN 0-674-67856-7.

S. Tacchella, C. M. Carollo, A. Renzini, N. M. F. Schreiber, P. Lang, S. Wuyts, G. Cresci, A. Dekel, R. Genzel, S. J. Lilly, C. Mancini, S. Newman, M. Onodera, A. Shapley, L. Tacconi, J. Woo, and G. Zamorani. Evidence for mature bulges and an inside-out quenching phase 3 billion years after the Big Bang. *Science*, 348:314--317, April 2015. doi: 10.1126/science.1261094.

B. A. Terrazas, E. F. Bell, B. M. B. Henriques, and S. D. M. White. The diversity of growth histories of Milky Way-mass galaxies. *MNRAS*, 459:1929--1945, June 2016. doi: 10.1093/mnras/stw673.

J. L. Tonry, A. Dressler, J. P. Blakeslee, E. A. Ajhar, A. B. Fletcher, G. A. Luppino, M. R. Metzger, and C. B. Moore. The SBF Survey of Galaxy Distances. IV. SBF Magnitudes, Colors, and Distances. *ApJ*, 546:681--693, January 2001. doi: 10.1086/318301.

P. Torrey, G. F. Snyder, M. Vogelsberger, C. C. Hayward, S. Genel, D. Sijacki, V. Springel, L. Hernquist, D. Nelson, M. Kriek, A. Pillepich, L. V. Sales, and C. K. McBride. Synthetic galaxy images and spectra from the Illustris simulation. *MNRAS*, 447:2753--2771, March 2015a. doi: 10.1093/mnras/stu2592.

P. Torrey, S. Wellons, F. Machado, B. Griffen, D. Nelson, V. Rodriguez-Gomez, R. McKinnon, A. Pillepich, C.-P. Ma, M. Vogelsberger, V. Springel, and L. Hernquist. An analysis of the evolving comoving number density of galaxies in hydrodynamical simulations. *MNRAS*, 454:2770--2786, December 2015b. doi: 10.1093/mnras/stv1986.

P. Torrey, S. Wellons, C.-P. Ma, P. F. Hopkins, and M. Vogelsberger. Forward and backward galaxy evolution in comoving cumulative number density space. *MNRAS*, 467:4872--4885, June 2017. doi: 10.1093/mnras/stx370.

C. Tortora, A. J. Romanowsky, and N. R. Napolitano. An Inventory of the Stellar Initial Mass Function in Early-type Galaxies. *ApJ*, 765:8, March 2013. doi: 10.1088/0004-637X/765/1/8.

C. Tortora, F. La Barbera, and N. R. Napolitano. Dark matter and IMF normalization in Virgo dwarf early-type galaxies. *MNRAS*, 455:308--317, January 2016. doi: 10.1093/mnras/stv2250.

J. W. Trayford, T. Theuns, R. G. Bower, J. Schaye, M. Furlong, M. Schaller, C. S. Frenk, R. A. Crain, C. Dalla Vecchia, and I. G. McCarthy. Colours and luminosities of z = 0.1 galaxies in the EAGLE simulation. *MNRAS*, 452:2879--2896, September 2015. doi: 10.1093/mnras/stv1461.

J. W. Trayford, T. Theuns, R. G. Bower, R. A. Crain, C. d. P. Lagos, M. Schaller, and J. Schaye. It's not easy being green: The evolution of galaxy colour in the EAGLE simulation. *MNRAS*, May 2016. doi: 10.1093/mnras/stw1230.

J. W. Trayford, P. Camps, T. Theuns, M. Baes, R. G. Bower, R. A. Crain, M. L. P.

Gunawardhana, M. Schaller, J. Schaye, and C. S. Frenk. Optical colours and spectral indices of z = 0.1 eagle galaxies with the 3D dust radiative transfer code skirt. *MNRAS*, 470:771--799, September 2017. doi: 10.1093/mnras/stx1051.

T. Treu, M. W. Auger, L. V. E. Koopmans, R. Gavazzi, P. J. Marshall, and A. S. Bolton. The Initial Mass Function of Early-Type Galaxies. *ApJ*, 709:1195--1202, February 2010. doi: 10.1088/0004-637X/709/2/1195.

F. van de Voort. Galaxy growth from redshift 5 to 0 at fixed comoving number density. *MNRAS*, 462:778--793, October 2016. doi: 10.1093/mnras/stw1690.

P. G. van Dokkum and C. Conroy. The Stellar Initial Mass Function in Early-type Galaxies from Absorption Line Spectroscopy. I. Data and Empirical Trends. *ApJ*, 760:70, November 2012. doi: 10.1088/0004-637X/760/1/70.

P. G. van Dokkum, K. E. Whitaker, G. Brammer, M. Franx, M. Kriek, I. Labbé, D. Marchesini, R. Quadri, R. Bezanson, G. D. Illingworth, A. Muzzin, G. Rudnick, T. Tal, and D. Wake. The Growth of Massive Galaxies Since z = 2. *ApJ*, 709:1018--1041, February 2010. doi: 10.1088/0004-637X/709/2/1018.

P. G. van Dokkum, J. Leja, E. J. Nelson, S. Patel, R. E. Skelton, I. Momcheva, G. Brammer, K. E. Whitaker, B. Lundgren, M. Fumagalli, C. Conroy, N. Förster Schreiber, M. Franx, M. Kriek, I. Labbé, D. Marchesini, H.-W. Rix, A. van der Wel, and S. Wuyts. The Assembly of Milky-Way-like Galaxies Since z ˜ 2.5. *ApJ*, 771:L35, July 2013. doi: 10.1088/2041-8205/771/2/L35.

P. G. van Dokkum, R. Bezanson, A. van der Wel, E. J. Nelson, I. Momcheva, R. E. Skelton, K. E. Whitaker, G. Brammer, C. Conroy, N. M. Förster Schreiber, M. Fumagalli, M. Kriek, I. Labbé, J. Leja, D. Marchesini, A. Muzzin, P. Oesch, and S. Wuyts. Dense Cores in Galaxies Out to z = 2.5 in SDSS, UltraVISTA, and the Five 3D-HST/CANDELS Fields. *ApJ*, 791:45, August 2014. doi: 10.1088/0004-637X/791/1/45.

A. Vazdekis, E. Casuso, R. F. Peletier, and J. E. Beckman. A New Chemo-evolutionary Population Synthesis Model for Early-Type Galaxies. I. Theoretical Basis. *ApJS*, 106:307, October 1996. doi: 10.1086/192340.

A. Vazdekis, E. Ricciardelli, A. J. Cenarro, J. G. Rivero-González, L. A. Díaz-García, and J. Falcón-Barroso. MIUSCAT: extended MILES spectral coverage - I. Stellar population synthesis models. *MNRAS*, 424:157--171, July 2012. doi: 10.1111/j.1365-2966.2012.21179.x.

B. Vulcani, D. Marchesini, G. De Lucia, A. Muzzin, M. Stefanon, G. B. Brammer, I. Labbé, O. Le Fèvre, and B. Milvang-Jensen. Mergers and Star Formation: The Environment and Stellar Mass Growth of the Progenitors of Ultra-massive Galaxies since z = 2. *ApJ*, 816:86, January 2016. doi: 10.3847/0004-637X/816/2/86.

C. Weidner, P. Kroupa, J. Pflamm-Altenburg, and A. Vazdekis. The galaxy-wide initial mass function of dwarf late-type to massive early-type galaxies. *MNRAS*, 436:3309--3320, December 2013. doi: 10.1093/mnras/stt1806.

D. R. Weisz, M. Fouesneau, D. W. Hogg, H.-W. Rix, A. E. Dolphin, J. J. Dalcanton, D. T. Foreman-Mackey, D. Lang, L. C. Johnson, L. C. Beerman, E. F. Bell, K. D. Gordon, D. Gouliermis, J. S. Kalirai, E. D. Skillman, and B. F. Williams. The Panchromatic Hubble Andromeda Treasury. IV. A Probabilistic Approach to Inferring the High-mass

Stellar Initial Mass Function and Other Power-law Functions. *ApJ*, 762:123, January 2013. doi: 10.1088/0004-637X/762/2/123.

D. R. Weisz, L. C. Johnson, D. Foreman-Mackey, A. E. Dolphin, L. C. Beerman, B. F. Williams, J. J. Dalcanton, H.-W. Rix, D. W. Hogg, M. Fouesneau, B. D. Johnson, E. F. Bell, M. L. Boyer, D. Gouliermis, P. Guhathakurta, J. S. Kalirai, A. R. Lewis, A. C. Seth, and E. D. Skillman. The High-mass Stellar Initial Mass Function in M31 Clusters. *ApJ*, 806:198, June 2015. doi: 10.1088/0004-637X/806/2/198.

S. Wellons and P. Torrey. An improved probabilistic approach for linking progenitor and descendant galaxy populations using comoving number density. *MNRAS*, 467:3887--3897, June 2017. doi: 10.1093/mnras/stx358.

K. E. Whitaker, M. Franx, R. Bezanson, G. B. Brammer, P. G. van Dokkum, M. T. Kriek, I. Labbé, J. Leja, I. G. Momcheva, E. J. Nelson, J. R. Rigby, H.-W. Rix, R. E. Skelton, A. van der Wel, and S. Wuyts. Galaxy Structure as a Driver of the Star Formation Sequence Slope and Scatter. *ApJ*, 811:L12, September 2015. doi: 10.1088/2041-8205/811/1/L12.

R. P. C. Wiersma, J. Schaye, and B. D. Smith. The effect of photoionization on the cooling rates of enriched, astrophysical plasmas. *MNRAS*, 393:99--107, February 2009a. doi: 10.1111/j.1365-2966.2008.14191.x.

R. P. C. Wiersma, J. Schaye, T. Theuns, C. Dalla Vecchia, and L. Tornatore. Chemical enrichment in cosmological, smoothed particle hydrodynamics simulations. *MNRAS*, 399:574--600, October 2009b. doi: 10.1111/j.1365-2966.2009.15331.x.

R. F. G. Wyse, G. Gilmore, and M. Franx. Galactic Bulges. *ARA&A*, 35:637--675, 1997. doi: 10.1146/annurev.astro.35.1.637.

D. Zaritsky, J. E. Colucci, P. M. Pessev, R. A. Bernstein, and R. Chandar. Evidence for Two Distinct Stellar Initial Mass Functions: Probing for Clues to the Dichotomy. *ApJ*, 796:71, December 2014. doi: 10.1088/0004-637X/796/2/71.

J. Zavala, C. S. Frenk, R. Bower, J. Schaye, T. Theuns, R. A. Crain, J. W. Trayford, M. Schaller, and M. Furlong. The link between the assembly of the inner dark matter halo and the angular momentum evolution of galaxies in the EAGLE simulation. *MNRAS*, 460:4466--4482, August 2016. doi: 10.1093/mnras/stw1286.

J. Zjupa and V. Springel. Angular momentum properties of haloes and their baryon content in the Illustris simulation. *MNRAS*, 466:1625--1647, April 2017. doi: 10.1093/mnras/stw2945.

Curriculum Vitae

I was born on a clear midnight in 1981 in the rustic village of Veghel (Brabant) where I also enjoyed my upbringing. After a small and thoroughly fruitless detour to Delft I finished my Master of Science in Astrophysics at the University of Leiden in 2007. The only logical continuation seemed to be to start a wine import business, which I thus pursued diligently, resulting in a company which still today spreads its wings over the best hilltops north of the Mediterranean and south of the Rhine. However my true calling in life turned out to be not drinking wine, but rather looking at the stars. So in 2013 I started my PhD in Leiden as a `de Sitter' fellow, studying the cosmos both from the perspective of a theoretical physicist as well as from the perspective of an astronomer. The rest is history confided to these pages.

List of publications

1. Bart Clauwens, and Rachel Jeannerot. *D-term inflation after spontaneous symmetry breaking*. Journal of Cosmology and Astroparticle Physics, Issue 03, id.016, 37 pp. (2008).

2. Chael Kruip, Jan-Pieter Paardekooper, Bart Clauwens, and Vincent Icke. *Mathematical properties of the SimpleX algorithm*. Astronomy and Astrophysics, Volume 515, id.A78, 18 pp. (2010).

3. Bart Clauwens, Joop Schaye, and Marijn Franx. *An assessment of the evidence from ATLAS^{3D} for a variable initial mass function*. Monthly Notices of the Royal Astronomical Society, Volume 449, Issue 4, p.4091-4104 (2015). [Chapter 2]

4. Bart Clauwens, Joop Schaye, and Marijn Franx. *Implications of a variable IMF for the interpretation of observations of galaxy populations*. Monthly Notices of the Royal Astronomical Society, Volume 462, Issue 3, p.2832-2846 (2016). [Chapter 3]

5. Bart Clauwens, Marijn Franx, and Joop Schaye. *A large difference in the progenitor masses of active and passive galaxies in the EAGLE simulation*. Monthly Notices of the Royal Astronomical Society: Letters, Volume 463, Issue 1, p.L1-L5 (2016). [Chapter 4]

6. Allison R. Hill, Adam Muzzin, Marijn Franx, Bart Clauwens, Corentin Schreiber, Danilo Marchesini, Mauro Stefanon, Ivo Labbé, Gabriel Brammer, Karina Caputi, Johan Fynbo, Bo Milvang-Jensen, Rosalind E. Skelton, Pieter van Dokkum, and Katherine E. Whitaker. *The Mass, Color, and Structural Evolution of Today's Massive Galaxies Since $z \approx 5$*. The Astrophysical Journal, Volume 837, Issue 2, id.147, 17 pp. (2017).

7. Bart Clauwens, Allison Hill, Marijn Franx, and Joop Schaye. *The average structural evolution of massive galaxies can be reliably estimated using cumulative galaxy number densities*. Monthly Notices of the Royal Astronomical Society: Letters, Volume 469, Issue 1, p.L58-L62 (2017). [Chapter 5]

8. Camila A. Correa, Joop Schaye, Bart Clauwens, Richard G. Bower, Robert A. Crain, Matthieu Schaller, Tom Theuns, and Adrian C. R. Thob. *The relation between galaxy morphology and colour in the EAGLE simulation*. Monthly Notices of the Royal Astronomical Society: Letters, vol. 472, issue 1, pp. L45-L49 (2017).

9. Bart Clauwens, Joop Schaye, Marijn Franx, and Richard G. Bower. *The three phases of galaxy formation*. Submitted to Monthly Notices of the Royal Astronomical Society (2017). [Chapter 6]

Acknowledgements

First of all, I would like to thank my promotors Joop Schaye and Marijn Franx for their guidance in defining clear research goals, for the many interesting conversations, and for their scientific rigour which helped me to become an independent scientist.

I would like to thank all those who helped to shape my scientific ideas in these last years through a constructive dialogue, especially: Ana Achúcarro, Vicente Atal, Chris Barber, Rychard Bouwens, Alexey Boyarsky, Jarle Brinchmann, Margot Brouwer, Camila Correa, Eric Emsellem, Jeroen Franse, Madusha Gunawardhana, Allison Hill, Bin Hu, Artem Ivashko, Walter Jaffe, Fabian Köhlinger, Koen Kuijken, Ivo Labbe, Hongyu Li, Mark Lovell, Sean McGee, Adam Muzzin, Enrico Pajer, Pablo van Pippen, Sylvia Ploeckinger, Joachim Rosdahl, Marijke Segers, Chiara Spiniello, Caroline Straatman, Geert Jan Talens, Jesus Torrado, James Trayford, Valeri Vardanyan, Glenn van de Ven, Wessel Valkenburg and Yvette Welling.

Furthermore, I would like to thank Bruno Henriques and various anonymous referees for a careful review of the papers in this thesis.

Finally, I would like to thank my family for their support which allowed me to rise far above the treetops, above the Oort cloud and beyond the confines of the Milky Way, without losing touch to the ground and earthly matters like the birth of our son Jesper Albert Clauwens and the continuation of our company Pandora's Bottle.